Alexander N. Evgrafov   *Editor*

Advances in Mechanical Engineering

Selected Contributions from the Conference "Modern Engineering: Science and Education", Saint Petersburg, Russia, June 2016

Springer

Lecture Notes in Mechanical Engineering

About this Series

Lecture Notes in Mechanical Engineering (LNME) publishes the latest developments in Mechanical Engineering—quickly, informally and with high quality. Original research reported in proceedings and post-proceedings represents the core of LNME. Also considered for publication are monographs, contributed volumes and lecture notes of exceptionally high quality and interest. Volumes published in LNME embrace all aspects, subfields and new challenges of mechanical engineering. Topics in the series include:

- Engineering Design
- Machinery and Machine Elements
- Mechanical Structures and Stress Analysis
- Automotive Engineering
- Engine Technology
- Aerospace Technology and Astronautics
- Nanotechnology and Microengineering
- Control, Robotics, Mechatronics
- MEMS
- Theoretical and Applied Mechanics
- Dynamical Systems, Control
- Fluid Mechanics
- Engineering Thermodynamics, Heat and Mass Transfer
- Manufacturing
- Precision Engineering, Instrumentation, Measurement
- Materials Engineering
- Tribology and Surface Technology

Alexander N. Evgrafov
Editor

Advances in Mechanical Engineering

Selected Contributions from the Conference
"Modern Engineering: Science
and Education", Saint Petersburg, Russia,
June 2016

Springer

Editor
Alexander N. Evgrafov
Saint-Petersburg Polytechnic University
Saint-Petersburg
Russia

Preface

The "Modern Engineering: Science and Education" (MESE) conference was initially organized by the Mechanical Engineering Department of Peter the Great St. Petersburg Polytechnic University in June 2011 in St. Petersburg (Russia). It was envisioned as a forum to bring together scientists, university professors, graduate students, and mechanical engineers, presenting new science, technology, and engineering ideas and achievements.

The idea of holding such a forum proved to be highly relevant. Moreover, both location and timing of the conference were quite appealing. Late June is a wonderful and romantic season in St. Petersburg—one of the most beautiful cities, located on the Neva riverbanks, and surrounded by charming greenbelts. The conference attracted many participants, working in various fields of engineering: design, mechanics, materials, etc. The success of the conference inspired the organizers to turn the conference into an annual event.

More than 130 papers were presented at the fifth conference MESE-2016. They covered topics ranging from mechanics of machines, materials engineering, structural strength, and tribological behavior to transport technologies, machinery quality, and innovations, in addition to dynamics of machines, walking mechanisms, and computational methods. All presenters contributed greatly to the success of the conference. However, for the purposes of this book only 19 papers, authored by research groups representing various universities and institutes, were selected for inclusion. I am particularly grateful to the authors for their contributions and all the participating experts for their valuable advice. Furthermore, I thank the staff and management of the university for their cooperation and support, and especially, all members of the program committee and the organizing committee for their work in preparing and organizing the conference.

Last but not least, I thank Springer for its professional assistance and particularly Mr. Pierpaolo Riva who supported this publication.

Saint-Petersburg, Russia   Alexander N. Evgrafov

Contents

The Combined Cold Axial Rotary Forging of Thick Hollow Flanges

L.B. Aksenov and S.N. Kunkin

Abstract The paper presents the research on two technologies of cold axial rotary forging, which combine the traditional rotary forging with multi-upsetting and radial extrusion. Technologies are developed for the manufacture of thick flanges, i.e., flanges thicker than the wall thickness of the original tube blank, when the process is limited by the buckling of the workpiece. The proposed technologies provide for stability of the workpieces during processing and enable manufacturing of flanges with dimensions DN 150–450 of the European Standards 42.05.04, 42.05.07. Rotary forging can also be carried out with conical or cylindrical rolls. The results of modeling technologies are detailed employing in the simulation software Deform 3D. The combined rotary-forging technologies are particularly effective for the production of flanges from tube blanks, including stainless steel, the connection to which they are intended to effect.

Keywords Axial rotary forging · Multi-upsetting · Radial extrusion · Stability of the workpiece · Hollow flanges · Conical roll · Cylindrical rolls · Computer simulation

Introduction

Large quantities of parts such as flanges are used in a variety of industries. The nomenclature of these parts is very diverse and subject to various standards. Manufacture of the flange parts is carried out according to several technologies, but most of them do not result in a high utilization rate of the metal [1]. Many of the technologies for production of flanges are based on using hot forming with subsequent additional machining [2]. In this case, higher-ductility deformation occurs

L.B. Aksenov (✉) · S.N. Kunkin
Peter the Great St. Petersburg Polytechnic University, St. Petersburg, Russia
e-mail: l_axenov@mail.spbstu.ru

S.N. Kunkin
e-mail: kunkin@spbstu.ru
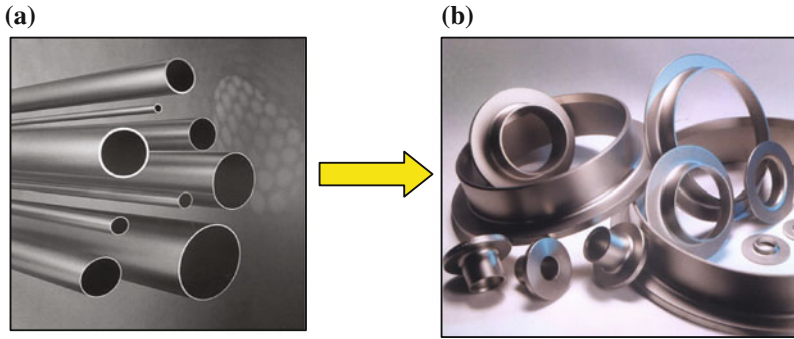
Fig. 1 Metal blanks for axial rotary forming (a) and rotary formed details (b)

Fig. 2 Schemes of axial rotary forging technologies by conical (a) and cylindrical rolls (b)
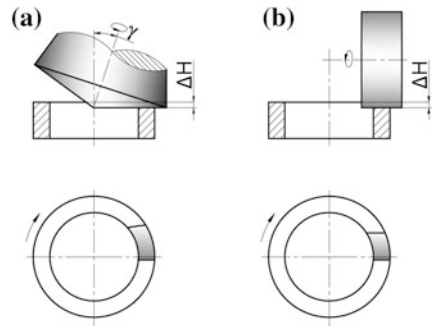
at low technological power. However, the processes of hot deformation incur considerable costs for heating metal, and the forging parts are covered with scale and require subsequent machining. Therefore, the application of these processes is not very effective for the industry.

The technology of axial-rotary forging was designed for the production of axisymmetric parts from bar or tubular workpieces (Fig. 1). Rotary forging is representative of the processes involving the local deformation of the treated metal [3–6] and has more than a century of history [7, 8]. While only part of the workpiece is in contact with the forming tool (Fig. 2), this reduces the contact area, the magnitude of the contact stresses, and, consequently, the required technological force.

The advantages of cold rotary forging are that it requires no heating and is characterized by the high accuracy and good quality of formed surface. At the same time, the technological force necessary for cold rotary forming will be higher than for the hot one, but the plasticity of the formed metal is lower. That is why this technology involves higher requirements for their analysis [9]. Currently processes of rotary forming are distributed worldwide, and machines for implementing them are manufactured in all industrialized countries [10, 11].
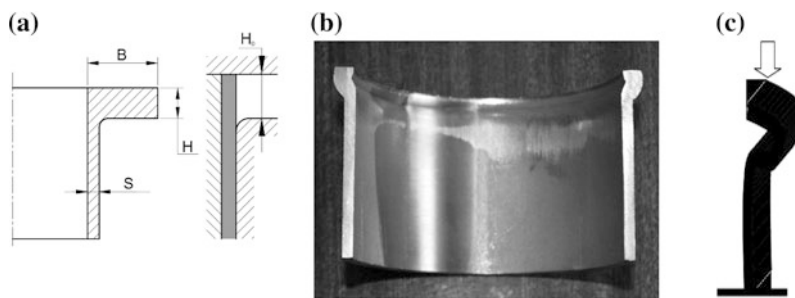
Fig. 3 Loss of stability of the workpiece at the initial moment of rotary forging: a the workpiece at the initial moment of rolling; b the tube blank with losing of stability; c deformation of the rod under axial force

This paper investigates the production of flanges with the thickness of the flange part greater than the wall thickness of a tube blank. Flanges with thickness about the thickness of the tube wall can be successfully produced by a rotary outward flanging [12]. Thickened flanges with the small width of the flange (less than two of the wall thickness of the original tube blank) can be manufactured by rotary forging with one operation of rotary upsetting of the upper part of the workpiece [13, 14]. The problem is the production of thickened flanges with the wide flange part [15].

The recommended value of the forming part of the H_0 is determined by the stability of the workpiece and does not exceed the value 2S, where S is the wall thickness of the tube blank (Fig. 3a). At such a value of the forming portion, its volume is not enough to form the desired flange geometry. The height of the forming part of the workpiece cannot be increased because of the buckling that leads to the formation of folds and cracks on the inside of the flange (Fig. 3b). The loss of stability of the tube blank is very similar to the loss of stability of the rod under the action of longitudinal force (Fig. 3c). It should be noted that the formation of the flanges, with thickness $H_0 = 1.5S$ and width $B = 4C$, requires the equivalent volume of the outer metal blanks $H_0 = 4S$. It is not realizable with the usual technology of rotary forging.

The paper presents the results of a study of two cold axial rotary forging technologies, which combined the basic principle of the face rotary forging with multi-upsetting or radial extrusion of the workpiece.

The Tool for Axial Rotary Forging

Schemes of the rotary forging of thickened flanges can be implemented with conical rolls (Fig. 4a) or cylindrical rolls (Fig. 4b). The conical rolls have a more complex geometry, and their size is related to the size formed from the details. The diameter of the cylindrical rolls does not depend on the size of the formed details, but only on
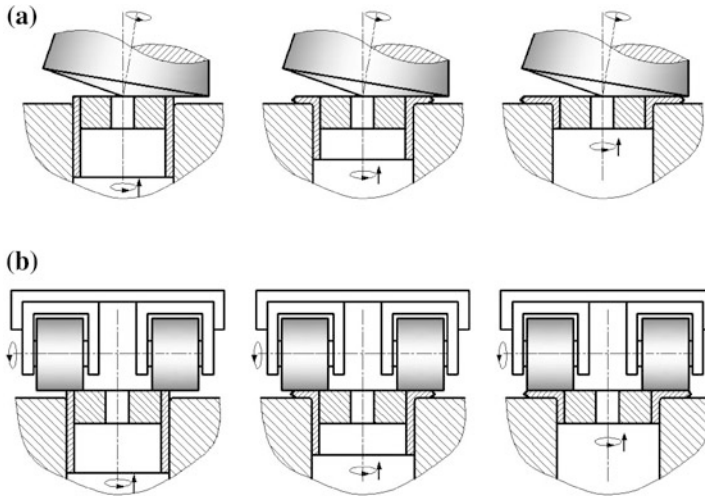
Fig. 4 Schemes of the axial rotary forging of flanges by conical (a) and cylindrical rolls (b)

the design features of rotary forging machine. The rotational motion of the work-piece is performed by the drive of the machine, while forging rolls may be driven from the workpiece due to friction or have their own drive.

For the implementation of the technological process of rotary forging, the workpiece is placed in the die with a radial clearance not more than 0.3 mm, which is needed to fix the workpiece during the period of forming. At the initial stage of rotary forging, the workpiece is fixed by friction between the workpiece and the forming roll. Next, the workpiece is pressed in the die that ensures the transfer of the torque necessary for rotation of the forming roll. For rotary forging, the profile of the flange is formed in the space between the die, mandrel and forming roll. The die and forming roll are made of tool steel and hardened to hardness HRC = 56–63. The roughness of the tool determines the surface quality of formed parts and should be no worse than Ra = 0.63.

The Technology of Rotary Forging, Combined with Multi-Upsetting

For this technology, the tube blank is placed above the die at some value H_0, then the rotary forging is carried out and workpiece is deformed up to the flange thickness H (Fig. 5). Because it is impossible to achieve the formation of the required width of the flange at a single step, the workpiece is lifted and deformed again. This is repeated several times until the desired width of flange is achieved.
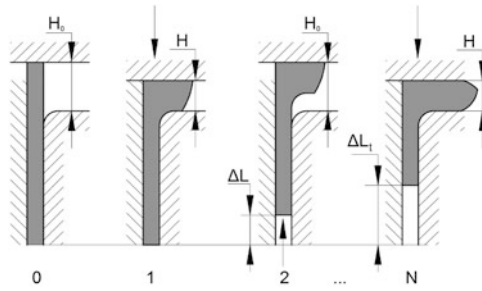
Fig. 5 Scheme of the rotary forging of thickened flanges with multi-upsetting: ΔL—feed of the workpiece at each step of upsetting; ΔL_t—the total feed of the workpiece
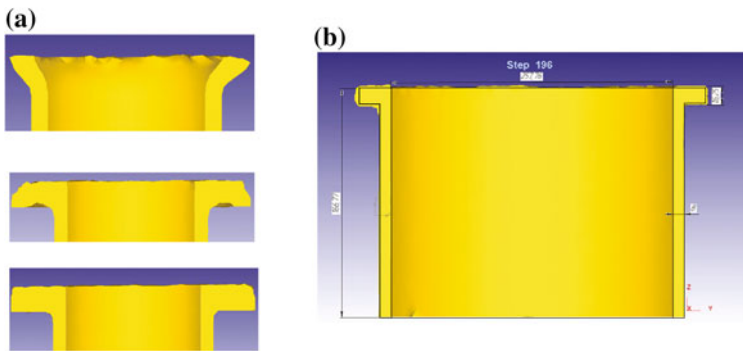
Fig. 6 Simulation of the rotary forging of a flange with multi-upsetting of the tube blank (a) and comparison of a formed profile with required profile of the flange (b)

Thus, the technology is discrete. After each upsetting, stopping the rotary forging and lifting the workpiece to a new height are required. Furthermore, the physical contact of the workpiece with the forming roll may be avoided, but the deformation is not performed. The number of steps of upsetting is determined by the geometry of the manufactured flanges, and it may be 5–15. The time for one stage of rotary forging is 5–10 s. Initially, the workpiece is lifted to a small height (1.5–2.0)S, which prevents the loss of stability of the workpiece. At subsequent steps, when part of flange has been formed, this height may be increased to (2.0–2.5)S which provides rotary forging of the flanges with the dimensions H = (1, 2–1, 3)S and B = (5–7)S.

Simulation of the rotary-forging process with the software "Deform 3D" enables analyzing the stress-strain state of the workpiece during the forming process. Figure 6 shows the various stages of the forming process of the flange of a tube blank with a diameter of 250 mm and a wall thickness of 7 mm.

The rotary forging was done with a conical roll with angle of inclination $\gamma = 10^{\circ}$. The magnitude of a single feed of workpiece was ΔL = 0.3 mm/rev. The rotation

speed of the die installed in its tube blank was n = 100 rev/min. Simulation showed stability of the process of deformation of a flange of the desired size and a sufficient reserve of plasticity of a metal to be deformed without breaking. Finite element modeling of the rotary-forging process has been effectively used by many researchers [16–18], but it has some features that increase the computation time [19]. For the computer simulation, 20–24 work hours were requires with a four-core computer.

Face Rotary Forming Technology Combined with Radial Extrusion

This technology, unlike the previous one, is continuous. The first stage is identical to axial rotary-forging technology, combined with multi-upsetting, in which the workpiece is lifted some height, providing a single upsetting without buckling. Next, the constant gap is maintained between the forging roll and the die, and the workpiece is continuously fed towards up to the forging roll(s), ensuring the forming of the flange part (Fig. 7). The technology requires that the axial feed of the device feeding the workpiece is of a sufficiently large force, because it should provide axial displacement of the workpiece to overcome the friction force in a tool set. But it must also be sufficient for radial extrusion of the workpiece into the space formed by the forging roll and the die.

   Figure 8 illustrates details on the simulation of the flange rotary forging by two cylindrical rolls from a tube blank (welded pipe AISI 360L) with an outer diameter of 219.1 mm and a wall thickness of 7.8 mm. The amount of feed per revolution $\Delta L = 1.0$ mm/rev, the speed of rotation of the die with tube blank installed in it—n = 60 rpm. This simulation showed stability of the process of deformation of a flange of the desired size and a sufficient reserve of plasticity of a metal to be deformed without breaking. Cylindrical forging rolls do not require the extra drive and rotate due to the friction forces at the contact of rolls with a rotating workpiece.

Fig. 7 Scheme of the axial rotary forging of thickened flanges with extrusion: ΔL—feed of the workpiece per one revolution of the workpiece; ΔL_t—the total feed; H—flange thickness; stages of rotary forging: (*0*) primary, (*1, 2*) intermediate, (*3*) final
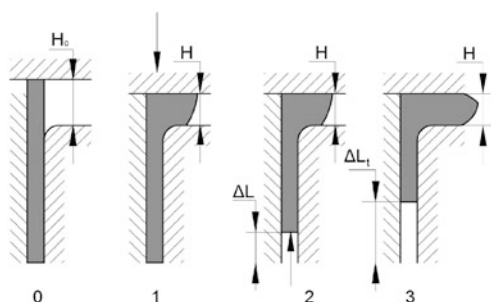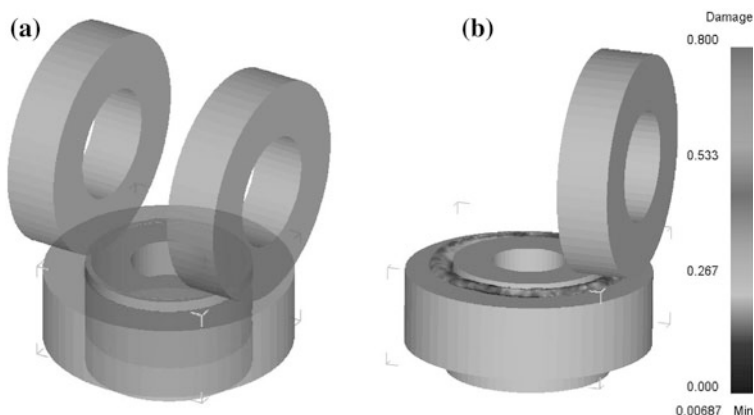
Fig. 8 Computer simulation of rotary forging of flange with extrusion by two cylindrical rolls: a design scheme; b distribution of the damage criterion in the workpiece

Fig. 9 The flange, rotary forged from a tube blank with a diameter of 219.1 mm

Discussion

The technologies enabled manufacturing various flanges with size DN 150–450 of European standards 42.05.04 and 42.05.07. An example of a rotary forged flange from a tube blank with a diameter of 219.1 mm and a wall thickness of 7.8 mm is shown in Fig. 9: flange thickness—9.5 mm, flange width—31 mm, the radius of the transition from the tubular part to the flange R = 12.7 mm, material AISI 316L. The kinematics of the machine ensures implementation of combined technologies for rotary forging is shown in Fig. 10.

The research found that, when rotary forging from certain types of flanges, mainly thick, but not wide, there are two problems related to accurate formation of the flange geometry. The first is the forming of the outer cutoff of the flange. This problem is successfully solved when using forging rolls with rims that stop the

Fig. 10 Kinematic scheme of the machine for axial combined rotary forging
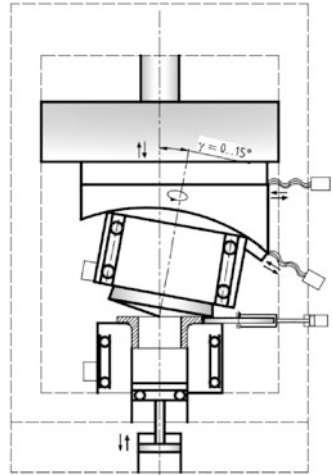
metal flow from the flange center to its periphery and promotes forming of a smooth side surface of the flange.

The second problem relates to the forming of the internal right angle of the flange (transition of end surface of the flange to the internal diameter of the tube blank). This angle is sometimes not formed completely, because the main flow of metal during rotary forging is directed to the outside of the flange. This inner angle may be formed at the last stage of the process, when the deformed metal is in a confined space framed by tools—forging roll, a die and a mandrel. However, the formation of the internal angle in the state of nonuniform compression requires a significant increase in the required force of deformation. In the computer simulation, the process employed such a solution, and it showed a good formation of the flange.

Another possible way of forming the inner corner of the flange is to change the direction of metal flow at the latter stages of the rotary forging by moving the rolls relative to the axis of the workpiece [20, 21]. This initially achieves a complete forming of the outer part of the flange, and then the metal flow is redirected into the inner area of the flange. The required forming force in this case is less, but it is necessary to implement the movement of the forming roll (or rolls) in the forming process. Then the rotary-forged flanges are subjected to slight machining of the end and side surfaces of a flange part. The utilization rate of the metal case of rotary forging with the extrusion, multi-upsetting, or combination thereof is about 95%. Combined technologies of rotary forging can be successfully implemented at the rotary-forging machines of the current generation with numerical control and, in particular, with multi-axis tool motion [22].

Resume

- The combined cold axial rotary forging can significantly expand the technological capabilities of the metal forming and realize the manufacturing of thicker flanges from the tube blanks.
- The technology of axial rotary forming with multi-upsetting is effective for producing thickened flanges in a range of sizes DN 150–450, the relevant European Standard 42.05.07. The technology is designed for modern rotary-forging machines with programmed control.
- The axial rotary-forging technology with radial extrusion provides manufacturing thickened flanges ranging sizes DN150–300, the relevant European standard 42.05.04. This technology requires increased force for ejection of workpieces for its implementation.
- The geometry of the formed flanges can be significantly improved by the use of forming rolls with rims and an active control of metal flow in the process of rotary forming.

References

1. Han X, Hua L (2009) Comparison between cold rotary forging and conventional forging. J Mech Sci Technol 23:2668–2678
2. Plancak ME, Vilotic DZ, Stefanovic MC, Movrin DZ, Kacmarcik IZ (2012) Orbital forging—a plausible alternative for bulk metal forming. J Trends Dev Mach Assoc Technol 16(1):35–38
3. Nowak J, Madej L, Ziolkiewicz S, Plewinski A, Grosman F, Pietrzyk M (2008) Recent development in orbital forging technology. Int J Mater Form (Supp 1):387–390
4. Groche P, Fritsche D, Tekkaya EA, Allwood JM, Hirt G, Neugebauer R (2007) Incremental bulk metal forming. Ann CIRP 56:635–656
5. Standring PM (1999) The significance of nutation angle in rotary forging. In: Proceeding of the 6th ICTP in advanced technology of plasticity, vol III, pp 1739–1744
6. Nowak J, Madej L, Ziolkiewicz S, Plewinski A, Grosman F, Pietrzyk M (2008) Recent development in orbital forging technology. Int J Mater Form (Supp 1):387–390
7. Slick EE (1918) The slick wheel mill. The Iron Age 102(9):491–498
8. Massey HF (1929) British Patent Specification, #319065
9. Deng XB, Hua L, Han XH (2011) Numerical and experimental investigation of cold rotary forging of a 20CrMnTi alloy spur bevel gear. Mater Des 32:1376–1389
10. Global Metal Spinning Solutions Inc. (2016) CNC wheel forming and rotary forging machines. Retrieved: http://www.globalmetalspinning.com/. Accessed 10 Apr 2016
11. Orbitform Group (2016) Roller forming. Retrieved: http://www.orbitform.com/. Accessed 29 Mar 2016
12. Aksenov LB, Kunkin SN (2014) Cold axial rotary outward-flanging of tube blanks by cylindrical rollers. In: Global science and innovation: materials of the III international scientific conference, Accent Graphics communications, Chicago, USA, pp 306–310
13. Aksenov LB, Kunkin SN (2014) Cold axial rotary forging of hollow shaft flanges.In: European science and technology: materials of the VII international research and practice conference, vol II. Vela Verlag Waldkraiburg, Munich, Germany, pp 393–396

14. Aksenov LB, Elkin NM, Kunkin SN (2011) Tortsevaya raskatka flantsevyih detaley trubnyih soedineniy // Metalloobrabotka, 3(63):31–36 (in Russian)
15. Aksenov LB, Kunkin SN (2014) Razvitie processov torcevoyj raskatki v Sankt-Peterburgskom gosudarstvennom politekhnicheskom universitete. Cvetnihe metalli 4:24–28 (in Russian)
16. Deng XB, Hua L, Han XH (2011) Numerical and experimental investigation of cold rotary forging of a 20CrMnTi alloy spur bevel gear. Mater Des 32:1376–1389
17. Liu G, Yuan S, Zhang M (2001) Numerical analysis on rotary forging mechanism of a flange. J Mater Sci Technol 17(1):129–131
18. Wang GC, Zhao GQ (2002) Simulation and analysis of rotary forging a ring workpiece using finite element method. Finite Elem Anal Des 38(12):1151–1164
19. Munshi M, Shah K, Cho H, Altan T (2005) Finite element analysis of orbital forming used in spindle/inner ring assembly. In: 8th ICTP 2005—International conference on technology of plasticity, Verona, 9–13 October 2005
20. Evgrafov A (ed) (2016) Advances in mechanical engineering. (Lecture notes in mechanical engineering). Springer International Publishing, Switzerland, pp 175–181. doi:10.1007/978-3-319-29579-4
21. Sovremennoe mashinostroenie: nauka i obrazovanie: Materialyi 4-y Mezhdunarodnoy nauchno-prakticheskoy konferentsii / pod red. M.M.Radkevicha i A.N.Evgrafova – SPb.: Izd-vo Politehn. un-ta, 2014, pp 608–614 (in Russian)
22. MJC Engineering & Technology. Rotary forging equipment. Retrieved: http://www.mjcengineering.com/. Accessed 13.04.2016

Bench Tests of Vibroacoustic Effects

Pavel A. Andrienko, Vladimir I. Karazin and Igor O. Khlebosolov

Abstract The paper touches upon issues of vibroacoustic tests of manufactured and assembled units because the final assembly of units or equipment usually enables limiting the range of effects and modeling the actual behavior of the equipment under test. A characteristic property of the required test equipment is the possibility to initiate combined vibroacoustic loads on various mechanical systems. This imposes a number of requirements upon the designed equipment. The paper gives a number of examples for calculating the design parameters of vibroacoustic test benches.

Keywords Test equipment · Vibroacoustic test benches · Acoustic test benches · Vibrorotary test benches · Electro-pneumatic generator

The process of simulating various systems' behavior in liquid or gaseous media for many years has been of interest among scientists and developers in various fields of science and technology. The traditional method to simulate occurring loads, when testing units, uses shock and vibrating tables [1, 2] which use various layouts of impact simulation (mechanical, hydraulic, pneumatic, electric, etc.). A distinctive feature of such tests is that each unit or piece of equipment is impacted separately. This, in turn, leads to the "overtesting" effect because there has to be overlapping impact ranges (duration, frequency, forcing, etc.), significantly exceeding actual values of operational conditions of the equipment itself.

However, it is obvious that, in the case of moving some body in liquid or gaseous media, the equipment's frame or casing consumes power load (overload),

P.A. Andrienko (✉) · V.I. Karazin · I.O. Khlebosolov
Peter the Great Saint-Petersburg Polytechnic University, Saint Petersburg, Russia
e-mail: andrienko-p@mail.ru

V.I. Karazin
e-mail: visv05@mail.ru

I.O. Khlebosolov
e-mail: khlebosolov@mail.ru

and interior units and apparatus are subject to composite action. As a matter of fact, this action is a combination of vibratory load and acoustic action.

In this case, not only are the aerodynamic properties of the equipment (or its outer frame) of great interest, but also a number of other parameters. An important group of such parameters of systems and equipment is the inertial properties. They significantly influence the system's behavior when it is moving, its stability and controllability [3–6]. It is obvious that coordinates of the center of mass and inertia components should be determined after the final assembly of the equipment unit in the frame.

Besides, it should be noted that mathematical description (modeling) of such processes, despite the development of modern computational technologies and software, usually requires experimental verification, especially at the stage of final adjustment and improving the technology of producing, installing, integrating, and placing fixing and anchoring elements, etc.

There occurs the necessity of creating hybrid testing machines to test the produced and assembled units of the equipment before their launching into manufacture (in the case of stock-produced equipment) or their final acceptance (in the case of one-off equipment), because the final assembling of units or the equipment generally allows limiting the range of generated effects and modeling the actual behavior of the equipment under test. The characteristic feature of such testing equipment should become the opportunity to create combined vibroacoustic loads upon the various mechanical systems.

The combined vibratory and acoustic actions are implemented in a test bench [7], which has a reverberation chamber of about 3 m^3 in volume and electro-pneumatic sound generators. The table for placing the test object is combined with the vibrator's instrument table, which is installed in the lower part of the test bench. The combination of mechanical and acoustic vibrations creates a specific medium according to the chosen simulation action.

An alternative to such a way of load simulation is using electro-pneumatic vibrators, which enable combining acoustic pressure upon the object with the point-recurrent force action within the set range of frequencies [8].

The purpose of this paper is to analyze a number of parameters of made effects and how they can affect the design of the testing equipment.

Let us note that vibroacoustic loads are created by one or several electro-pneumatic vibrators. The operation principle of pneumatic vibrators is based on creating air flows aimed at the test object.

The most important parameters are the parameters of the air medium that create the impact: the correlation of pressures inside the pneumatic vibrator and of the environment; air density; the ratio of specific heats; and acoustic speed. Besides, the design parameters of the pneumatic vibrator and the test object should also be taken into account: the diameter of the nozzle and nozzle throat; the distance between the nozzle and the object; and the jet angle towards the object.

One of the important factors of the created action is the speed of the air stream, coming out of the electro-pneumatic vibrator. The initial data for calculation is the working air pressure within the pneumatic generator P_p, the air density $\rho = 1.29$

kg/m^3, the ratio of specific heats $k = 1.4$, and the acoustic speed of the air $v_s = 322$ m/s.

If the section of the outlet, from which the flow emerges, has a constant diameter, then the flow speed is determined by the equation:

$$v = \sqrt{\frac{2 \cdot k \cdot P_p \left[1 - \left(\frac{P_{out}}{P_p}\right)^{\frac{k-1}{k}}\right] \cdot \left(\frac{P_{out}}{P_p}\right)^{\frac{1}{k}}}{(k-1) \cdot \rho}}, \tag{1}$$

where P_{out} is the pressure at the nozzle outlet.

Allowing for the stated parameters enables determining the dependence of the flow speed on the pressure difference inside and outside the electro-pneumatic vibrator (it should be noted that, depending on the pressure difference, the flow mode can be precritical and critical, at which the flow speed equals the speed of sound):

According to the shape of the section through which the air flow emerges, the flow speed can vary over a wide range of values. Figure 1 shows the dependencies of the speed of the flow coming out of the nozzle with a round section and of the flow coming through the de Laval nozzle. The nozzles, according to theory [9, 10], ensure the maximum flow speed of the gas

The impact force of the air flow out of the nozzle is determined by the formula [11]:

$$F = \left(1.06 - 4 \cdot 10^{-4} \cdot \frac{l}{d_0}\right) \cdot \rho \cdot v^2 \cdot S, \tag{2}$$
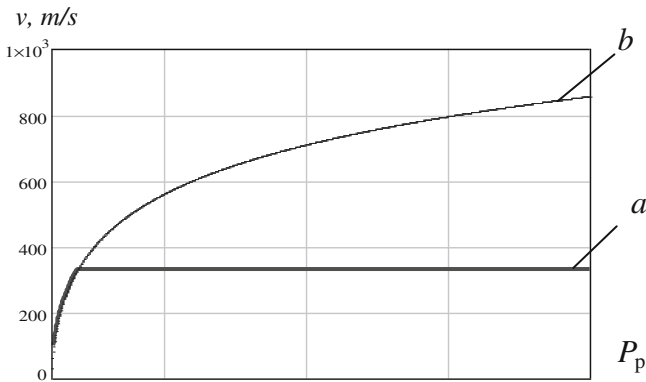
Fig. 1 The view of the dependency of the gas-flow speed on working pressure: *graph a*—out of the nozzle with the uniform round section; *graph b*—out of the de Laval nozzle

F
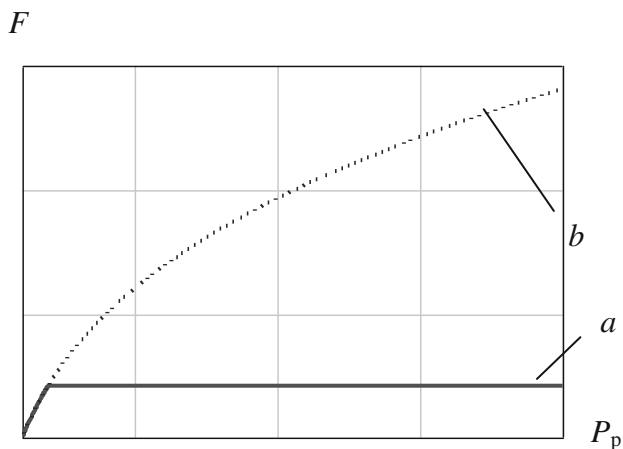
Fig. 2 The view of the dependency of the flow impact force on working pressure: *graph a*—out of the nozzle; *graph b*—out of the de Laval nozzle

where l is the distance between the nozzle and the test object, d_0 is the diameter of the nozzle, and S is the area of the nozzle's cross-section.

The approximate view of dependency (2) for the flow out of the nozzle and the de Laval nozzle is shown in Fig. 2.

It is obvious that the dependency of the flow-impact force on the distance between the nozzle and the object under action will be linear.

To increase the impact force, several gas flows can be used, aimed at one point. In this case, the flow will be directed at angle α towards the surface and dependency (2) takes the form of:

$$F = \rho \cdot v^2 \cdot S \cdot \sin \alpha, \tag{3}$$

An example of such a configuration is given in Fig. 3.

To create a transient load, the idea of creating intermittent air flows, directed at the test object, seems interesting. Such flows are obtained when the compressed air comes through spinning and immovable discs which have through-holes (the scheme is similar to a large number of schemes of gas passing through turbines).

The level and frequency of the vibratory action are regulated by pressure in the power-supply tube of pneumatic vibrators and the rotary speed of their electric motors. The number of holes and their relative positions in the discs can be used to regulate the pulse ratio (Fig. 4).

A wide range of generated frequencies imposes specific requirements upon the test object's suspension and restraint system, which should be untuned from natural frequencies and the frequencies of the testing action. The design model of the suspension is given in Fig. 5.
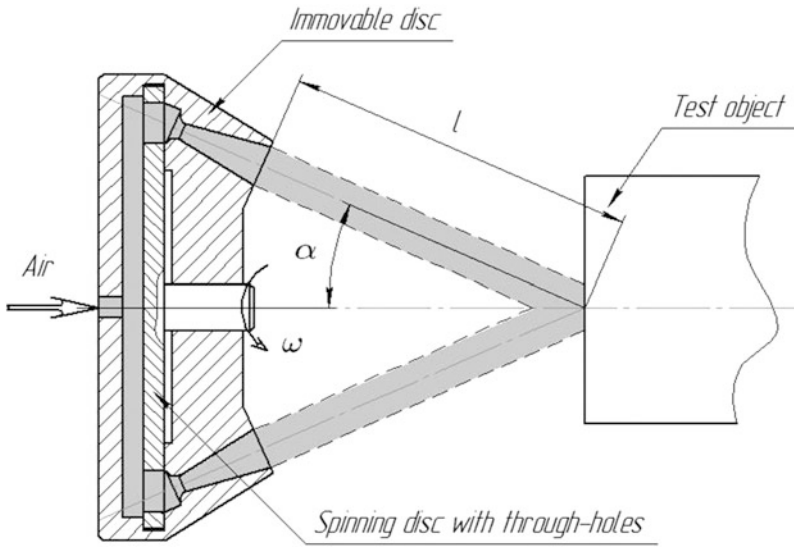
Fig. 3 The load configuration with the use of several gas flows

Fig. 4 An example of the dependency of the transient load F on the rotation angle q of the electro-pneumatic vibrator's moving disc
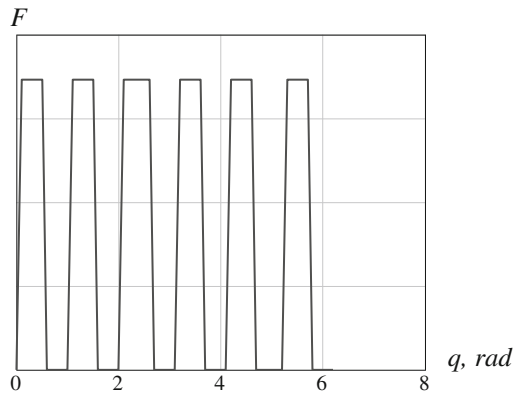
The design dependencies of the dimensioned low-frequency suspension are given below and enable determining the natural frequencies of the suspension. The initial parameters are the test object's mass, the length of wire ropes, and their diameter and quantity.

The natural (cross, vertical) frequency of the object f_{cross} is determined by the formula of a physical pendulum:

$$f_{\text{cross}} = \frac{1}{2\pi} \sqrt{\frac{g}{L_1}}, \tag{4}$$
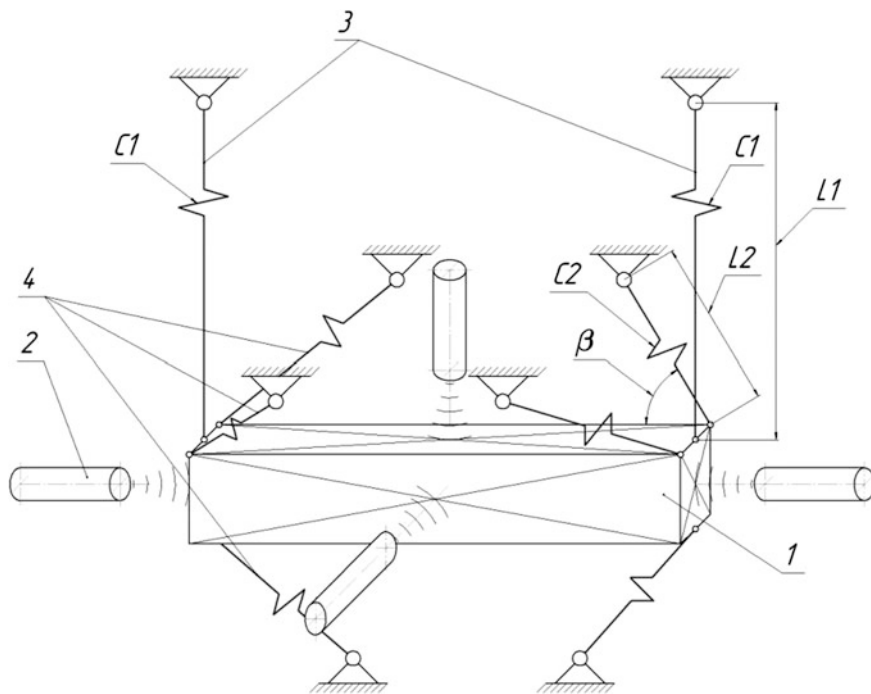
Fig. 5 The design model of the suspension: *1* test object; *2* electro-pneumatic generators; *3* vertical suspension; *4* tension cables

where g is gravitational acceleration and L_1 is the length of the vertical suspension.

The natural long (along axes X, Y) frequency f_{al} is determined by the expression:

$$f_{al} = \sqrt{\frac{E \cdot S_{wr} \cdot \cos \beta \cdot n}{L_2 \cdot M_{wr}}}, \tag{5}$$

where E is the Young's modulus of wire ropes' materials, S_{wr} is the area of the wire ropes' cross-section, β is the angle between a tension cable and a corresponding axis, L_2 is the length of the tension cable, and n is the number of tension cables.

The given dependencies (4) and (5) make possible determining the borders of toughness and the natural frequencies of the suspension, depending on the material and in various directions.

Based on the design dependencies given in the paper, it is possible to obtain the values of the design parameters complex of vibroacoustic test benches, which will enable creating load conditions within the required range and running valid tests of units and the assembled equipment.

References

1. Testing equipment: reference guide, 2 vol. In: Kluev VV, Mashinostroenie M (1982). Vol. 1, Batuev GS, Bolshikh AS, Golubkov VS et al (1982), 528 pp (illustrations)
2. Zlatin NA et al (1974) Ballistic installations and their application in experimental research.In: Zlatin NA, Mishin GI, Nauka M, 344 pp (illustrations)
3. Evgrafov AN, Karazin VI, Khlebosolov IO (2011) Experimental determination of inertia parameters of the equipment. In: Modern mechanical engineering. Science and education. Materials of the international scientific conference. Publishing house of the Polytechnic University, SPb.,vol 1, pp 205–211
4. Bergmann E, Dzielski J (1990) Spacecraft mass property identification with torque-generating control. Aerosp Eng 11
5. Zabegaev AI, Klyukvin DN, Pshennov BV (2011) Computational-experimental method of determining the center of mass altitude of statistically indeterminable damped structures/XXXV Academic readings on cosmonautics—"Korolev's readings".M.: Bauman MSTU
6. Ksenofontov AA, Nikolaev VN, Chernokrylov SY (1992) Multifunctional dynamic test bench. Testing and control benches, pp 29–32 (L: LSTU)
7. Andrienko PA, Karazin VI, Klebosolov IO (2012) On tests for composite action.In: Modern mechanical engineering. Science and education. Materials of the international scientific conference, Publishing house of the Polytechnic University, SPb., vol 2. pp. 142–149
8. Andrienko PA, Karazin VI, Klebosolov IO (2014) On complex approach to laboratory tests of navigation systems.In: Modern mechanical engineering. Science and education. Materials of the international scientific conference. Publishing house of the Polytechnic University, SPb., vol 4. pp 121–131
9. Loytsyanskiy LG (2003) Mechanics of the liquid and gas. M.: Drofa, 840 pp
10. Vibrations in machinery: Reference guide, 6 vol. Ed. board: Chelomei VN (chairman), M. Mashinostroenie (1981)
11. Nurok GA (1980) Hydromechanization of opencast minings [Text]/G.A. Nurok., M.: Nedra, 582 pp

Stability of Walking Algorithms

Anastasia Borina and Valerii Tereshin

Abstract This paper presents the synthesis of a control system for a biped, walking dynamic robot. Such control system should provide the stable walking [3]. In this paper, stability is defined as limited deviations of speed and coordinates of the center of gravity of the robot from its required values at the end of each step. The control system has a feedback containing "the ideal mechanism" [16]. The equations of the ideal mechanism enable to define the time and place of putting down the feet at the end of each step, on the basis of the general requirements of walking. An ideal mechanism should be similar to the object of control [2, 7]. In this case, such ideal mechanism is the turned spatial mathematical pendulum. To check the described control system, as a physical model of the object of control employs a solid body on two weightless feet [4, 10]. For stable walking, it is convenient to develop algorithms that define the coordinates and speed of the center of gravity at the end of a step. In this paper the limitation of a general member of the sequence of coordinates and speed is investigated on the simple examples of walking [14], and the operation of the control system of the mentioned physical model is illustrated.

Keywords Biped walking · Walking robots · Dynamic walking · Control system

Introduction

The walking robot is an operational mechanism that can be used as the mechanical device to replace humans or their legs [12] during operations that are the hazardous to the health and lives of people. Most of the developments in this field of the making and controlling walking robots involve stable and static systems, but their

A. Borina (✉) · V. Tereshin
Peter the Great Saint-Petersburg Polytechnic University, St. Petersburg, Russia
e-mail: kamchatka1@rambler.ru

V. Tereshin
e-mail: terva@mail.ru

main shortcomings are heavy weight and low speed. For increasing their speed [15] and maneuverability, it is necessary to raise their dynamic stability [6, 13]. It is supposed that a biped device with small point feet can attain the greatest speed and maneuverability.

Description of Control Algorithms

For defining control algorithms based on the ideal mechanism, let us use the movement equations of the spatial turned pendulum [1] for the moment at the end of a step:

$$
\begin{cases}
x_{tp} - x_l = \frac{1}{2}\left(x_0 - x_l + \frac{\dot{x}_0}{k}\right)\psi + \frac{1}{2}\left(x_0 - x_l - \frac{\dot{x}_0}{k}\right)\psi^{-1} \\
z_{tp} - z_l = \frac{1}{2}\left(z_0 - z_l + \frac{\dot{z}_0}{k}\right)\psi + \frac{1}{2}\left(z_0 - z_l - \frac{\dot{z}_0}{k}\right)\psi^{-1} \\
\dot{x}_{tp} = \frac{k}{2}\left(x_0 - x_l + \frac{\dot{x}_0}{k}\right)\psi - \frac{k}{2}\left(x_0 - x_l - \frac{\dot{x}_0}{k}\right)\psi^{-1} \\
\dot{z}_{tp} = \frac{k}{2}\left(z_0 - z_l + \frac{\dot{z}_0}{k}\right)\psi - \frac{k}{2}\left(z_0 - z_l - \frac{\dot{z}_0}{k}\right)\psi^{-1}
\end{cases}
\tag{1}
$$

Index «·» means a derivative over time. The system of four equations (1) contains twelve parameters, eight of them are set: $x_0, z_0, \dot{x}_0, \dot{z}_0$—coordinates and speeds of the center of gravity; $\psi = e^{kt_p}$, t_p—time of the step's ending (the rate of walking is usually the characteristic of a walking robot, which is calculated from the robot's physical properties); $k = \sqrt{g/L}$, L—height of the center of gravity, g—acceleration of a free fall. Also it is necessary to set two parameters from the list of final conditions: $x_{tp}, z_{tp}, \dot{x}_{tp}, \dot{z}_{tp}$. Some ways of setting are possible. The system (1) allows to define two final conditions at the end of a step and the coordinates of a foot x_l and z_l.

Let's illustrate simple algorithms of walking by numerical sequences [5] and study their properties. When the walking is synchronized along axes x and z, Eq. (1) breaks down into two identical subsystems. Let the robot walk along axis z.

$$
\begin{cases}
z_{tp} - z_l = \frac{1}{2}\left(z_0 - z_l + \frac{\dot{z}_0}{k}\right)\psi + \frac{1}{2}\left(z_0 - z_l - \frac{\dot{z}_0}{k}\right)\psi^{-1} \\
\dot{z}_{tp} = \frac{k}{2}\left(z_0 - z_l + \frac{\dot{z}_0}{k}\right)\psi - \frac{k}{2}\left(z_0 - z_l - \frac{\dot{z}_0}{k}\right)\psi^{-1}
\end{cases}
\tag{2}
$$

Add and subtract each parameter from both parts of Eq. (2):

$$
\begin{cases}
-\psi z_{tp} + z_0 = z_l(1 - \psi) - \psi\frac{\dot{z}_{tp}}{k} + \frac{\dot{z}_0}{k} \\
z_{tp} - \psi z_0 = z_l(1 - \psi) - \frac{\dot{z}_{tp}}{k} + \psi\frac{\dot{z}_0}{k}
\end{cases}
\tag{3}
$$

Subtract the first equation of system (3) from the second one to get rid parameter z_l:

$$\left(z_{tp} - z_0\right) \cdot (1 + \psi) = (\psi - 1) \cdot \left(\frac{\dot{z}_{tp}}{k} + \frac{\dot{z}_0}{k}\right) \tag{4}$$

or

$$\dot{z}_n + \dot{z}_{n-1} = \lambda(z_n - z_{n-1}), \tag{5}$$

where

$$\lambda = k\frac{\psi + 1}{\psi - 1} \geq 1, \quad z_n = z_{tp}, \quad z_{n-1} = z_0.$$

Let's designate

$$\dot{z}_n + \dot{z}_{n-1} = a_n, \quad z_n - z_{n-1} = b_n \tag{6}$$

where

$$a_n = \lambda(z_n - z_{n-1}), \quad b_n = \frac{(\dot{z}_n + \dot{z}_{n-1})}{\lambda}$$

These equations are convenient for the creation of iterative procedures [9].

- Let coordinates of the center of gravity of the device z_n at the end of the steps be set. From Eq. (6), the expression for sequence of speeds $\dot{z}_n$ during the same moments of time as functions from $\dot{z}_0$ and sequence of z_n can be calculated:

$$\begin{aligned}
\dot{z}_1 &= a_1 - \dot{z}_0 \\
\dot{z}_2 &= a_2 - \dot{z}_1 = a_2 - a_1 + \dot{z}_0 \\
\dot{z}_3 &= a_3 - \dot{z}_2 = a_3 - a_2 + a_1 - \dot{z}_0 \\
\dot{z}_n &= (-1)^n \left(\dot{z}_0 + \sum_{k=1}^{n} (-1)^k a_k\right)
\end{aligned} \tag{7}$$

1. Let the length of a step be constant

$$z_n - z_{n-1} = const \tag{8}$$

then:

$$a_n = \lambda(z_n - z_{n-1}) = a. \tag{9}$$

The expressions for the sum in Eq. (7):

$$\sum_{k=1}^{n}(-1)^k a_k = a \cdot \sum_{k=1}^{n}(-1)^k = a\frac{(-1)^n - 1}{2} \tag{10}$$

Therefore

$$\dot{z}_n = (-1)^n \dot{z}_0 + (-1)^n a\frac{(-1)^n - 1}{2}$$

$$= (-1)^n \dot{z}_0 + a\frac{(-1)^{2n}}{2} - \frac{(-1)^n a}{2} = (-1)^n \left(\dot{z}_0 - \frac{a}{2}\right) + \frac{a}{2} \tag{11}$$

or

$$\dot{z}_n = (-1)^n \left[\dot{z}_0 - \frac{\lambda}{2}(z_n - z_{n-1})\right] + \frac{\lambda}{2}(z_n - z_{n-1}). \tag{12}$$

So from Eq. (12), if subtractions $(z_n - z_{n-1})$ are constant, speeds $\dot{z}_n$ at the end of steps are periodic with an amplitude $2\left[\dot{z}_0 - \frac{\lambda}{2}(z_n - z_{n-1})\right]$ and their average values are $\frac{\lambda}{2}(z_n - z_{n-1})$.

2. Let:

$$|z_n - z_{n-1}| = const, \tag{13}$$

Then from Eq. (6):

$$a_n = (-1)^n a. \tag{14}$$

The expressions for the sum in Eq. (7) are:

$$\sum_{k=1}^{n}(-1)^k a_k = a \cdot \sum_{k=1}^{n}(-1)^k(-1)^k = a \cdot n \tag{15}$$

Therefore:

$$\dot{z}_n = (-1)^n(\dot{z}_0 + an) \tag{16}$$

or

$$\dot{z}_n = (-1)^n[\dot{z}_0 + \lambda(z_n - z_{n-1})n]. \tag{17}$$

If the length of the step is $z_n - z_{n-1}$, then speed $\dot{z}_n$ increases the amplitude of fluctuations with a growth of the number of a step at any small module of step length $|z_n - z_{n-1}|$, and, when $z_n = z_{n-1}$, speed $\dot{z}_n = (-1)^n \dot{z}_0$.

- Let the changing-of-the-center-of-gravity speed $\dot{z}_n$ be known at the end of each step. The expression for the sequence of coordinates z_n during the same moments of time is:

$$
\begin{aligned}
z_1 &= b_1 + z_0 \\
z_2 &= b_2 + z_1 = b_2 + b_1 + z_0 \\
&\cdots \\
z_n &= z_0 + \sum_{k=1}^{n} b_k
\end{aligned}
\tag{18}
$$

3. Let:

$$
\dot{z}_n = \dot{z} = const,
\tag{19}
$$

then:

$$
b_n = b = const, \quad z_n = z_0 + n \cdot b, \quad z_n - z_{n-1} = b
\tag{20}
$$

where

$$
b = \frac{\dot{z}_n + \dot{z}_{n-1}}{\lambda} = 2\frac{\dot{z}}{\lambda}
$$

4. Let:

$$
\dot{z}_0 = \dot{z}, \dot{z}_1 = 0, \dot{z}_2 = -\dot{z}, \dot{z}_3 = 0, \dot{z}_4 = \dot{z}, \dot{z}_5 = 0, \dot{z}_6 = -\dot{z} \text{ etc.}
\tag{21}
$$

then:

$$
z_n = z_0 + \frac{\dot{z}}{\lambda} \cos\left(\frac{\pi n}{2}\right).
\tag{22}
$$

In this case, the walking device makes oscillating motions about z_0 with amplitude $\frac{\dot{z}}{\lambda}$.

The described algorithms are realized for the walking, in the direct and in the lateral direction, in various combinations. Depending on the type of programmed walking, it is possible to set the following four options of parameters $(\dot{x}_{tp}, \dot{z}_{tp})$, $(\dot{x}_{tp}, z_{tp})$, $(x_{tp}, \dot{z}_{tp})$ and (x_{tp}, z_{tp}).

Trajectories of the biped robot during various types of programmed walking. The six subplots are labeled, respectively:

$$\left| x_{tp} \right| = const, \quad z_{tp} = const$$

$$\left| x_{tp} \right| = const, \quad \dot{z}_{tp} = const$$

$$x_{tp} = 0, \quad \dot{z}_{tp} = const$$

$$\dot{x}_{tp} = -\dot{x}_0, \quad z_{tp} = const$$

$$\dot{x}_{tp} = -\dot{x}_0, \quad \dot{z}_{tp} = const$$

$$\dot{x}_{tp} = -\dot{x}_0, \quad \dot{z}_{tp} = \dot{z}_0, 0, -\dot{z}_0, 0$$
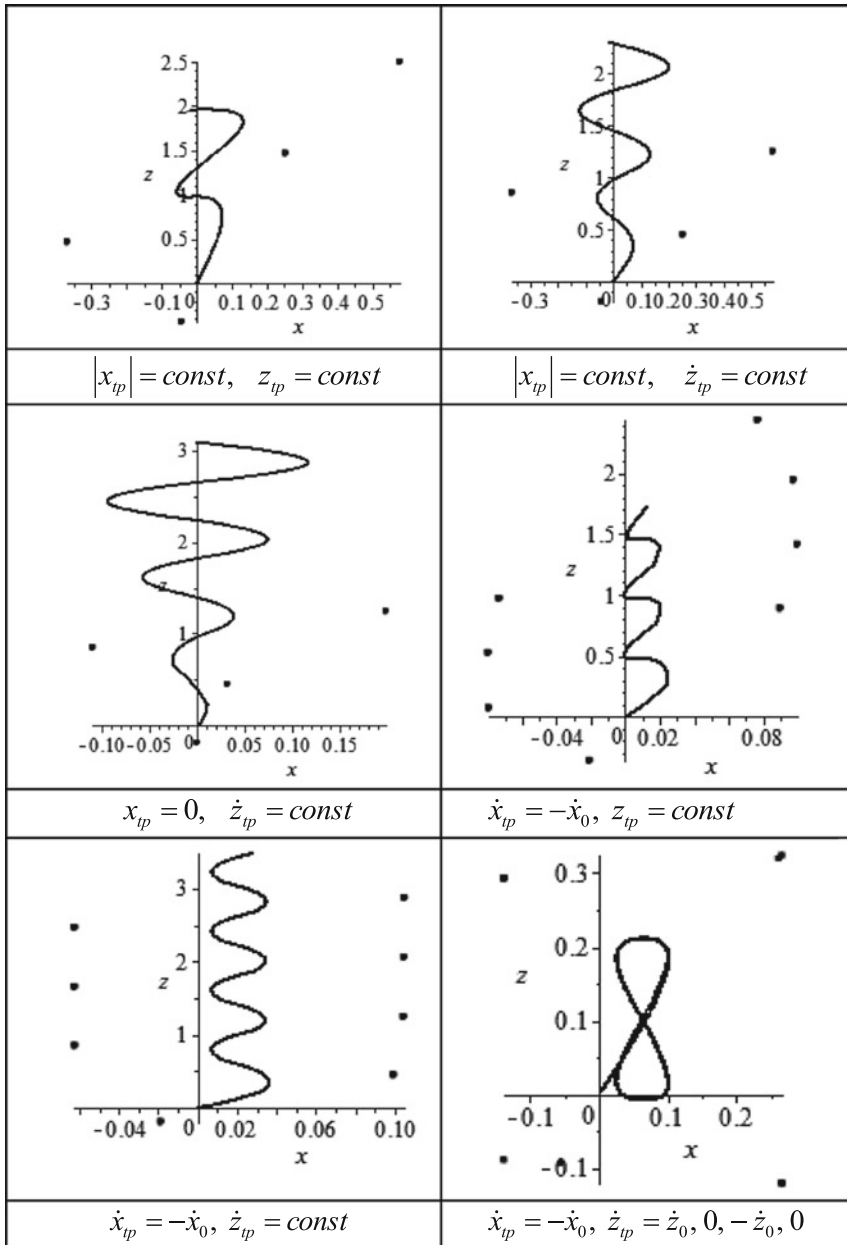
Fig. 1 Trajectories of the biped robot during various types of programmed walking

Trajectories of the center of gravity of the biped robot, calculated on the basis of described physical model at the simplest control algorithms, are presented on Fig. 1.

The locations of the feet are noted as points. It is necessary to limit all parameters [8, 17] defined by the design of the robot and by the level of walking comfort.

Conclusion

This paper determines that the limitation of step length leads to a loss of stability [11]. Algorithms with fixed speed or more difficult sequences with general parameters are stable.

References

1. Borina A, Tereshin V (2015) Control of biped walking robot using equations. In: Advances in mechanical engineering, lecture notes in mechanical engineering. Springer, Switzerland, pp 23–31
2. Borina AP, Tereshin VA (2013) Problem of spatial movement of dynamic walking device. In: Modern mechanical engineering, science and education, Saint-Petersburg, pp 631–641
3. Borina AP, Tereshin VA (2014) Even movement of humanoid robot. In: Modern mechanical engineering, science and education, Saint-Petersburg, pp 160–162
4. Borina AP, Tereshin VA (2012) Spatial movement of walking device under the influence of operating force from a foot. Modern mechanical engineering, science and education, Saint-Petersburg, pp 177–188
5. Brogliato B (2003) Some perspectives on the analysis and control of complementarity-systems. IEEE Trans Autom Control 48(6):918–935
6. Brogliato B, Niculescu SI, Monteiro-Marques M (2000) On the tracking control of a class of complementarity-slackness hybrid mechanical systems. Syst Control Lett 39:255–266
7. Brogliato B, ten Dam AA, Paoli L, Genot F, Abadie M (2002) Numerical simulation of finite dimensional multibody nonsmooth mechanical systems. ASME Appl Mech Rev 55:107–150
8. Chevallereau C (2003) Time-scaling control of an underactuated biped robot. IEEE Trans Robot Autom 19(2):362–368
9. Chevallereau C, Aoustin Y (2001) Optimal reference trajectories for walking and running of a biped robot. Robotica 19:557–569
10. Collins S, Wisse M, Ruina A (2001) 3-d passive dynamic walking robot with two legs and knees. Int J Robot Res 20(7):607–615
11. Dankowicz H, Adolfsson J, Nordmark A (2001) 3D passive walkers: finding periodic gaits in the presence of discontinuities. Nonlinear Dyn 24:205–229
12. Das SL, Chatterjee A (2002) An alternative stability analysis technique for the simplest walker. Nonlinear Dyn 28(3):273–284
13. Gienger M, Loffer K, Pfeiffer F (2003) Practical aspects of biped locomotion. In: Siciliano B, Dario P (eds) Experimental robotics. Springer, Berlin, Heidelberg, pp 95–104
14. Kar DC, Kurien IK, Jayarajan K (2003) Gaits and energetics in terrestrial legged locomotion. Mech Mach Theory 38:355–366
15. Lum HK, Zribi M, Soh YC (1999) Planning and control of a biped robot. Int J Eng Sci 37:1319–1349
16. Pervozvansky AA (2010) Course of automatic control theory. LAN, Saint-Petersburg
17. Saidouni T, Bessonnet G (2003) Generating globally optimised sagittal gait cycles of a biped robot. Robotica 21:199–210

Deleting Objects Algorithm
for the Optimization of Orthogonal
Packing Problems

Vladislav A. Chekanin and Alexander V. Chekanin

Abstract This paper considers the orthogonal packing problem that is a problem of placing all given orthogonal objects into a minimal set of orthogonal containers in the form of parallelepipeds of arbitrary dimension. It proposes an algorithm for deleting objects with the aim of effectively managing free spaces in containers. This algorithm provides a possibility of realization of heuristic methods, which are based on excluding some placed objects from a container and consequently filling the freed spaces within it more rationally.

Keywords Orthogonal packing problem · Bin packing problem · Recourse allocation · Optimization

Introduction

The solution of a large number of resource-optimization problems can be reduced to the solution of the orthogonal packing problem that is a classic problem of combinatorial optimization [19]. The orthogonal packing problem deals with the optimal placement of given orthogonal objects into a minimal number of orthogonal containers. The most commonly occurring orthogonal packing problems are bin packing problems [10, 17]. These are actually involved in the solution of many practical problems, including: container loading problems in transportation and logistics systems; traffic planning problems in computing and network systems; problems of rectangular cutting of materials; capital budgeting problem; calendar planning problem; and many other important problems that deal with the allocation and reallocation of resources in the form of orthogonal objects [1, 10, 13, 17–19].

V.A. Chekanin (✉) · A.V. Chekanin
Moscow State University of Technology "STANKIN", Moscow, Russia
e-mail: vladchekanin@rambler.ru

A.V. Chekanin
e-mail: avchekanin@rambler.ru

The number of dimensions of the most common problems of cutting and packing is not more than three [1]. Problems with a dimension higher than three, aside from only spatial dimensions, additionally often have non-spatial dimensions like time, cost, and some others [11, 20].

All orthogonal packing problems are NP-complete in the strong sense [15]. Application of exact methods based on exhaustive search for NP-complete problems is ineffective (for the vast majority of practical problems, it is impossible with limited resources of computer time). As a result, heuristic and metaheuristic optimization algorithms are widespread for the orthogonal packing problems [2, 4, 11, 12, 14, 16]. The effectiveness of an optimization algorithm first of all is determined by the depth of the search, which essentially depends on the amount of time reserved for obtaining the optimal solution. To estimate the quality of a solution coded in the form of a sequence of the objects to be placed, it is necessary to pack all the objects into containers and calculate the density of the resulting placement schemes. Since packing of objects is performed for each of interim solution (the number of which be as much as tens of thousands or more), hence it is necessary to use the efficient packing models and optimization methods, which provide the fast placement of objects and a description of all areas filled by objects containers.

To describe positions of all objects in orthogonal containers of arbitrary dimension, we use a previously developed model of potential containers [3, 7]. This model describes free spaces of a filled container by a set of so-called potential containers, which are orthogonal objects with the maximal dimensions that can be placed into the container with no overlap with the objects already packed into it. Quick access to potential containers is achieved though using of an effective multi-level linked-data structure [5, 9]. This paper describes a deleting-objects algorithm that is developed in relation to the model of potential containers. This algorithm provides flexibility in managing objects through the possibility of replacing them after their having been placed into a container. Usage of this algorithm allows using methods of local replacements of objects with the aim to increase the density of the resulting placement schemes.

Deleting Orthogonal Objects Algorithm

One of the effective methods applied for increasing the quality of a resulting packing is its local improvement, which can be realized by deleting one or more packed objects from a container with a consequently more rational filling of the freed space by other objects. When an object is deleted from a container, it is necessary to reorganize all potential containers around this object.

The superscript in the following formulas will be used to indicate the dimension.

Algorithm for deleting a D-dimensional orthogonal object i with the dimensions $\left\{ w_i^1, w_i^2, \ldots, w_i^D \right\}$ from a container j with the dimensions $\left\{ W_j^1, W_j^2, \ldots, W_j^D \right\}$ contains the following steps.

Step 1. Create a new empty D-dimensional orthogonal container j' with the dimensions equal to the dimensions of the original containers j, i.e. $W_{j'}^d = W_j^d \, \forall d \in \{1,\ldots,D\}$.

Step 2. Place into the container j' an object i' with the dimensions $w_{i'}^d = w_i^d \, \forall d \in \{1,\ldots,D\}$ at a point with the coordinates equal to coordinates of the object i placed into the container j: $x_{i'}^d = x_i^d \, \forall d \in \{1,\ldots,D\}$.

Step 3. Create a list $\{L'\}$ containing potential containers the position and dimensions of which can be modified in container j after deleting the object i. This list includes all potential containers k' under the condition $x_{k'}^d \le x_i^d + w_i^d \, \forall d \in \{1,\ldots,D\}$.

Step 4. Put into the container j' at points $x_{k'}^d$ a set of objects with the dimensions $w_{k'}^d = p_{k'}^d \, \forall d \in \{1,\ldots,D\}$, $k' \in \{L'\}$, where $p_{k'}^d$ is a dimension of a potential container k' measured in the direction of the coordinate axis d. When placing objects into the container j', allow them to overlap each other. Free orthogonal spaces remaining in the container j' are described by a set of potential containers placed in a list $\{L''\}$.

Step 5. Create a new empty D-dimensional orthogonal container j'' with the dimensions equal to the dimensions of the original container j, i.e. $W_{j''}^d = W_j^d \, \forall d \in \{1,\ldots,D\}$.

Step 6. Put into the container j'' at points $x_{k''}^d$ a set of objects with the dimensions $w_{k''}^d = p_{k''}^d$, $\forall d \in \{1,\ldots,D\}$, $k'' \in \{L''\}$. When placing objects into the container j'', allow them to overlap each other. Free orthogonal spaces remaining in the container j'' are described by a set of potential containers placed in a list $\{L'''\}$. This list of potential containers also describes a freed space of the original container j formed in the area of the object i which is to be deleted.

Step 7. Delete the object i from the container j.

Step 8. Change in the container j the list of its potential containers $\{L'\}$ to the obtained list of potential containers $\{L'''\}$.

As an example, we consider a rectangular two-dimensional container with the dimensions $W^1 = W^2 = 100$ as shown in Fig. 1. The parameters of the packed objects and potential containers are given in Tables 1 and 2, respectively.

When deleting an object with the number $i = 2$, it is necessary to reorganize all potential containers from the list $\{L'\}$ under the condition $x_{k'}^d \le x_i^d + w_i^d$, $k' \in \{L'\} \, \forall d \in \{1;2\}$, i.e., potential containers with the numbers 2, 3 and 4 (see Table 2).

The object 2, as well as objects with the dimensions $w_{k'}^d = p_{k'}^d, k' \in \{L'\} \, \forall d \in \{1;2\}$ given in Table 3, are placed into a new container 1'. In this container is formed a list of potential containers $\{L''\}$ given in Table 4 and shown in Fig. 2.

All objects with the dimensions $w_{k''}^d = p_{k''}^d$, $k'' \in \{L''\}$ (see Table 5) are placed in a new container with number 1'' (see Fig. 3); as a result, there is formed a set of potential containers $\{L'''\}$ given in Table 6.
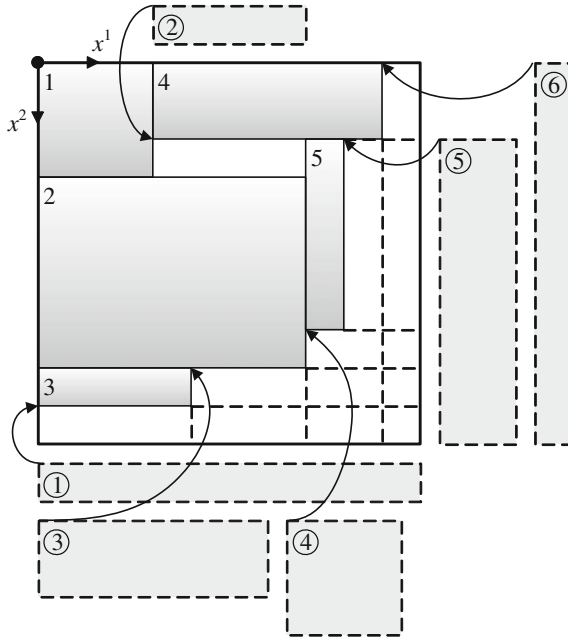
Fig. 1 Container 1 before deleting an object with number *2*

Table 1 Packed objects (container 1)

No.	Coordinate x^1	Coordinate x^2	Dimension w^1	Dimension w^2
1	0	0	30	30
2	0	30	70	50
3	0	80	40	10
4	30	0	60	20
5	70	30	10	50

Table 2 Potential containers (container 1)

No.	Coordinate x^1	Coordinate x^2	Dimension p^1	Dimension p^2
1	0	90	100	10
2	30	20	40	10
3	40	80	60	20
4	70	70	30	30
5	80	20	20	80
6	90	0	10	100

After deleting the object 2 from the container 1, it is necessary to replace all its potential containers taken from the list $\{L'\}$ to the potential containers from the list $\{L'''\}$ (given in Table 6). All the potential containers describing the free spaces remaining in the container 1 after deleting the object are given in Table 7 and shown in Fig. 4.

Table 3 Packed objects (container 1′)

No.	Coordinate x^1	Coordinate x^2	Dimension w^1	Dimension w^2
1	0	30	70	50
2	30	20	40	10
3	40	80	60	20
4	70	70	30	30

Table 4 Potential containers (container 1′)

No.	Coordinate x^1	Coordinate x^2	Dimension p^1	Dimension p^2
1	0	0	30	30
2	0	0	100	20
3	70	0	30	70
4	0	80	40	20

Fig. 2 Container 1′
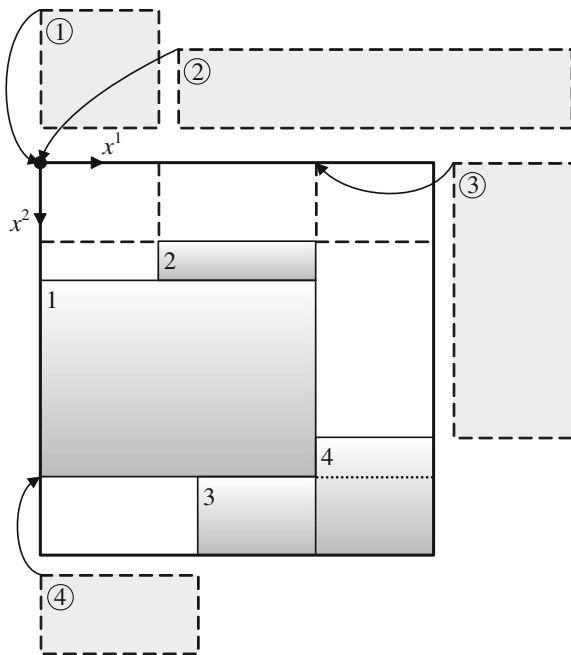
Table 5 Packed objects (container 1″)

No.	Coordinate x^1	Coordinate x^2	Dimension w^1	Dimension w^2
1	0	0	30	30
2	0	0	100	20
3	70	0	30	70
4	0	80	40	20
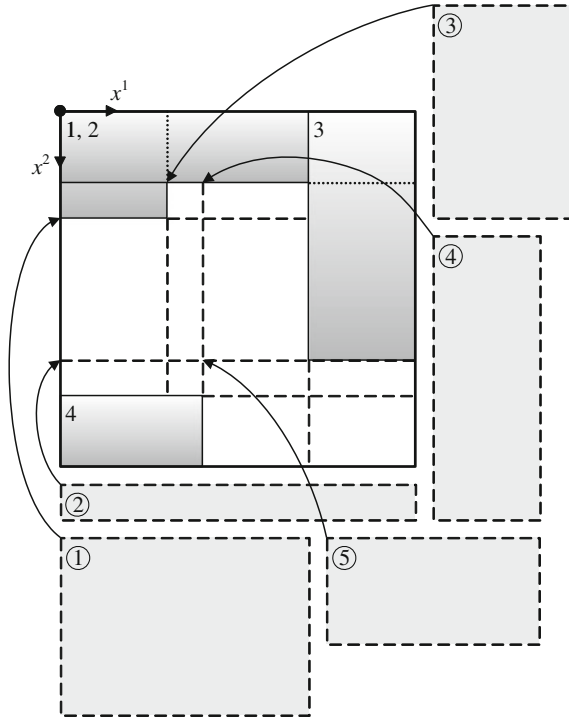
Fig. 3 Container 1″

Table 6 Potential containers (container 1″)

No.	Coordinate x^1	Coordinate x^2	Dimension p^1	Dimension p^2
1	0	30	70	50
2	0	70	100	10
3	30	20	40	60
4	40	20	30	80
5	40	70	60	30

Table 7 Potential containers after deleting the object (container 1)

No.	Coordinate x^1	Coordinate x^2	Dimension p^1	Dimension p^2
1	0	30	70	50
2	0	70	100	10
3	0	90	100	10
4	30	20	40	60
5	40	20	30	80
6	40	70	60	30
7	80	20	20	80
8	90	0	10	100

Fig. 4 Container 1 after deleting the object
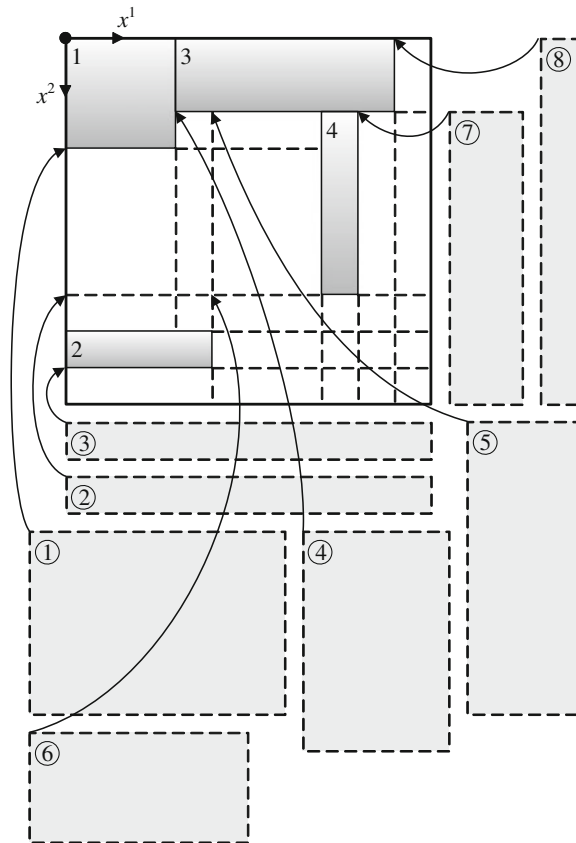
Conclusion

In this paper was considered the developed algorithm of deleting objects with the subsequent creation of a set of potential containers describing all existing free spaces around deleted objects. It is intended to use the algorithm for increasing the

quality of resulting placement schemes for orthogonal packing problems of arbitrary dimension. The algorithm is included in the basic set of algorithms realized in the developed application software, which is designed to optimize solutions of the orthogonal packing problems [6, 8]. One of the promising areas of our future research is related to the development and analysis of algorithms and methods of local replacements of objects for increasing the density of resulting placement schemes obtained with various heuristic and metaheuristic optimization algorithms.

References

1. Bortfeldt A, Wascher G (2013) Constraints in container loading—a state-of-the-art review. EJOR 229(1):1–20
2. Chekanin VA, Chekanin AV (2012) Researching of genetic methods to optimize the allocation of rectangular resources. In: Proceedings of 2nd international scientific conference on modern engineering: science and education, Izd-vo Politekhn. un-ta, SPb, pp 798–804 (in Russian)
3. Chekanin VA, Chekanin AV (2013) Improved packing representation model for the orthogonal packing problem. Appl Mech Mater 390:591–595
4. Chekanin VA, Chekanin AV (2014) Development of the multimethod genetic algorithm for the strip packing problem. Appl Mech Mater 598:377–381
5. Chekanin VA, Chekanin AV (2015) Data structure for the three dimensional orthogonal packing problem. Vestnik MSTU "STANKIN" (Vestnik MGTU "STANKIN") 1:112–116 (in Russian)
6. Chekanin VA (2014) Library class for solving packing problems via evolutionary algorithms In: Proceedings of 4th international scientific conference on modern engineering: science and education. Izd-vo Politekhn. un-ta, SPb, pp 789–796 (in Russian)
7. Chekanin VA, Chekanin AV (2015) An efficient model for the orthogonal packing problem. Adv Mech Eng 22:33–38
8. Chekanin VA, Chekanin AV (2015) Development of optimization software to solve practical packing and cutting problems. Adv Intell Syst Res 123:379–382
9. Chekanin VA, Chekanin AV (2016) New effective data structure for multidimensional optimization orthogonal packing problems. In: Advances in mechanical engineering. Springer International Publishing, pp 87–92
10. Crainic TG, Perboli G, Tadei R (2008) Extreme point-based heuristics for three-dimensional bin packing. INFORMS J Comput 20(3):368–384
11. Fekete SP, Schepers J, van der Veen JC (2007) An exact algorithm for higher-dimensional orthogonal packing. Oper Res 55(3):569–587
12. Filippova AS (2006) Modeling of evolution algorithms for rectangular packing problems based on block structure technology. In: Inf Technol (Informacionnye Tehnologii). Appendix, 32 p (in Russian)
13. Gao YQ, Guan HB, Qi ZW, Hou Y, Liu L (2013) A multi-objective ant colony system algorithm for virtual machine placement in cloud computing. J Comput Syst Sci 79(8): 1230–1242
14. Goncalves JF, Resende MGC (2013) A biased random key genetic algorithm for 2d and 3d bin packing problems. Int J Prod Econ 145(2):500–510
15. Johnson DS (2012) A brief history of NP-completeness, 1954–2012. Documenta Mathematica. Extra Volume ISMP, pp 359–376
16. Leung SCH, Zhang DF, Zhou CL, Wu T (2012) A hybrid simulated annealing metaheuristic algorithm for the two-dimensional knapsack packing problem. Comput Oper Res 39(1):64–73

17. Martinez MAA, Clautiaux F, Dell'Amico M, Iori M (2013) Exact algorithms for the bin packing problem with fragile objects. Discret Optim 10(3):210–223
18. Riff MC, Bonnaire X, Neveu B (2009) A revision of recent approaches for two-dimensional strip-packing problems. Eng Appl Artif Intell 22(4–5):823–827
19. Wascher G, Haubner H, Schumann H (2007) An improved typology of cutting and packing problems. EJOR 183(3):1109–1130
20. Westerlund J, Papageorgiou LG, Westerlund T (2007) A MILP model for N-dimensional allocation. Comput Chem Eng 31(12):1702–1714

Computational Technique of Plotting Campbell Diagrams for Turbine Blades

Vladimir V. Eliseev and Artem A. Moskalets

Abstract The technique of plotting the Campbell diagrams for turbine blades is developed by means of mathematical modeling. Equations of blade oscillations in the field of centrifugal forces are derived. The turbine blade is supposed to be a naturally twisted rod. The numerical solution of the eigenvalue problem gives the required dependencies of oscillation frequency on angular velocity. Calculations are performed using the shooting method in Mathcad. The computational results for a particular turbine blade are presented.

Keywords Turbine blade · Campbell diagram · Naturally twisted rods · ODE system · Shooting method · Natural frequencies and modes · Mathcad

Problem

Blades on rotating turbines are influenced by steam or fluid jets generating periodic excitation with rotational speed Ω. A blade as an oscillating system has a set of natural frequencies ω_k (in theory, its number is infinite). In order to prevent resonances, the inequality $\Omega \neq \omega_k$ must be satisfied. However, this statement should be clarified.

Firstly, the harmonics of frequencies $2\Omega, 3\Omega, \ldots$ arise from the load Fourier expansion. Secondly, the natural frequencies depend on angular velocity, because the increase of centrifugal forces causes an increase in bending stiffness. Therefore, this condition holds:

$$n\Omega \neq \omega_k(\Omega) \tag{1}$$

V.V. Eliseev · A.A. Moskalets (✉)
Peter the Great Saint-Petersburg Polytechnic University, Saint-Petersburg, Russia
e-mail: artem.moskalec@gmail.com

V.V. Eliseev
e-mail: yeliseyev@inbox.ru

for all n, k having natural values. The Campbell diagram illustrates this inequality graphically [1–3]. There are two families of functions of Ω: the left side of Eq. (1) represents rays from the origin, the right side of (1) represents curves for $\omega_k(0)$. These values can be determined by means of modal analysis of a fixed blade [4–10].

It is so important to meet the condition of Eq. (1) that expensive Campbell-machines are created [1] to find the right side of Eq. (1) experimentally. The purpose of this effort is to find $\omega_k(\Omega)$ by mathematical modeling.

One-, two- or three-dimensional models can be used for blade modeling. The number of dimensions depends on the proportions of the blade. It is naturally twisted and has variable section. It is naturally twisted and has variable section [11, 12]. The problem can't be solved by means of elementary considerations, so the nonlinear rod theory is required [13]. Modern approaches to the estimation of a blade's modal parameters are represented in articles [5–7]. These approaches are based on computer mathematics [14].

Equations of Rod Theory

These equations were derived by Kirchhoff and then generalized by Cosserat. In modern formulation [13], these equations can be written as:

$$\mathbf{Q}' + \mathbf{q} = \rho\ddot{\mathbf{r}}, \mathbf{M}' = \mathbf{Q} \times \boldsymbol{\tau},$$
$$\boldsymbol{\kappa} = \mathbf{A} \cdot \mathbf{M}, \boldsymbol{\tau} = \mathbf{P} \cdot \boldsymbol{\tau}_0 \tag{2}$$

Here $\mathbf{Q}, \mathbf{M}$ are the vectors of force and moment, respectively; $(\ldots)'$ and $(\ldots)^{\cdot}$ denote the derivatives with respect to material coordinate $\mathbf{s}$ and time $\mathbf{t}$, respectively; $\mathbf{r}(\mathbf{s}, \mathbf{t})$ is the radius vector of rod's particle; $\boldsymbol{\tau}_0 = \mathbf{r}'_0, \boldsymbol{\tau} = \mathbf{r}'$ are the unit tangent vectors of rod axis before and after deformation, respectively; $\boldsymbol{\kappa}$ is the strain vector of bending and torsion; $\mathbf{A}$ is the compliance tensor, $\mathbf{P}$ is the rotation tensor, ρ is the mass per unit length, and $\mathbf{q}$ is the load distributed per unit length.

The nonlinear equations [see Eq. (2)] are required for large deformation problems. Also, they are the basis for solving the problem of the superposition of small deformations upon finite ones. In this case, each quantity has a small increment denoted by a wave: $\tilde{\mathbf{r}} = \mathbf{u}, \tilde{\mathbf{P}} = \boldsymbol{\theta} \times \mathbf{P}, \tilde{\mathbf{q}}, \ldots$

Here, $\mathbf{u}, \boldsymbol{\theta}$ are the translation vector and the vector of small angular displacement, respectively. The varying the system (2) yields the following system:

$$\tilde{\mathbf{Q}}' + \tilde{\mathbf{q}} = \rho\ddot{\mathbf{u}}, \tilde{\mathbf{M}}' = \tilde{\mathbf{Q}} \times \boldsymbol{\tau} + \mathbf{Q} \times (\boldsymbol{\theta} \times \boldsymbol{\tau}),$$
$$\boldsymbol{\theta}' = \mathbf{A} \cdot (\tilde{\mathbf{M}} - \boldsymbol{\theta} \times \mathbf{M}), \mathbf{u}' = \boldsymbol{\theta} \times \boldsymbol{\tau} \tag{3}$$

It is a linear system, but its coefficients are determined by the state condition before the variation and must be precomputed as functions of s and t.

Blade in the Field of Centrifugal Forces

The blade is supposed to be a straight-line, naturally-twisted rod [12] stretched by centrifugal forces. The rotating frame of reference is used to account for inertial forces as in the effort [15]. The system of ordinary differential equations (ODE) in components becomes, from Eq. (3) in the case of harmonic oscillations at frequency ω:

$$
\begin{aligned}
&Q_x' + q_x = -\omega^2 \rho u_x, \ Q_y' + q_y = -\omega^2 \rho u_y, \\
&M_x' = -Q_y + Q\theta_x, \ M_y' = Q_x + Q\theta_y, \\
&\theta_x' = A_{xx}M_x + A_{xy}M_y, \ \theta_y' = A_{xy}M_x + A_{yy}M_y, \\
&u_x' = -\theta_y, \ u_y' = \theta_x
\end{aligned}
\tag{4}
$$

Here, the wave (symbol of variation) is omitted. The Cartesian coordinates x, y, z are used: axis z is directed along the rod axis, while axes x, y are in the sectional plane (Fig. 1).

The bending compliances A_{xx}, A_{yy}, A_{xy} are evaluated using simple engineering formulas. The tension force Q is determined by the formula:

$$
Q(z) = \Omega^2 \int_z^L \rho(R_1 + \xi)d\xi,
\tag{5}
$$

where L is the length of blade, and R_1 is the radius of rotor. The formula Eq. (5) is derived from the balance equation for longitudinal forces. For the blade made at a Russian factory, the relationship Eq. (5) is shown in Fig. 2 ($\Omega = 3000$ rev/min):
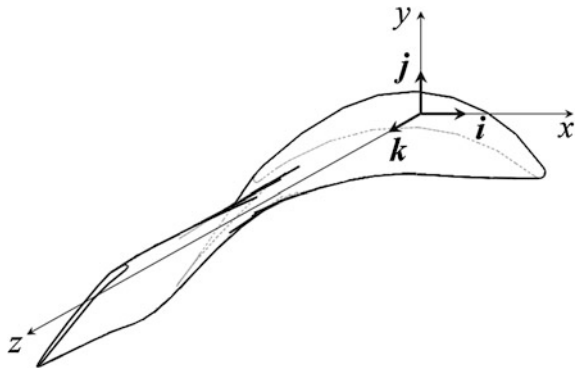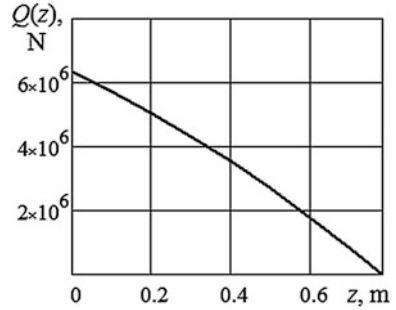

Fig. 1 System of coordinates for the blade

Fig. 2 Tension force

The stiffness and inertial characteristics can be variable along the blade. To account for this, the characteristics of both end sections and a few intermediate sections are computed, and then the functional relationships are determined by interpolation.

Eight boundary conditions must be specified for the system of Eq. (4). Translational and angular displacements are zero at rigid support $z = 0$; transverse forces and bending moments are zero at free end $z = L$.

The problems can be solved only numerically. Note that the system of Eq. (4) is eighth-order in the case of forced vibrations (q_x, q_y are nonzero).

The equation $\omega' = 0$ must be added to that system for the free vibration case (the order of the system Eq. (4) increases by one). The additional boundary condition is a constant value of any quantity at one of the ends. The normalizing constant should be included at the last stage of analysis, as is accepted in the theory of vibrations [11, 12]. When plotting the Campbell diagrams, the case of free vibrations must be considered.

Computation in Mathcad

The system of Eq. (4) in matrix form is:

$$\mathbf{Y}' = \mathbf{F}(s, \mathbf{Y}), \mathbf{Y} = \begin{pmatrix} Q_x & Q_y & M_x & M_y & \theta_x & \theta_y & u_x & u_y & \omega^2 \end{pmatrix}^{\mathrm{T}} \qquad (6)$$

where the form of the column $\mathbf{F}$ is clear from Eq. (4).

The boundary value problem for system Eq. (6) is solved by means of Mathcad using the built-in functions sbval–rkfixed [14]. Calculated values of the first five natural frequencies are:

$$\omega_1 = 741, \omega_2 = 1,59 \cdot 10^3, \omega_3 = 3,95 \cdot 10^3,$$
$$\omega_4 = 7,47 \cdot 10^3, \omega_5 = 1,28 \cdot 10^4$$
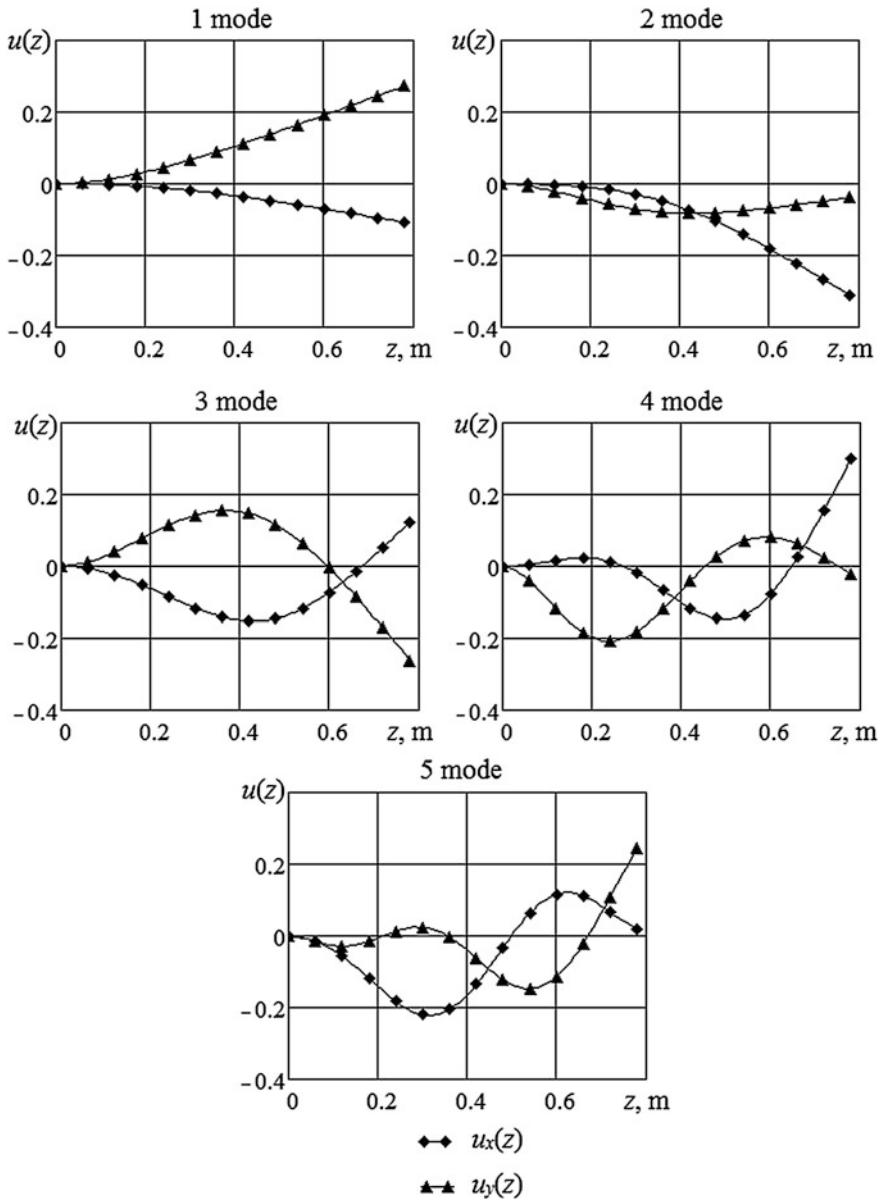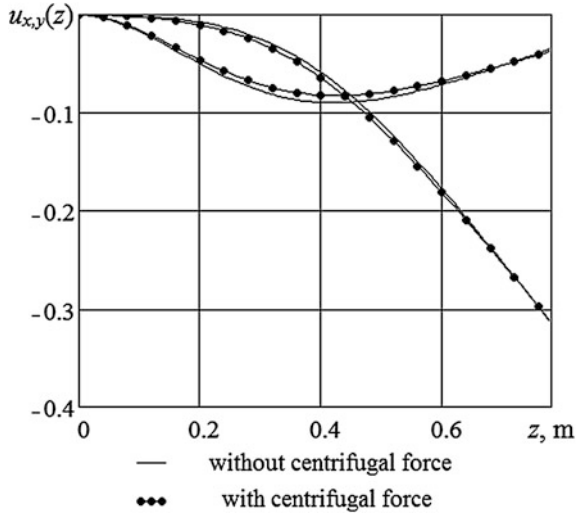
The corresponding eigenmodes are shown in Fig. 3.

Fig. 3 Normalized eigenmodes

As shown in Fig. 4, these graphs are quite similar to those for the case without centrifugal force.

Fig. 4 Second eigenmode. The **solid line** is the model with centrifugal forces, and the **line with points** is the model without centrifugal forces

However, the centrifugal forces influence the lower frequencies considerably:

$$\frac{\Omega_{cf} - \Omega}{\Omega_{cf}} \cdot 100\% = (\,35.6 \quad 9.4 \quad 5.5 \quad 3.3 \quad 1.2\,)\%,$$

where Ω_{cf}, Ω are natural frequencies for the case that accounts for centrifugal forces and for the case without it, respectively.

The algorithm described above is not the only way to solve the problem. Also, the variational method based on the Lagrange equations [7] enables evaluation of all natural frequencies and plotting the diagrams for the right-hand side of Eq. (1). However the expression for potential energy is needed, and centrifugal force must be taken into account in it, which goes beyond the scopes of the present paper.

Campbell Diagram

An important stage of turbine design is plotting the Campbell diagram that represents the dependence of vibration frequencies on rotor speed. This diagram enables finding the potential resonance regions. Initially, these diagrams were plotted using experimental data: turbine blades were tested in the so-called Campbell-machines. The main part of this facility is the vacuum chamber which contains the observable bladed disc. The blades are excited by steam or water jets; electromagnets may be used also.

Nowadays, there is a possibility of plotting the Campbell diagrams using a computational approach. In this effort, the foregoing theory and Mathcad [14] are used. The diagram for the blade under consideration is shown in Fig. 5.

Fig. 5 Campbell diagram for first three natural frequencies
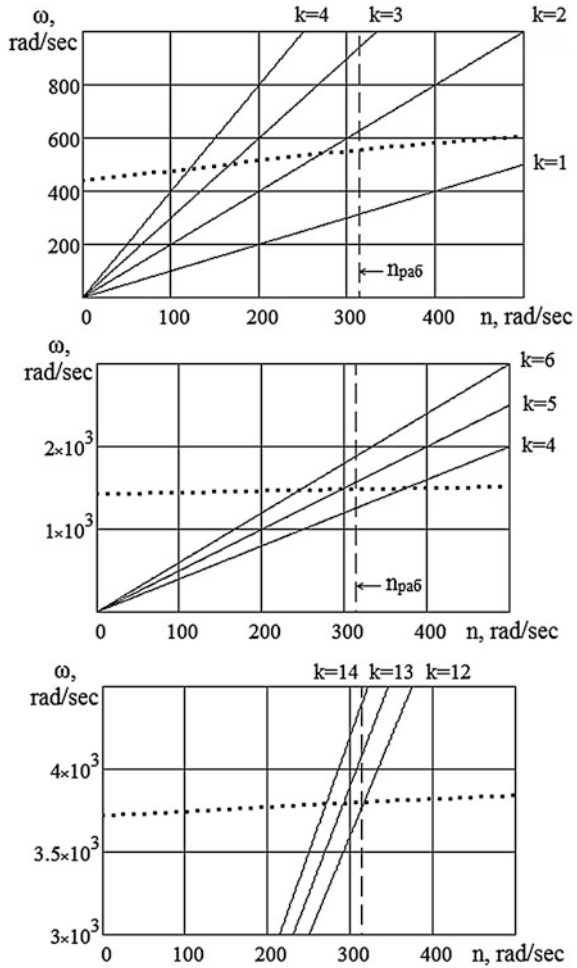
However, the curve of natural frequencies is represented as a band, because the frequencies have a spread of values. The permissible difference between the maximum and minimum values of natural frequency is regulated by specifications. The resonance region is the area defined by points of intersection between the frequency band and the lines of harmonics. The resonances can be avoided by detuning. In the case of transient motion, the dangerous resonant regime must be passed through as quickly as possible [7], although the turbine can sometimes operate in the resonance mode due to damping.

It should be noted that the Campbell diagram is intended for estimating the resonance regimes graphically. However, the foregoing technique makes it possible to find all these regimes simultaneously. Assuming in Eq. (4) $\omega = n\Omega$, the resonance speed values Ω can be found. It appears that these diagrams become useless. However, since the set of resonance speeds is quite dense, therefore the process of speed estimation by the shooting method is laborious. Nevertheless, the Campbell diagrams are effective.

Conclusion

The elementary computational technique of plotting the Campbell diagrams was developed. The equations of small deformations upon the finite stress-strain state were used as the theoretical basis. The shooting method was employed to solve the boundary eigenvalue problem for ninth-order ODE systems with Mathcad.

References

1. Kirillov ON (2009) Campbell diagrams of weakly anisotropic flexible rotors. Proc R Soc A: Math Phys Eng Sci 465(2109):2703–2723. doi:10.1098/rspa.2009.0055
2. Lee CW, Han DJ (2008) Strength of modes in rotating machinery. J Sound Vib 313(1): 268–289. doi:10.1016/j.jsv.2007.11.038
3. Lee CW, Seo YH (2010) Enhanced Campbell diagram with the concept of H∞ in rotating machinery: Lee diagram. J Appl Mech 77(2):021012. doi:10.1115/1.3173610
4. Ritto TG, Lopez RH, Sampaio R, Souza de Cursi JE (2011) Robust optimization of a flexible rotor-bearing system using the Campbell diagram. Eng Optim 43(1):77–96. doi:10.1080/03052151003759125
5. Eliseev VV, Moskalets AA, Oborin EA (2016) One-dimensional models in turbine blades. Advances in mechanical engineering, Lecture notes in mechanical engineering, Springer, Berlin, pp 93–104. doi:10.1007/978-3-319-29579-4
6. Eliseev VV, Moskalets AA, Oborin EA (2015) Deformation analysis of turbine blades based on complete one-dimensional model. Russ J Heavy Mach 5:35–38 (in Russian)
7. Eliseev VV, Moskalets AA, Oborin EA (2015) Applying of Lagrange equations to calculation of turbine blade vibration. Handbook Eng J 8:21–24. doi:10.14489/hb.2015.08 (in Russian)
8. Bloch HP, Singh MP (2009) Steam turbines: design, applications and rerating. McGraw-Hill, New York, p 433
9. Brondsted P, Nijssen RPL (2013) Advances in wind turbine blade: design and materials. Woodhead Publishing Limited, Cambridge, p 484, doi:10.1533/9780857097286
10. Leyzerovich AS (2005) Wet-steam turbines for nuclear power plants. PennWell, USA, p 481
11. Eliseev VV, Piskunov VA (2016) Composite gas-turbine Blades. Russ Eng Res 36(10): 819–822 (in Russian). doi:10.3103/S1068798X16100087
12. Khanh CL (1999) Vibrations of shells and rods. Springer, Berlin, p 423, doi:10.1007/978-3-642-59911-8
13. Eliseev VV (2003) Mechanics of elastic bodies. St. Petersburg State Polytechn, University Publishing House, St Petersburg, p 336 (in Russian)
14. Kiryanov D, Kiryanova E (2007) Computational science. Infinity Science Press, Hingham
15. Yeliseyev VV (2015) Dynamics, critical speeds and balancing of thermoelastic rotors. Lecture Notes in control and information sciences. Advances in mechanical engineering, Springer, Berlin, pp 129–136. doi:10.1007/978-3-319-15684-2

Computer Simulation of Mechanisms

Alexander N. Evgrafov and Gennady N. Petrov

Abstract This article presents 2D and 3D models of the mechanisms created with the tools "Model Vision" and "AnyLogic". For the purpose of this research, mechanisms with the following computing features were selected: redundant links, redundant inputs, and singular positions, as well as multidirectional mechanisms.

Keywords Computer simulation · Interactive models · Model vision · Anylogic · Turbulence mixer · Stewart platform · Hooke's joint · Automobile differential

Introduction

The development of computer technology increases the importance of simulation experiments for various mechanical problems, including the calculations for mechanisms and machines. At the initial stage of a simulation experiment, the object under study is replaced by the mathematical model presented in the form of, for instance, differential equations. Subsequently, a program is created that solves those equations with appropriate numerical methods. Modern means of visualization enable us to see results not only as numerical tables and charts, but also as objects with varied degrees of detail. Creation of interactive animated models is of particular interest to researchers [1, 2].

These days, there appears to be many works on computer simulation methods of mechanical systems animation that use visual animation effects instead of special software applications [3]. Mathematical toolboxes such as MATLAB [4, 5] and Mathcad [6–9] are considered to be particularly suitable for addressing the problems of visualization of the calculation results. Similarly, the referenced work [10] provides an interesting example of the use of GeoGebra software in the study of

A.N. Evgrafov (✉) · G.N. Petrov
Peter the Great Saint-Petersburg Polytechnic University, St.-Petersburg, Russia
e-mail: a.evgrafov@spbstu.ru

G.N. Petrov
e-mail: gnpet@mail.ru

kinematic geometry of planar mechanisms, while other works [11, 12] describe animation of the various mechanisms' kinematic schemes.

This article presents the use of the tools "Model Vision" and "AnyLogic", which can significantly simplify the solution and the visualization of a mathematical model. More details on these software applications are available at: www.xjtek.com.

Toolboxes enable:

To carry out a simulation experiments, based on the principles of object-oriented programming. The model can be divided into various individual devices, which, in turn, could be taken from an existing library or created by the user. Relationships between the devices are established using a user-friendly graphical interface.

To solve the algebraic and differential equations. Language resembling the one utilized by Mathcad tools is used to present differential-algebraic equations.

To create a behavior model for each device that describes the change of behavior of dynamical systems.

Simulation environments are intuitive and easy to use. This article provides descriptions of several mechanical systems models created using these toolboxes.

Each model utilized:

Built-in 2D animation tools, which enabled the creation of the "remote control" which included a variety of indicators, buttons, sliders. This "remote control" was used to discretely or continuously change certain parameters of the model during the simulation.

3D-animation tools that which made possible the observation of the object's movement in space during the simulation experiment ("Model Vision").

Timeline and phase diagrams:

This article reviews several models, created with the above-mentioned tools.

Computer Simulation in "Model Vision"

1. Turbulence mixer

Figure 1 demonstrates the operation of the closed six-link spatial mechanism. The mechanism connects two parallel axes 1 and 5, whereas five mobile units are interconnected by six rotational kinematic pairs.

Fig. 1 The operation of the closed six-link spatial mechanism
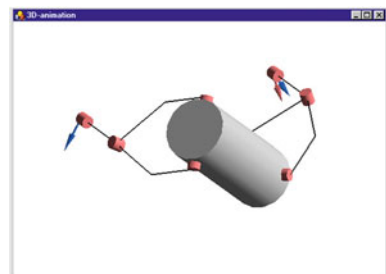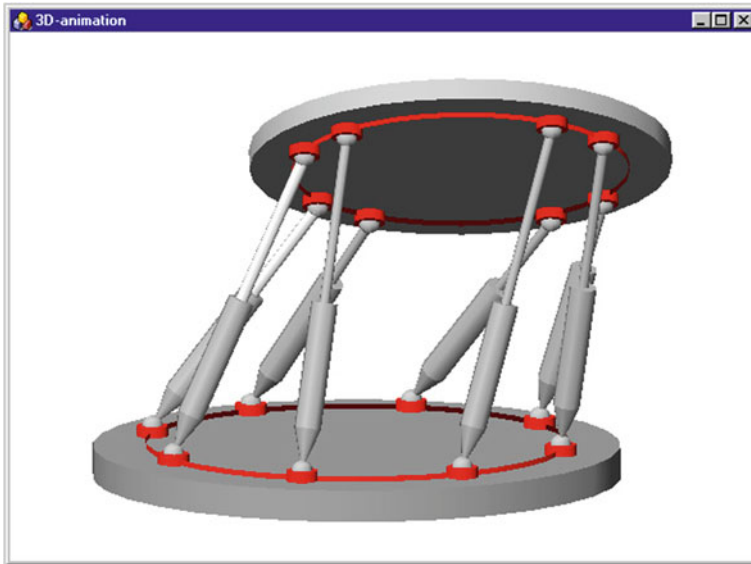
Fig. 2 The mechanism designed for positioning of the platform in space

The mechanism has a redundant (excess) link, due to the fact that the axis of the kinematic pairs that are connecting the links are mutually perpendicular. Link 3 is shaped as a hollow sealed cylinder. Liquids or granular materials that are placed inside this cylinder become mixed during the complex spatial movement.

2. Stewart platform with redundant inputs

The mechanism, presented in Fig. 2, is designed for positioning of the platform in space. Platform jacks ("legs") are shaped as hydraulic cylinders, which are linked to the platform and the platform base by spherical joints. It is sufficient to have six inputs for the normal operation of the mechanism, so each time two hydraulic cylinders are disconnected. Active (running) cylinders are marked with a light gray colour, and inactive—with a dark gray. Referenced work [13] describes the force calculation for closed-linkage mechanisms, while another work [14] focuses on the selection of six active drives, which ensure optimal operation of the mechanism. Calculation of the geometry and kinematics of closed mechanisms, as described above, is presented in detail in works [15, 16].

3. Coupling ("Model Vision")

The coupling transmits rotation between the two shafts with parallel axes. Figure 3a shows a 2D-animation window, where we establish the following values: angle of the axes crossing $F = 0$, the distance between the guides $h = 1.5$; misalignment by axes $dx = 1$, $dy = 1$. Figure 3b presents the coupling design concept, while Fig. 3c illustrates the kinematic scheme (the transition from one

(a)

(b)

(c)
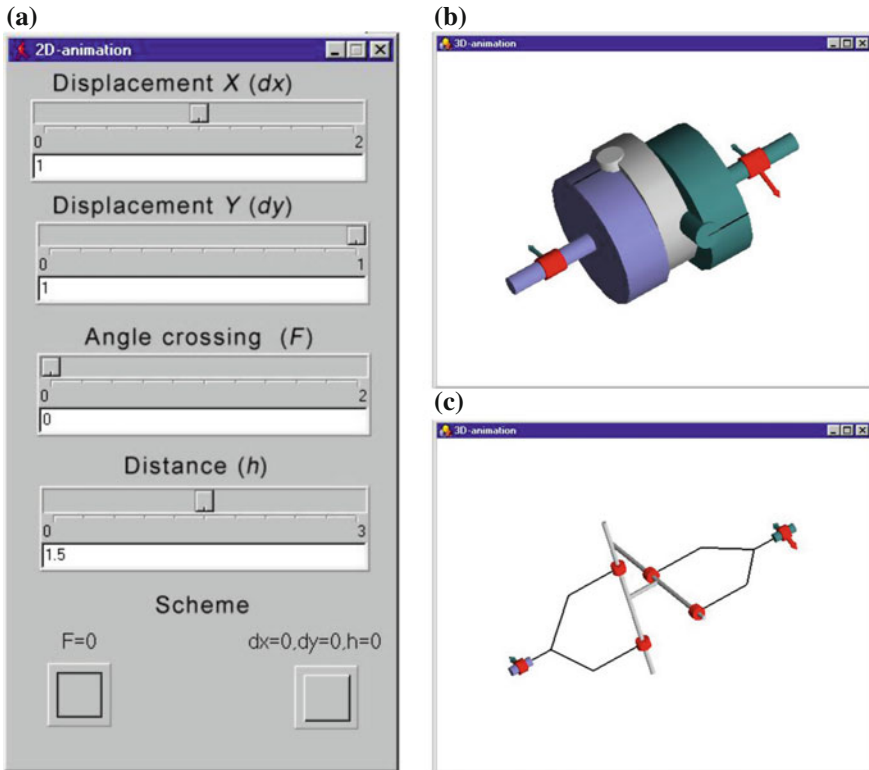
Fig. 3 Examples of 2-D animation window (**a**), coupling design scheme (**b**) and kinematics scheme (**c**) in Model Vision

scheme to another is performed by pressing the corresponding button in the 2*D*-animation window).

Axes 1 and 3 are connected to the liner 2 by two mutually-perpendicular rectilinear kinematic pairs and have the same angular velocity.

4. Hooke's joint

Hooke's joint is designed to transmit the rotation between shafts with crossed axes. In the 2*D*-animation window (Fig. 3a), we establish the angle of the axes crossing as $F = 1$, while $dx = dy = h = 0$. Figure 4 shows design concept (*a*) and kinematic scheme (*b*) of the joint. In this case, the links 1 and 3 are connected to the liner 2 by rotational kinematic pairs with axis intersecting at an angle of 90°.

5. Spatial mechanism

Figure 5a shows the 2*D*-animation panel that enables setting the desired length of the links (*OA*, *AB*, *BC*, *CD*) and coordinates the joint-*D* connection to the pillar
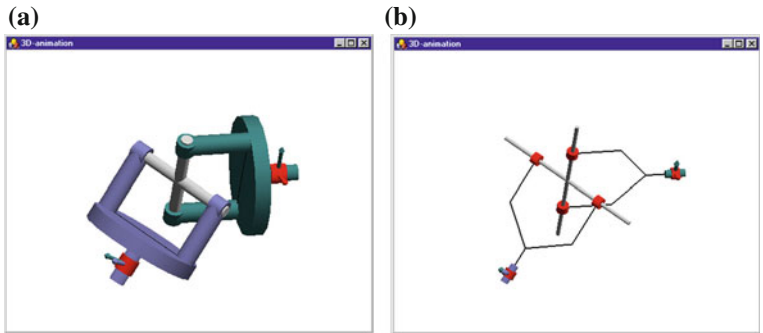
Fig. 4 Design concept (**a**) and kinematic scheme (**b**) of the Hooke's joint
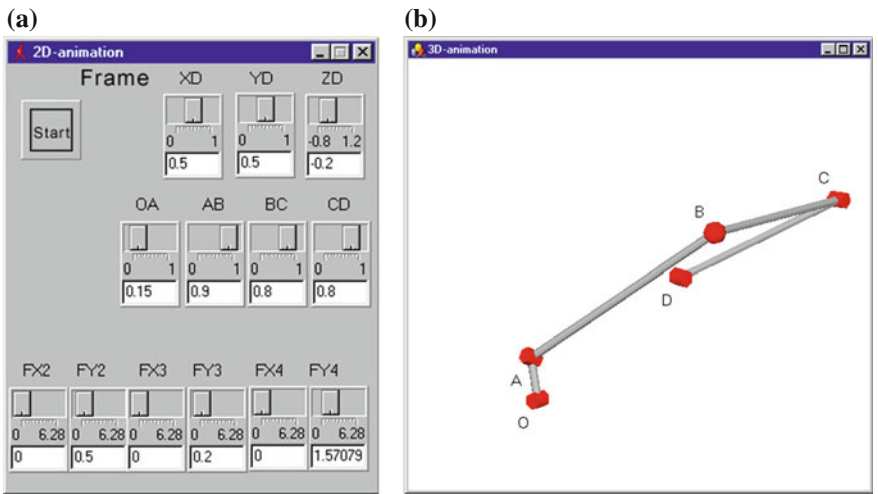
Fig. 5 2-D animation panel (**a**) and the spatial five-link mechanism with a single degree of mobility (**b**)

(XD, YD, ZD) of the spatial five-link mechanism with a single degree of mobility (Fig. 5b). Four mobile links compose a closed kinematic chain.

Joints O, A, C, D are cylindrical, while joint B is spherical. The 2D-animation panel indicates the orientation with respect to the local coordinate systems (FX, FY) for cylindrical kinematic pairs. This example demonstrates that even a slight change in the size of the mechanism causes it to adopt so-called "special positions" when it could not pivot.

6. Rear axle of the car ("Model Vision")

Figure 6a shows the 2D animation panel. Figure 6b is the design concept of the rear axle of the rear-drive car. By pressing the buttons "Body" and "Differential" on

(a)

(b)

(c)
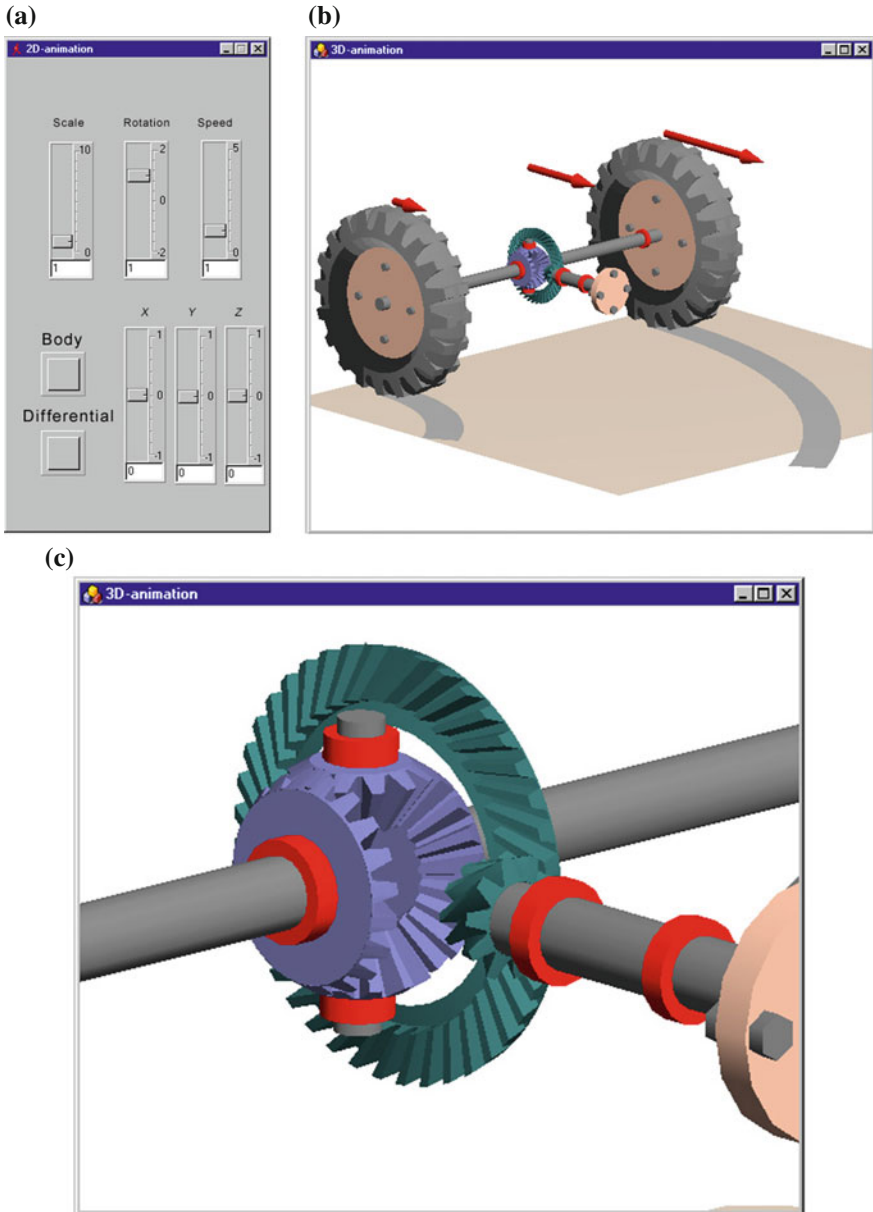
Fig. 6 The 2*D*-animation panel (**a**), design concept of the rear axle of the rear-drive car (**b**), and example of zooming into an image (**c**)

(a)   **(b)**
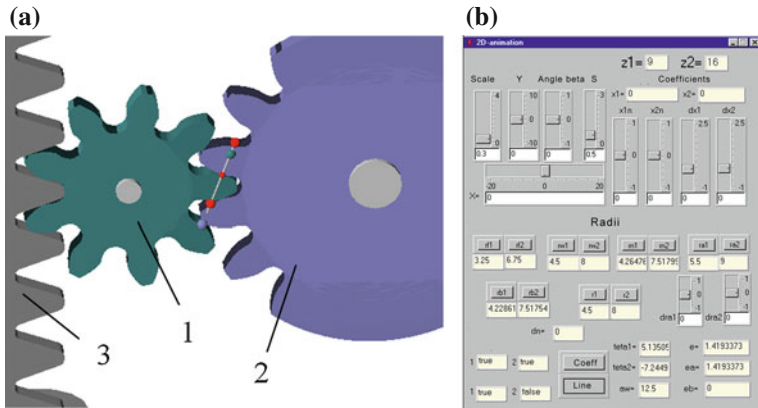
Fig. 7 Engagement of the gear wheel 1 with the wheel 2 and the tool rack 3 (**a**) and many points of background information are changeable on the panel (**b**)

the 2*D*-animation panel, it is possible to "remove" (make invisible) the axle body and differential cover. By moving the corresponding sliders, it is possible to shift the image in *X*, *Y*, *Z* coordinates, as well as to zoom in and out (Fig. 6c). Coefficient *KV* ("Rotation") shows the ratio of the left wheel's speed to the average axle speed (2 < KV < 2). By changing this ratio, the differential operation can be observed when the left and the right wheels are rotating at different speeds. Slider "velocity" makes it possible to increase or decrease the average speed of the motor.

7. Toothed gearing

Figure 7a shows the engagement of the gear wheel 1 with the wheel 2 and the tool rack 3. The gearing module m[1] is established to be 1 mm. The following parameters and settings can be changed on the 2D animation panel (Fig. 7b):

$x1n$, $x2n$—nominal offset coefficients for cutting wheels (for backlash-free gearing);
$dx1$, $dx2$—additional offset coefficients for cutting wheels (those that do not affect the **center distance**, and thus there is backlash in gearing);
X, *Y*, "Scale"—shifting the image in *X*, *Y* coordinates as well as zooming in and out;
"beta"—helix angle (for helical gearing);
S—tooth thickness;
$dra1$, $dra2$—additions to the corner radius.

By pressing the corresponding buttons, it is possible to make various radii of the wheels, gearing lines, gearing-entry points, etc. visible. Figure 7a shows only the gearing line and gearing-entry points. The 2*D* animation panel (Fig. 7b) shows the following background information: the number of gear teeth, displacement factors, radii of the circles (including pitch circles, base circles, top circles and root circles),

---

[1] $m = 25.4p$, where p is the diametric pitch.

minimum radii with in volute profiles, center distance, coefficient of overlap butting, specific sliding coefficients, and the presence of interference and undercutting. Correspondingly, it is possible to specify the desired number of teeth of the wheels in the "Model Vision" environment (before creating the executive file).

Computer Simulation in "AnyLogic"

The AnyLogic toolbox by AnyLogic Company (former XJ Technologies) makes it possible to create dynamic models that are compact and thus can be uploaded to the Internet and used in an online mode. AnyLogic is a professional computer program designed to model and visualize the behavior of various systems, including mechanical ones. To significantly simplify creation of new models of plane lever mechanisms for users, authors have created an object library. An object is a model that describes any part of the mechanism: e.g., link or an *Assur* group. Objects "link" or "Assur group" are similar, but not identical, to links and Assur groups typical for the theory of mechanisms and machines. For instance, the library includes six types of object "link": pillar with the revolute pair or the rectilinear sliding pair; and crank with the revolute pair or the rectilinear sliding pair, as well as the connection link with the revolute pair or the rectilinear sliding pair. Two later objects are designed for calculation of the coordinates of the aiming point or the attachment point. The library utilizes double-link Assur groups. They differ not only in the combination of revolute and rectilinear sliding pairs, but also in the link number in the group (which is of a variable length). For instance, in the link group R_PR (Pair RPR1), the first link has variable length, while in the link group RP_R (Pair RPR2), the second link does. Thus, the library contains ten objects "Assur group". Another object—the motor—is designed to change the input position. With these objects, the user can easily create a model of any Assur mechanism of the 2nd class.

With the created model, the user can:

observe the mechanism in motion;

change all the parameters of the mechanism;

create graphs of functions $xE(t)$ and $yE(t)$ of the randomly selected aiming point E;

investigate the effect of the mechanism parameters on its performance; and

observe special (singular) positions.

It is also possible to zoom in and out and to change the rotation speed of the crank, as well as to change the mechanism position in the animation window.

Figure 8 presents the program's interface. It includes an animation window, control panel, and graph-output windows. The animation window is intended to
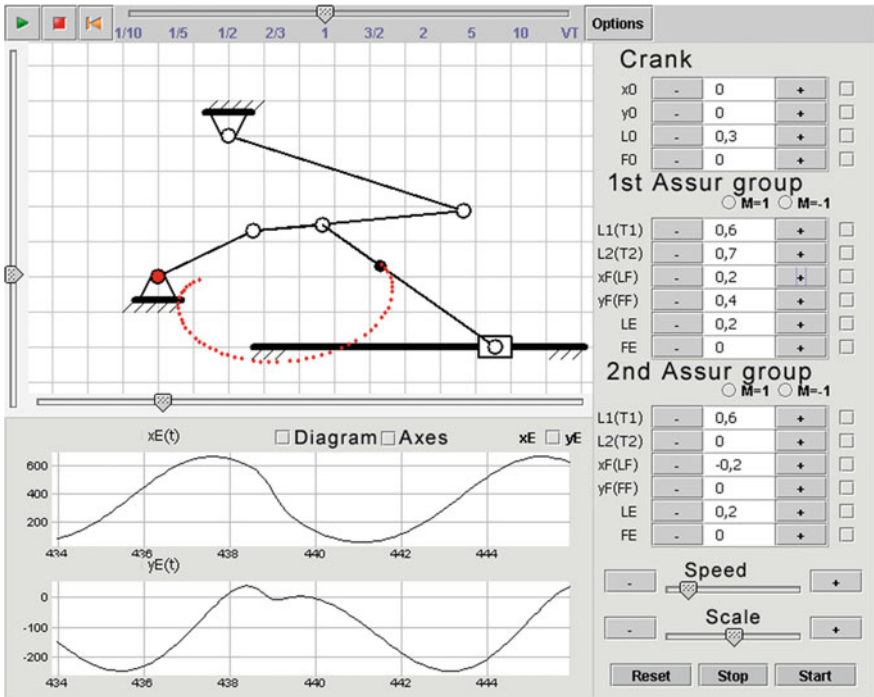
Fig. 8 Program interface of the AnyLogic toolbox

display an animation of the mechanism, geometric variable parameters, and position of the aiming point E, as well as to signal if the mechanism falls into a "special" position. Using the sliders on the bottom of the window, it is possible to change the position of the fixed coordinate-system origin in the animation window.

The control panel contains operating and control elements to start and stop the animation mechanism, to set and modify the parameters of the mechanism and to position the aiming point, as well as to manage information output in the animation window.

Graph-output windows display the graphs of functions $xE(t)$ and $yE(t)$, where E is the defined aiming point. Pressing the switch "Scheme" results in the display of the mechanism's kinematic scheme with the symbols of changeable parameters, instead of graphs. The following are the dynamical models, created with the AnyLogic toolbox.
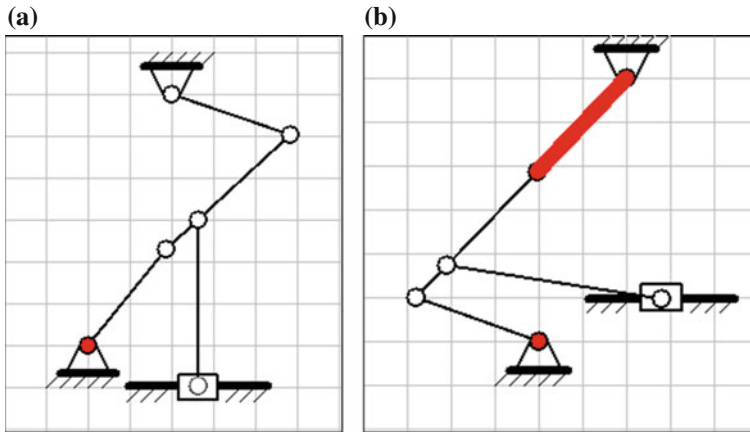
Fig. 9 Model of the mechanism in a special position (**a**) and a model of the mechanism for which a solution of the equations does not exist (**b**)

8. Six-bar linkage

Two Assur groups are attached to the crank: *RRR* and *RRP* (Fig. 8). The second Assur group is attached to the first link of the first group (connecting rod). The aiming point E is located at the first link of the second group.

The resulting visualized model of the mechanism can be used for both research and educational purposes (for example, to solve the trajectory problem).

It is worth mentioning that, in case the mechanism is unable to pivot, the program does not "freeze" and crash, but automatically adjusts the size of one of the links to achieve the condition of the crank existence; the adjusted part of the link then is highlighted in red, and the line thickness is increased.

Figure 9a shows a model of the mechanism in a special position (connecting rod is perpendicular to the crosshead's line of motion). Figure 9b shows a model of the mechanism, for which the solution of a system of equations for a group *RRR* does not exist. To allow the mechanism to pivot, the link length is increased (adjustment highlighted by a thickened line).

Several examples of ready-made mechanisms (ten four-link and 15 six-link) are already contained in the AnyLogic library.

9. V-shaped internal combustion engine

The model demonstrates the four-stroke internal combustion engine (Fig. 10): the movement of links, change in pressure in the cylinders, and opening and closing of the valves. The model allows adjusting the size of links, angle V, and the parameters of camshaft lobes.
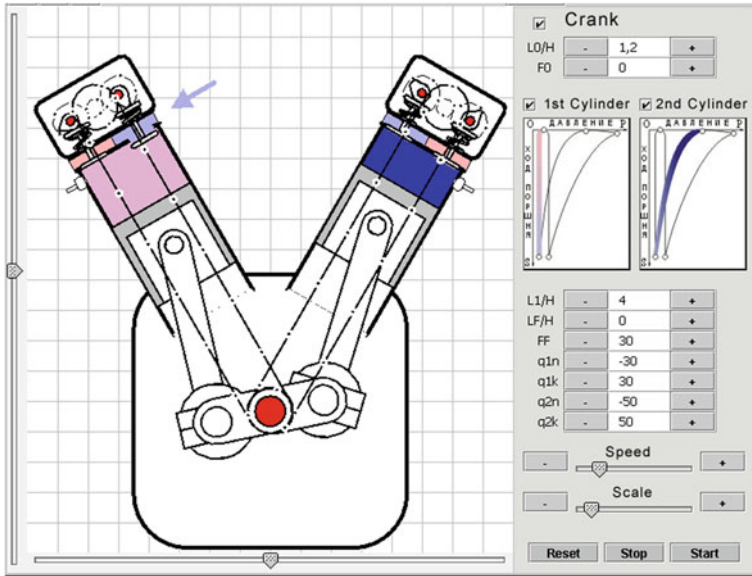
Fig. 10 Model demonstrating the four-stroke internal combustion engine

Conclusion

The packages described not only provide the solution of algebraic and differential equations in real time, but also visualize the behavior of the mathematical model. User-friendly interface enables quick creation of 2D and 3D images and necessary graphics. Using a variety of libraries makes the creation of the same-type models even easier.

The examples presented in this article can be found via the "Theory of mechanisms and machines" portal at: http://tmm.spbstu.ru/download.html.

References

1. Betrancourt M (2006) The animation and interactivity principles in multimedia learning. In: Mayer RE (ed) The Cambridge handbook of multimedia learning. Cambridge University Press, New York, 287 p
2. Rick Parent (2012) Computer animation. In: Algorithms and techniques, 3rd edn. The Morgan Kaufmann Series in Computer Graphics. Morgan Kaufmann Publishers Inc., San Francisco, CA, 542 p
3. Vulfert FN, Kochegarov BE (2016) Computer modeling animation of mechanical systems. Far Eastern Federal Univ: School Eng Bull 1(26):24–32 (in Russian)
4. Mkrtychev OV (2012) Computer modeling at the kinematic analysis of flat mechanisms. Theory Mech Mach 10(1)(19):46–52 (in Russian)

 5. Mkrtychev OV (2013) Computer modelling at force calculation of flat mechanisms. Theory Mech Mach 11(1)(21):77–83 (in Russian)
 6. Orlovskiy BV, Dvorzhak VM, Savchenko IV (2013) Circuitry Modeling of crochet-base machines mechanisms with tree degree of freedom with structure group 3rd class 4th order. Hmelnickiy National University Herald, Technical sciences, No 3, pp 174–181
 7. Matsyuk IN, Tretyakov WM, Shlyahov EM (2012) A kinematics analysis of flat lever mechanisms of high classes is in the program MathCAD. Theory Mech Mach 10(1)(19):65–70 (in Russian)
 8. Ziborov KA, Matsyuk IN, Shlyahov EM (2010) A power analysis of mechanisms is by the program MathCAD. Theory Mech Mach 8(1):83–88 (in Russian)
 9. Doronin FA (2014) The power analysis of some space frames and mechanisms by means of a MathCAD package. Theory Mech Mach 12(1)(23):59–69 (in Russian)
10. Verhovod VP (2013) Study of kinematic geometry plane mechanisms in GeoGebra. Mod Mech Eng: Sci Educ (3):659–669 (in Russian)
11. Babichev DT (2011) Computer simulation of planar mechanisms and design of multivariate reducers. Theory Mech Mach 9(2)(18):38–47 (in Russian)
12. Evgrafov AN, Petrov GN (2008) Computer animation of kinematic chains using Excel and MathCAD. Theory Mech Mach 6(1)(11):71–80 (in Russian)
13. Evgrafov AN, Petrov GN (2016) Drive selection of the multidirectional mechanism with excess inputs. Springer, Lecture Notes in Mechanical Engineering, pp 31–37
14. Petrov GN (1993) Algorithm of kinetostatic calculation with computer of closed lever mechanisms. J Mach Manuf Reliab 3
15. Semenov YA, Semenova NS (2015) Theory of machines and mechanisms with samples and tasks, part 1: textbook. Publishing House of the Polytechnic University, St.-Petersburg, 286 p (in Russian)
16. Hrostickiy AA, Evgrafov AN, Tereshin VA (2011) Geometry and kinematics of spatial six-membered mechanism with redundant links. Science technic sheets of SPbSTU. Publishing House of the Polytechnic University, St.-Petersburg, No 2(123). pp 170–176 (in Russian)

Energy-Flux Analysis of the Bending Waves in an Infinite Cylindrical Shell Filled with Acoustical Fluid

George V. Filippenko

Abstract This paper considers the problem of joint oscillations of an infinitely-thin cylindrical shell entirely filled with an ideal acoustical fluid, including the free vibrations of the system. The propagating waves and energy flux are analyzed in the system shell-liquid. It also compares various mechanisms of energy transmission in the shell and the input of the energy flux in the water.

Keywords Propagation of the waves · Cylindrical shell · Vibrations of the shells · Local and integral energy fluxes

Statement of the Problem

Nowadays, cylindrical shells are widely used in the construction of various pipelines, the supports of hydraulic engineering constructions, oil platforms, wind-based electric powers, standing on a shelf, etc. Calculation of these complicated systems demands major computing resources. Therefore, the consideration of simpler model problems that have exact analytical solutions [1–21] is realized. With these models, it is possible to analytically explore the main effects and also to use them as test problems for computing packages.

Let us start by considering an infinite cylindrical shell filled with an ideal compressible liquid, where the acoustic pressure P(x, y, z) is described by the Helmholtz equation Eq. (1) in the cylindrical system of coordinates—where axis z

G.V. Filippenko
Institute of Mechanical Engineering of RAS, Vasilievsky Ostrov,
Bolshoy Prospect 61, 199178 St. Petersburg, Russia

G.V. Filippenko (✉)
Saint Petersburg State University, 7-9 Universitetskaya nab,
199034 St. Petersburg, Russia
e-mail: g.filippenko@gmail.com; g.filippenko@spbu.ru
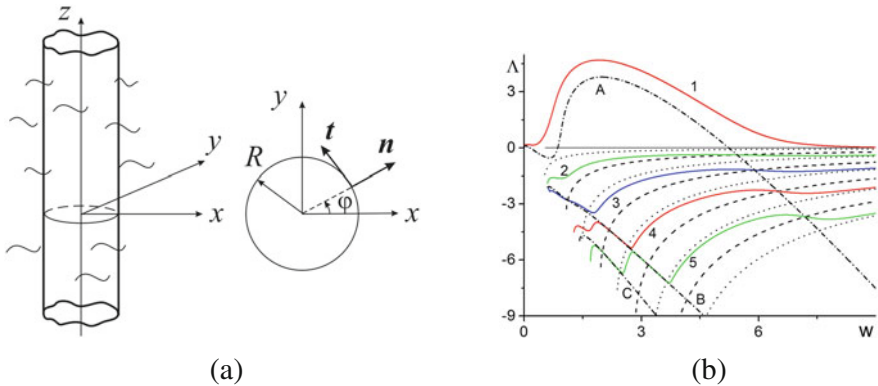
Fig. 1 Physical model (**a**); dispersion curves (**b**)

coincides with axis of the cylinder (see Fig. 1a). All processes are supposed to be harmonic with frequency ω [7–12].

$$(\Delta + k^2)P(r, z, \varphi) = 0; \quad k = \omega/c_w,$$
$$0 \le r \le R, \quad 0 \le \varphi \le 2\pi, \quad -\infty < z < +\infty. \tag{1}$$

The factor $e^{-i\omega t}$ describes the time-dependence and is omitted. The liquid is supposed to be ideal and compressible. The density is ρ_w, and the velocity of sound is equal to c_w.

Two relations take place at the shell–fluid boundary: kinematic (the adhesion condition)

$$u_n(z, \varphi) = \frac{1}{\rho_w \omega^2} \left. \frac{\partial P(r, z, \varphi)}{\partial r} \right|_{r=R} \tag{2}$$

and dynamic (balance of forces acting on the shell)

$$\frac{\rho c_s^2}{R^2} \mathbf{L}_w \mathbf{u} = (0, 0, P)^t. \tag{3}$$

The following notations are also used: $\mathbf{I}$ is the unit matrix operator, and $\mathbf{L}_w$ and $\mathbf{L}$ are matrix differential operators [13]. All these operators are represented by the matrices 3×3. For example, $\mathbf{L} \equiv [L_{ij}]$, and i, j = 1, 2, 3 consists of elements (see [13])

$$L_{11} = \alpha_1 [\nu_- \widetilde{\partial_z}^2 + \partial_\varphi^2], \quad L_{12} = \nu_+ \partial_\varphi \widetilde{\partial_z},$$
$$L_{13} = \partial_\varphi (1 + 2\alpha^2 [1 - \partial_\varphi^2 - \widetilde{\partial_z}^2]),$$
$$L_{22} = \nu - \partial_\varphi^2 + \widetilde{\partial_z}^2, \quad L_{23} = \nu \widetilde{\partial_z},$$
$$L_{33} = \alpha^2 (2\partial_\varphi^2 - 2 + 2\nu \widetilde{\partial_z}^2 - [\partial_\varphi^2 + \widetilde{\partial_z}^2]^2) - 1,$$
$$L_{21} = L_{12}, \quad L_{31} = -L_{13}, \quad L_{32} = -L_{23},$$

where $\widetilde{\partial}_z = R\partial_z$, $\alpha_1 = 1 + 4\alpha^2$, $\nu\pm = (1 \pm \nu)/2$. Here the following geometrical parameters of the shell are used: R is radius, h is thickness. The properties of the cylinder material are characterized by E, ν and ρs—Joung's module, Poisson coefficient, and volumetric density accordingly. The surface density of $\widetilde{\rho}$ ($\widetilde{\rho} = \rho_S h$) of the cylindrical shell c_s are introduced $c_s = \sqrt{E/((1 - \nu^2)\rho_s)}$.

The following dimensionless parameters are put in: $\alpha = \left(\frac{h}{R}\right)/\sqrt{12}$ (the relative thickness of the cylindrical shell) and $w = \omega R/c_s$ (the dimensionless frequency). The important roles in shell-fluid interaction are played by the dimensionless velocity $c = c_s/c_w$ and dimensionless density $\rho = \rho_s/\rho_w$. It can be noted that operator $\mathbf{L}_w$ in Eq. (3) governing the motion of a thin-walled shell came from [14]. The dispersion analysis of a cylindrical shell of this kind was fulfilled in [15, 16].

The source of an acoustic field in a waveguide is the vibration of the cylinder shell, caused by the incident wave propagating from the infinite part (z = −∞) of the shell. The frequency of this incident harmonic wave is equal to ω. All processes in the system shell–liquid are supposed to be harmonic at this frequency.

Determination of the General Representation for Acoustic and Vibrational Fields

Further, it is more convenient to involve the new vector $(u_t, u_z, P)^t$ (4) using Eq. (2):

$$\begin{pmatrix} u_t \\ u_z \\ u_n \end{pmatrix} = M \begin{pmatrix} u_t \\ u_z \\ P \end{pmatrix}; \quad M = \begin{pmatrix} 1 & 0 & 0 \\ 0 & 1 & 0 \\ 0 & 0 & \frac{1}{\rho_w \omega^2} \frac{\partial}{\partial r}\big|_{r=R} \end{pmatrix}. \tag{4}$$

Then, Eq. (3) can be rewritten in the form:

$$S \begin{pmatrix} u_t \\ u_z \\ P \end{pmatrix} = \begin{pmatrix} 0 \\ 0 \\ 0 \end{pmatrix} \equiv 0; \quad S = LM + N, \quad N = \frac{w^2}{\widetilde{\rho}\omega^2} \begin{pmatrix} 0 & 0 & 0 \\ 0 & 0 & 0 \\ 0 & 0 & 1 \end{pmatrix}. \tag{5}$$

The solution of Eq. (5) is searching in the form:

$$\begin{pmatrix} u_t \\ u_z \\ P \end{pmatrix} = Ae^{i\lambda z} \begin{pmatrix} \varsigma \sin m\varphi \\ \xi \cos m\varphi \\ \gamma J_m(r\sqrt{k^2 - \lambda^2}) \cos m\varphi \end{pmatrix}, \tag{6}$$

where $|\varsigma|^2 + |\xi|^2 + |\gamma|^2 = 1$. Here, the following notations are used: A, ζ, ξ, γ are arbitrary constants; J_m is the Bessel function with index m, and λ is the wavenumber which we are looking for. It can be noted that if $k < \lambda$, then the Bessel

function J_m is converted to I_m function. After substituting Eq. (6) into Eq. (5), the following algebraic system is obtained:

$$\hat{S}x = 0; \quad x = (\varsigma, \xi, \gamma)^t. \tag{7}$$

Operator $\hat{S}$ is the Fourier image of operator $\mathbf{S}$. The dispersion Eq. (8) is obtained from the condition of existence of nontrivial solution of this system

$$\det \hat{S} = 0. \tag{8}$$

We are looking for the real positive solutions of this equation. If the corresponding set of wavenumbers is founded one can solve Eq. (7) and define the previously unknown constants ζ, ξ, γ. After defining the constants, the complete solution of the problem, in terms of displacements of the shell $\mathbf{u}(\varphi, z)$ and pressure $P(r, \varphi, z)$ in the liquid, is determined.

As was mentioned above, all processes in the liquid and shell are supposed to be harmonic with frequency ω. It is convenient to average the energy streams on a period of oscillations $T = 2\pi/\omega$. The integral energy stream Υ in the liquid along axes z through the cross-section of the cylinder can be written in the form:

$$\Gamma = \frac{\omega}{2} \frac{1}{2\rho_w \omega} \int_0^{2\pi} d\varphi \int_0^R \mathrm{Im} \left(\bar{P} \frac{\partial P}{\partial z} \right) r dr. \tag{9}$$

The integral stream of the energy along axes z through the cross-section of the cylinder shell looks like this:

$$\Pi = \frac{\omega}{2} \int_0^{2\pi} \mathrm{Im}(u^4, \mathbf{F}u^4)_{C4} R d\varphi = \Pi_t + \Pi_z + \Pi_n + \Pi_p, \tag{10}$$

where $\mathbf{u}^4 = (u_t, u_z, u_n, u_p)^t$, $u_p = -\partial_z u_n$ is the vector of generalized displacements, $\mathbf{f}^4 \equiv \mathbf{F}u^4 = (u_t, u_z, u_n, u_p)^t$ is the vector of generalized forces, $\mathbf{F}$ is the matrix differential operator 4×4 [13],

$$\Pi_t = \pi\rho c_s^2 \frac{\omega}{2} \mathrm{Im}\Big\{ (2\alpha^2(1-v)\partial_\varphi \tilde{\partial}_z u_n - v - (\alpha_1 \tilde{\partial}_z u_t + \tilde{\partial}_\varphi u_z))\bar{u}_t \Big\},$$

$$\Pi_z = \pi\rho c_s^2 \frac{\omega}{2} \mathrm{Im}\Big\{ (-v\partial_\varphi u_t - \tilde{\partial}_z u_z - vu_n)\bar{u}_z \Big\},$$

$$\Pi_t = \pi\rho c_s^2 \frac{\omega}{2} \mathrm{Im}\Big\{ \alpha^2 \bar{u}_n (((2-v)\partial_\varphi^2 - v + \partial_\varphi^2)\tilde{\partial}_z u_n - 2\partial_\varphi \tilde{\partial}_z u_t) \Big\}, \tag{11}$$

$$\Pi_p = \pi\rho c_s^2 \frac{\omega}{2} \mathrm{Im}\Big\{ \alpha^2 (v(\partial_\varphi^2 - 1)u_z - 2v\partial_\varphi u_t + \tilde{\partial}_\varphi^2 u_n)(-\tilde{\partial}_z \bar{u}_n) \Big\}.$$

Here letters t, z, n, and ρ marked tangential (rotating), longitudinal, normal and momentum components of energy flux Π and components of vector of generalized displacements $\mathbf{u}^4$.

In the particular case of axisymmetric rotating movements of the cylindrical shell, the integral energy flux in it looks like this:

$$\Pi^0 = 2\pi\rho c_s^2 \frac{\omega}{2}|A|^2\,\beta \equiv \Pi_t^0; \quad \beta = w\sqrt{(1+4\alpha^2)(1-\nu)/2}. \tag{12}$$

Numerical Calculations

Equations (9)–(10) can be used to obtaining the normalized energy stream S in the shell and its components $S = \Pi/(\Pi+\Gamma)$, $S_{t,z,n,p} = \Pi_{t,z,n,p}/(\Pi+\Gamma)$. The vectors of generalized displacements $\mathbf{u}^4$ and forces $\mathbf{f}^4$ are also normalized: $\mathbf{u}^4 := \mathbf{u}^4/\|\mathbf{u}^4\|, \mathbf{f}^4 := \mathbf{f}^4/\|\mathbf{f}^4\|$. In the figures, the curves corresponding to rotational (t), longitudinal (z), bending (n), and moment (p) components of the energyfluxes and generalized vectors are marked by digits 1–4. The following values of parameters of the system are assumed for calculations $\nu = 0.3, c_s/c = 3.6, \rho_s/\rho_w = 7.8, h/R = 0.05$ that correspond to the interaction of water with a shell made of steel.

In Fig. 1b, the dependence of dimensionless wavenumber $\Lambda \equiv \lambda - \omega R/c_w$ on nondimensional frequency w is shown for the first five dispersion curves (these curves are marked by digits 1–5). The multiple veering (quasi-intersection) of these curves is well noted. It is caused by interaction of the two waveguides (liquid and cylindrical shell). The dispersion curves corresponding to the "dry" shell (dash-dotted lines) are marked by letters A, B, and C.

The elastic wall of the shell is the intermediate case between absolutely rigid and absolutely soft bounds of the liquid waveguide. According to the variation of the system parameters, it becomes more rigid or softer. In Fig. 1b, the dispersion curves corresponding to absolutely rigid and absolutely soft boundary conditions are marked by dashed and dotted lines, respectively. These lines are reciprocated due to the features of the Bessel function's zeroes in the dispersion Eq. (8). The dispersion curves of the elastic system follow (with frequency increasing) to dashed or dotted lines after passing the points of veering. Partly these curves follow the lines of the "dry" shell. The character of the waves on different part of the dispersion curves can be obtained by the analyzing the energy-flux components. According to Eq. (11), the integral fluxes (curves 5) and its components S_t, S_z, S_n, and S_p (curves 1–4) are represented on Fig. 2b, 3 and 4 as functions of dimensionless frequency w.

Various energy-flux components are dominated in different parts of dispersion curves. For example, the behavior of the wave from the first dispersion branch Fig. 2a differs from the others significantly. It is very apparent that the wave-energy flux from the first dispersion branch is significant in a wider span of frequencies, and the banding component of the energy flux is dominant in it. The rotation
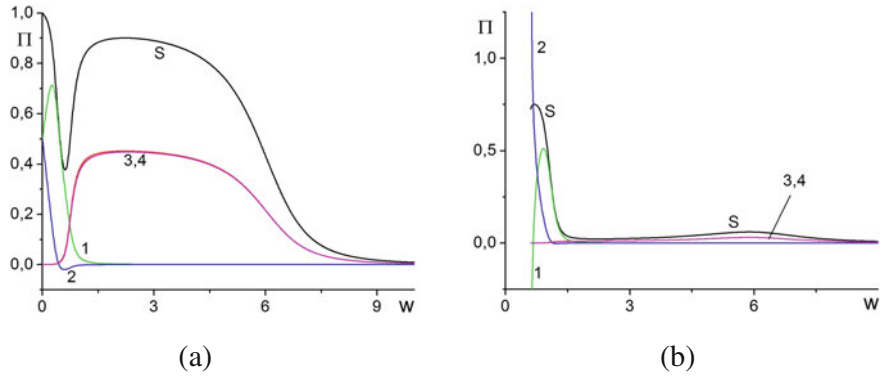
Fig. 2 Energy flux components in the shell for the wave from the first dispersion branch (**a**); from second dispersion branch (**b**)
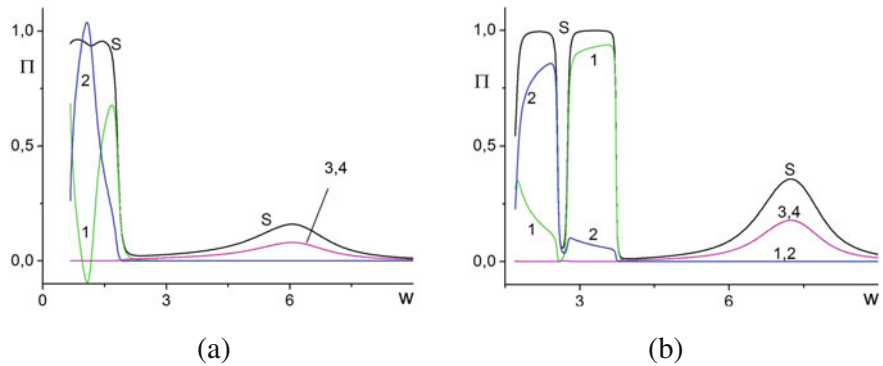
Fig. 3 Energy-flux components in the shell for the wave from the third dispersion branch (**a**); from the fifth dispersion branch (**b**)

and longitudinal components of the energy flux are dominant in other waves (Figs. 2b and 3b).

The veering of the dispersion curves corresponds well with the changing of the specific weight of various components of the energy fluxes (Figs. 2 and 3). Figure 3 for the wave from the fifth dispersion curve well illustrates this effect. The rotational, longitudinal, and bending character of the wave is consequently changed after passing the points of veering (Fig. 1b). Some components of the energy flux can be negative in a small span of frequencies (for example, "z" component for the first branch and "t" component for the second and third branches).
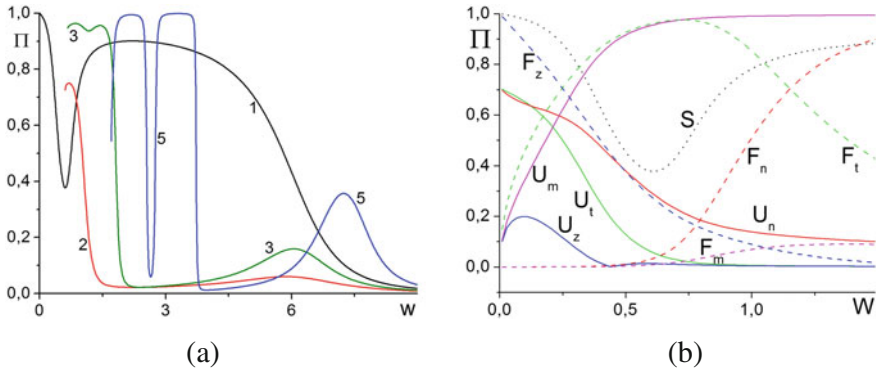
Fig. 4 Integral energy fluxes (1, 2, 3, 5) for the waves from 1, 2, 3, and 5 branches (**a**); integral flux (S) and absolute values of generalized vectors components for the wave from the first branch (**b**)

The dependence of integral energy fluxes on w for various branches (1–5) is shown in Fig. 4a. The maximums of integral energy fluxes are moving to the higher frequencies, and the role of the bending component is increased when the number of branches increase.

The normalized integral-energy flux and the absolute values of generalized vectors components for the wave from the first branch are represented on Fig. 4 as functions of dimensionless frequency w. Displacements and forces do not "feel" the points of veering well and show erratic behavior.

Conclusions

The considered exploration of wave processes shows that energy-flux analysis provides additional opportunities for detailed analysis of shell-liquid interaction. The components of displacement vectors (the usual method) and forces can show the erratic behavior. The energy flux is more informative, because it takes into account not only the displacement and force vectors, but also the shift of phase between them.

References

1. Filippenko GV (2016) The vibrations of reservoirs and cylindrical supports of hydro technical constructions partially submerged into the liquid. In: Evgrafov A (ed) Selected contributions from the Conference Modern Engineering: Science and Education, Saint Petersburg, Russia.

Lecture Notes in Mechanical Engineering. Springer, Switzerland, June 2014, ISSN 2195-4356, ISSN 2195-4364 (electronic), ISBN 978-3-319-29578-7 ISBN 978-3-319-29579-4 (eBook). doi:10.1007/978-3-319-29579-4 (Library of Congress Control Number: 2016931213)

2. Filippenko GV (2012) The vibrations of pipelines and thin-walled supports of hydro technical constructions sub merged into the liquid. In: Proceedings of second international scientific and practical conference. Published by State Polytechnic University, SPb, Russia, pp 769–778. http://www.mmfspbstu.ru/mese/2012/769-778.pdf

3. Zinovieva TV (2012) Computational mechanics of elastic shells of revolution in mechanical engineering calculations. In: Modern engineering: science and education. Proceedings of second international scientific and practical conference. Published by State Polytechnic University, SPb, Russia, pp 335–343

4. Sorokin SV, Nielsen JB, Olhoff N (2004) Greensmatrix and the boundary integral equation method for the analysis of vibration and energy flow in cylindrical shells with and without internal fluid loading. J Sound Vibr 271:815–847

5. Blaauwendraad J, Hoefakker JH (2014) Structural shell analysis. Springer, Netherlands, p 300. doi:10.1007/978-94-007-6701-0

6. Yeliseyev VV, Zinovieva TV (2014) Two-dimensional (shell-type) and three-dimensional models for elastic thin-walled cylinder. PNRPU Mech Bull 3:50–70. doi:10.15593/perm.mech/2014.3.04

7. Fuller CR, Fahy FJ (1982) Characteristics of wave propagation and energy distributions in cylindrical elastic shells filled with fluid. J Sound Vib 81(4):501–518

8. Pavic G (1990) Vibrational energy flow in elastic circular cylindrical shells. J Sound Vib 142 (2):293–310

9. Pavic G (1992) Vibroacoustical energy flow through straight pipes. J Sound Vib 154(3):411–429

10. Feng L (1994) Acoustic properties of fluid-filled elastic pipes. J Sound Vib 176(3):399–413

11. Filippenko GV (2014) Analyzing of energy fluxes in the infinite cylindrical shell contacting with compressible liquid. In: Proceedings of the conference "XXVII session of Russian Acoustical Society, 16–18 Apr 2014, St. Petersburg, Russia, CD format, 8 p (in Russian). http://rao.akin.ru/Rao/sess27/proceedings27.htm

12. Ter-Akopyants GL (2015) Axisymmetrical wave processes in cylindrical shells filled with fluid. Estestvennye-i-tehnicheskie-nauki (Nat Eng Sci) 85(7):10–14. ISSN 1684-2626

13. Filippenko GV (2011) The energy analysis of shell-fluid interaction. In: Proceedings of the international conference "Days on Diffraction 2011", St. Petersburg, Russia, pp 63–66

14. Yeliseev VV (2003) Mechanics of elastic bodies, SPb., SPbSPU, Russia, 336 p (in Russian)

15. Zinovieva TV (2007) Wave dispersion in cylindrical shell, Acta of SPb-SPU, Engineering. SpbSPU press, St. Petersburg, No 504, pp 112–119

16. Yeliseev VV, Zinovieva TV (2014) Two-dimensional (shell-type) and three-dimensional models for elastic thin-walled cylinder. PNRPU Mech Bull 3:50–70

17. Veshev VA, Kouzov DP, Mirolyubova NA (1999) Energy flows and dispersion of the normal bending waves in the X-shaped beam. Acoust Phys 45(3):331–337

18. Sorokin SV (2011) The Green's matrix and the boundary integral equations for analysis of time-harmonic dynamics of elastic helical springs. J Acoust Soc Am 129(3):1315–1323

19. Kouzov DP, Mirolubova NA (2012) Local energy fluxes of forced vibrations of a thin elastic band. Vycisl. meh. splos. sred Comput Continuum Mech 5(4):397–404

20. Filippenko GV (2014) Energy aspects of wave propagation in an infinite cylindrical shell fully submerged in liquid. Vycisl. meh. splos. sred Comput Continuum Mech **7**(3):295–305

21. Filippenko GV (2013) Energy aspects of axisymmetrical waves propagation in the infinite cylindrical shell fully submerged into the liquid. Vy-cisl. meh. splos. sred Comput Continuum Mech 6(2):187–197

Principle of Compatibility of Heterogeneous Additives in Triboactive Metalworking Fluids for Edge Cutting of Metals

Vladimir A. Godlevskiy, Vladimir V. Markov and Nadezhda V. Usoltseva

Abstract The problem of the combined usage of surface and chemically-active additives within metalworking fluids (MWF) for edge-cutting processing has been studied. The test results of MWFs containing surface-active additives with oxygen-containing reactive components have been demonstrated. The hypothesis of the special structure of boundary lubrication layers formed by two triboactive components of different chemical nature has been defined.

Keywords Edge cutting · Metalworking fluids · Additives · Surfactants · Peroxide

Introduction

Highly-active MWFs are usually used in the case of cutting metals and compounds of low processability. This activity is stimulated by introducing reactive additives containing sulfur, phosphorus, and halogens. Due to ecological reasons, these materials are not advisable to use. And here we need to solve a problem of devising a safer method of processing.

It was suggested using a surfactant's solution supplemented by a reactive oxygenated compound—highly-dispersed inorganic peroxide—as a way to solve this problem [1]. The possibility of using hydrogen peroxide as a MWF has already been mentioned before, but the fact that this compound quickly decomposed in

V.A. Godlevskiy (✉) · N.V. Usoltseva
Ivanovo State University, Ivanovo, Russia
e-mail: godl@yandex.ru

N.V. Usoltseva
e-mail: nv_usoltseva@mail.ru

V.V. Markov
Ivanovo State Power University, Ivanovo, Russia

water solutions made this method unreliable [2]. In this respect, changing hydrogen peroxide to more thermodynamically-stable metal peroxides gives a new chance for creating a stable technological composition, separating the active component directly in the contact zone. However, an additional problem occurs here: how to provide colloid stability of the solid peroxide powder in liquid media. This task could be solved by selecting a certain surfactant serving not only as a lubricant agent but also as a stabilizer of suspension.

Testing of WMF-model compositions containing additives selected according to the above principle enabled reanalysis of the interaction process of the two types of components (surface-active and reactive) during the boundary-layer formation in the contact zone of cutting.

Short Preview

There has been a long scientific discussion over the mechanism of outer-media influence during metal processing with cutting. The special features of penetration kinetics of the lubrication material into the contact zone have been in the center of these discussions. Also, a lot of attention has been given to the role of physical and chemical processes in boundary-layer formation. Outer-media penetration into the cutting zone has received a very transparent explanation within the framework of micro-capillary model [3–5], which is based on considering consequential phases correlating with certain processes of interaction between the media and solid surfaces. It is quite logical to surmise that, due to the high temperature in the contact zone of the tool with the processed material, the lubrication layer is formed mainly as a result of chemo-sorption of the additives' active components and the products of destruction of the lubrication material's organic components [6].

Up to now, a number of the experimental facts within these views has not been clearly understood. For example, why do the colloid surfactant's solutions possess the lubrication effect when cutting and nonpolar organic components (e.g., benzol) turn out to be ineffective [5]? Why do surfactants having different extensional molecular structures, but almost the same composition of elements, so strongly vary with regards to tribological activity? Even within the surfactant's homological array, one can see significant differences in the lubrication activity and, at the same time, it is clear that, when the radical chain is lengthened, the additive efficiency grows [7] (the so called Traube effect).

The fact that surfactant start having an antifriction effect when cutting even in small concentrations (less than hundredth of percent) confirms that the lubrication efficiency of these additives is first of all connected to the surface processes. We have justly pointed out the fact that the concentration curve of the surface-active additive efficiency is very similar to the isotherm curve of the surface-tensions of the same additive [8].

The joint activity of surfactants and reactive components is still left unclear. One of the suggestions was that reactive particles introduced into the MWF and

contained in the additives of high-pressure (HP additives), such as oxygen, sulfur, and chloride, due to the smallness and higher mobility of particles, must comparatively more quickly reach the surface and form the hemosorption layer earlier than the physically-adsorpted film made of amphiphiles is formed.

However, in the case of WMF composed of active molecules of both types, the action of surface-active additive would be insignificant, while the experiments show that, within the composition, these additives act synergistically in the cutting. In the meantime, it has been discovered that, in common friction processes, the presence of oxygen significantly lowers the effects of adsorptional plastification and dispersal [9].

Hypothesis of a Lubrication Layer's Combined Structure

Now we have data that the organic mesogenes, forming developed and ordered (epitropic) supramolecular structures (for example, entities of heterocyclic type) on the surface, are quite efficient as additives for metalworking [10–12] though it is unlikely that the structural order of large molecules on the surface could play a significant role under such high temperatures.

It is a well-known fact that compositions of two surfactants with different molecular structures (for example, ionic with non-ionic surfactants) have a much better tribological efficiency than each of these components used separately [13, 14]. In our view, nothing can explain this fact except the specifics of the surface supramolecular structure of the boundary layer.

The multitude of the above-listed facts confirms that, during the process of lubrication-layer formation in cutting, macromolecular components, such as colloid surfactants, preserve to some extent their molecular specifics, and do not disintegrate in spite of high-contact temperatures (400–1100 °C), which, in the majority of real technological activities of mechanical processing, exceeds the thermo-deconstruction temperature of the given compounds. Hence, it would be logical to try to find the factors which allow organic agents to preserve their lubrication ability under the high-temperature cutting conditions. In order to make the described situation clear, we have come up with the following working hypothesis:
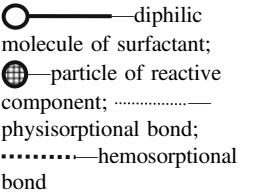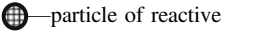
- Abnormal thermostability of colloid surfactants and other mesogenic amphiphiles macromolecules appear as a result of their joint activity with reactive media components (e.g., air oxygen and HP-additives).
- As a result of the process similar to the hypothetic process of "tribopolymerization" [15] "the third body", "secondary structure" is formed on the surface of the microcapillary cavity between the tool and chips which represents a lubrication film of the complex composition the basis of which is formed by amphiphile molecules.

- The role of the reactive component in forming such a film is as follows: (a) it chemically connects the part of active surface centers; (b) it forms chemical "bridges" connecting radical chains of amphiphile and forming solid and thermostable supramolecular structure.

In Fig. 1, the hypothetical structure of the boundary lubrication composed of different types of particles is shown. One can see that, in the case of the joint usage of adsorption and reactive components within a MWF, a more extensionally developed and evidently more solid structure of the layer is formed on the surface (Fig. 1c). A process of vulcanization of elastomers can serve as a very close analogy to our hypothetical process.

A reasonable objection to the described process could be the assertion that it is difficult for this type of complex structure to be formed in high temperatures when the entropy of the molecular structure is increased and tends to become disordered. However, we must take into account the fact that the temperature role in such a process is ambivalent.

Fig. 1 Schematic image of the structure of the boundary-lubrication layer formed on the surfaces of chips and tools at cutting in MWF containing: **a** surface-active additive; **b** reactive additive; **c** additives of the both types; ⊙————diphilic molecule of surfactant; ⊕—particle of reactive component; ·············— physisorptional bond; ··········—hemosorptional bond
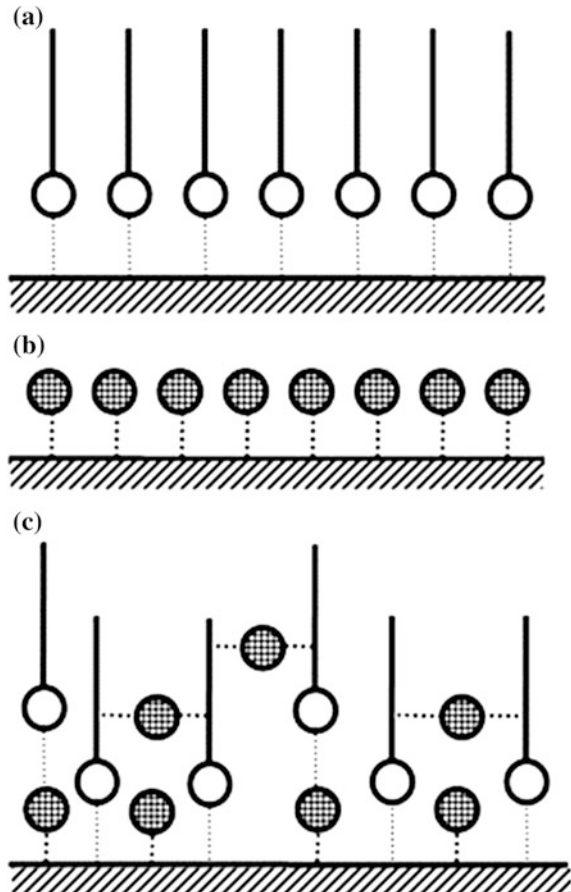
Along with the disorder tendency, the temperature growth accelerates the thermodynamically possible processes and diffusion gets quicker—and these factors provide for more rapid lubrication-layer formation and its faster structural ordering long before it is rigidly fixed by chemical bonds. Besides, we can't but underline the fact that the process of such a "composite"-layer formation is irreversible, because bonding between its elements is a chemical process and to disorder such a layer means to fully destroy it.

As we have already noted, the idea of a composite, "polymerized" lubrication layer is well matched by the multiple experiments which we would like to confirm with our empirical data.
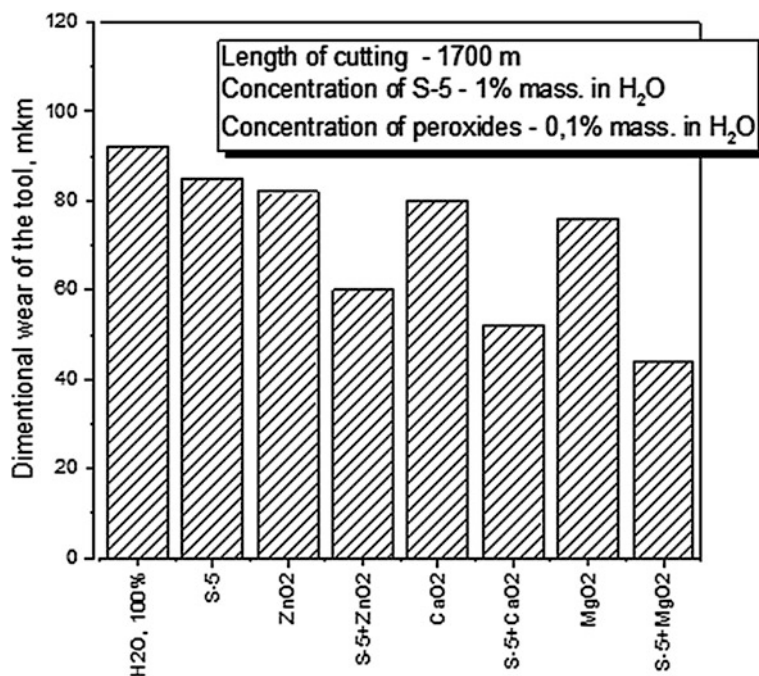

Experimental

We have performed experiments involving semi-rough turning of stainless steel 12X18H10T with cutters possessing a cutting part made of carbides of VK8 and T5K10 brands. The turning was made with the following modes of cutting: cutting speed v = 3.2 m/c, feed s = 0.13 mm/rot, cutting depth t = 0.5 mm. WMF were fed into the cutting zone as a free-falling stream at an expense of 500 ml/min. The geometry of the cutters had the following parameters: γ = 9°; α = 9°; φ = 90°; φ_1 = 9°; λ = 0°.

The experiments were conducted at a turning machine supplied with devices for simultaneous registration of several parameters of processing. Three orthogonal components of the cutting force [EMF of the natural thermocouple and dimensional wear and tear of the tool in radial direction (coordinate y)] were measured. The influence of the additive of a non-ionic, surface-active additive to water under the name of Syntamid-5 (S-5) over the above parameters is shown in Fig. 2.

The diagram show that, over the significant cutting path during processing of solid and viscous material, a small amount of surface-active additive significantly lowers the dimensional wear of the tool.

From the diagram (Fig. 2), one can conclude that increasing the surfactant's concentration above some minimum value (apparently necessary for formation of continuous adsorptional layer) meaning does not provide for efficiency growth. It confirms the surface-adsorption nature of this additive activity. A small amount of peroxide added to the surfactant's solution leads to the immediate lowering of the tool-wear intensity (irrespectively of surfactant concentration). Very similar results have been achieved with using the solid fine peroxides MgO_2, CaO_2 and ZnO.

From Fig. 2, it follows that the addition of a small amount of an additive of surfactant, as well as peroxide additives, results in a substantial reduction of tool wear. And, with the joint application of surfactant and solid-peroxide suspension, the synergic effect is observed, i.e., joint application of additives reduces deterioration more strongly, rather than application of each additive separately. Such an effect is called synergism. The reason, in our opinion, resides in features of a

Fig. 2 The results of experiments on turning of stainless steel 12H18N10T by a carbide tool of VK-8 in water solution of nonionic surfactant Syntamide 5 (S-5) with the addition of pulverized non-organic solid peroxides

"hybrid" structure of a boundary layer as shown on Fig. 1. To confirm our suggestions, it is necessary to conduct specialized experiments for the instrumental investigation of the layer structure formed after cutting.

Conclusion

Thus, the above-listed experimental data on using simultaneously surface- and chemical-active additives within a WMF are in compliance with the proposed working hypothesis based on the proposal of a special "hybrid" structure of the boundary-lubrication layer, similar to the structure of tribo-polymeric films.

References

1. Godlevskiy VA, Markov VV (2004) Synergic interaction of superficial- and chemically-active metalworking fluids components. Mater Int Sci Conf SLOVIANTRIBO-6. St. Petersburg, vol 2, pp 41–46 (in Russian)
2. Latyshev VN, Markov VV (1974) The peroxyde substances application as metalworking fluids. Mach Technol 10:6–12 (in Russian)
3. Williams JA, Tabor D (1977) The role of lubricants in machining. Wear 43(3):275–292
4. Godlevskiy VA, Latyshev VN, Volkov VV, Maurin LN (1997) The kinetics of lubricant penetration action during machining. Lubr Sci 9(2):127–140
5. Astakhov VP, Godlevskiy VA, Joksch S et al (2012) Metalworking fluids for cutting and grinding: fundamentals and recent advances. Woodhead Publishing Ltd., Cambridge, UK, 413 p
6. Latyshev VN (1985) Increasing of metalworking fluids effectivity. Mashinostrojenije, Moscow, 65 p (in Russian)
7. Mizuhara K (1992) Experimental evaluation of cutting fluid penetration. Tribologia 11 (2):20–29
8. Godlevskiy VA, Markov VV, Volkov AV (2009) Description of surface active lubrication materials action at edge cutting with model of mono-molecular adsorption. In: Liquid crystals and their practical application, vol 3, pp 61–66 (in Russian)
9. Kostetskiy BI, Natanson ME, Bershadskiy LI (1972) Mechano-chemical processes during boundary friction. Nauka, Moscow, 214 p (in Russian)
10. Berezina EV, Godlevskiy VA, Latyshev VN et al (1995) To the mechanism of phthalocyanine derivatives solutions lubrication action at metal cutting processes. Izvesija AN RF. Physical series, vol 59(3), pp 161–165 (in Russian)
11. Berezina EV, Godlevskiy VA, Usoltseva NV (2007) Phenomena of supramolecular self-organization in boundary lubrication layer. In: Friction and lubrication in machines and mechanisms, vol 4, pp 30–36 (in Russian)
12. Godlevskiy VA, Berezina EV, Volkov AV, Zheleznov AG, Fomichev DS (2015) On the research technique of mesogene lubrication layer optical properties. In: Lecture notes in mechanical engineering. Springer Int. Publ., Switzerland, pp 7–12
13. Pletnev MJ (1987) About the interaction nature in a solution of non-ionogenic and ionogenic surfactants mixtures. In: Kolloidny zhurnal, vol 49(1), pp 184–187 (in Russian)
14. Lazjuk LN (1985) Influence of surface-active COTC on machining of silicon and gallium arsenide. Dissertation … cand. chem. science, Ivanovo, 165 p (in Russian)
15. Zaslavskiy JS, Zaslavskiy RN (1978) The action mechanism of oils anti-wear additives. Chimija, Moscow, 224 p (in Russian)

Some Ways of Stable Counterbalancing in Respect to Moving Masses on Centrifuges

Vladimir I. Karazin, Denis P. Kozlikin, Alexander A. Sukhanov, Valery A. Tereshin and Igor O. Khlebosolov

Abstract The paper looks into methods of balancing centrifugal forces of inertia in vibro-rotational stands. It tackles the problem related to defining the generalized condition for stable operation of the balancing unit, which is built on the principle of a compound lever.

Quite a number of papers are dedicated to the issues of simulation of the combined influences in a field of linear acceleration [1–11]. The authors emphasize the specific importance of this research area, since, no doubt, it is economically feasible to use laboratory equipment for testing items at various stages of its development.

Broadband vibration on the basis of constant and variable linear accelerations [12, 13] is simulated on vibro-rotational balancing stands, which are hard to create since non-standard solutions are to be used and the scopes of research are large.

Such balancing stands are specific to operate because of reciprocal transportation of the table with a test item. Moreover, the centrifugal force is variable, since it

V.I. Karazin (✉) · D.P. Kozlikin · A.A. Sukhanov · V.A. Tereshin · I.O. Khlebosolov
Peter the Great Saint-Petersburg Polytechnic University, Saint-Peterburg, Russia
e-mail: visv05@mail.ru

D.P. Kozlikin
e-mail: kozlikindenis@gmail.com

A.A. Sukhanov
e-mail: Alexeevich@post.ru

V.A. Tereshin
e-mail: terva@mail.ru

I.O. Khlebosolov
e-mail: khlebosolov@mail.ru

depends on the radius of mass position and is continuously preventing the system from returning towards radius shortening.

Further on, there is a brief review of well-known design solutions aimed at counterbalancing of inertia forces exerted on relatively mobile elements of the stand, which carry out controllable radial back-and-forth motions during tests [14–17].

In Fig. 1 the rotor of centrifuge 1 is rigidly connected to the body of vibration stand 2. Test item 3 is positioned on the table of vibration stand 4. The centrifugal force F, which occurs as the centrifuge rotates at the angle velocity Ω, tends to prevent the back-and-forth motion Δx of the relatively mobile system 3 and 4. The inertia force is compensated by balancing mass 5 connected by link 6 to table 4. Such a counterbalancing scheme can be used with small values of Δx, realized within the elastic strength of link 6. In other cases, the lost stability of the system is obvious, which occurs due to the lack of restoring forces [14, 16].

Figure 2 shows a scheme where linear compression springs 7 are used to compensate the inertia force F. The former ones are established between shaker table 4 and stop 8, which is an element of platform 2. The restoring force, proportional to displacement Δx according to the stiffness of the spring, ensures the required balance during back-and-forth motion. However, the efficiency of such a scheme is limited by the range of linear accelerations of the centrifuge [16].

If the upper limit of the test range of linear accelerations simulated on the centrifuges increases, there is a bigger displacement of stop of Δx, which, in turn, imposes design features in the context of the implemented compression springs and the stop on the plant. For example, to compensate for the centrifugal force of inertia of 60,000 H, ten coil springs are needed, and the stop must be displaced by 1.5 m.

Both schemes presented in Figs. 1 and 2 are united in the following solution in Fig. 3. Springs 7 are transferred into the left part of platform 1 and form a restoring force on balancing mass 5. In such a combination, springs 7 are loaded to a lesser extent and their practical implementation becomes possible.

Fig. 1 The rotor of centrifuge 1 is rigidly connected to the body of vibration stand 2
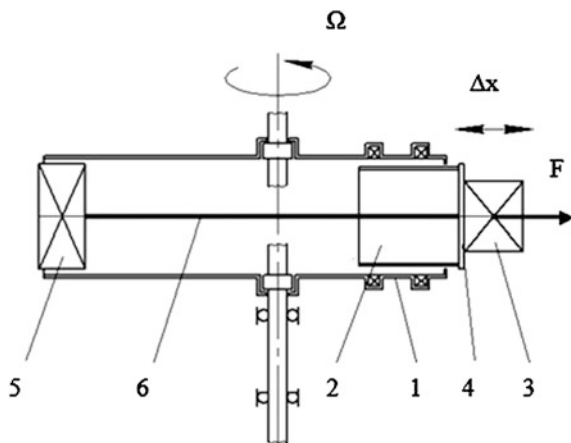
Fig. 2 Scheme where linear compression springs 7 are used to compensate the inertia force F
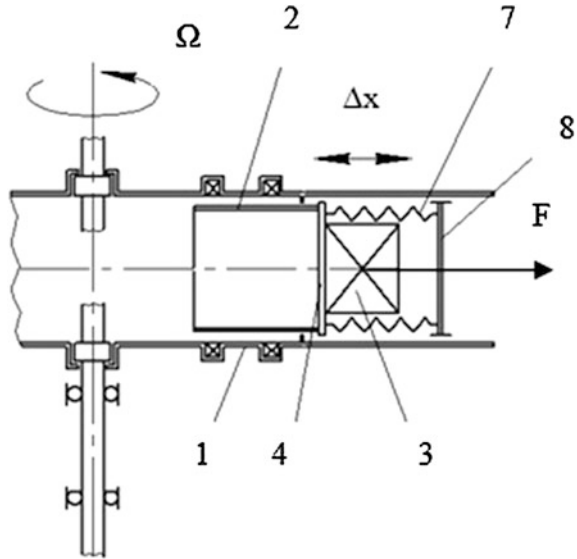
Fig. 3 Schemes presented in Figs. 1 and 2 are united in solution
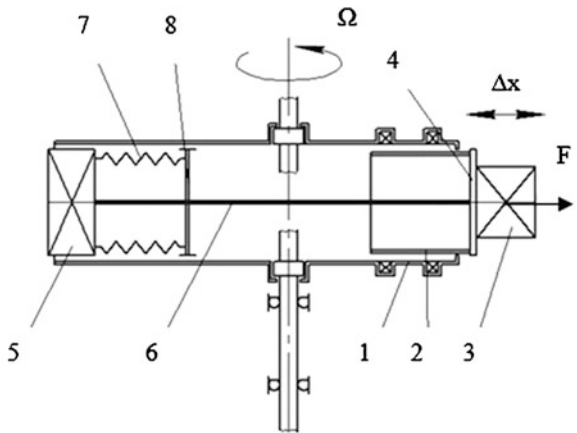
When springs are used for a restoring force, it ensures the stability of the system's operation, but this solution has a specific feature. The fact is when the rotation velocity of the centrifuge Ω changes, the initial interacting force of springs 7 and balancing mass 5 must be changed too. Such adjustment may be provided with a radial displacement of stop 8, which is rigidly linked to platform 1.

One more scheme that makes stable balancing of the mobile systems of the vibro-rotational stand possible is presented in Fig. 4. Instead of coil mechanical springs, elastic properties of compressed air may be used [15]. The necessary inertia force F is created by delivering air under design pressure in enclosed volume 7. Balancing mass 5 performs the role of a piston component, whereas the enclosed volume carries out the functions of a cylinder.

Fig. 4 One more scheme that makes stable balancing of the mobile systems of the vibro-rotational stand possible. Instead of coil mechanical springs, elastic properties of compressed air may be used
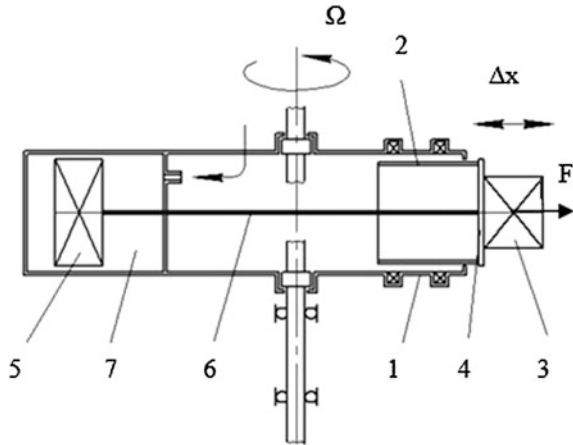
Fig. 5 The first of two design schemes that show unloading of inertia forces on the rotor of the centrifuge with the use of pneumatic cushions 7
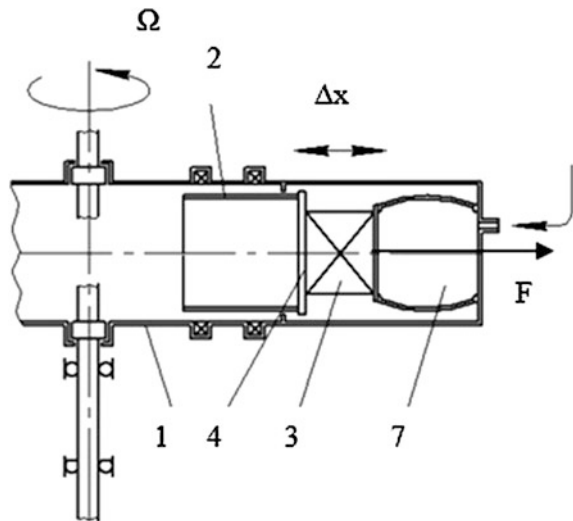
In Figs. 5 and 6 two design schemes are presented. They show unloading of inertia forces on the rotor of the centrifuge with the use of pneumatic cushions 7 [15]. They have been widely used in the production industry and are good for tackling our problem due to a number of characteristics. First, they have a low proper frequency, which is why vibrations can be simulated without distortion. Second, the carrying capacity is high and deformation can be considerable in the working direction, but virtually absent in other directions. Third, positions and carrying capacity can be fairly easily adjusted. Forth, there are no connections which have to be sealed, like those, for example, as in the scheme in Fig. 4.

The schemes in Figs. 5 and 6 vary in terms of the position of pneumatic cushions. In the first case, it is located on the periphery of the rotor and serves as a

Fig. 6 The second of two design schemes that show unloading of inertia forces on the rotor of the centrifuge with the use of pneumatic cushions 7
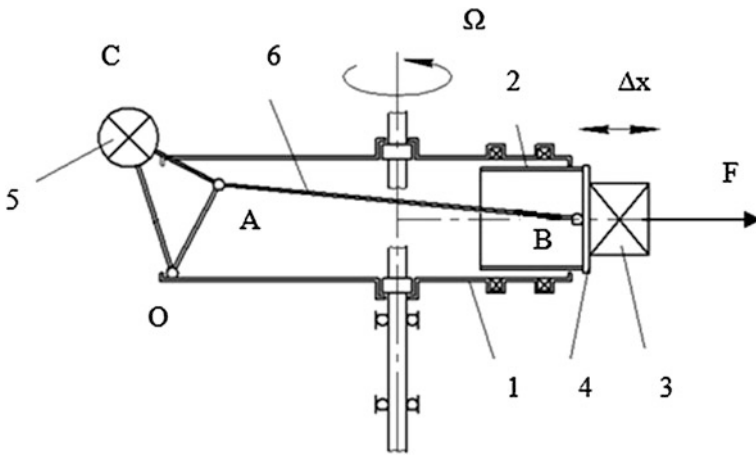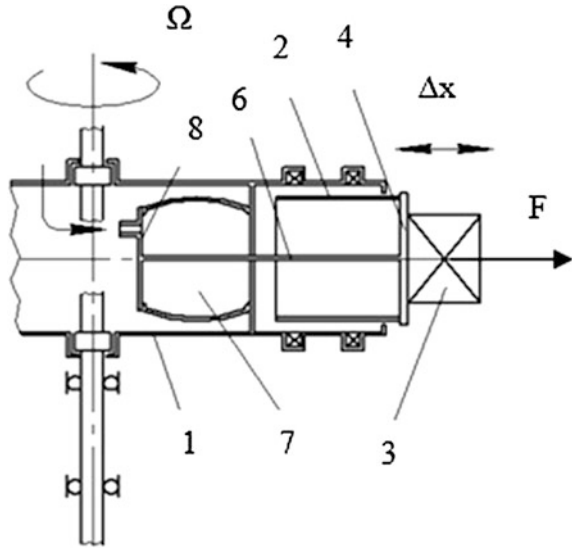
Fig. 7 Design scheme of centrifugal forces counterbalancing where a lever mechanism is used

buffer for the inertia forces to be counterbalanced. In the second scheme, link 6 is used, which connects the table of vibrator 4 and the bottom of cushion 8.

The drawback of these schemes is the need to supply air under controlled pressure.

In Fig. 7 there is a design scheme of centrifugal forces counterbalancing where a lever mechanism is used [16, 17]. Unloading mass 5 is stiffly connected with the apex C of the rigid triangle OAC, in the corners of which there are swivel joints of a

slider-crank mechanism OAB. Masses 3 and 4 are its slide plate. Their sliding mobility is ensured by suspension—the guide of table 4 and vibration stand 2. In this case, the rotor of the centrifuge is an immovable element of this mechanism.

Further, it is investigated how stably this scheme functions in the field of linear acceleration so as to prove that it can be used in a real structural design. A computational model is presented in Fig. 8.

In order to explain the motion, let us use the second kind of the Lagrange equation, where the right part equals zero, since the generalized driving force $Q = 0$ and the resisting force $Q_C = 0$.

$$\frac{d}{dt}\left(\frac{\partial T}{\partial \dot{q}}\right) - \frac{\partial T}{\partial q} = 0. \tag{1}$$

where T is the kinetic energy of the mechanism, q is a generalized coordinate, and $\dot{q}$ is generalized velocity.

The kinetic energy of the mechanism T is combined kinetic energies of each element T_i, where $i = 1 \ldots N$. N is the number of mobile elements. According to König's theorem:

$$T_i = \frac{m_i}{2} v_{Ci}^2 + \frac{J_{Ci}}{2} \Omega_i^2, \tag{2}$$

where m_i is the mass of the element i, v_{Ci} is the absolute linear velocity of the center of gravity of the ith element, J_{Ci} is the product of inertia of the element i in relation to its center of gravity, and Ω_i is the absolute angular velocity of the ith element.

According to the theorem on composition of velocities, the absolute linear velocity can be represented as:

$$\vec{v}_{Ci} = \vec{v}_{Ci}^r + \vec{\Omega} \times \vec{r}_{Ci}, \tag{3}$$

Fig. 8 Computation model to learn how stably the scheme functions in the field of linear acceleration
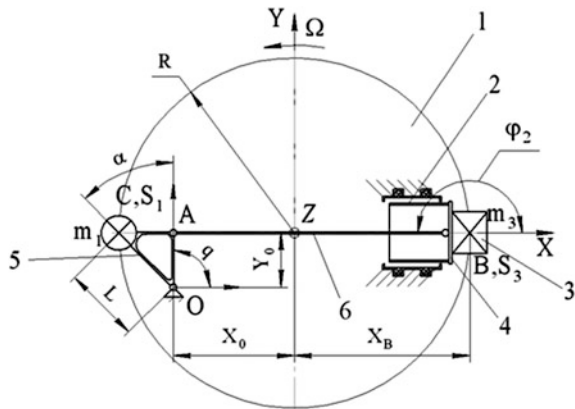
while the absolute angular velocity can be shown according to the rule of composition of rotations:

$$\vec{\omega}_i = \dot{\vec{\varphi}}_i + \vec{\Omega},$$

where $\vec{\Omega}$ is the angular velocity of rotation of the centrifuge platform, $\vec{v}_{Ci}^{\,r}$ is the linear velocity of the center of gravity of the i-th element in relation to the platform, $\vec{\Omega} \times \vec{r}_{Ci}$ is the transport velocity of the center of gravity of the i-th element, $\vec{r}_{Ci}$ is the distance from the rotation axis of the platform to the center of gravity of the i-th element, and $\dot{\vec{\varphi}}_i$ is the angular velocity of the ith element in relation to the platform.

If the vector (Eq. 3) is presented in a form of projections on the axis of the rotating system of coordinates $OXYZ$, connected to the platform and inserted into Eq. (2), we obtain:

$$T_i = \frac{m_i}{2}\left[(\dot{X}_{Ci} - \Omega \cdot Y_{Ci})^2 + (\dot{Y}_{Ci} + \Omega \cdot X_{Ci})^2\right] + \frac{J_{Ci}}{2}(\dot{\varphi}_i + \Omega)^2,$$

the axis OZ is the axis of rotation of the centrifuge frame while the motion plane of the elements of the mechanism is parallel to the plane OXY. X_{Ci} and Y_{Ci} are coordinates of the center of mass of the ith element, and $\dot{X}_{Ci}$ and $\dot{Y}_{Ci}$ are projections of the relative velocities of the center of mass of the ith element on the same axes.

Then we convert this expression:

$$T_i = \frac{m_i}{2}\left[\dot{X}_{Ci}^2 - 2 \cdot \Omega \cdot Y_{Ci} \cdot \dot{X}_{Ci} + \Omega^2 \cdot Y_{Ci}^2 + \dot{Y}_{Ci}^2 + 2 \cdot \Omega \cdot X_{Ci} \cdot \dot{Y}_{Ci} + \Omega^2 \cdot X_{Ci}^2\right]$$
$$+ \frac{J_{Ci}}{2}\left(\dot{\varphi}_i^2 + 2 \cdot \Omega \cdot \dot{\varphi}_i + \Omega^2\right).$$

We move to the analogues of velocities:

$$T_i = \frac{m_i}{2} \cdot [X_{Ci}'^2 \cdot \dot{q}^2 - 2 \cdot \Omega \cdot Y_{Ci} \cdot X_{Ci}' \cdot \dot{q} + \Omega^2 \cdot Y_{Ci}^2 + Y_{Ci}'^2 \cdot \dot{q}^2$$
$$+ 2 \cdot \Omega \cdot X_{Ci} \cdot Y_{Ci}'\dot{q} + \Omega^2 \cdot X_{Ci}^2] + \frac{J_{Ci}}{2}\left(\varphi_i'^2 \cdot \dot{q}^2 + 2 \cdot \Omega \cdot \varphi_i' \cdot \dot{q} + \Omega^2\right).$$

Then we combine the summands with the same powers $\dot{q}$:

$$T_i = \left[m_i \cdot \left(X_{Ci}'^2 + Y_{Ci}'^2\right) + \cdot \varphi_i'^2\right] \cdot \frac{1}{2}\dot{q}^2$$
$$+ \left[m_i\left(X_{Ci} \cdot Y_{Ci}' - Y_{Ci} \cdot X_{Ci}'\right) + J_{Ci} \cdot \varphi_i'\right] \cdot \Omega \cdot \dot{q} + \left[m_i \cdot \left(X_{Ci}^2 + Y_{Ci}^2\right) + J_{Ci}\right] \cdot \frac{1}{2} \cdot \Omega^2.$$

$$(4)$$

And put down the kinetic energy of the whole mechanism:

$$T = \frac{1}{2} \cdot J_{\Pi P}(q) \cdot \dot{q}^2 + A(q) \cdot \Omega \cdot \dot{q} + \frac{1}{2} \cdot J_Z(q) \cdot \Omega^2, \tag{5}$$

where:

$$J_{\Pi P}(q) = \sum_{i=1}^{N} \left[m_i \cdot \left(X_{Ci}'^2 + Y_{Ci}'^2 \right) + J_{Ci} \cdot \varphi_i'^2 \right],$$

$$A(q) = \sum_{i=1}^{N} \left[m_i \left(X_{Ci} \cdot Y_{Ci}' - Y_{Ci} \cdot X_{Ci}' \right) + J_{Ci} \cdot \varphi_i' \right], \quad J_Z(q) = \sum_{i=1}^{N} \left[m_i \cdot \left(X_{Ci}^2 + Y_{Ci}^2 \right) + J_{Ci} \right].$$

We insert Eq. (5) in Eq. (1):

$$\frac{\partial T}{\partial \dot{q}} = J_{\Pi P}(q) \cdot \dot{q} + A(q) \cdot \Omega,$$

$$\frac{d}{dt} \frac{\partial T}{\partial \dot{q}} = J_{\Pi P}(q) \cdot \ddot{q} + J_{\Pi P}'(q) \cdot \dot{q}^2 + A'(q) \cdot \dot{q} \cdot \Omega,$$

$$\frac{\partial T}{\partial q} = \frac{1}{2} \cdot J_{\Pi P}'(q) \cdot \dot{q}^2 + A'(q) \cdot \Omega \cdot \dot{q} + \frac{1}{2} \cdot J_Z'(q) \cdot \Omega^2$$

Finally, the equation of the mechanism motion in a centrifugal field (Eq. 1) can be written as:

$$J_{\Pi P}(q) \cdot \ddot{q} + \frac{1}{2} \cdot J_{\Pi P}'(q) \cdot \dot{q}^2 - \frac{1}{2} \cdot J_Z'(q) \cdot \Omega^2 = 0. \tag{6}$$

In comparison to the classical equation of a mechanism moving on immovable foundation with a zero right part, in this case, a third summand has appeared. It has a negative sign and defines the value of counter-balance moment.

Let us look into the problem of stability of small oscillations in the neighborhood of the coordinate q_0. Let us assume that;

$$q = q_0 + \psi, \tag{7}$$

where ψ—the amount of deviation from the equilibrium position q_0,

$$\begin{aligned} \dot{q} &= \dot{\psi}, \\ \ddot{q} &= \ddot{\psi}. \end{aligned} \tag{8}$$

Let us insert Eqs. (7) and (8) into Eq. (6):

$$J_{\Pi P}(q_0 + \psi) \cdot \ddot{\psi} + \frac{1}{2} \cdot J'_{\Pi P}(q_0 + \psi) \cdot \dot{\psi}^2 - \frac{1}{2} \cdot J'_Z(q_0 + \psi) \cdot \Omega^2 = 0. \qquad (9)$$

Let us expand the amounts as a power series:

$$J_{\Pi P}(q_0 + \psi) = J_{\Pi P}(q_0) + J'_{\Pi P}(q_0) \cdot \psi,$$
$$J'_{\Pi P}(q_0 + \psi) = J'_{\Pi P}(q_0) + J''_{\Pi P}(q_0) \cdot \psi,$$
$$J'_Z(q_0 + \psi) = J'_Z(q_0) + J''_Z(q_0) \cdot \psi.$$

And insert them into Eq. (9):

$$J_{\Pi P}(q_0) \cdot \ddot{\psi} + J'_{\Pi P}(q_0) \cdot \psi \cdot \ddot{\psi} + \frac{1}{2} \cdot J'_{\Pi P}(q_0) \cdot \dot{\psi}^2 + \frac{1}{2} \cdot J''_{\Pi P}(q_0) \cdot \psi \cdot \dot{\psi}^2$$
$$- \frac{1}{2} \cdot J'_Z(q_0) \cdot \Omega^2 - \frac{1}{2} \cdot J''_Z(q_0) \cdot \psi \cdot \Omega^2 = 0.$$

Let us ignore in this expression the non-linear summands in relation to ψ and its derivatives. So we get linear equations of motion:

$$J_{\Pi P}(q_0) \cdot \ddot{\psi} - \frac{1}{2} \cdot \left[J'_Z(q_0) + J''_Z(q_0) \cdot \psi \right] \Omega^2 = 0. \qquad (10)$$

This equation will be solved by a method of successive approximations. In a zero approximation:

$$\psi = 0, \ddot{\psi} = 0,$$

then:

$$J'_Z(q_0) = 0. \qquad (11)$$

From this equation, it is possible to find the coordinate q_0, which defines the equilibrium position of the mechanism in a centrifugal field. The equilibrium position will be at the points of the extremum of function $J_Z(q_0)$. Given Eq. (11), the equation of small oscillations in relation to the equilibrium position will take the form:

$$\ddot{\psi} - \frac{J''_Z(q_0)}{2 \cdot J_{\Pi P}(q_0)} \cdot \Omega^2 \cdot \psi = 0. \qquad (12)$$

The multiplier at ψ in Eq. (12) represents the frequency of free oscillations of the system [18]:

$$k = \Omega \cdot \sqrt{-\frac{J_Z''(q_0)}{2 \cdot J_{\Pi P}(q_0)}}. \tag{13}$$

The frequency will be real-valued and non-zero, in case

$$J_Z''(q_0) < 0, \tag{14}$$

since, according to Eq. (5), $J_{\Pi P}(q_0)$ is always a positive value. Equation (14) is the condition for stability of the equilibrium position q_0 of the lever mechanism in a centrifugal field. This condition shows that motion of the mechanism is possible in case the function $J_Z(q)$ in the position q_0 will have a maximum.

The value $J_Z(q)$ represents, according to Eq. (5), the product of inertia of the mechanism in relation to the axis of motion of the centrifuge (Steiner's theorem). It is remarkable that the obtained condition of stability is applicable for any scheme of a lever mechanism as it is written in a general form. It is possible to choose the parameters of the mechanism that affect stable operation of the system.

For the scheme in Fig. 8, the expression $J_Z(q)$ according to Eq. (5) will look as:

$$\begin{aligned} J_Z(q) &= m_1 \cdot \left(X_{S1}^2(q) + Y_{S1}^2(q)\right) + J_1 + m_2 \cdot \left(X_{S2}^2(q) + Y_{S2}^2(q)\right) + J_2 \\ &\quad + m_3 \cdot \left(X_{S3}^2(q) + Y_{S3}^2\right). \end{aligned} \tag{15}$$

where m_1, m_2, m_3 are the masses of the crank, piston rod and sliding plate correspondingly (the total mass of the test item and mobile table of the vibration stand is considered in m_3), J_1, J_2 are products of inertia of the first and second elements, since they perform rotation motions, $X_{S1}(q)$, $Y_{S1}(q)$, $X_{S2}(q)$, $Y_{S2}(q)$, $X_{S3}(q)$, Y_{S3} are coordinates of the centers of masses of the first, second and third elements correspondingly in relation to the system of coordinates $Oxyz$.

In order to define the coordinates of the centers of masses, equations of geometrical analysis must be worked out for the mechanism under consideration. These equations will be written as:

$$\begin{cases} X_O + OA \cdot \cos(q) = X_B(q) + AB \cdot \cos(\varphi_2(q)) \\ Y_O + OA \cdot \sin(q) = Y_B + AB \cdot \sin(\varphi_2(q)) \end{cases}$$

The system is written in relation of two group coordinates $X_B(q)$, $\varphi_2(q)$. A solution to this system should be searched in relation to these unknown quantities:

$$\begin{aligned} \sin(\varphi_2(q)) &= \frac{Y_O + OA \cdot \sin(q) - Y_B}{AB}, \\ \cos(\varphi_2(q)) &= -\sqrt{1 - \sin(\varphi_2(q))^2}, \\ X_B(q) &= X_O + OA \cdot \cos(q) - AB \cdot \cos(\varphi_2(q)). \end{aligned}$$

Since the group coordinates are known, the expressions for the coordinates of the centers of masses can be easily written. For this, let us assume that the mass of the second element is much smaller than that of the first and the third elements $(m_2 = 0)$. Hence:

$$X_{S1}(q) = L \cdot \cos(q + \alpha) + X_O,$$
$$Y_{S1}(q) = L \cdot \sin(q + \alpha) + Y_O,$$
$$X_{S3}(q) = X_B(q),$$
$$Y_{S3}(q) = Y_B.$$

The values J_1 and J_2 do not affect the definition of the extremums of the function $J_Z(q)$, as they are constant. Let us assume that

$$m_1 = 50\kappa\varepsilon, \quad m_3 = 50\kappa\varepsilon.$$

Let us work out the geometrical parameters of the mechanism:

$$OA = 200MM, \quad AB = 4800MM, \quad Y_B = 200MM, \quad Y_O = -200MM,$$
$$X_O = -2300MM, \quad \alpha = 45°.$$

Let us decide that $L = \sqrt{2 \cdot OA^2}$, since we consider that ΔOAC is right-angled and isosceles.

According to this initial data, dependence $J_Z(q)$ can be built according to Eq. (15), and its extremums can be defined in the variation interval of the coordinate q from $0°$ to $360°$.

As it can be seen from Fig. 9, the maximum of the function $J_Z(q)$ is achieved at $q \approx 90°$. This position will be an equilibrium position, and it will be stable by virtue of the reasoning above.

Fig. 9 The maximum of the function $J_Z(q)$ is achieved at $q \approx 90°$
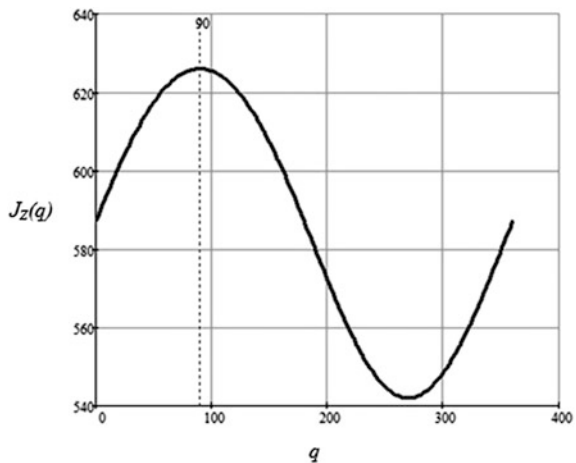
It can be easily shown that, in case the initial geometrical or mass values change, the value of coordinate q will change too. For example, let us assume that the vibration moving mass has increased by 10 kg with all the other parameters remaining the same:

$$m_1 = 50кг, \quad m_3 = 60кг.$$

The new position of balance is achieved at $q_0 \approx 74°$. In this case, the sliding plate will vibrate in relation to the new position. In order to return to the position of vibration assumed as the initial one (for example, at $q_0 \approx 90°$), as shown in [16], either the mass m_1 must be corrected, or the position of the bearing part O must be changed.

The obtained result of the research study makes possible choosing the relieving apparatus built according to the scheme of lever mechanisms. Since the condition of stability is expressed in the form of analytical dependence, it can be easily analyzed to identify the parameters which affect the operation of the apparatus itself. According to Eq. (13), it is sufficient to evaluate just the frequency of free oscillations occurring in the system and judge about the resonance zones.

References

1. Kluev VV (ed) (1982) Test equipment: reference book, in 2 volumes. Mechanical Engineering, Moscow, 528 pp (Book 1, 1982)
2. Chelomei VN (Editorial board) (1981) Vibrations in equipment. Reference book, in 6 volumes. Mechanical Engineering, Moscow. Genkin MD (1981) Tests and trials, vol 5, 496 pp
3. Evgrafov AN, Karazin VI, Smirnov GA (1999) Rotary stands for simulation of motion parameters. SPbSTU J #3(17):89–94 (SPb.: SPbSTU)
4. Evgrafov AN, Karazin VI, Khlebosolov IO (2003) Simulation of motion parameters on rotary stands. Theory Mech Mach #1:92–96 (SPb.: SPbSTU)
5. Ksenofontov VI, Nikolaev VN, Chernokrylov SY (1992) Dynamic multifunctional stands. Test and trial stands. LSTU, Leningrad, pp 29–32
6. Rodgers JD, Cericola F, Doggett JW, Young ML (1989) Vibrafuge: combined vibration and centrifuge testing. In: Shock and vibration symposium, SAND89–1659C
7. Doggett J, Cericola F (1989) Vibrafuge—a combined environment testing facility vibration testing on a centrifuge. SAE technical paper 892368. doi:10.4271/892368
8. Van Goethem D, Jepsen R, Romero E (2006) Vibrafuge: re-entry and launch test simulation in a combined linear acceleration and vibration environment. In: 44th AIAA aerospace sciences meeting and exhibit, aerospace sciences meetings
9. Kang J, Arute F, Yoel D, Littlefield J, Harris T (2013) Testing using combined environments to reduce payload mass, cost and mission risk. In: 27 annual AIAA/USU conference on small satellites
10. Jepsen RA, Edward FR (2005) Testing in a combined vibration and acceleration environment. IMAC XXIII, Orlando, FL
11. Rojers JD (1993) Testing in combined dynamic environments. J IES36 6:19–25
12. Karazin VI, Kozlikin DP, Sloush AV, Khlebosolov IO (2007) A dynamic model of a vibro-rotational stand. Theory Mech Mach Periodical J #1(9) 5:38–45

13. Karazin VI, Kozlikin DP, Khlebosolov IO (2008) About simulation of vibro-rotational effects. Science and technology, Section 3, dynamics and strength: short reports of XXVIII Russian School, pp 42–43
14. Karazin VI, Kozlikin DP, Khlebosolov IO (2006) Dynamic stands for vibro-rotational tests. SPbSTU J #3(45):44–49 (SPb: SPbSTU Publishing House)
15. Karazin VI, Kozlikin DP, Khlebosolov IO (2007) About counterbalancing of inertial forces in vibrating centrifuges. Theory Mech Mach Periodical Sci Methodol J #2(10), 5:63–71
16. Karazin VI, Kozlikin DP, Sukhanov AA, Khlebosolov IO (2014) About one scheme of stable dynamic unloading of centrifugal forces. Mod Mech Eng Sci Edu #4:203–216
17. Karazin VI, Kozlikin DP, Sukhanov AA, Khlebosolov IO (2016) One stable scheme of centrifugal forces dynamic balance. In: Evgrafov A (ed) Advances in mechanical engineering. Lecture Notes in Mechanical Engineering. Springer International Publishing, Switzerland, pp 75–87. doi:10.1007/978-3-319-29579-4
18. Panovko YG (1980) Introduction to the theory of mechanical oscillations. Science (rus. Nauka), Moscow, 272 pp

Self-oscillations of Machines and Mechanisms

Mikhail J. Platovskikh and Mikhail M. Vetyukov

Abstract Initiation of self-oscillations causes movement in a number of machines and mechanisms. The anchor mechanism in a mechanical clock, a combustion engine, or any bow-string musical instrument are examples of mechanisms and machines whose cornerstone is the phenomenon of self-oscillation. On the other hand, the self-oscillations in brake mechanisms, friction couplings, and sleeve-type bearings often lead to negative consequences. The character of self-oscillations is diverse, but in any case they are excited without participation of an external periodic energy source. In the offered paper, the path of development of the theory of self-oscillatory processes is traced by researching the development of such "self-oscillatory" mechanisms. The special part is assigned to original research on frictional self-oscillations in one-mass and two-mass systems caused by nonlinear frictional force. The authors' research results on friction auto-oscillations are reported in the article, both in classic a unidimensional model and in a two-mass model with relative slipping of bodies.

Keywords Anchor mechanism · Froud's pendulum · Frictional self-oscillations (FSO) · Friction behavior · Relaxation oscillations · Phenomenon shimmy · Crystal franklin's harmonica

Introduction

As in most of the mechanical systems with inelastic resistance, stable oscillating processes are possible only in the presence of external periodic excitation. However, in some systems, stationary fluctuations are possible without periodic

M.J. Platovskikh (✉)
University of Mines, St. Petersburg, Russia
e-mail: mplat.63@gmail.com

M.M. Vetyukov
St. Petersburg Polytechnic University, St. Petersburg, Russia
e-mail: vetyukov.m@mail.ru

influences from the outside. Such systems are called self-oscillatory. As in any actual oscillating process in which there is a dissipation of energy, any self-oscillatory system has to possess an energy source. This source compensates for power losses, without possessing oscillating properties. It is possible to tell that the self-oscillatory system represents one which, excited by a non-periodic power source, creates a batch process. Self-excitation of oscillations often occurs as a result of the unstable position of equilibrium of the system. Any perturbation of this state does not disappear with time, and, on the contrary, builds-up oscillations in the system. Contrary to forced oscillations, the auto-oscillations frequency and amplitude are defined not by the nature of external disturbance, but by properties of the system. The term "self-oscillations" (SO) was for the first time used by A. Andronov at the IV congress of Russian physicists in 1928. Then in 1929, in short communications of the French Academy of Sciences was published a study "The limit cycles of the Poincare and the theory of self-oscillations". In it, concrete examples of self-oscillations are given: self-oscillations of a violin string, fluctuation of stars known as Cepheids, Froud's pendulum, a valve oscillator, and periodic reactions in chemistry [1–4].

Existence on the phase plane $(x, \dot{x})$ of one or several limit cycles is characteristic of self-oscillatory systems with one degree of freedom (Fig. 1). The closed isolated phase trajectory is known as the limit cycle. The term "isolated" means that, in its sufficiently small (ring-shaped) neighborhood, there are no other closed phase trajectories. This distinguishes the limit cycles from the closed phase trajectories corresponding to periodic oscillations of a conservative nonlinear oscillator. The limit cycle is steady if all trajectories approach it at t → ∞. It will be unstable if the next trajectories move away from it at t → ∞. Eventually, the phase trajectory aspires to some attracting set called an attractor. Movement of representative point on attractor corresponds to steady-state self-oscillations in system. Such oscillations depend only on parameters of system, not on initial conditions. There may be some attractors, each of which has area in a phase plane. Emanating from this area, phase trajectories aspire to this attractor.

An important attribute of self-oscillations is the independence of their amplitude over a wide range beginning with the initial conditions. Amplitude of

Fig. 1 The limit cycle of self-oscillations (soft excitation)
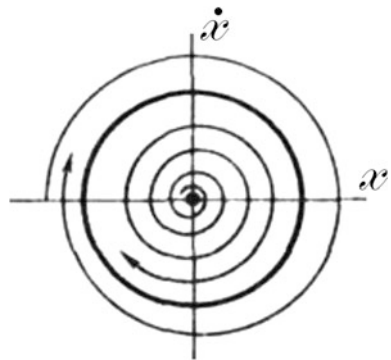
Fig. 2 Dependency graphs of the coordinate (*full curves*) and velocity (*dotted curves*) for quasi-harmonic (**a**) and relaxational (**b**) SO
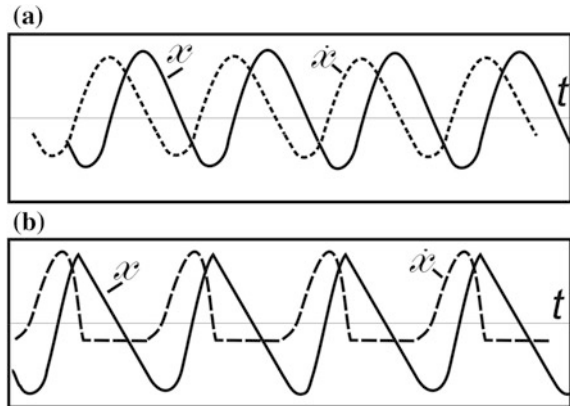
self-oscillations is defined by properties of the system, but not an initial deviation or impulse, such as at the free oscillations. There are various areas of initial conditions. To the initial conditions belonging to each of these areas, there will correspond the same amplitude. In some self-oscillatory systems, existence of several stable processes with various amplitudes are possible, to each of which there corresponds the particular area of initial conditions. If, for example, one inflects the pendulum of a clock too strongly, the friction losses will be more than the energy inflow from the stem of the watch. Amplitude will thus decrease. On the contrary, if one reduces the initial amplitude, the excess of the energy received by a pendulum from a running wheel will lead to an increase of amplitude. Automatically, such oscillations of amplitude, at which the expenditure and receipt of energy are balanced, will be established.

Self-oscillations can be in a form proximal to harmonic (quasi-harmonic SO (Fig. 2a)) and can significantly differ from them (relaxational SO (stick-slip) (Fig. 2b)). There are also chaotic self-oscillations, which are random, though they are made under the influence of nonrandom energy sources. The vibration spectrum of chaotic self-oscillations is the continuum. A mathematical image of quasi-harmonic self-oscillations in a phase space is the n-dimensional torus, and stochastic—the strange attractor, i.e., the attracting set having extremely complex internal structure in which everything (or nearly all) trajectories are unstable.

Self-oscillations of Clock Drives

Possibly the most striking example of a mechanical self-oscillatory system is the clock mechanism. The first mention of a mechanical clock is contained in the Byzantine anthology of the 6th century [1–7]. In the modern age, the mechanical clock began in Europe only at the end of the 13th century. In 1288, the tower clock was installed in Westminster abbey in London. In 1354, a clock with a calendar,

chimes, and moving figures was placed in the Strasburg cathedral. In Russia, the first tower clock was crafted in the Moscow Kremlin by the monk Lazar Serbin. It was a weight-driven clock having a planetary mechanism and was also equipped with an alarm. The design of clocks underwent qualitative changes after the proposal by Galileo Galilei to apply a pendulum to it. Galilei's clocks used the isochronia of oscillations of a pendulum which had been discovered to be intrinsic in them. According to this discovery, the oscillation period of a pendulum does not depend on the pendulum mass.

$$T = 2\pi\sqrt{\frac{\ell}{g}}.$$

However the patent for clocks was obtained by another scientist Christian Huygens. He claimed that he knew nothing about the project of Galilei. The clocks of Galilei, as an external source, used the potential energy of the falling poise, which was transformed to the kinetic energy of the rotating cog-wheels. 'Dissipating the vibratory energy arising the Galilei clocks was accomplished through a twist-type trigger in the original design—for a prototype of the modern anchor mechanism of Graham see Fig. 3. The cog-wheel 1 receives angular momentum from the poised or spring drive. Anchor 2, rigidly bound to a pendulum, swings on an axis and incorporates pallets 3 and 4. Because of the shape of the pallets, energy is transferred to pendulum two times for one each swing when it passes the equilibrium of a static position. Being shaken together with a pendulum, pallets alternately engage with a running wheel, subordinating its rotation to the period of oscillations of a pendulum. The tooth of a wheel under the action of a twisting moment pushes an anchor and also a pendulum. At this time, the second pallet falls and the next gear tooth of the wheel stops. At each oscillation, the wheel manages to turn by one tooth. Because of such a trigger mechanism, the pendulum receives periodic pushes that do not allow it to stop. In the modern wrist watch, the energy feed regulator in system uses the balance weight instead of a pendulum. It represents the large ring connected with a balance spring.

The foundation of the self-oscillatory approach in the theory of clocks was laid down in Andronov's monograph (Witt, Khaykin) [2]. Thus, the clock mechanism


Fig. 3 Anchor mechanism Graham
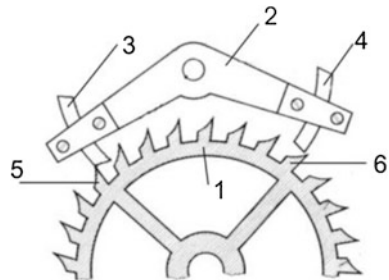
was considered as system with one degree of freedom. Consideration of a clock mechanism as a system with two degree of freedoms was initiated in Butenin's works [5–7].

Metal-Cutting's Tool Self-oscillations

Under certain conditions, the process of cutting metal loses stability. Loss of stability is characterized by initiation of extraneous vibrations. Oscillations of the tool related to the stock material (or, on the contrary, stock material related to the tool) cause an alternation of thickness of the cut-down layer and of the forces of cutting and the size and characteristic of the loads of the machine (loading can increase by a factor of 10 and more). With vibrations, the quality of the processed surface worsens. Depending on the working conditions, excited oscillations of a detail and the tool may be low-frequency (50–300 Hz) or high-frequency (800–3000 Hz), existing at the same time or independently from each other. As a rule, the detail has low-frequency oscillations, and–the tool has high-frequency. Low-frequency oscillations create a rough undulation of the processed surface, and high-frequency oscillations create ripplets (Fig. 4).

The absolute importance of frictional self-oscillations is seen in machine tool building wherein two major criteria of functional quality of operation of tools are apparent: the movements' steadiness and the accuracy of the adjusting movements. The roughness of supplied blanks is noted in machines of almost all types: miller, grinder, and lathe [8]. In most cases, it is inadmissible, especially in the modern, numerically-controlled machine tool. The idea of the self-oscillatory nature of vibration when cutting was introduced for the first time by N. Drozdov who disproved the interpretation of this oscillation as forced. He showed that observed vibrations cannot be explained by resonance owing to coincidence of frequency of shear of the shaving elements to natural frequencies of the system–the tool and the base metal. One of the first origins of self-excited cutting vibration is based on the assumption of the incident dependence of force of cutting on speed.

Fig. 4 The self-oscillations arising when processing stock metal preparation are caused by occurrence of a corrugated surface
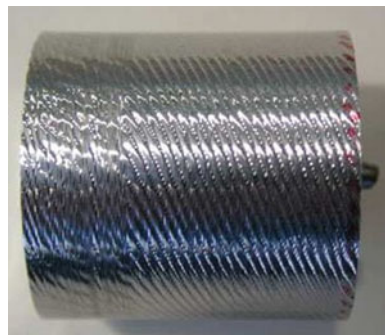
Mathematically, this theory is similar to the description of frictional self-oscillations of the sprung body which is moving on the rough tape with constant speed. At some level of the negative dissipation (existence of a dropping section on a cutting curve), equilibrium becomes unstable, and there is a self-excitation of oscillation. It was established (Kudinov [9]) that the dynamics system has a saddle, i.e., the in-process part in the research on self-oscillations has to have at least two degrees of freedom. From the analysis of the bound self-oscillations, the conclusion was based on the action of the correct orientation of axes of a rigidity of system for receiving steady oscillating motion when cutting. The mechanical energy in shaving cutting will be transformed to heat energy which leads to heating in the cutting zone (to 1000 °C). During research on self-oscillations involved in the cutting of metal, a substantial connection between mechanical and thermal processes was revealed. The decreasing nature of dependence of the cutting force on temperature transforms the system of cutter-preparation into a system with negative dissipation (a self-oscillatory system).

Self-excited Frictional Oscillations

Among vibration sources in cars and mechanisms, the frictional self-oscillations (FSO) assumes a special role. They are one of the most widespread types of mechanical self-oscillations and are related to the instability in the process of a sliding friction at rather low sliding speeds. Such speeds become very common in the modern technique, especially for processes of fine positioning, and also start-up and braking of clusters of various devices. Besides the apparently negative consequences of this phenomenon, sometimes its occurs and can be very useful. Playing the bow on musical instruments can be the most striking example. However, in the majority of the machinery and appliances, the role of FSO can change from very undesirable to catastrophic. Frictional self-oscillations arise in such devices, e.g., brakes and mechanisms of frictional coupling, which are widespread in cars and on tractors [10–12].

Frictional self-oscillations often appear as the reason for the increased vibroactivity of the driveshaft of the power equipment in ships. In this case, oscillation onset can be explained by the instability of the process of a sliding friction under the conditions of deficiency of water greasing. This phenomenon, known as "fog horn" is described, in particular, in Den-Gartog's works [13]. In the vibration spectrum of such oscillations, usually there are no components with the frequencies depending on the rotation frequency. The frequency of vibration is close to one of natural frequencies f_c of the system, corresponding to the preferred development of oscillations of an element's subject frictional influence. The increased vibration levels with the characteristic discrete components, i.e., the multiple of some fixed frequency, were observed in one ship with stern-tube bearings from two caprolon boxes [14] (Fig. 5). Increase of air noise and vibration at turns of a shaft at 75–80 rpm was noted. The narrow-band analysis of vibration

of a stern-tube showed that this noise is caused by the existence of discrete components at frequencies of 127, 254 and 380 Hz. Another characteristic of FSO is a rather sudden disappearance (or a substantial decrease in levels of vibration) upon the shaft's achieving some boundary speed of rotation.

The research on FSO are conducted, first of all, into the tribological aspect including study of tribotechnical characteristics of frictional contact and development of new antifriction materials. Secondly, the dynamic systems containing frictional elements are investigated. Thus, the problem of the definition of various self-oscillations modes, clarifications of the question about their stability depending on the general parameters of a system, and the characteristics of frictional contact in particular are cast.

The history of research on the dynamics of frictional systems dynamics amounts already to more than a half century. During this time, the most noted results are from N. Butenin, M. Ishlinsky, N. Kaydanovsky, M. Kolovsky, Le Xuan Anh, R. Nagayev, Ya. Panovko, V. Petrov, A. Tondl, S. Khaykin, et al.. Rigid solid on a moving rubber tape—one of the first mechanical FSO-models—was offered by Balthazar van der Pol in 1930, in material on the theory of self-oscillations of radio-electronic systems [2, 10, 15]. He connected the emergence of self-oscillations with the nonlinearity caused by dry friction. Relaxation of FSO are characterized by the existence in the process of body oscillations of intervals during which there is no movement relative to the tape. They are, for the first time, rigorously mathematically described by N. Kaydanovsky and S. Khaykin [9–14]. These authors showed that all frictional systems, in which self-oscillations are possible, have to possess nonlinearity of a particular type. In some areas, the characteristic of a sliding friction (dependence of a friction coefficient on the relative sliding speed) has to be sloping. An important feature of FSO—the existence of critical speed of sliding above which self-oscillations are impossible, is then found. This value of speed corresponds to the transition from a dropping section of the characteristic of a sliding friction to an increasing one. Thus, if the change in frictional force is not enough, its role is reduced only to self-excitation of

Fig. 5 Vibration spectrum of the propeller-shaft bearing
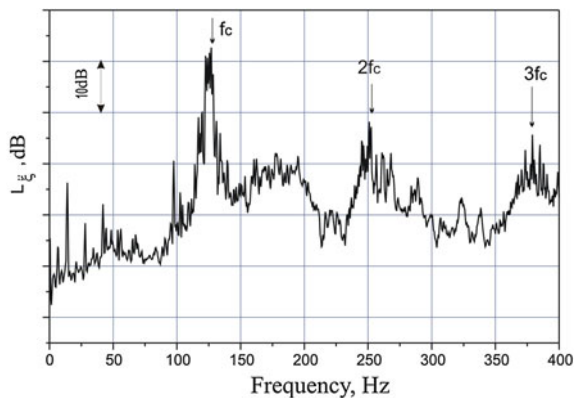
self-oscillations. In systems, thus there are quasi-harmonic oscillations with a frequency close to a natural frequency of system and an amplitude depending on tape speed.

This point of view about the dropping characteristic is the reason that FSO is not unique. Many authors see the reason of FSO (appearing) as a difference between static friction force and sliding frictional force [10, 16].

According to the theory put forward in 1944 by A. Ishlinsky and I. Kragelsky, the frictional force increases with the duration of the fixed contact [17]. That's exactly why, in an experiment, the first jump in amplitude exceeds the subsequent. On the basis on this theory, subsequently in works [9–14], the FSO models in which the stochastic modes are found were constructed. However, Le Xuan Anh, analyzing the experiments, came to a conclusion about the independence of breakaway force from the duration of the non-sliding contact [18, 19]. This force, in his opinion, is defined by the speed of tangential loading, decreasing with an increase of this speed [15]. V. Kudinov, in the conditions of semi-fluid lubrication on frictional contact, connects the onset of FSO with dependence of a frictional force on contact deformation in the direction normal to a contact surface.

Besides those mentioned, there are a number of FSO models related to to the rheological and thermodynamic processes on frictional contact [10]. Each of the listed models has a restricted range of application. However, the most common in research is the speculation that the reason is the nonlinear dependence of self-oscillations of a friction coefficient (with a dropping section) on the relative speed. Thus the characteristic of a sliding friction can be described in various ways, i.e., in the form of the jumping, exponential, piecewise line, or cubic, dependences.

The dynamics of frictional systems are described by means of nonlinear differential equations. Their solving is the tricky problem, in many cases undecidable by analytical methods.

Let's review the research on FSO in one-mass system based on the example of a traditional model by considering a spring-fastened solid body on the tape moving with constant speed (Fig. 6a). Between a body and a tape, the force exerts a dry non-Coulomb friction (a dry and viscid friction in a combination) [20]. This problem is absolutely identical to the problem about moving through a resilient element of a solid body on an imperfect plane (Fig. 6b). The friction behavior is plotted in the form of a cubic parabola [16] (Fig. 6c). The equation of motion of the considered system at $\dot{x} \neq 0$ can be written in form of:

$$m\ddot{x} + c(x - Vt) = -Pf(\dot{x}),$$

where x—the absolute coordinate of a body, P-pressure force on contact, and dependence of a sliding friction on speed is accepted in the form of (Fig. 6c):

$$f(\dot{x}) = f^* sign\dot{x} - f_1\dot{x} + f_3\dot{x}^3, \quad \dot{x} \neq 0; \quad -f^* < f(\dot{x}) < f^*, \quad \dot{x} = 0,$$

($f_* = \min f(\dot{x})$ when $\dot{x} > 0$).   It is supposed that the size of the friction coefficient changes slightly when a driving, small parameter is introduced:

Fig. 6 One-mass model of
frictional self-oscillatory
system (**a**, **b**); cubic friction
behavior (**c**)
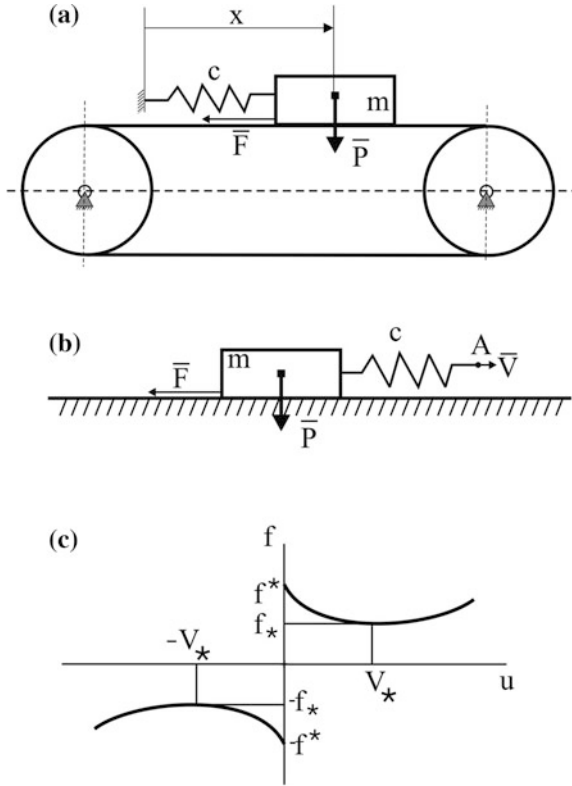
$\varepsilon = (f^* - f_*)/2f^*$. Another constitutive parameter when studying FSO is
$\sigma = V/V_*$.

Research on these equations enables learning the following main results about
the nature of oscillations of system.

1. On the rising branch of the friction behavior at $\sigma > 1$, the equilibrium position is
   stable and self-oscillations in system are impossible.
2. In the narrow range the translational velocity of body $0.89 < \sigma < 1$ in the
   system, there are quasi-harmonic non-stop self-oscillations.
3. At $0 < \sigma < 0.89$ in the system, the following modes can be realized:

(a) oscillations with stagnation zones, namely, relaxational oscillations;
(b) oscillations with the instantaneous change of sign of the speed;
(c) oscillations of the mixed type.

For the research on FSO in a two-mass system of bodies, see Fig. 7 for, the
model in which bodies are directly tied by forces of a dry non-Coulomb friction is
offered [21]. Thus one of bodies (top) is stretched through a resilient element over
lower body and is elastically fixed horizontally. Such a scheme can serve as a model

Fig. 7 Two-mass model of frictional self-oscillatory system
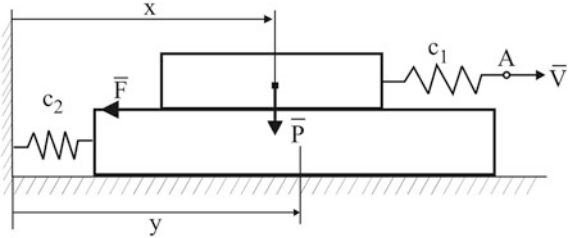
for actual friction units, e.g., coupling devices, friction clutch couplings, slider bearings, and braking mechanisms. The equations of motion are

$$m_1\ddot{x} + c_1(x - Vt) = -f(u)P, \quad m_2\ddot{y} + c_2 y = f(u)P.$$

Here x, y, m_1, m_2, c_1, c_2 are the coordinates, masses, and rigidities corresponding to a top and bottom body, and f is friction behavior depending on their relative speed $u = \dot{x} - \dot{y}$. In the problem, only continuous oscillations of bodies are considered ($u > 0$). Function f, as shown, is approximated by cubic dependence. The averaging method is applied to the analysis. Two various cases, i.e., the main resonance and non-resonance, are considered. The relative coordinate of $u = \xi - \eta$ and variable $w = (1 - \chi)\xi - (1 - \chi)\eta$, where $\chi = (m_2 - m_1)/(m_2 + m_1)$ and ξ, η are dimensionless coordinates of bodies. The average equations for a resonance case at a first approximation look like this:

$$a' = \frac{\varepsilon}{2}z\left[\frac{6z}{1 - \chi^2}\left(1 - \sigma^2 - \frac{a^2}{4}\right)a - b\sin\theta\right],$$

$$b' = \frac{\varepsilon}{2}z(1 - \chi^2)a\sin\theta,$$

$$\theta' = \frac{\varepsilon}{2}z\left[(1 - \chi^2)\frac{a}{b}\cos\theta - \frac{b}{a}\cos\theta - 2\chi\right].$$

Here a and b are the vibration amplitudes for variables u, and w, and θ is the difference in phase. This system of equations has four stabile stationary points. One solution of the problem correspond to oscillations only of the top body (with the body lower at first approximation fixed). The oscillations amplitudes on the ξ, η variables thus will be $A_\xi = a_*$, $A_\eta = 0$. Another solution of the problem involves oscillations of the lower body: $A_\xi = 0$, $A_\eta = a_*$. Here the variable of $a_* = 2\sqrt{1 - \sigma^2}$ is the dimensionless amplitude of quasi-harmonic self-oscillations in a one-mass system. It is clear that stationary oscillations are possible also only on the dropping section of the friction behavior, when $\sigma < 1$.

By means of a numerical integration of the average equations, the domains of attraction of the two modes of oscillations are constructed. From the analysis of areas, it is evident that, if the mass of bodies are sufficiently close, the static friction is also not small; the lower body oscillate, in the converse case—of top-body oscillation. In the non-resonance case, similar results are obtained.

Thus, in a system of two bodies, connected by forces of a dry non-Coulomb friction both in resonance and in non-resonance cases, the effect of dynamic self-oscillation suppression is possible. At that, the translating body is fixed in a first approximation, and another body oscillates. This effect is caused by the small increment of the frictional force operating between the bodies at oscillation.

Also, we investigated FSO spring-fastened body (material point) on the plane moving bodily with a speed of V (Fig. 8) [20]. The point from the plane is affected by a force of a dry non-Coulomb friction:

$$\bar{F} = -f(u)\frac{\bar{u}}{u},$$

where $\bar{u} = (\dot{x} - V \cos \alpha)\bar{i} + (\dot{y} - V \sin \alpha)\bar{j}$—vector of the relative speed of a point; $u = |\bar{u}|$. The characteristic of a sliding friction is accepted as cubic (Fig. 6c). Equations of motion of a point can be written down in the following form:

$$m\ddot{x} + c_1 x = -f(u)\frac{\dot{x} - V \cos \alpha}{u},$$
$$m\ddot{y} + c_2 y = -f(u)\frac{\dot{y} - V \sin \alpha}{u}.$$

Research on these equations on a method of averaging makes possible to draw the following conclusions (Fig. 9).

1. The one-dimensional regimes of self-oscillations are realized not only when the direction of speed is close to the direction of the corresponding axis of a rigidity, but also when the vector of speed is significantly rejected from this axis. And this deviation can be larger than the force of static friction.
2. The two-dimensional regime is possible at rather small values of a static friction force.

One of the most striking examples of frictional mechanisms in which the self-oscillatory motion regimes of driving are realized is Froud's pendulum [1–3] (Fig. 10). The pendulum is rigidly bound to the friction-bearing bushing which made

Fig. 8 Model of point self-oscillations on the plane
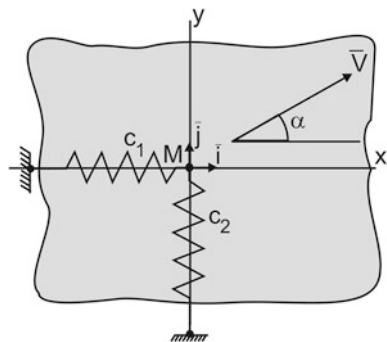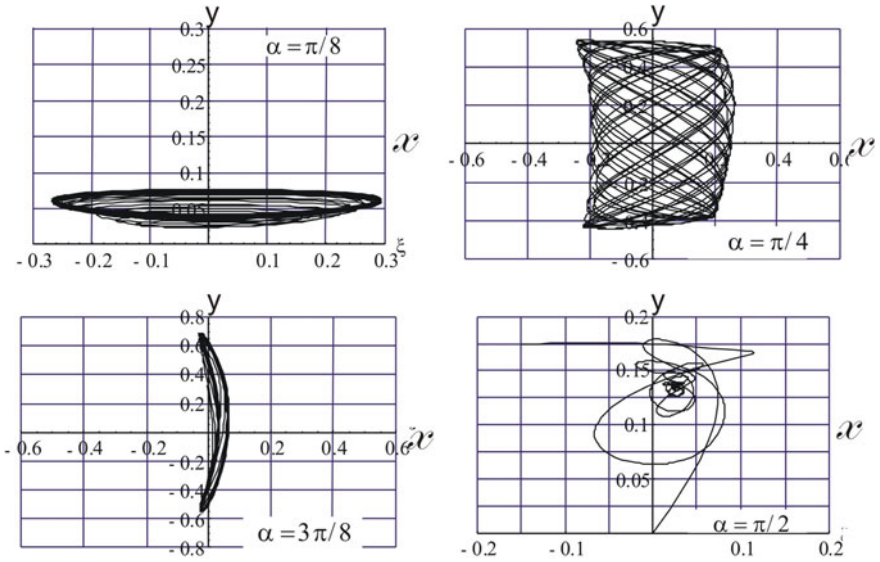
Fig. 9 FSO on the plane. Phase trajectories at various values of the angle between the direction of speed and one of flexural axis (x) are shown
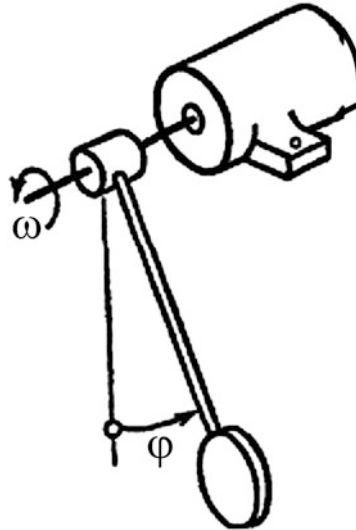
Fig. 10 Froud's pendulum

to rotate with constant speed on a shaft. The bearing is captured by sliding friction and the pendulum deviates. Between the bearing and the rotating shaft, there is a friction moment depending on the relative speed of rotation of the bearing relative to the shaft.

Existence of the dropping section on the friction behavior is the reason of self-oscillations. Depending on the size of external damping, the parameters of the friction behavior and axis rotation velocity of the drive with various forms of motion of a pendulum are possible: quiescent state, oscillations, or uniform rotation. At small rotational velocities of axes, the oscillations of a pendulum are not damping. The pendulum starts making fluctuations in a range that does not decrease over time. Moreover, if the pendulum was forcibly stopped and then was activated, it begins oscillating under the influence of the rotation. As a result, the pendulum adopts a former mode of motion with the same peak-to-peak value. At a rather high value of static friction force, there is no jump-over on self-oscillations, and the pendulum rotates together with shaft as though rigidly fixed on it.

In brake assemblies the negative sliding friction leads to intensive FSO of a brake shoe (Fig. 11a) too. This oscillations involves an increase of braking torque (Fig. 11b).
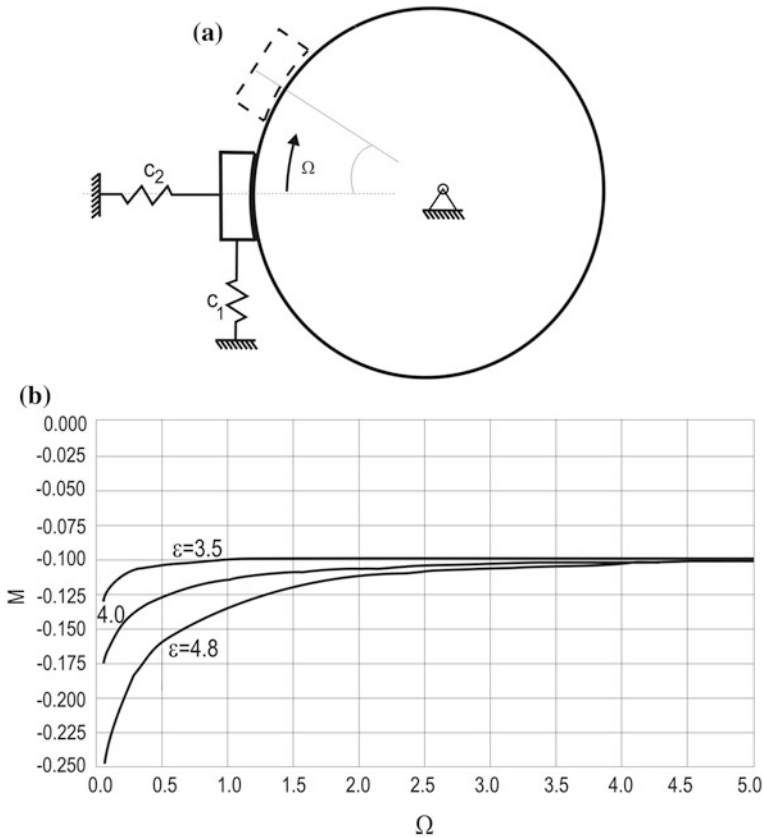

Fig. 11 The calculated scheme (**a**) and dependency graphs (**b**) of the braking moment from time at various ratios of a coefficient of sliding friction and coefficient of friction in rest

Braking the disk's rotational motion by action of frictional force on the side of spring-mounted brake shoe is considered in practice [22]. It is shown that self-oscillations of a brake shoe, depending on initial velocity of a disk and a ratio of friction coefficients at rest and on the run, can be not only quasi-harmonic (unceasing), but also relaxational. Relaxation oscillations in this case are characterized by the existence of stages of cooperative motion of a disk and shoe, when their relative velocity becomes zero. Quasi-harmonic self-oscillations lead to an increase of the average braking torque in modulus (Fig. 11b). Relaxational self-oscillations act on the average braking torque if only the force of static friction does not exceed triple the value of a force of sliding friction. However, it should be noted that FSO brake assemblies promote wear of the connecting surfaces of a disk and a shoe, owing to the increase during oscillations of their relative movements [23].

Phenomenon of Shimmy

One more phenomenon of the self-oscillations connected to the nonlinear nature of powers of friction is shimmy [1]. Shimmy represents the phenomenon of intensive coupled angular and transverse vibrations of the wheels of the transportation vehicle. Most dramatically, this problem arises for the forward landing gear of an aircraft when moving with rather high speed on the ground. The name comes from the name of a dance popular at the beginning of the 20th century. In this dance, the signature movement is a fast wiggle by the shoulders from the right to the left. The oscillation frequency depends on parameters of the support of the landing gear and can have the range 5–25 Hz. At shimmy, wheels make the angular oscillations concerning an axis, a perpendicular plane of the earth matched up with oscillations of the same frequency in the transverse direction. This phenomenon arises under the influence of the transversal frictional force operating from the ground on the tire of the rolling wheel during its oscillations. The phenomenon of shimmy is very dangerous because it can lead to destruction of a landing gear and, as a result, to structural failure of the entire airplane. Shimmy essentially depends on elastic deformations of the pneumatic tire [2]. It is possible to consider the main deformations as two: a lateral displacement of a wheel of Δz and an angle of torsion of a wheel concerning the area of contact of $\Delta \theta$. Both of these deformations impart to a wheel a tendency to move on a curve (Fig. 12). The problem of shimmy was solved by the academician Keldysh [1, 2, 24]. In his work, he proposed not only the theoretical description of the problem of shimmy (it derived a differential equation for the phenomenon), but also offered the concrete engineering recommendations enabling to eliminate the shimmy phenomenon. Moving the wheel axis forward, relative to the landing-gear leg, was a radical measure to fight against shimmy (Fig. 13). The emergent deformations of twisting play a positive role, and the oscillations become damping effects. Later research on shimmy enabled the explanation of this phenomenon, proceeding from the theory of a two-component friction: interaction of sliding friction and pivoting friction [25]. From these

Fig. 12 The initiation
phenomenon of shimmy
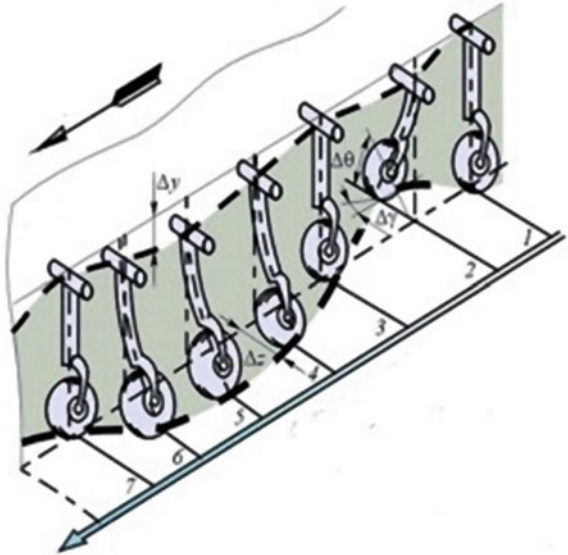
Fig. 13 Engineering solution
for elimination of shimmy
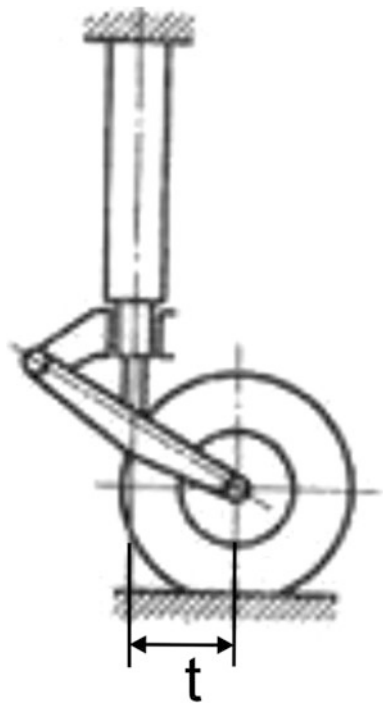
perspectives, it is possible to explain shimmy for rigid wheels. According to this theory, to fight against shimmy it is necessary to increase the rotating rigidity of the support and to reduce sliding friction. If the frequency of torsional vibrations is less, or is equal to, the frequency of flexural oscillations, shimmy is impossible.

Conclusion

In the report, self-oscillations in various machines and mechanisms are considered: clock mechanism, feed mechanism of the metal-cutting machine, bearings of ship shafts, landing gear, and musical instruments. The principle at work of some of them is based on the phenomenon of self-oscillations. For durability and operability of the majority of machines, self-oscillation do not assume substantial significance. In some instances, on the contrary, their role is catastrophic (e.g., a flutter, shimmy of wheels). Research on frictional self-oscillations are given for one- and two-mass systems. In two-mass model, the effect to reduce oscillations is studied, when one of masses commits oscillations with considerable stationary amplitude and the other is quite motionless at first approximation. The attraction areas of such conditions for a non-resonance case are built with the help of the averaging method; this example is interesting for applications. The influence of a brake block FSO on an average, retarding torque is studied for the arresting arrangement. It is shown that such oscillations result in an increase of the moment.

References

 1. Kharkevich A (2009) Self-oscillations (in Russian)
 2. Andronov A, Vitt A, Khaykin S (2009) Theory of oscillations (in Russian)
 3. Jenkins A (2013) Self-oscillations. Phys Rep 552(2):167–222
 4. Agnilar L, Boiko I, Fridman L, Iriatre R (2015) Self-oscillations in dynamic systems. Springer series: system control. Foundations & Applications, pp 110–115
 5. Bautin N (2012), Dynamic theory of clocks (in Russian)
 6. Butenin N (1940) About one problem of Calvin, relating to theory of clocks. J Exp Phys 10(11):68–80 (in Russian)
 7. Butenin N (1955) Dynamic models of the free hour travels. In: Proceedings of the USSR academy of sciences. Collected papers memory of A. Andronov (in Russian)
 8. Elyasberg M (1993) Self-oscillations of metal-cutting machines: theory and practice (in Russian)
 9. Kudinov V (1967) Dynamics of machine-tool. Mech Eng (in Russian)
10. Kragelsky I, Gitis N (1987) Frictional self-oscillations (in Russian)
11. Sergienko V, Bukharov S (2015) Noise and vibration in friction systems. Springer Ser Mater Sci 212:106–112
12. Hoffmann N, Fischer M, Allgaier R, Gaul L (2002) A minimal model for studying properties of the mode-coupling type instability in friction induced oscillations. Mech Res Commun 197–205
13. Den Hartog J (1956) Mechanical vibrations, 4th edn. McGraw-Hill, New York

14. Komarov S, Merkulov V, Platovskikh M, Chernyshev A (2000) Vibration and noise of bearings of a deadwood and ways of their decrease. In: *Works* of the 5th international symposium: noise and vibration on transport (in Russian)
15. Van der Pol B (1922) On oscillation hysteresis in a triode generator with two degrees of freedom. Mag ser, Philos, p 6
16. Tondl A (1970) Self-excited vibrations. National Research Institute of Machine Design, n. 9, Prague
17. Ishlinsky A, Kragelsky I (1944) About jumps at a sliding friction. Tech Phys 14(45):276–282 (in Russian)
18. Le Xuan A (1972) The experimental studies of mechanical self-oscillations at a sliding friction. In: Proceedings of the USSR academy of sciences. Mechanics of rigid body. n. 3 (in Russian)
19. Le Xuan A (2003) Dynamics of mechanical systems with Coulomb friction. Springer series: foundation of engineering mechanics, pp 11–36
20. Vetyukov M, Platovskikh M (2001) Frictional self-oscillations in one—two-mass systems. In: Works of the 5th international conference on problems of oscillations (ICOVP) (in Russian)
21. Vetyukov M, Nagayev R, Platovskikh M (1993) Self-oscillations in system of the bodies tied by forces dry friction. Russian Academy of Science. Problems of mechanical engineering and reliability of machines, n. 1, pp 37–41 (in Russian)
22. Vulfson I, Kolovsky M (1968) Non-linear problems of dynamics of cars (in Russian)
23. Vetyukov M, Platovskikh M (1988) Influence of relaxational oscillations of a brake shoe on braking process. Notes of leningradsky mining institute, vol 117 (in Russian)
24. Keldysh M (1945) Shimmy of a forward wheel of the three-wheeled chassis, Selected works. Mechanics 491–530 (in Russian)
25. Zhuravlyov V, Klimov D (2009) About the mechanism of the phenomenon of a shimmy. Rep Russ Acad Sci 428(6):761–765 (in Russian)

Analysis of Machine Tool Installation on the Base

Yuri A. Semenov and Nadezhda S. Semenova

Abstract Vibrations that emerge when parts are being processed on a machine tool may result in the malfunction and premature wear of the given tool. A wide range of vibration sources and the effects they cause requires various means of vibration protection to be used. For this purpose, machine tools are installed directly on the shop floor with, various foundations and anti-vibration mountings. This article deals with the efficiency of these vibration-isolation devices.

Keywords Machine tool · Means of vibration protection · Anti-vibration mounting · Foundation

Introduction

Vibrations that emerge when parts are being processed on a machine tool may result in the malfunction and premature wear of the said tool, as well as deterioration of the quality of the processed parts, which makes such vibrations undesirable. However, in some cases, vibrations are used for chip control, reduction of friction, and conditions for the movement of the tool's operating elements or cutting conditions.

Machine tool vibrations can be forced or, parametric, or they can be self-vibrations. Forced vibrations emerge during cutting due to periodic external actions or periodic variation of the cut layer of metal. Forced vibrations appear most prominently during the milling of workpieces. In this case, a coercive force emerges due to the periodic penetration and withdrawal of the milling cutter teeth.

Unbalanced workpieces or rotating groups of a machine tool (couplings, chucks, etc.), as well as reciprocating masses (supports, etc.), cause temporary coercive

Y.A. Semenov (✉) · N.S. Semenova
Peter the Great Saint-Petersburg Polytechnic University, Saint-Petersburg, Russia
e-mail: tmm-semenov@mail.ru

N.S. Semenova
e-mail: tmm-nss@yandex.ru

forces to emerge. As these forces are transmitted further to the base, they cause the machine tool and the building that houses it to vibrate. Therefore, the reason for machine-tool vibration may lie in its vibration-active groups and the vibrations of other machinery.

Parametric vibrations appear during the variation of the bending stiffness of the machine tool spindle and during its extension.

Self-vibrations are observed in machine tools during the movement of heavy units on slideways and during metal cutting. Such vibrations emerge due to non-linear friction forces and variable cutting forces with "incident" features.

The wide variety of vibration sources and the effects they cause require different means of vibration protection to be used. For this purpose, machine tools are installed directly on the shop floor, with various foundations (Fig. 1) and anti-vibration mountings (Fig. 2) [1–4].

Small (up to 10 tons) machine tools with rigid and semi-rigid machine frames ($\ell/h \leq 7-8$, where l is the sectional length and h is the sectional height of a machine frame) are installed on the shop floor.

Fig. 1 Example of a machine tool installed directly on a shop floor
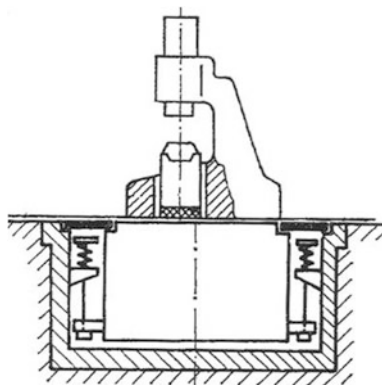
Fig. 2 Examples of anti-vibration mountings for shop tools

Medium-sized machine tools with rigid machine frames ($\ell/h < 4 - 5$) that have no unbalanced forces and can be slanted without compromising operational comfort or workpiece processing quality are installed on anti-vibration mountings [3, 5, 6].

Machine tools with non-rigid machine frames ($\ell/h > 8$) and heavy machine tools that generate significant unbalanced forces are installed on foundations [6, 7].

Heavy machine tools that do not generate significant unbalanced forces are installed on special vibration-isolated foundations that use springs as elastic elements.

In some cases when horizontal excitation forces are prevalent in a machine tool, special vibration-isolation schemes are applied: machine tools are fixed to supporting structures with cables or pinned-pinned beams. Let us consider several ways of machine-tool installation [7–11].

Installation on Anti-vibration Mountings

Figure 3 shows a schematic representation of such an installation. As a first approximation, let us regard a machine tool with a base as perfectly rigid bodies. Let us assume that the machine tool has a mechanism that sets mass μ (e.g., a support) in motion. Generation of this motion is associated with the effect of force P that occurs in the mechanism. The model under consideration disregards the forces exerted upon the base by any independent sources (e.g., an adjacent machine tool).

Equations of motion for the system under consideration are:

$$m\ddot{y} + b\dot{y} + cy = P, \tag{1}$$

$$\mu(\ddot{y} + \ddot{u}) = -P, \tag{2}$$

where m is mass of the machine tool's stationary parts; $y(t)$ is a motion law of machine tool body; $u(t)$ is a given law of mass μ motion in relation to the machine tool body; c, b are stiffness and anti-vibration mounting damping coefficient.

Fig. 3 Schematic representation of such an installation with anti-vibration mounting
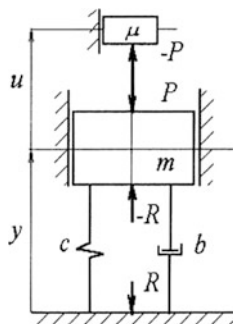
The force acting on the base

$$R = cy + b\dot{y}. \tag{3}$$

In operational form, we have:

$$\left(mp^2 + bp + c\right)y = P; \quad \mu p^2 y = -P - \mu\ddot{u}(t); \quad R = (bp + c)y,$$

where p is an operator which differentiates with respect to time.

Solving these operator equations, we find:

$$R = -w_R(p)\mu\ddot{u}(t); \quad P = -w_P(p)\mu\ddot{u}(t), \tag{4}$$

where transfer functions that tie together forces R and P characterizing the external vibration activity of a machine tool with a given law of motion $u(t)$ are:

$$w_R(p) = \frac{bp + c}{(m + \mu)p^2 + bp + c}; \quad w_P(p) = \frac{mp^2 + bp + c}{(m + \mu)p^2 + bp + c}. \tag{5}$$

Providing that the machine tool's attachment to the base is rigid, we have:

$$R^0 = P^0 = -\mu\ddot{u}(t). \tag{6}$$

Obviously, transfer functions $K_R(p) = R/R^0$, $K_P(p) = P/P^0$, match $w_R(p)$ and $w_P(p)$ respectively. Assuming that law of motion $u(t)$ is harmonic, coefficients $|K_R(j\omega)|$ and $|K_P(j\omega)|$ can serve as a measure of efficiency on frequency ω. Figure 4 shows approximate diagrams $|K_R(j\omega)|$ and $|K_P(j\omega)|$. Values ω, for which $|K_R(j\omega)| < 1$ and $|K_P(j\omega)| < 1$, determine the efficiency regions. The diagrams show that anti-vibration mountings can reduce forces R and P only in a high-frequency region. Force P decreases insignificantly as it depends on the proportion $m/(m + \mu)$.
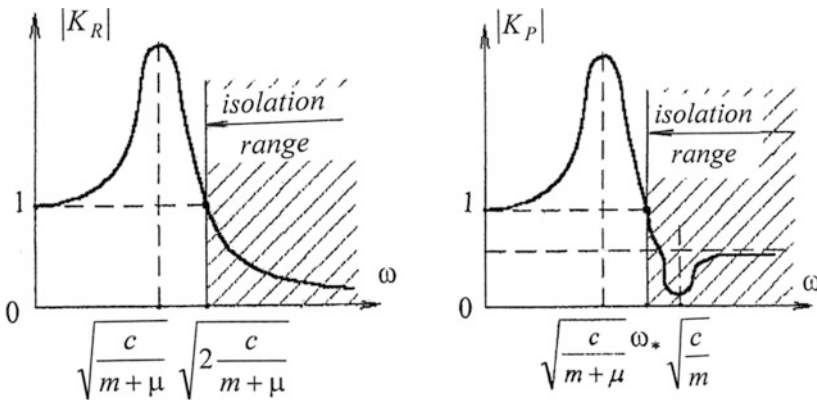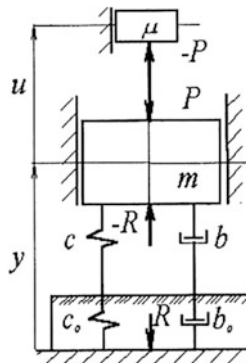

Fig. 4 Approximate diagrams $|K_R(j\omega)|$ and $|K_P(j\omega)|$

The efficiency region for $P(t)$ is derived from the condition $\left| c - m\omega^2 \right| < \left| c - (m+\mu)\omega^2 \right|$. Vibration isolation is efficient if $\omega > \omega_* = \sqrt{c/(m+0.5\mu)}$. The efficiency region for $R(t)$ is as follow: $\omega > \sqrt{2c/(m+\mu)}$.

Let us further assume that the base (ground) on which a machine tool is installed is elastic. Figure 5 shows a schematic representation corresponding to this case.

Here, c_0 and b_0 are stiffness and elastic base damping coefficient. Let us set $c_{\text{red}} = cc_0/(c+c_0)$; $b_{\text{red}} = bb_0/(b+b_0)$ and substitute c for c_{red} and b for b_{red} in the expressions obtained for the previous case. This way, we shall find

$$R = -\frac{b_{\text{red}}p + c_{\text{red}}}{(m+\mu)p^2 + b_{\text{red}}p + c_{\text{red}}}\mu\,\ddot{\mu}(t), \quad P = -\frac{mp^2 + b_{\text{red}}p + c_{\text{red}}}{(m+\mu)p^2 + b_{\text{red}}p + c_{\text{red}}}\mu\,\ddot{\mu}(t).$$

Providing that the machine tool's attachment to the elastic base is rigid ($c_{\text{red}} = c_0, b_{\text{red}} = b_0$), we have:

$$R^0 = -\frac{b_0 p + c_0}{(m+\mu)p^2 + b_0 p + c_0}\mu\,\ddot{\mu}(t), \quad P^0 = -\frac{mp^2 + b_0 p + c_0}{(m+\mu)p^2 + b_0 p + c_0}\mu\,\ddot{\mu}(t).$$

Hence, in this case:

$$K_R(p) = \frac{R}{R^0} = \frac{(b_{\text{red}}p + c_{red})[(m+\mu)p^2 + b_0 p + c_0]}{(b_0 p + c_0)[(m+\mu)p^2 + b_{\text{red}}p + c_{\text{red}}]}, \tag{7}$$

$$K_P(p) = \frac{P}{P^0} = \frac{(mp^2 + b_{\text{red}}p + c_{\text{red}})[(m+\mu)p^2 + b_0 p + c_0]}{[(m+\mu)p^2 + b_0 p + c_0][(m+\mu)p^2 + b_{\text{red}}p + c_{\text{red}}]}. \tag{8}$$

Figure 6 shows a dependency graph for $\left| K_R(j\omega) \right|$ and $\left| K_P(j\omega) \right|$ in this installation scheme.

In this case, the efficiency region includes a medium frequency zone between $\sqrt{c_{\text{red}}/m}$ and $\sqrt{c_0/(m+\mu)}$. Efficiency growth obviously requires an increase in
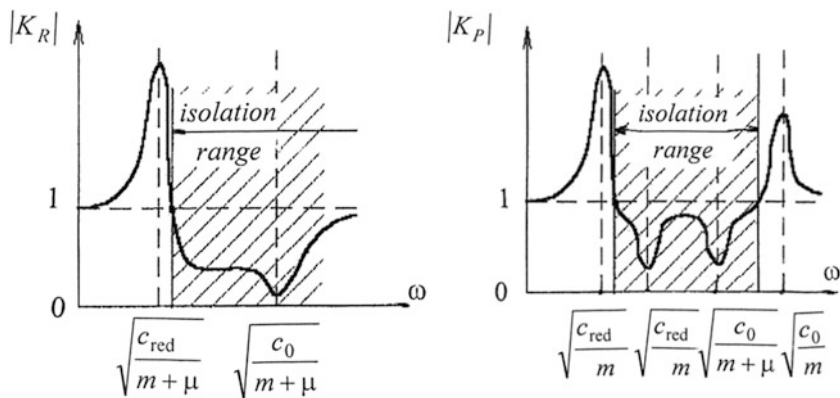
Fig. 6 Dependency graph for $|K_R(j\omega)|$ and $|K_P(j\omega)|$ in the case of an elastic base

Fig. 7 Scheme of machine-tool installation on a standard individual foundation positioned on an elastic base
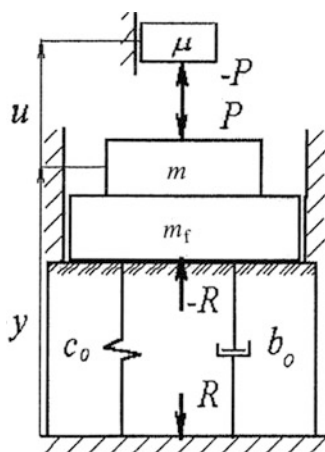
proportion $c_0/c_{\mathrm{red}} = 1 + c_0/c$, i.e. vibration isolator stiffness must be lower than the base stiffness $(c < c_0)$.

For certain types of machine tools, such installation on the base is indeed possible and viable. However, for a large group of machine tools, such an installation method brings about negative effects. Notably, a machine tool becomes more slanted, more susceptible to static effects that may be caused, among other things, by the displacement of discrete masses, etc.

Machine-Tool Installation on the Foundation

Machine tools are installed on individual and strip foundations equipped with rubber mats and springs. Let us consider a scheme of machine-tool installation on a standard individual foundation positioned on the elastic base (Fig. 7).

Let us present the equations of motion for such a system in the operational form:

$$\left.\begin{array}{c} [(m+m_{\mathrm{f}})p^2 + b_0 p + c_0]y = P, \\ \mu p^2 y = -P - \mu\ddot{\mu}, \\ R = (b_0 p + c_0)y, \end{array}\right\} \tag{9}$$

where m_{f} is the foundation mass.

From Eq. (9), we shall derive the force transmitted to the base,

$$R = -\frac{b_0 p + c_0}{(m+\mu+m_{\mathrm{f}})p^2 + b_0 p + c_0}\mu\ddot{\mu}(t). \tag{10}$$

With $m_{\mathrm{f}} = 0$, i.e., with a machine tool installed directly on the elastic base, we shall have:

$$R^0 = -\frac{b_0 p + c_0}{(m+\mu)p^2 + b_0 p + c_0}\mu\,\ddot{\mu}(t). \tag{11}$$

The transfer function

$$K(p) = \frac{R}{R^0} = \frac{(m+\mu)p^2 + b_0 p + c_0}{(m+\mu+m_{\mathrm{f}})p^2 + b_0 p + c_0} \tag{12}$$

that ties together the effort transmitted to the base and the effort with $m_{\mathrm{f}} = 0$ characterizes base efficiency as a means of vibration isolation. In the case of harmonic action of frequency ω, the coefficient

$$|K_R(j\omega)| = \sqrt{\frac{[c_0 - (m+\mu)\omega^2]^2 + b_0^2\omega^2}{[c_0 - (m+\mu+m_{\mathrm{f}})\omega^2]^2 + b_0^2\omega^2}} \tag{13}$$

is a measure of base efficiency: the lower $|K_R(j\omega)|$ is, the more efficient the base shall be. Figure 8 shows an approximate $|K_R(j\omega)|$ dependency graph.

The isolation range, determined by the condition $|K_R(j\omega)| < 1$, is derived from the proportion:

$$\omega > \omega_* = \sqrt{\frac{c_0}{m+\mu+0.5m_{\mathrm{f}}}}. \tag{14}$$

The higher m_{f} is, the lower ω_* shall be, i.e., the frequency at which the foundation starts providing vibration isolation.

With $\omega < \omega_*$, the coefficient $|K_R(j\omega)| > 1$. With $\omega_{**}^2 = c_0/(m+\mu+m_{\mathrm{f}})$, it reaches its approximate maximum value of:

Fig. 8 An approximate |$K_R(j\omega)$| dependency graph
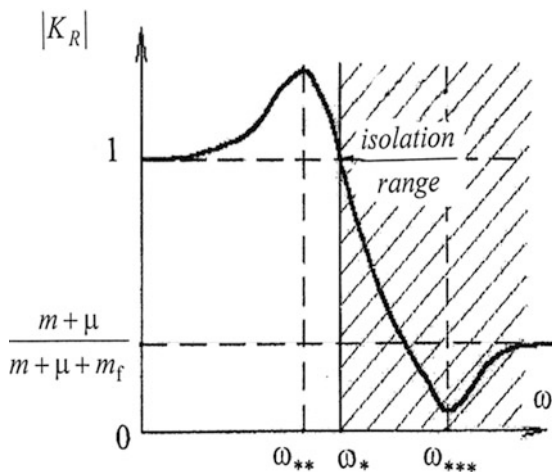
$$|K_R(j\omega)|_{\max} = \sqrt{\frac{m_f^2 c_0}{(m+\mu+m_f)b_0^2} + 1} \approx \frac{m_f}{b_0}\sqrt{\frac{c_0}{m+\mu+m_f}}. \tag{15}$$

Thus, with the rise of m_f, $|K_R(j\omega)|_{\max}$ increases as well. Therefore, frequency ω_{**} should be located outside the external action spectrum.

With $\omega^2 \gg c_0/(m+\mu)$, the coefficient $|K_R(j\omega)|$ is almost independent from ω and tends to $(m+\mu)/(m+\mu+m_f)$ with the increase of ω. In order to reduce the force transmission by N, the following condition should be met:

$$\frac{m+\mu+m_f}{m+\mu} > N. \tag{16}$$

From Eq. (15), let us derive:

$$m_f > 2(m+\mu)\left[\left(\frac{\omega_{***}}{\omega}\right)^2 - 1\right], \tag{17}$$

where $\omega_{***}^2 = c_0/(m+\mu)$. Thus, complete detuning of the system from the external actions requires the mass of the foundation to be $2\left[(\omega_{***}/\omega)^2 - 1\right]$ times higher than the mass of the machine tool.

The lower limit of the efficiency range can be reduced without increasing the mass of the foundation by installing springs or rubber mats between the foundation and the base. In some cases, a machine tool is installed on the foundation using

Fig. 9 Scheme for a machine tool installed on the foundation using isolators
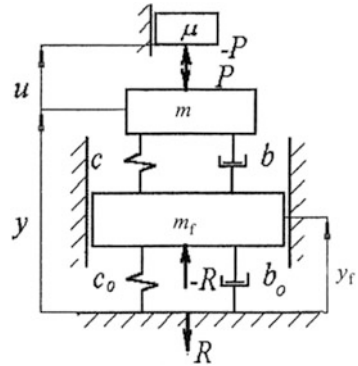
Fig. 10 $|K_R(j\omega)|$ and $m + \mu \ll m_f$ dependency graph
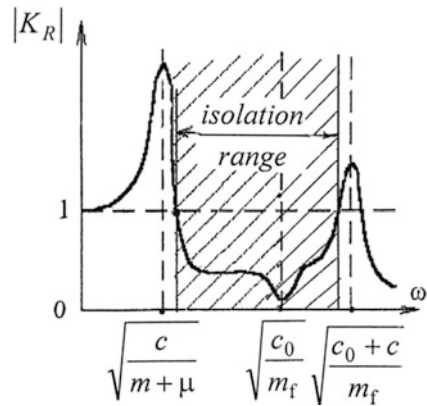
isolators. Figure 9 shows such an installation scheme. The system has two degrees of freedom; let us choose displacement y and y_f as generalized coordinates. Then the equations for the system motion shall look as follows:

$$\left.\begin{aligned} \mu(\ddot{y}+\ddot{u}) &= -P, \\ m\ddot{y} + b(\dot{y} - \dot{y}_f) + c(y - y_f) &= P, \\ m_f\ddot{y}_f + b(\dot{y}_f - \dot{y}) + c(y_f - y) &= -R, \\ b_0\dot{y}_f + c_0 y_f &= R. \end{aligned}\right\} \quad (18)$$

Solving Eqs. (19) in an operational form, we find:

$$R = -\frac{(bp+c)(b_0 p + c_0)}{[m_f p^2 + (b+b_0)p + c + c_0][(m+\mu)p^2 + bp + c] - (bp+c)^2}\mu\ddot{u}. \quad (19)$$

Replacing isolators with a rigid machine tool mounting on the foundation, we have:

$$R^0 = - \frac{(b_0 p + c_0)}{[(m + \mu + m_{\text{f}})p^2 + b_0 p + c_0]} \mu \, \ddot{\mu}. \tag{20}$$

In this case, the efficiency operator is:

$$K_R(p) = \frac{(bp + c)[(m + \mu + m_{\text{f}})p^2 + b_0 p + c_0]}{[m_{\text{f}} p^2 + (b + b_0)p + c + c_0][(m + \mu)p^2 + bp + c] - (bp + c)^2} \, .$$

Figure 10 shows $|K_R(j\omega)|$ and $m + \mu \ll m_{\text{f}}$ dependency graph. It can be seen that the external vibration activity decreases in the medium frequency range.

References

1. Kolovsky MZ (1999) Nonlinear dynamics of active and passive systems of vibration protection. Springer-Verlag, Berlin, Heidelberg 426 pp
2. Karnovsky IA, Lebed E (2016) Theory of vibration protection. Springer, Berlin 708 pp
3. Semenov YA (2012) Dynamics of machines, Part 2. University press, Saint Petersburg, 252 pp (rus)
4. Kolovsky MZ, Evgrafov AN, Semenov YA, Slousch AV (2000) Advanced theory of mechanisms and machines. Springer, Berlin 394 pp
5. Kolovsky MZ (1976) Nonlinear theory of vibration protection, Moscow, USSR: "Science", 320 pp (rus)
6. Rivin EI (2003) Passive vibration isolation. ASME Press
7. Swami S (1999) Soil dynamics and machine foundation. Galgotia Publications Private Limited, New Delhi 352 pp
8. De Silva CW (2005) Vibration and shock handbook. Taylor & Francis, N.-Y, 1872 pp
9. Gans RF (2015) Mechanical systems: a unified approach to vibrations and controls. Springer, Cham, 437 pp
10. Genta G (2009) Vibration dynamics and control. Springer, New York 806 pp
11. Sinha A (2010) Vibration of mechanical systems. Cambridge University Press, 324 pp

About the Nature of Dissipative Processes in Cutting Treatments of Titanium Vanes

Margarita A. Skotnikova and Nikolay A. Krylov

Abstract This article reports on a systematic study of temperature-speed features of structural and phase transformations in machined blades of titanium billets, performed with the assistance of optical metallography techniques, electron microprobe analysis, and electron microscopy. The work resulted from evaluation of the mean effective thermal anisotropy stresses on the boundary of two hcp crystals with the corresponding angles between the hexagonal axes (HA), as well as between HA and the interface with changes in temperature by one degree.

Keywords Steam turbines · Titanium alloy · Structural and phase transformation · Electron microscopy

Introduction

The difficult problem of the cutting treatment of metal blanks, for example, from titanium alloys, because of the reduction in the tools' resistance to wear is currently rather well known. There is a hypothesis about presence here connection with change degree of localization plastic deformation in metal blank at cutting formation. The knowledge of conformities and phenomena accompanying process of cutting treatment, will allow to find ways increase of treatment quality, accuracy of details, decrease of cutting capacity. As follows from the earlier carried out works [1–4], in the investigated alloys structures of the hot-deformed (initial) state are formed nonequilibrium β(α)- and α(β)-solid solutions, which being in an elastic—intense condition, enriched with vacancies, α-, β-stabilizing elements, and inclined to decomposition.

The purpose of the given work consist in development of representations about temperature-time features of formation and decomposition enriched solid solutions,

M.A. Skotnikova (✉) · N.A. Krylov
Peter the Great Saint-Petersburg Polytechnic University, St. Petersburg, Russia
e-mail: skotnikova@mail.ru

N.A. Krylov
e-mail: cry_off@mail.ru

with the account is elastic—intense the states created in the volume of deformed metal blank during its technological treatment by cutting, in an establishment of nature of deformation localization and in development ways of increase of the tool wearproofity at the expense of choice of an optimum regime of the deformation speed and temperature.

The materials for investigation were OT4, PT3V, VT23 alloys. Their treatment was carried out without lubricant to a hard-facing alloy cutting tool T15K6 with speed of feed S = 0.26 mm/revolutions and depth of cutting t = 3 mm, in the range of cutting speeds 2–250 m/mines. The geometrical parameters of a cutter made corners: $\varphi = 45°$; $\varphi_1 = 15°$; $\alpha = 6°$; $\gamma = 12°$.

Formation of Elastic—Intense State in Material at Cutting Treatment

At technological treatment by cutting, at presence of gradients of stresses and temperatures on the blanks section: a crystallographic anisotropy of thermal expansion coefficients; phase transformations with change of the phases specific volume, there can be significant internal stresses, forming in processable blank the state is elastic—intense.

Formation Thermal Stresses

It is known, that the titan has the specific features: by which, first of all, its high chemical activity, polymorphism and high sensitivity low-temperature α—modification to concentrators of stresses, concerns, that, probably, is caused by an anisotropy of its HCP—lattice and, hence, anisotropy of elastic and diffusive properties, and also, low heat conduction of titan.

It is known, that the internal stresses in metals caused by the temperature gradient, are proportional to the ratio of the thermal expansion coefficient to the heat conduction. As it is visible from submitted Table 1 for Ti, Hf, Zr (with HCP—lattice) these ratios appear on the order above, than in copper (with FCC) or molybdenum (with BCC—lattice).

Table 1 Comparison of meanings of the ratio of thermal expansion coefficient to heat conduction for metals

Metal	W	Mo	Cu	Al	Ni	Fe	Mg	Zr	Hf	Ti
The ratio of a coefficient of thermal expansion to a heat conduction, $\times 10^{-6}$ (cal/cm² s)$^{-1}$	11	14	17	45	63	67	74	83	106	182

In zone of the cuttings formation in processable titanium blanks under thermal and mechanical influences the elastic—intense state is formed. There is significant temperature and strain inhomogeneity resulting in occurrence mechanical and thermal macro and micro of stresses, especially, on the grains borders from HCP—lattice having anisotropy of thermal expansion coefficients. At heats change these stresses in the state to surpass a crystallographic yield stress.

Formation Thermal Anisotropy Stresses

In development of works N.N. Davidenkov's and V.A. Likhachev's, the theoretical estimation of the thermal anisotropy stresses ($\sigma/\Delta T$), arising on border two next α—grains from HCP—lattice was made, depending on the corner crystallographic orientation (ψ) of their hexagonal close-packed axes (H.A.). And corner of their orientation (β) of rather general of the unit border, at change of the temperature on $1°$ [5]. Account of an average working stress of the thermal anisotropy according to the formula (1) made under the specially developed program on the computer, provided that the hexagonal close-packed axes of both grains, and as a normal to the unit border lay in one plane,

$$\sigma/\Delta T = \left(\alpha_{\parallel} - \alpha_{\perp}\right)\left[\cos^2\beta - \cos^2(\beta + \psi)\right]/S_{11}\left[\sin^4\beta + \sin^4(\beta + \psi)\right] + S_{33}\left[\cos^4 b + \cos^4(b + \psi)\right] + (2S_{13} + S_{44})\left[\cos^2\beta \sin^2\beta + \cos^2(\beta + \psi) \cdot \sin^2(\beta + \psi)\right]$$

(1)

where, $\alpha_{\parallel}$—coefficient of linear expansion along an axis "c"; $\alpha_{\perp}$—coefficient of linear expansion along an axis "a"; S_{ik}—coefficients of elasticity.

The coefficients of linear expansion α—titan along axes "c" and "a" at room temperature are equal: $\alpha_{\parallel} = 9.5 \times 10^{-6}$ grad^{-1}; $\alpha_{\perp} = 5.6 \times 10^{-6}$ grad^{-1} [6]. The meanings of elasticity coefficients were accepted on the basis of the literary data [7]: $S_{11} = 0.958 \times 10^{-5}$; $S_{33} = 0.698 \times 10^{-5}$; $S_{13} = -0.189 \times 10^{-5}$; $S_{44} = 2.14 \times 10^{-5}$ MPa. The received dependencies of thermal anisotropy stresses, $\sigma/\Delta T$ at meanings of corners β and ψ from 0 up to 180 grad., are given in Fig. 1a, b.

As have shown results of account, for titan by most favourable, causing stresses of compression ($\sigma/\Delta T = 0$ to -1.44 MPa/grad) were basic borders of grains with 90—grad orientations, or close to them, of a H.A. ($\beta = 90 \pm 45$ grad.). By most dangerous, causing stresses of a stretching ($\sigma/\Delta T = +0.7$–1.8 MPa/grad.), were prismatic borders α—grains with hexagonal close-packed axes approximately parallel to general border of the unit ($\beta \approx 0 \pm 45$ grad.) and which on the data Kolachev [8], should work as drains of vacancies, that is why, according to our concept, along such prismatic borders should be formed nonequilibrium $\alpha(\beta)$-solid solutions by enriched vacancies and β-stabilizers.

During cutting treatment of blank, in zone of interaction with driven the cutting tool, is observed the structural and crystallographic textured of processable material
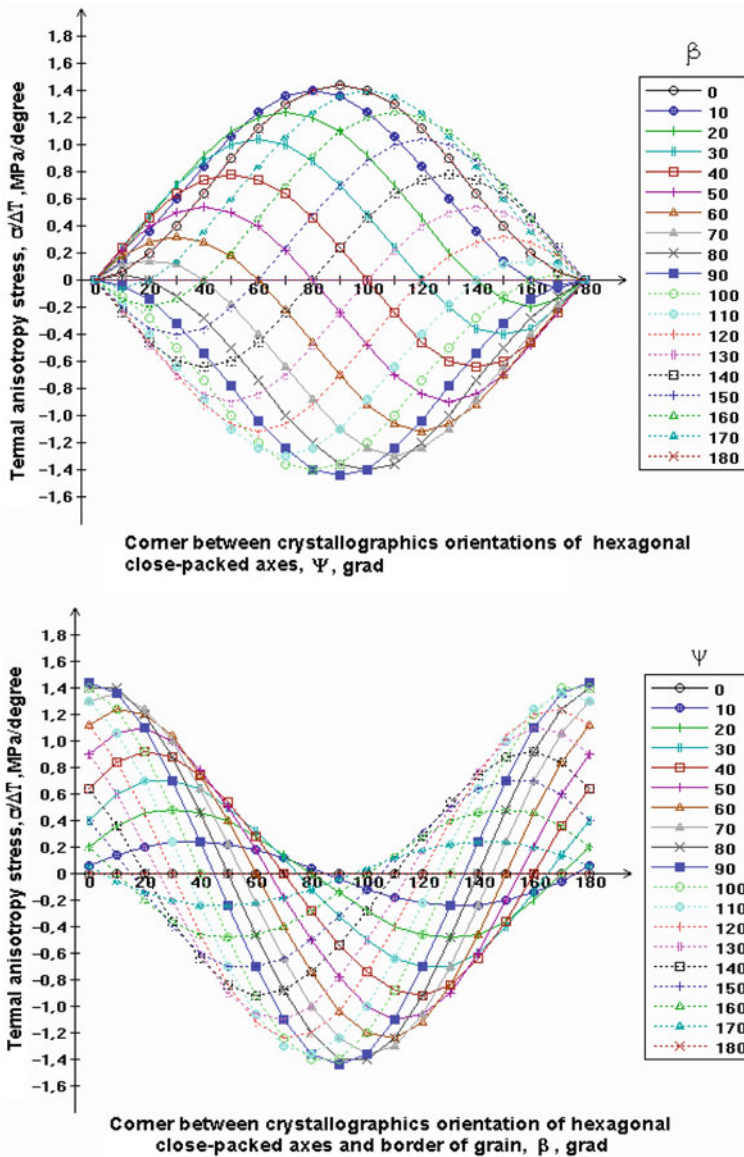
Fig. 1 Thermal anisotropy stresses on border of two HCP crystals with the appropriate corners between their hexagonal close-packed axes (H.A.) (**a**), and also between a H.A. and border of the unit (**b**), at change of a temperature on 1°

and formation of prismatic orientation of borders having preferable orientation in planes of shift. On such grains borders from HCP—lattice, as a result of heats change, can arise appreciable thermal stresses, which, probably, result in metal to

change structure, redistribution of alloying elements, impurity atoms and vacancies, further, to localization temperatures, plastic deformation, and also to decrease of wearproofity of tool [9].

Chip Microstructure

At cutting metal blanks, in zone of contact interaction of processable detail and cutter there is a complex manyfactor process of interaction of deformation, friction, adhesion and destruction, the ratio of which values is influenced by physical—mechanical and chemical properties of contacting materials, geometry of cutting, lubricant, speed and temperature of deformation. On Fig. 2 are represented a processable detail, cutter and formed element chip.

Study of geometrical parameters, the evolutions of formed chip structure on macro-, micro- and submicro-levels carried out in longitudinal and cross its sections with the help of optical metallography, transmission and scanning electronic microscopy with attraction of microdiffraction analysis and computer. Samples (foil) for a transmission electronic microscopy cut out by tubular electrode by diameter 3 mm in longitudinal section of chip.

In Fig. 3a, b the photos of structure of alloy BT23 are submitted before (Fig. 3a) and after (Fig. 3b) cutting treatment. Is shown, that at cutting treatment, beginning already from speed 2 m/min, the non-uniform plastic deformation, its strong localization in periodic narrow volumes of metal on the mechanism of formation of superfine dislocation cellular structures, Fig. 3b took place. Conditions for strong localization in volumes of metal of temperature and plastic deformation here are created. The free surface of a chip is formed on the complex mechanism with attributes of destruction in conditions of superplasticity, Fig. 4a, b.

In process of cutter movement, at the same time with frictional heat, in segment of material, formed before it, there is an accumulation of crystal structure defects and their evolution, down to formation a ultimate structure resulting in localization of plastic deformation and in destruction. The size of a segment depends from temperature—kinetic conditions of cutting and from relaxation ability (structural and concentration) processable material. Increase of speed of cutting over ultimate, the causing backlog of frictional heat-generating from heat-absorbing (increase of

Fig. 2 The circuit of formation of an element chip at metal blank by cutting treatment
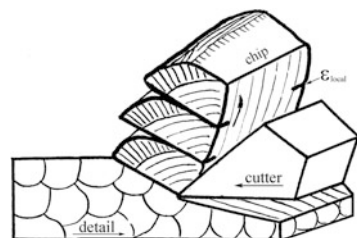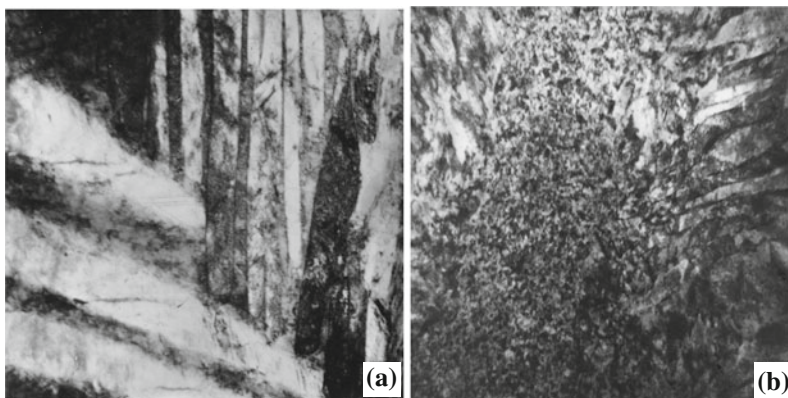
Fig. 3 Structure of chip from alloy VT-23 before (**a**) and after (**b**) cutting treatment with speed 120 m/min

Fig. 4 Characteristic photos of a surface chip from an alloy BT-23 after cutting treatment with speed 230 m/min. ×200 (**a**); ×400 (**b**)

dissipation of energy at the expense of structural and phase transformations), results in localization of heat in narrow periodic volumes of metal, where there is formation ultimate structure, redistribution of alloying elements, impurity atoms, vacancies and localization there of plastic deformation to simultaneous shift and displacement of segments.
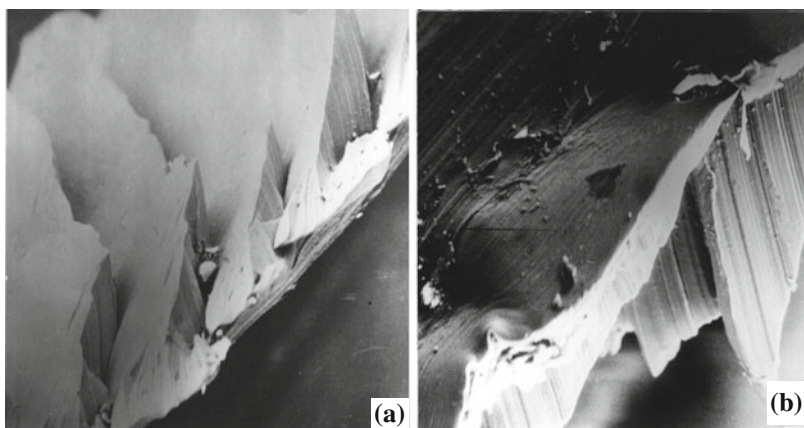
In process of cutter movement, at the same time with frictional heat, in segment of material, formed before it, there is an accumulation of crystal structure defects and their evolution, down to formation the ultimate structure resulting in plastic deformation localization and in destruction. The size of the segment depends from temperature—kinetic conditions of cutting and from relaxation ability (structural

and concentration) processable material. Increase of the cutting speed over ultimate, the causing backlog of frictional heat-generating from heat-absorbing (increase dissipation of energy at the expense of structural and phase transformations), results in localization of heat in narrow periodic volumes of metal, where there is formation ultimate structure, redistribution of alloying elements, impurity atoms, vacancies and localization there of plastic deformation to simultaneous shift and displacement of segments.

At a cuttings formation in titanium alloys having a high frictional heat, the low heat conduction and significant relaxation ability (structural and concentration), creates conditions for dissipative modification of structure and chemical composition of periodic narrow layers of material. It results in so-called frictional accommodations (period of a wear-in material. In a contact zone the wearproof secondary structure essentially lowering wear of processable detail, but raising wear of cutting edge of tool is formed.

Conclusion

During thermomechanical treatment, for example, cutting treatment, the accumulation of external energy by system of basis atoms and alloying elements causes their displacement from the equilibrium positions (units of crystal lattice), that creates in a superficial layer of processable detail complex elastic—intense state, at all structural levels. The dislocated atoms formed at it, and vacancies are carriers of superfluous energy and promote increase of phases solubility limit. Thus, it is possible to believe, that in contact zone the nonequilibrium solid solutions enriched by superfluous alloying elements and vacancies are formed which, being in is elastic—intense state, appear inclined to decomposition. For the self-organizing, transition to relative balance, the system realizes various ways of dissipation of superfluous energy: besides transformation of mechanical energy in thermal (the increases of temperature in contact zone), proceed two polystage relaxation processes—structural and concentration [10]. The structural relaxation is shown as structural transformations on the mechanism of formation of narrow zones of secondary dislocation substructures. The increase of regularity and frequency of dislocation congestion's distribution promotes similar distribution in a cutting edge zone of true stresses at the expense of redistribution them lengthways of rather advanced subborders. The concentration relaxation is shown as phase transformations on the mechanism of decomposition of nonequilibrium solid solution and redistribution (mass transfer) in secondary structures of superfluous alloying elements, impurity atoms, vacancies and oxygen from external environment. It is possible to believe, that in a contact zone the secondary structures alloying by oxygen [11], raising a wearproofity of a processable material are formed.

The cuttings formation includes two basic moments. At the first stage at compression there is a crumplety of a processable detail as a result of uniform plastic deformation, increase of actual contact area and, hence, reduction of true stresses in

a zone of cutting. In too time, in a cutting edge zone there are frictional forces, which grow simultaneously with growth of actual contact area. Thus, the plenty of heat is located in contact zone between cutting tool and detail. At the second stage at compression there is formation a ultimate structure, mass transfer and localization of plastic deformation in high plastic narrow zones, to simultaneous shift and displacement of segment. In this moment the actual contact area decreases, and in zone of cutting the true stresses are increased. The cyclic change of resulting stresses results in fatigue phenomena in zone of chip formation. Besides a deformational -mechanical wear in cutter material and processable detail in addition arises fatigue wear, that is the reason of decrease of wearproofity of the tool at the certain high speeds of machining of materials with a low heat conduction.

Thus, the analysis of the received results allows to conclude, that during cutting treatment of metal blanks, in them the nonequilibrium solid solutions are formed which for the self-organizing, transition to relative balance, realize various ways of dissipation of superfluous energy. The cuttings formation can be considered as process of go-ahead redistribution of the stress concentrator along edges of processable detail and necessities of its periodic relaxation by means of local structural and phase transformations in a crystal, which as a whole remains structural—stable. The period of deformation localization (size of chip segment) depends from temperature—kinetic conditions of cutting and from relaxation ability (structural and concentration) processable material. For effective increase of a wearproofity of the tool, it is necessary to create conditions for power balance between a brought up thermal energy and its dissipation at the expense of structural and phase transformations in processable material.

References

1. Parshin AM, Ushkov SS, Skotnikova MA (1995) Decomposition diagram and heat—treatment schedule of titanium α-alloy. In: Proceedings 8th world conference on titanium, vol 1. The Institute of Materials, Birmingham, pp 2515–2522
2. Skotnikova MA (1997) Investigation the structural and phase transformations and mechanical tests of titanium alloys. In: Proceedings the second international conference and exhibition on marine intellectual technologies, Saint Petersburg, vol 4, pp 251–255
3. Skotnikova MA (1998) Crystalgeometrical model of high-temperature bcc—modification of titanium enriched of vacancies. In: Metal science and heat treatment, Moscow, vol 3, pp 22–24
4. Skotnikova MA (1998) Perfection of the heat treatment of titanium alloys intended for an energymachinebuilding. In: Tool, Saint Petersburg, vol 11, pp 34–35
5. Davidenkov NN, Likhachev VA, Malygin GA (1960) Research of an irreversible thermal formchange Zn. Phys Metal Metal Sci 10(3):412–424
6. Kolachev BA (1976) A physical metallurgy of titanium. Metallurgy, Moscow, p 184
7. Predvoditelev AA, Troickii OA (1973) Dislocations and dot defects in hexagonal close-packed metals. Atompublisher, Moscow, p 200
8. Gabidulin RM, Kolachev BA, Kolpachev AA (1976) The diagram of state metal—vacancy. In: News high schools. Colour metallurgy, vol 4, pp 87–91

9. Komanduri R (1981) New observations on the mechanism of chip formation when machining titanium alloys. Wear 69:179–188
10. Skotnikova MA (1997) Decomposition of nonequilibrium solid solutions and mechanical properties, of hot-strained alloys of titanium. In: High technologies in a modern material competence, Saint Petersburg, pp 24–25
11. Likhachev VA, Panin VE, Zasimchuk EE et al (1989) Cooperative processes and localization of deformation. Sciences Dumka, Kiev, 320 p

The Model of the Elastic–Plastic Deformation of a Structural Member

Sergei A. Sokolov

Abstract The model of the elastic–plastic deformation of a structural member containing the stress concentrator is proposed. The model enables visualization of the deformation process under irregular, cyclic loading and considering the instability of cyclic material properties. The model can be implemented in Mathcad. The model is designed for the analysis of the operational loading of structures and components in predicting their strength and resistance to low-cycle fatigue.

Keywords Stress concentrator · Elastic–plastic deformation · Cyclic loading

The fatigue damage and fracture in metal structures and machine elements generally occur in the stress concentrators. To predict these damages, it is necessary to know the distribution of stresses in these areas and how they change in the course of operational loading [1–6]. The stress field in objects of arbitrarily complex shape, with monotonic loading including consideration of the elastic–plastic material properties, can be calculated by the finite element method. However, the modeling of the material elastic–plastic deformation in the stress concentrator under cyclic loading presents certain difficulties for using both analytical and numerical methods. Particular difficulties arise if one needs to consider the cyclic instability of the material mechanical properties [4.13]. The change parameters of the material mechanical properties under cyclic loadings are investigated on samples without concentrators according to known methods, but using these parameters to structural member with stress concentrators necessary to introduce a number of assumptions, which are applicable only in elementary cases of loading and deformation [1, 2, 7–11].

In order to solve the above-mentioned problem, this paper proposes the elastic–plastic deformation model of the structural element or component under the conditions of a non-homogeneous state of stress. The model provides a simplified picture of the material stress–strain state at the stress concentrator, but makes possible visual tracking of the deformation in the case of irregular loading and

S.A. Sokolov (✉)
Peter the Great Saint-Petersburg Polytechnic University, Saint-Petersburg, Russia
e-mail: sokolov-sa@rambler.ru

unstable material cyclic properties. The initial data used in this model are the following:

– the material yield strength value σ_T in the stress concentration zone and the equation of the material elastic–plastic deformation curve;
– the parameters of material cyclical instability, if it exists;
– the elastic analysis results of the stress structural member state, which gives the value of the theoretical stress concentration factor α_σ and the stiffer modulus of stiffness stress state at the stress concentrator $\eta = \sigma_I/\sigma_e$ [12], (σ_I is the first major stress, σ_e is the equivalent stress according to the Mises theory).

The model assumptions are:

(a) the plastic zone in the stress concentration zone covers not more than 10–20% of the section area of the structural element. In addition, in the cross sections remote at some distance from the stress concentration zone. The element stress state is independent of plastic processes in the stress concentrator.
(b) the deformation curve of steel, when subjected to cyclic loading, is described by the generalized Masing principle [2].

For the stress-strain state simulation of the structural member part with a stress concentrator, we use a frame structure consisting of two rods (Fig. 1). The rod 1 of length L_1 with the cross sectional area A_1 is the material model in that cross-section part, which is not affected by stress concentration. It remains in an elastic state when subjected to all loadings. The rod 2 of length L_2 with the cross-sectional area A_2 simulates the material deformation in the elastic–plastic zone. The upper ends of rod connect and move together. Let us set:
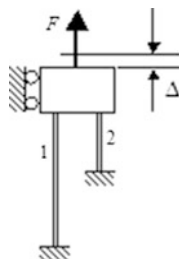
$$\varphi = \frac{A_2}{A_1 + A_2}.$$

The deformation diagram of rod 1 material is described by Hooke's law:

$$e_1 = \frac{\sigma_1}{E}. \tag{1}$$

The elastic–plastic properties of the rod 2 material are described by the power-law of the relative strain/stress dependence, which in a zero-half-cycle, is as follows [2, 8, 9]:

Fig. 1 The bar model of elastic–plastic structure

$$e_2 = \begin{cases} \dfrac{\sigma_2}{E} & \text{if } \sigma_2 \leq \eta\sigma_T; \\[2ex] \dfrac{a}{2}\left[\dfrac{\sigma_2}{E} + \dfrac{\eta\sigma_T}{E}\left(\dfrac{\sigma_2}{a\eta\sigma_T}\right)^{\frac{1}{m}}\right] & \text{if } \sigma_2 > \eta\sigma_T; \end{cases} \qquad (2)$$

and at the following loading half cycles is so:

$$e_2 = \frac{a}{2}\left[\frac{\sigma_2}{E} + \frac{\eta\sigma_T}{E}\left(\frac{(\sigma_2 - \sigma_{2c})(-1)^k}{a\,\eta\sigma_T}\right)^{\frac{1}{m}}\right]. \qquad (3)$$

where σ_1 и σ_2 are the stress of the rods 1 and 2 respectively; E is Young's modulus; σ_{2c} is the value of the previous stress extremum σ_2; m is a strain-hardening coefficient in the elastic–plastic zone; a is the scaling parameter in accordance with the assumption of "b" in the zero-half-cycle for $k = 0$ which is given as $a = 1$ and further on when the following $k = 1, 2, 3, \ldots a = 2$. The strain-hardening exponent can be determined experimentally or calculated as suggested in [4.13].

At all deformation stages of the frame structure, both in elastic and elastic–plastic deformation, the balance condition and compatibility of strains are valid. They are written in the differential form as:

$$d\sigma_n(A_1 + A_2) = d\sigma_1 A_1 + d\sigma_2 A_2. \qquad (4)$$

$$d\Delta = de_1 L_1 = de_2 L_2. \qquad (5)$$

where σ_n is the net nominal stress of the structural member cross section with a stress concentrator; Δ is the movement of coupled rod ends (Fig. 1). Equation (5) disregards changes in the rod lengths L_1 and L_2 under the deformation, since, using the validity assumptions, "a" of this factor influence will be negligible.

In the zero-half-cycle for $\sigma_2 \leq \eta\sigma_T$, both rods are elastically deformed and the equality has to hold only for:

$$d\sigma_2 = \alpha_\sigma d\sigma_n. \qquad (6)$$

From Eq. (6), using Eq. (5) and Hooke's law, we can find the ratio of the rods' length, which we take as a model parameter, i.e.:

$$\frac{L_1}{L_2} = \frac{\alpha_\sigma(1 - \varphi)}{1 - \alpha_\sigma\varphi}. \qquad (7)$$

Thus, the entire system under the elastic deformation is described as follows:

$$d\sigma_1 = \frac{1-\alpha_\sigma\,\varphi}{1-\varphi}d\sigma_n; \quad de_1 = \frac{d\sigma_1}{E};$$
$$d\sigma_2 = \alpha_\sigma d\sigma_n; \quad\quad de_2 = \frac{d\sigma_2}{E}. \tag{8}$$

To find the like dependencies under conditions of the deformation of the elastic–plastic system, i.e., for $\sigma_2 > \eta\sigma_T$, from Eq. (4), the stress increments in the rods are expressed in terms of load increment $d\sigma_n$ as:

$$d\sigma_1 = \frac{d\sigma_n}{1-\varphi+\varphi\frac{d\sigma_2}{d\sigma_1}} \quad \text{and} \quad d\sigma_2 = \frac{d\sigma_n}{\varphi+(1-\varphi)\frac{d\sigma_1}{d\sigma_2}}$$

From Eqs. (5) and (7) we find:

$$\frac{de_1}{de_2} = \frac{1-\alpha_\sigma\varphi}{\alpha_\sigma(1-\varphi)}. \tag{9}$$

Differentiating Eq. (3) and plugging in Eq. (9), we obtain

$$\frac{d\sigma_1}{d\sigma_2} = \frac{1-\alpha_\sigma\varphi}{\alpha_\sigma(1-\varphi)}U_e,$$

where

$$U_e = \frac{a}{2}\left[1 + \frac{1}{am}\left(\frac{(\sigma_2-\sigma_{2c})(-1)^k}{a\,\eta\sigma_T}\right)^{\frac{1}{m}-1}\right]. \tag{10}$$

Thus, the stress and strain increments under the elastic–plastic deformation of model are calculated as:

$$d\sigma_1 = \frac{(1-\alpha_\sigma\varphi)U_e}{\alpha_\sigma(1-\varphi)}d\sigma_2; \quad\quad de_1 = \frac{d\sigma_1}{E};$$
$$d\sigma_2 = \frac{\alpha_\sigma}{\alpha_\sigma\varphi+(1-\alpha_\sigma\varphi)U_e}d\sigma_n; \quad de_2 = U_e\frac{d\sigma_2}{E}. \tag{11}$$

The parameter value φ is set by comparison with the results of finite element analysis of the stress-strain state of components with concentrators and accepted $\varphi = 0.15$.

The presented simulation algorithm of the material elastic–plastic deformation in the stress concentrator is realized without difficulty, for instance, in Mathcad. The program block-scheme is shown in Fig. 2.

In this scheme, block 7 defines the extremum transition point of the loading process. The scheme may be supplemented by the accounting algorithm of the material cyclical instability parameters in block 8. The engineering unrelieved stresses in the concentrator may be introduced as initial data, such as $\sigma_2 = \sigma_{2r}$ and $\sigma_1 = -\sigma_{2r}\varphi/(1-\varphi)$.
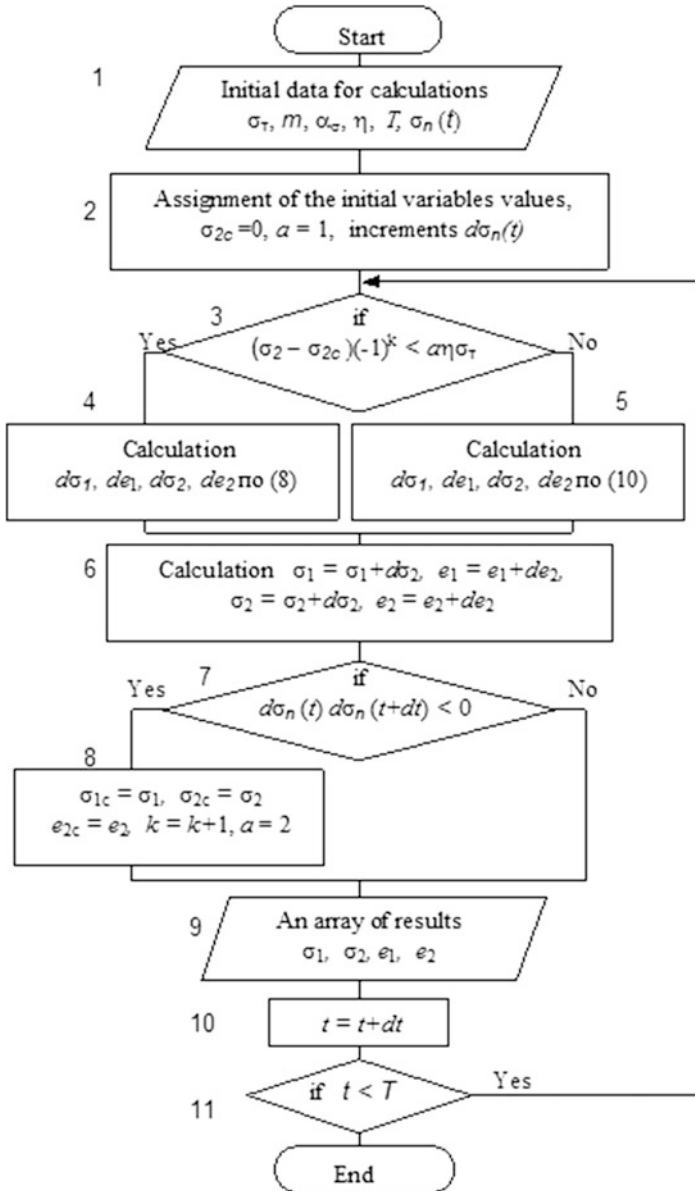
Fig. 2 The block-scheme of the calculation algorithm for the process of elastic-plastic deformation of the material in the concentrator

The adequacy testing of the proposed algorithm was performed by comparison with the results of finite element calculations. The two bands with a circular opening and an edge neckline are used as two stress concentrators (models 1 and 2). With
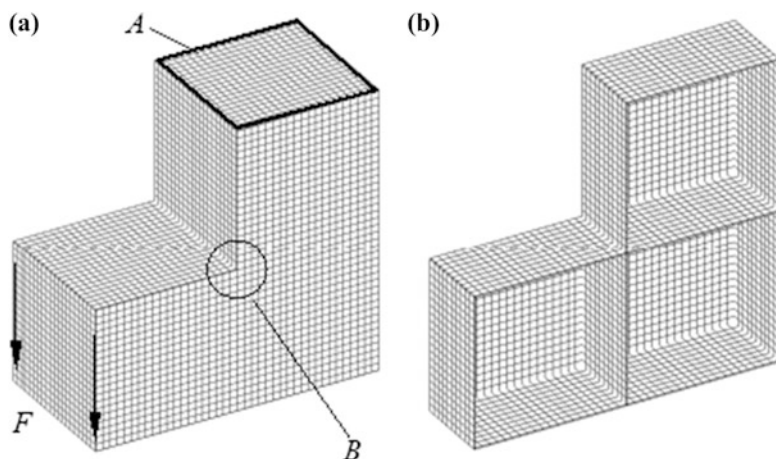
Fig. 3 Finite element model of the thin-web structure fragment (**a**) and the neckling (**b**)

allowance for the symmetry, the properties of the finite-element models reflect only a quarter of these objects with the assignment of appropriate boundary conditions on the trimming line. The third stress concentrator is the thin-slab structure fragment (model 3, Fig. 3b). The finite element model is fixed along the outline A and loaded by transverse force F, which is applied to the flange face. The highest stress concentration occurs in zone B. The plate elements (plate) were used in all models. The models have the following parameters:

model 1: $\alpha_\sigma = 2.3$; $\eta = 1.0$; $\sigma_n = 200$ МПа;
model 2: $\alpha_\sigma = 3.9$; $\eta = 1.0$; $\sigma_n = 162$ МПа;
model 3: $\alpha_\sigma = 3.8$; $\eta = 1.1$; $\sigma_n = 176$ МПа.

The theoretical stress concentration factors for all models are calculated as $\alpha_\sigma = \sigma_I/\sigma_n$. Since the plate elements' bending occurred in model 3, accordingly, all stresses for this model are calculated as an average of the two element sides. The model material has the deformation diagram by Eqs. (2) and (3). The yield strength $\sigma_T = 300$ MPa, and strain-hardening exponent $m = 0.21$. All the models are subjected to one cycle, which consists of loading and unloading (zero-to-compression cycle).

The calculation results of the material deformation process in the stress concentrator for the three models are presented as graphs in coordinates $\sigma_x - e_x$. That is, the normal stress and the linear deformation act in the direction that coincides with the direction of the first major stress under a concentrator tension (Fig. 4). As shown, the proposed algorithm exhibits satisfactory agreement with the results of finite element analysis. In particular, both calculation variants give similar values of unrelieved stress in a concentrator, resulting from local plastic deformation.
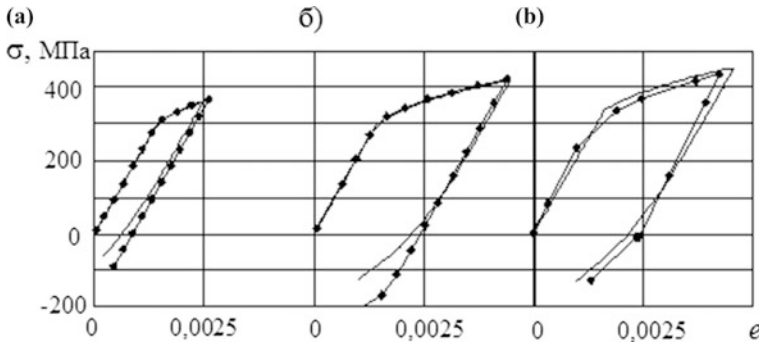
Fig. 4 The graphs of material deformation in the concentrator calculating by FEM (–♦–) and by the presented algorithm (–)
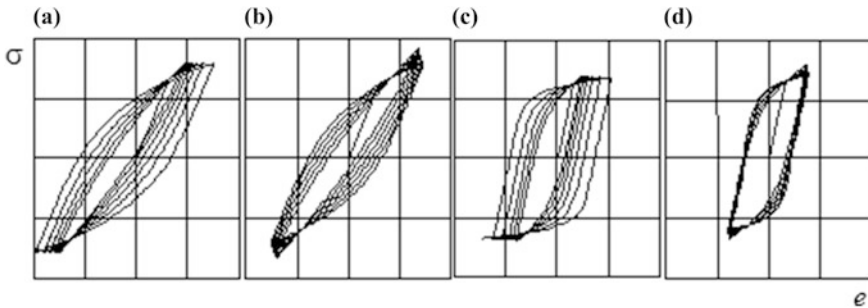
Fig. 5 Deformation curves for samples from hardening (**a–b**) and unhardening material (**c–d**)

The properties of cyclically weakening or strain-hardening material can be handles in the calculation algorithm. As in the example, the deformation/straining curves are calculated for the sample without a stress concentrator $\alpha_\sigma = 1$ and $\varphi = 0.99$ for $\sigma_n > \sigma_T$ (Fig. 5a) and with a stress concentrator $\alpha_\sigma = 2.5$ and $\varphi = 0.15$ for $\sigma_n < \sigma_T$ (Fig. 5b) of the strain-hardening material, for which the value m is increasing from cycle to cycle as $m_k = 1.1^k m_0$ (where k is the half-cycle number, m_0 is the zero half-cycle index value). As seen, the sample without a stress concentrator, when subjected to soft loading, causes the hysteresis loop to narrow at constant strain. The loop also narrows in the concentrator, but hereby the strain is growing. The calculation results for the same samples, but from the softening material with $m_k = 0.9^k m_0$, are shown in Fig. 5c–d. In this case, the hysteresis loop in/on the sample without a stress concentrator expands significantly and, in the concentrator, the loop's width varies very little.

Thus, the proposed model of material elastic–plastic deformation in the concentrator enables analysis of the kinetics of the deformation process under an arbitrary process of cyclic loading, set by function $\sigma_n(t)$ and considering the instability of material cyclical properties. This instrument needs for predicting

low-cycle fatigue and the strength of heavily-loaded structural members and elements.

References

1. Kogaev VP, Makhutov NA, Gusenkov AP (1985) Calculations of strength and durability of machine parts: reference book. Mashinostroenie, Moscow, 224 p
2. Troshchenko VT (1971) Fatigue and inelasticity of metals. Naukova Dumka, Kiev, 268 p
3. Agrawal R, Uddanwadiker R, Padole P (2014) Low cycle fatigue life prediction. Int J Emer Eng Res Technol 2(4):5–15
4. Borrego LP, Abreu LM, Costa JM (2003) Analysis of low cycle fatigue in AlMgSi aluminium alloys. Anales de mecánica de la fractura. 20:179–184
5. Daunys M, Norkuvienė D (2007) Investigation of stress and strain state in concentration zones under low cycle loading. MECHANIKA N2(64):5–11
6. Klysz S (2005) Load sequence influence on low cycle fatigue life. Techn Sci 8:193–209
7. Bondar' VS, Burchakov SV, Danshin VV (2010) Mathematical modeling of the processes of plasticity and materials destruction under non-stationary and non-symmetric cyclic loading. Izvestija Tulskogo gosudarstvennogo universiteta (Izvestija TulGU). Nat Sci (1):64–74
8. Moskvitin VV (1981) Cyclic loadings for elements of structures. Nauka, Moscow, 344 p
9. Fomichev PA, Zvyagintsev VV (2000) Forecasting the durability of bodies with cuts based on local stress strain states. Report 1. Defining stresses and deformation in a cut during elastic-plastic deformation. Durability Issues, vol 3, pp 37–45
10. Khazhinsky GM (2011) Models of metals deformation and destruction. Naychny Mir, Moscow, 321 p
11. Anand L, Parks DM (2002) Defect–free fatigue. Massachusetts Institute of Technology. Department of Mechanical Engineering. Cambridge, Massachusetts 02139. 2002 Mechanics and Materials II SPRING 2004. Supplementary notes
12. Kopel'man LA (1978) Resistance of welded assemblies to brittle fracture. Mashinostroenie (Leningrad Department), Leningrad, 232 p

Parametric Vibrations Excitation in Cyclic Mechanisms

Iosif I. Vulfson

Abstract With regard to the problems of the dynamics of machines and mechanisms, the dynamic stability conditions are derived for the joint account of parametric and forced vibrations and the impact of nonlinear elastic and dissipative characteristics. It also proposes a new modification of the method of conditional oscillator by which it is possible to analytically study the oscillating systems with rheonomic and nonlinear constraints. For typical vibrational regimes, computer simulation results are presented.

Keywords Vibrations · Mechanisms · Method of conditional oscillator · Nonlinear elastic and dissipative characteristics · Dynamic stability · Parametric resonance

Introduction

The actuators of many technological machines make periodic program movement, which are carried out by so-called cyclic mechanisms (linkages, cams, steppers, etc.). The kinematic characteristics of cyclic mechanisms are not only a source of perturbation, but also form a nonlinear and time-dependent dynamic constraints, which can lead to increase the vibroactivity and even to dynamic instability of vibration systems [1–3]. The relationship between coordinates of the cyclic mechanisms at the "entrance" and "outlet" is described by a nonlinear position function $y = \Pi(\varphi)$. For an ideal mechanism, in which there are no gaps and all links are made completely rigid, $\varphi = \varphi_* = \omega t$ where $\omega = \mathrm{const}$ is the angular velocity of the input link. Let $\varphi = \varphi_* + q$; here q corresponds to the absolute coordinate with the absence of vibrations (absolute dynamic errors). After linearization of the position function in the neighborhood of the programmed motion,

I.I. Vulfson (✉)
Saint Petersburg State University of Industrial Technologies and Design,
Bolshaya Morskaya Str.18, 191186 Saint Petersburg, Russia
e-mail: jvulf@yandex.ru

we have $\Pi(\varphi_* + q) \approx \Pi(\varphi_*) + \Pi'(\varphi_*)q$, where $\Pi' = d\Pi/d\varphi$ is the first geometrical transfer function (velocity analog). Thus, almost without compromising for accuracy, the nonlinear constraint is transformed into a non-stationary one.

The implemented frequency range of parametric resonance is usually far enough away from the most dangerous main parametric resonance; the higher-order resonances are suppressed even at low dissipation. However, in modern technological machines and automatic lines, there are cases when the programmed motion contains high-frequency components. Furthermore, during a kinematic cycle may occur connection and disconnection of some mechanisms or change the mass of moving objects. Then the inertial and elastic characteristics may contain not only low frequency, but also high-frequency, components. In such cases, we are faced with the problem of suppression of parametric resonance with a polyharmonic nature of parametric excitation. Practical methods for identifying areas of dynamic instability are usually based either on various modifications of the method of a small parameter and other asymptotic methods, or on numerical methods [4–7].

The procedure for solving such problems is far from elementary, especially if we consider not only a simplified reference model with one degree of freedom and single-frequency parametric excitation, but the real oscillatory system of modern machines and mechanisms, in which the dynamic model and parametric excitation have a complex structure. The problem is even more complicated when nonlinear characteristics should be taken into account. As the basis, the following factors should be considered:

- The variability of inertial and elastic characteristics, which in zones of parametric resonance can disrupt the dynamic stability conditions;
- The presence of fast and slow components of the position functions and forces that, by taking into account the nonlinear dissipative forces, affect the thresholds of parameter's depth pulsation;
- Interaction of forced and parametric oscillations;
- Interrelationships of rheonomic and nonlinear constraints.

In the article, the problem is solved on the basis of a new modification of the method of conditional oscillator [1, 3, 8] that, in this class of problems, enables one to avoid a number of problems arising when using the traditional methods.

Conditions of Dynamic Stability

Dynamic models depicting oscillatory systems with cyclic mechanisms are very diverse [1–3], so here we restrict the analysis to the following differential equation of the general form that enables one to describe the problem just mentioned:

$$J_1\left(1+\mu\,\Pi_*'^2\right)\ddot{q} + R(q,\dot{q}) + 2\mu J_1\Pi_*'\Pi_*''\omega\,\dot{q} + c_1\left(1+\zeta\,\Pi_*'^2\right)K(q)$$
$$= M(t)\Pi_*' - \mu J_1\Pi_*'\Pi_*''\omega^2. \tag{1}$$

Here $a(\varphi_*) = J_1\left(1+\mu\Pi_*'^2\right)$; $c(\varphi_*,q) = c_1\left(1+\zeta\Pi_*'^2\right)K(q)$ are reduced moments of inertia and rigidity coefficient, $K(q)$ is a nonlinear function; $\mu = J_2/J_1$, $\zeta = c_2/c_1$, where J_i, c_i are the moments of inertia and stiffness coefficients of the input and output units; $R(q,\dot{q})$ is the positional dissipative force corresponding to the scattering coefficient ψ (see below); $M(\varphi_*)$ is an external torque applied to the output member; $\Pi_*' = \Pi'(\varphi_*)$; $\Pi_*'' = \Pi''(\varphi_*)$; $()' = d/d\varphi_*$.

Temporarily in Eq. (1), we exclude from consideration the nonlinear terms. Then, the corresponding homogeneous differential equation can be represented in the form:

$$a(t)\ddot{q} + b(t)\dot{q} + c(t)q = 0. \tag{2}$$

Based on the method for a conditional oscillator, the solution of Eq. (2) is [1–3, 8]:

$$q = A_0\exp\left[-\delta_0\int_0^t\Omega(u)du\right]\sqrt{\frac{a(0)\Omega(0)}{a(t)\Omega(t)}}\sin\left[\int_0^t\Omega(u)du+\alpha\right]. \tag{3}$$

Here, $\delta_0 = \psi/(4\pi)$ is a dissipative factor; ψ is the scattering coefficient; A_0, α are determined by the initial conditions.

The function and the variable "natural" frequency $p(t) = \sqrt{c(t)/a(t)}$ in Eq. (3) are related by the following equation:

$$\ddot{z} - 0.5\dot{z}^2 + 2\Omega_*^2e^{2z} = 2p^2(t), \tag{4}$$

where $z = \ln(\Omega/\Omega_*)$, Ω_* is an arbitrary parameter with frequency dimension, playing the role of a normalizing factor.

The differential equation (Eq. 4) corresponds to a fictitious oscillating system with "hard" nonlinear characteristics, which is called the conditional oscillator. The role of the driving force here plays the function that is proportional to the square of the "natural" frequency. It is enough to have a particular solution of this equation to convert Eq. (3) into the calculation dependence describing the oscillatory process. With a slow change of the parameters, $p = p_0 \approx \Omega$. Then the solution of Eq. (4) coincides with a WKB approximation of the first order [9]. Let, $\Pi' = \Pi_0' + \Pi_v'$, where the terms correspond to slow and fast movements. For definiteness, we will take $\Pi'(\varphi) = h[\sin\varphi + \varepsilon\sin(v\varphi + \gamma)]$, where the first term corresponds to the "slow", and the second to the "fast" harmonic with the frequency v and depth of pulsation ε. (Here and below an asterisk by φ_* is omitted.). Now, instead of a fixed constant the function Ω_*, we should use the function $p_0(t)$ that corresponds to the

slowly varying component of the "natural" frequency $p(t) = \sqrt{c(t)/a(t)}$. On the basis of Eqs. (3) and (4), we determine the change of the oscillation amplitude:

$$A(\varphi) = A_0\sqrt{a(0)/a(\varphi)}\exp\left[-\delta\int_0^\varphi p_0(\varphi)d\varphi - 0.5[z(\varphi) - z(0)]\right], \qquad (5)$$

Typically, sufficient accuracy for engineering applications is achieved through linearization of Eq. (4) by changing from the exponential term to the first two terms of the Taylor series [3, 4]:

$$\ddot{z} + 4p_0^2(t)z = 2\left[p^2(t) - p_0^2(t)\right]. \qquad (6)$$

Now, a slow varying function is retained as a parameter on the left-hand side of the equation. The resonance of a linearized conditional oscillator corresponds to the main parametric resonance that arises in the vicinity of the "floating" frequency $2p_0$. The particular solution of Eq. (6) has the form of a modified Duhamel's integral:

$$z = \frac{1}{\sqrt{p_0(\varphi)}}\int_0^\varphi \frac{\left[p(u)^2 - p_0(u)^2\right]}{\sqrt{p_0(u)}}\sin\left[2\int_u^\varphi p_0(\tau)d\tau\right]du. \qquad (7)$$

When performing engineering calculations, we can also use the numerical solution of the nonlinear equation (Eq. 4).

Note that the analytical approach is necessary to a greater extent in this case for the qualitative evaluation and by the optimization of parameters at dynamic synthesis. On the basis of Eq. (7) at the joint account of the fast and slow changes of parameters, we get—with some margin—a laconic condition of dynamic stability in the area of the main parametric resonance:

$$\vartheta > \vartheta^* = -0.5\Delta z/p_*, \qquad (8)$$

where, $\Delta z = z(2\pi) - z(0)$; $p_* = (2\pi)^{-1}\int_0^{2\pi} p_0(\varphi)\,d\varphi$; $\vartheta = 0.5\psi$ is the logarithmic decrement.

As is evident from Eq. (5), the condition Eq. (8) excludes growth of the amplitude when $t \to \infty$, but that opportunity can be retained inside of the kinematic cycle due to the variability of the inertia parameter $a = a(\varphi)$. Because $a(\varphi) = a(2\pi)$, the work of this component for the period of rotation of the input link is equal to zero, which is inherent for gyroscopic forces. However, within a cycle, there may be a zone when $dA/d\varphi > 0$, which often results in the essential dynamic errors in the program's motion [10, 11]. The condition $dA/d\varphi < 0$ can be written as:

$$\vartheta > \vartheta^* = \pi p_0^{-1}|(a'/a + z')| = \pi p_0^{-1}|a'/a + p'/p - p_0'/p_0|. \qquad (9)$$

Change of "natural"
frequency: *1*—$\mu = 0.25$;
$\zeta = 0$; *2*—$\mu = 0$; $\zeta = 0.25$;
*3*—$\mu = \zeta = 0.25$
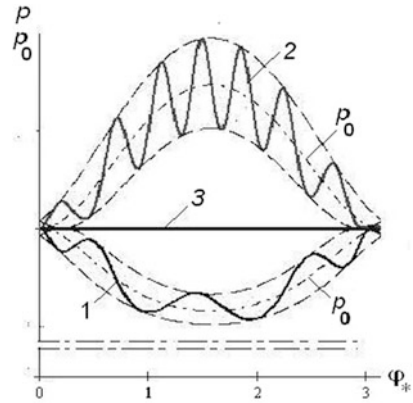
Note that the inequality Eq. (9) coincides with the results obtained on the basis of the direct Lyapunov method, which establishes a sufficient condition for dynamic stability [1–3]. A very effective way to eliminate the possibility of excitation of parametric resonance is to introduce quasi-stationary conditions [10, 11]. With the implementation of these conditions, in spite of the variability of the parameters of the system, the "natural" frequency in the first approximation remains constant, and there is no energy growth during the period of the kinematic cycle. According to Eq. (1), when $\mu = \zeta$, the conditions of quasi-stationarity are satisfied. Then, on the basis of Eq. (7), $z \equiv 0$, and should meet the condition Eq. (8), which excludes the excitation of the main parametric resonance. In Fig. 1, graphs $p(\varphi_*), p_0(\varphi_*)$ for a number of typical cases are shown with $h = 1; \varepsilon = 0.2; \nu = 7$.

Nonlinear Dissipative Forces

The nonlinear positional dissipative force can be represented as $R(q, \dot{q}) = -|R|u(|\dot{q}| - |\mathrm{v}|)\mathrm{sign}\dot{q}$, where v is the velocity that is associated with the additional movement ("aliens" harmonics, transportation motion, etc.); u is the unit function ($u = 1$ if $|\dot{q}| > |\mathrm{v}|$ and $u = 0$ if $|\dot{q}| < |\mathrm{v}|$). According to the conditions in Eqs. (8) and (9), the dissipative forces were taken into account on the basis of the given value ψ (or ϑ, δ). However, these values need to be corrected, because at the same time the effective values of the dissipative characteristics depend on forced oscillations and can be significantly reduced: $\psi_* = \sigma(\lambda)\psi$. The correction factor defined by the relationship $\sigma = \lambda(0.4 + 0.5\lambda)/(1 + 0.5\lambda^2)$, where $\lambda = \max\dot{q}/\max \mathrm{v}$ [1–3, 12].

The physical meaning of the correction is associated with the fact that we usually have limited initial information from the experimental data in the form of some integral dissipative characteristics, such as scattering coefficient ψ or logarithmic decrement ϑ, which are obtained by the harmonic vibrations for some standard
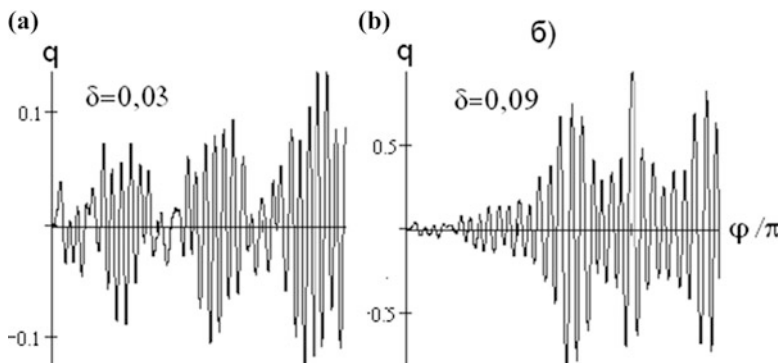
Fig. 2 The analysis of dissipative parameter's correction: **a** without correction dissipative parameters, and **b** with correction

models. Thus, "harmonic linearization" of dissipative forces is carried out by experimental techniques. In this case, the obtained information on the dissipative properties of the system reflects them only to the extent that harmonically linearized dissipative force corresponds to the actual resistance. Naturally, with multi-frequency oscillations, this correspondence is violated, and, in some cases, significantly so. For small values of λ, the function $\sigma(\lambda)$ is close to linear, i.e., proportional to the amplitude. This, in particular, is used for vibration linearization of dry friction.

Figure 2 shows graphs obtained by computer simulation of Eq. (1) with a threshold value corresponding to the boundary of a dynamic instability for the two cases: without correction dissipative parameters (Fig. 2a) and with correction that excited due forced vibrations (Fig. 2b). As follows from the analysis of the graphs, to perform dynamic stability conditions the original value of the dissipative parameter $\delta = \vartheta/(2\pi)$ grows by a factor of three. Furthermore, this increases the intensity of the parametric excitation.

Interaction of Forced and Parametric Oscillations

In the case of the coincidence of the harmonic frequency of the driving force with the frequency of the main parametric resonance, the amplitude is inversely proportional to function $|\vartheta - \vartheta^* \cos 2\Delta\gamma|$, where $\Delta\gamma$ is the phase shift between the forced and the parametric excitation [1–3]. Thus, the resonant amplitude corresponds to some vibration system with altered levels of dissipation (Fig. 3).

We investigate three resonance modes for a given value of logarithmic decrement $\vartheta = 0.39$. The regime 1 corresponds to forced vibrations, in which the dynamic factor (dimensionless amplitude-frequency characteristic) $\kappa = \pi/\vartheta = 8.05$. In regimes 2 and 3, in addition to the forced excitation, parametric
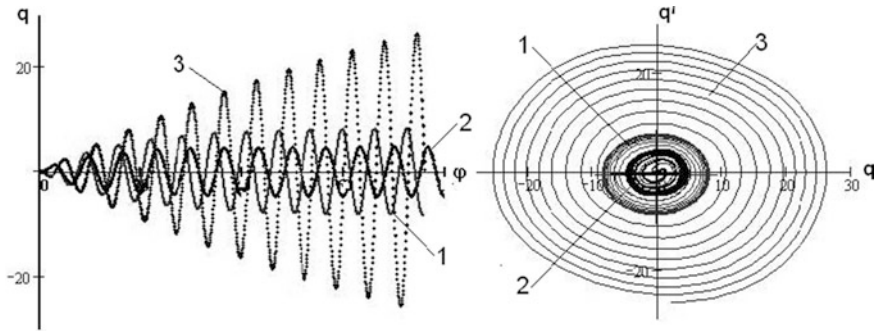
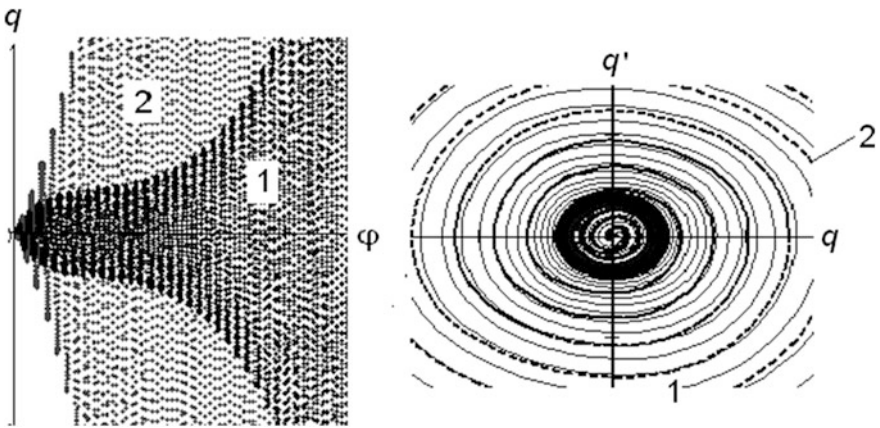**Fig. 3** The impact of the phase shift on the resonant mode: *1*—regime 1; *2*—regime 2; *3*—regime 3

Fig. 4 Impact on the resonance at $\vartheta^* < \vartheta < 2\vartheta^*$: *1*—$\Delta\gamma = \pi/2$; *2*—$\Delta\gamma = 0$

excitation takes place with the depth of pulsations $\varepsilon = 0.2$ and $\Delta\gamma = \pi/2; 0$ (curves 2 and 3). According to Eq. (9), $\vartheta^* = 0.31$; then, for the regime 2, we have $\vartheta_{pe3} = \vartheta_{max} = 0.7$, and for regime 3—$\vartheta_{pe3} = \vartheta_{min} = 0.08 < \vartheta^*$. Of course, if $\vartheta_{pe3} < \vartheta^*$, the issue of the maximum amplitude is meaningless, since in this case the system is dynamically unstable. When $\vartheta^* < \vartheta < 2\vartheta^*$, the phase shift $\Delta\gamma$ significantly impacts the growth rate of the resonance amplitude (Fig. 4). The chart $q(\varphi)$ clearly shows that a relatively large effective value ϑ_{max} (curve 1) is implemented at the initial stage of the forced resonance mode, which is then transformed to the exponential increase of amplitude that is typical for parametric resonance. When ϑ_{min} (curve 2), the phase of forced excitation is virtually invisible.

Now, we shall perform the correction of the results obtained with the joint accounting of forced and parametric excitation and also of high-frequency effects on the resonant vibrations. When taking into account the received corrected dissipative

parameters, it can be shown that, by the most unfavorable ratio of the resonance phase, the maximum amplitude in this case is defined as $A^* = \chi A$. Here A is the amplitude in the absence of the high-frequency excitation; χ is the coefficient of the increasing resonance amplitude, which is defined as:

$$\chi = 0.5 \left[1 + sL + \sqrt{(1 + sL)^2 + 4s(1 - L)} \right] / (1 - L),$$

where $L = 2\pi\varepsilon/\vartheta, s = \sigma^{-1}(\lambda) - 1$.

The parameters L reflects the influence of parametric excitation on the driving force, and the parameter s is the influence of the high-frequency component. If $L \to 1$, the conditions of dynamic stability are violated, so $\chi \to \infty$, and it is not dependent on s.

Interrelation of Rheonomic and Nonlinear Constraints

Next, take into account the non-linearity of elastic characteristic. Equation (1) may be written as:

$$\left(1 + \mu \Pi_0'^2\right)\ddot{q} + f(q, \dot{q}) + k^2 \left(1 + \zeta \Pi_0'^2\right)K(q) = w(t) - \mu \omega^2 \Pi_*' \Pi_*'', \qquad (10)$$

where $f(q, \dot{q}) = R(q, \dot{q})/J_1; w(t) = M_* \cos(\Omega t)\Pi_*'/J_1; k = \sqrt{c_1/J_1}; M_*, \Omega$ are the amplitude and frequency of moment applied to the output link.

This vibration system is subject to the biharmonic excitation $\Omega \gg \omega$. In Eq. (10), the gyroscopic force is lowered, because the corresponding work of this component during the period $2\pi/\omega$ is zero. Suppose $\Pi_0' = h \sin\varphi, \Pi_0'' = h \cos\varphi$, and a nonlinear restoring force corresponds to the coupling with a cubic elastic characteristic. Then, $K(q) = q(1 + \beta q^2)$ and the "normal" frequency after the harmonic linearization is:

$$p(\varphi, A) = k\sqrt{\left(1 + \zeta \Pi_0'^2\right)((1 + 0,75\beta A^2)/\left(1 + \mu \Pi_0'^2\right)}. \qquad (11)$$

For the analytical solution, the method of a conditional oscillator was used in combination with the harmonic linearization method. In Fig. 5a is shown the significant change of a conditional oscillator's phase portraits taking into account the nonlinear elastic characteristic. That leads to an increase of the pulsation of "natural" frequency p (Fig. 5b), and consequently, to a change in the threshold conditions of parametric excitation. In this case, the amplitude of the forced oscillations significantly increases even if the dynamic stability conditions are implemented (Fig. 5c). It should also be noted that, by low dissipation, the transient process up to the attainment of a steady process results in the loss of stability and is drawn into a
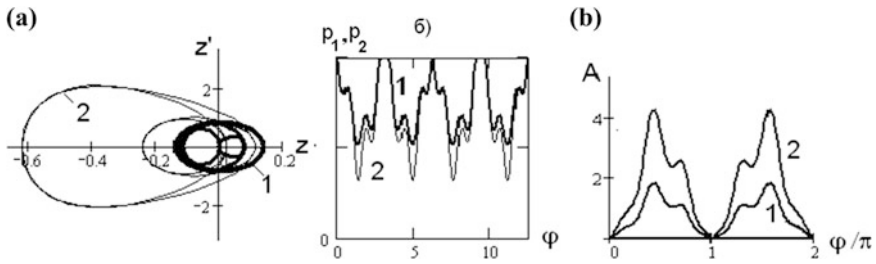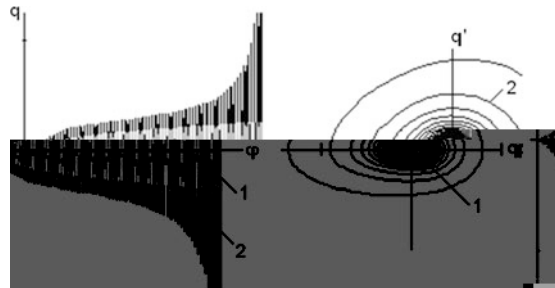
Fig. 5 The effect of nonlinearities: *1*—β = 0; *2*—β = −0.25

Fig. 6 To analyze the effect of tightening: *1*—δ = 0.036; *2*—δ = 0.07

zone with increased values of the amplitudes *A* (Fig. 6). A similar pattern is observed at the phase shift between the forced and parametric excitations.

For a clearer identification of the dynamic effects associated with the amplitude modulation of the driving force, we assume in Eq. (1) that $\mu = \zeta$, which corresponds to the quasi-stationary condition (see above). Then the time-dependent constraint in an explicit form is absent and, at first glance, parametric effects do not expect. But, the graphs in Fig. 7 show that regimes close to the parametric excitation with the nonlinear elastic characteristics lead to the local violations of dynamic stability, which alternates with break-downs of vibrations, creating an intense beat regime.

In connection with the investigated issue, great interest is shown in the dynamic effect that was discovered by M.Z. Kolovskiy. This effect consists of the fact that, under certain conditions, a low-frequency beat's resonance occurs, which arises from the amplitude modulation of high-frequency vibrations [13]. Applications in machines dynamics of this effect are partially considered in [14]. It can be shown that the nonlinear component of the restoring force is described by the dependence:

$$K(q) = \left[1 + 1.5\beta\,h\left(\omega^2/\Omega^2\right)\sin^2\varphi + \beta q^2\right]q.$$

The beats result in the pulsation of the natural frequency $p(A)$, which in turn, creates a situation that is close to the parametric excitation.
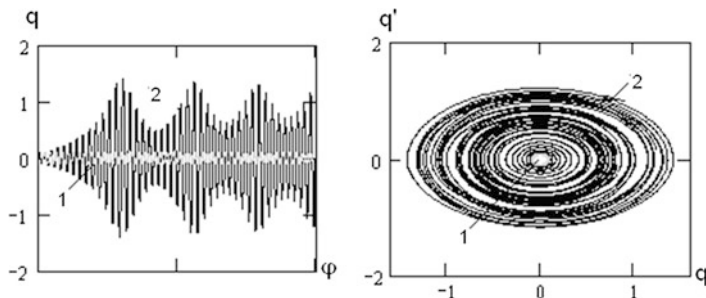
Fig. 7 A comparison of the vibrational modes: *1*—β = 0; *2*—β = −0.25

Conclusion

In this article, we have further developed methods for the solution of a number of nonlinear dynamics problems of mechanisms and machines. In particular, we have examined proposed and investigated ways to reduce vibrational activity by suppressing some dynamic effects arising from the joint influence of parametric and forced vibrations for both slow and fast movements.

References

1. Vulfson II (1990) Vibrations in machines with cyclic action mechanisms. Mashinostroenie, Leningrad (in Russian)
2. Vulfson I (2015) Dynamics of cyclic machines. Springer, London (Trans. from Russian, Politechnika, 2013)
3. Vulfson II (2013) Vibrations excitation in cyclic mechanisms due to energy generated in nonstationary constraints. Adv Mech Eng (Ed. A. Evgrafov). Springer, New York, pp 117–128
4. Bogoliubov NN, Mitropol'sky JA (1958) Asymptotic methods in the theory of nonlinear oscillations. Gordon & Breach, New York
5. Mitropol'sky JA (1964) Problems of the asymptotic theory of nonstationary vibrations. Nauka, Moscow (in Russian)
6. Bolotin VV (1956) Dynamic stability of elastic systems. Gostekhteoretizdat, Moscow (in Russian)
7. Schmidt G (1978) Parametric oscillations. Mir, Moscow (in Russian)
8. Vulfson II (1969) Oscillations of systems with parameters depending on the time. Prikladnaya matematika i mechanika 33(2):331–337 (in Russian)
9. Freman N, Freman P (1967) JWKB-approximation. North Holland Publ. Comp, Amsterdam
10. Vulfson II (2015) Quasistationarity of dynamic modes in cyclic mechanisms forming rheonomic oscillating systems with lattice structure. J Mach Manuf Reliab 44(4):312–318
11. Vulfson II (2015). To the problem of quasi-stationary dynamic characteristics of cyclic mechanisms. Theory Mech Mach (1):6–15 (in Russian)
12. Vulfson II (2008) Some nonlinear effects of machine dynamics. J Vibroeng 10(4):442–450

13. Kolovsky MZ (1963) On the effect of high-frequency of perturbations on resonant oscillations in a nonlinear system. In: Dynamics and strength of machines. Proceedings of the LPI. No 226. Mashgiz, Leningrad, pp 7–17 (in Russian)
14. Vulfson II (2005) Nonlinear resonant oscillations of a drive at the amplitude-modulation frequency of high-frequency excitation. J Mach Manuf Reliab (6):13–17

Theoretical and Practical Conditions of Bennett Mechanism Workability

Munir Gumerovich Yarullin and Fanil Fargatovich Khabibullin

Abstract The paper investigates the theoretical and practical conditions of Bennett mechanism workability. The technology of specific links' design is developed, which enable that the mechanism's cranks do not interfere with other components. The design features of "zero" and "nonzero" links are investigated. The paper analyzes the full-reverse rotation ability of the studied devices based on the Bennett parallelogram and the anti-parallelogram modifications. Practical conditions for full-reverse rotation of this mechanism are formulated.

Keywords Bennett mechanism · Full rotation conditions · "Zero" link · "Non-zero" link

Introduction

Currently, design features of the Bennett's linkage [1–10] attract great interest. A series of attempts, which can be named "bennettiana", to explore the phenomenon and to explain mechanism operability has become apparent.

The mechanism comprises four links (see Fig. 1a) connected in series with four rotary pairs. The mechanism is considered "paradoxical" because of the fact that the mechanism's freedom is equal to minus two, so that the construction should be supposedly fixed so:
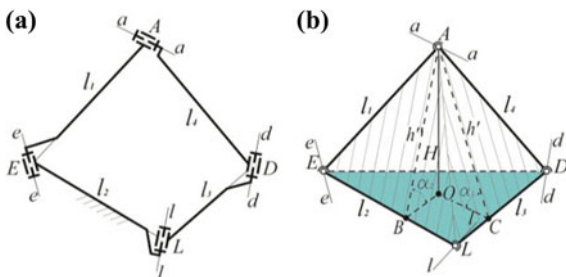
$$W = 6 \cdot (m - 1) - 5p_1 = 6(4 - 1) - 5 \cdot 4 = -2. \tag{1}$$

M.G. Yarullin (✉) · F.F. Khabibullin
Kazan National Research Technical University named after A.N. Tupolev,
Kazan, Russia
e-mail: Yarullinmg@yahoo.com

F.F. Khabibullin
e-mail: fanil_arsk@mail.ru

Fig. 1 Structural diagram of
a Bennett's linkage
b four-links with ball joints

However, the Bennett's linkage is movable, and its freedom is determined by additional conditions that are imposed on the mechanism.

First, let's consider simple and a reliably scrollable, spatial, four-link mechanism, with ball joints and equal-length opposite links (Fig. 1b). The degree of freedom of the mechanism can be determined by the formula of Somov–Malyshev:

$$W = 6(n-1) - 5p_1 - 4p_2 - 3p_3 - 4p_2 - 1p_5, \qquad (2)$$

where n *is* the number of links,
W *is* the degrees of freedom,
p_5, p_4, p_3, p_2, p_1 are the kinematic number of 1–5 classes.

$$W = 6(4-1) - 5 \cdot 0 - 4 \cdot 0 - 3 \cdot 4 - 2 \cdot 0 - 1 \cdot 0 = 6. \qquad (3)$$

This means that the mechanism has five local mobilities:

1) links EA, AD, and DL can rotate around lines EA, AD, and DL respectively (three mobilities)

2) links EA and AD together can rotate around ED line (fourth mobility)

3) links AD and DL together can rotate around AL line (fifth mobility).

In addition the mechanism acquires the general mobility when rotating EA link. But, such kind of mechanism can not be used in practice.

We shall verify the theoretical conditions for existence of two cranks. Let the links occupy the position in space where diagonals DE and LA are of the same length $(DE = LA = L_0)$ (Fig. 1b). We get the triangular pyramid *LDAE* with opposite edges identical in length, equal to l_1, l_2, and ribs L_0. The surface area of the pyramid consists of triangles with sides l_1 *and* l_2, and edges L_0. Let's assume that the area of each of the triangles is equal to K. We drop a perpendicular from the peak A to the EL edge. The length of the perpendicular $h'' = 2K/l_2$. If we designate the angle of inclination of this perpendicular to the plane *LAE through* α_2, then the height, dropped from the top A onto this plane, may be calculated as:

$$H = h'' \sin \alpha_2 = \frac{1}{l_2} \cdot 2K \sin \alpha_2, \tag{4}$$

Similarly, let's take h' as the length of the perpendicular, dropped from the same point onto the *LD edge*

$$h' = 2K/l_1$$

Hence, in this case, denoting the angle of inclination of the perpendicular h' to the plane *LAE through* α_1, we obtain the similar formula:

$$H = h' \sin \alpha_1 = \frac{1}{l_1} \cdot 2K \sin \alpha_1. \tag{5}$$

From the expressions in Eqs. (4) and (5), we obtain the dependence of length and rotation angles of the rod from the crank:

$$l_1/\sin \alpha_1 = l_2/\sin \alpha_2. \tag{6}$$

We replace the three-degree-of-freedom spherical hinges for one-degree-of-freedom rotatory hinges. At that, the axis of the rotational kinematic pairs we describe strictly as follows:

– the axis *e-e is* parallel to *AC*;
– the axis *a-a is* parallel to *OC*;
– the axis *d-d* is parallel to *AB*;
– the axis *l-l is* parallel to *BO*.

The obtained mechanism is the Bennett linkage, the degree of freedom of which in accordance with Eq. (1) is equal to minus two.

Despite the negative value of the degree of freedom of the mechanism, under certain conditions this mechanism can be rotated [11]. The theoretical conditions of Bennett linkage rotation are:

(1) **The opposing links of the mechanism are the same**:

(a) the length of the shortest distances of opposing units are equal, i.e., $l_1 = l_3$ are the lengths of the shortest distances between hinges of driving and driven cranks and $l_2 = l_4$ *are* the lengths of the shortest distances between axes of hinges of the connecting rod and the frame;

(b) the geometrical axes of hinges of opposing links are deployed relative to each other at equal angles, i.e., $\alpha_1 = \alpha_3$ are the angles of crossings of hinges of the driving and driven cranks, $\alpha_2 = \alpha_4$ are the angles of crossing axes of hinges of the connecting rod and the frame.

(2) **The edges of the shortest distances of the neighboring links coincide**.
(3) **The following condition is satisfied**:

$$\frac{l_1}{l_2} = \pm \frac{\sin \alpha_1}{\sin \alpha_2}. \tag{7}$$

Mobility of the Bennett linkage has been theoretically proven on animated models [12, 13]. But there is a sufficiently small quantity of practically constructed devices and machines based on this linkage. The devices created by the scientists of the Kazan School of Mechanics [14–16] are the exception. The reason for this is that the Bennett linkage has two cranks, and the full-motion freedom of these cranks is provided only in the manufacture of the mechanism links in a special way. The key point of this method is that, in order to provide the full-motion ability of the mechanism, some of its links must be "non-zero". Existing models of the Bennett linkage, constructed by other researchers and made without the "non-zero" links, do not possess the full-motion ability of their cranks: the mechanism are superimposed on one another and prevent the full-turn motion (Fig. 4b).

This article is devoted to the research conducted on the creation of full-space specimens of the devices based on Bennett linkage through development of "non-zero" links to ensure its full-turn motion.

The Design Features of "Zero" and "Non-zero" Links of the Bennett Mechanism

(1) Let's consider the method of obtaining the construction of a "zero" connecting rod and frame.

The structural parameters of the connecting rod and the frame of the Bennett linkage are:

$l_2 = l_4$—the shortest distance between the hinges' axes (Fig. 2).
$a_2 = a_4$—angles of crossing of axes of links hinges (Fig. 2).

Figure 2a shows the model of "zero" connecting rod in three projections. Here, the shortest distance between the axes of the hinges of this link coincides with the symmetry axis of the connecting rod. AD line AD is the shortest distance between the link and its symmetry axis.

This link has two important structural parameters: the first—the specified center distance, the second—the angle of crossing of the axes. Fig. '2b' shows the "non-zero" link derived on the basis of the "zero" link, by the method of biasing the hinges centers of the "zero" connecting rod to the distance of $A_0''A''$ and $D_0'D'$, respectively. Thus, the obtained "non-zero" link has no geometric symmetry axis, and the shortest distance between the axes of the hinges of the connecting rod is outside the body. Dimensions of sections $A_0''A'' = h''$, $D_0'D' = h'$ are determined
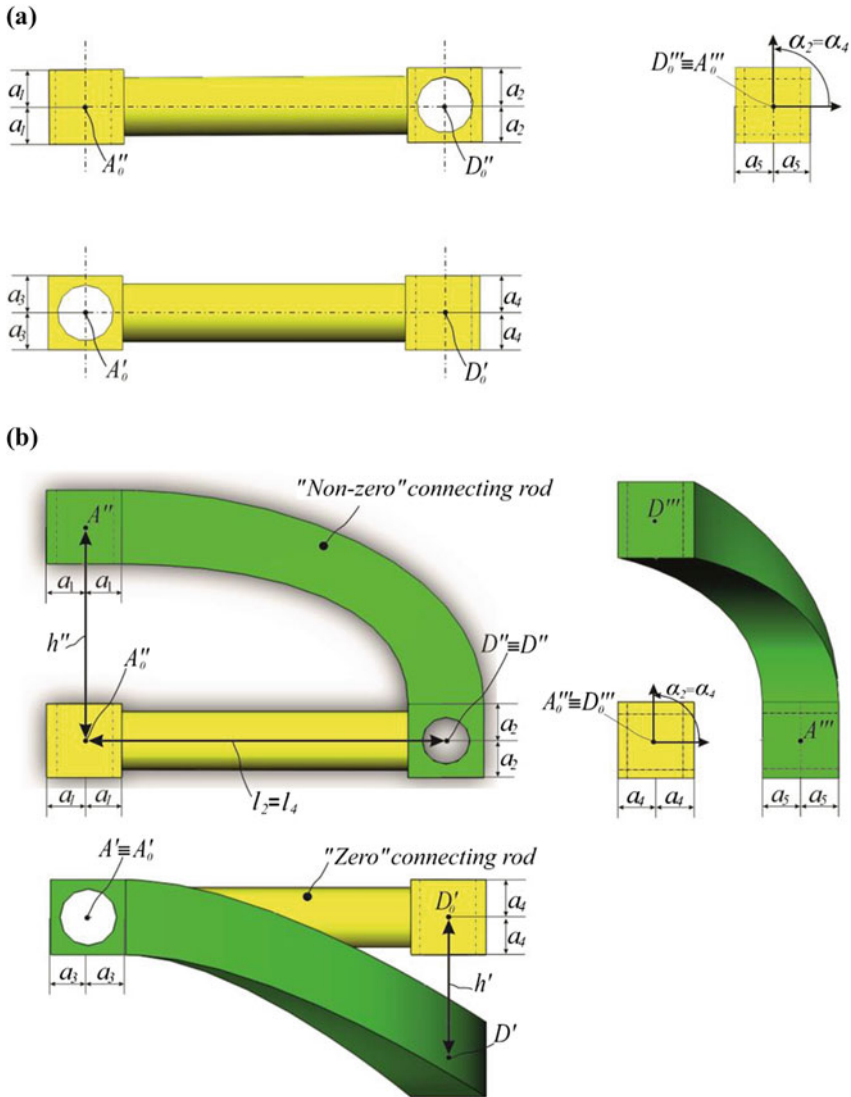
Fig. 2 Link of the Bennett mechanism: **a** "zero" connecting rod, **b** relationship between "zero" and "non-zero" links

freely by a constructor to provide rotation of the mechanism depending on dimensions of the other links to avoid imposition of mechanism construction links.

Figure 2b in three projections shows the relationship between "zero" and "non-zero" links. The figure shows that the shortest distance and the angle of the axes of hinges are absolutely the same, although the actual bodies of the links are different.

The crossing angle between the axes of hinges of the connecting rod will be considered positive if the alignment of the axis of the hinge, remotest from the observer along the shortest distance, is executed contra-clockwise. The link opposite to the connecting rod is taken as the frame of the Bennett mechanism. Generally, the frame is the "non-zero" link. For ease of design and to simplify the manufacturing process, the angle of crossing of axes of hinges of the connecting rod and frame are usually taken to be 90°.

(2) Let's consider the method of obtaining the construction of the "non-zero" cranks. Structural parameters of driving and driven cranks are similar:

$l_1 = l_3$—the shortest distance between the hinge axes (Fig. 3).
$\alpha_1 = \alpha$—angles of crossing of hinge centers of these links (Fig. 3).
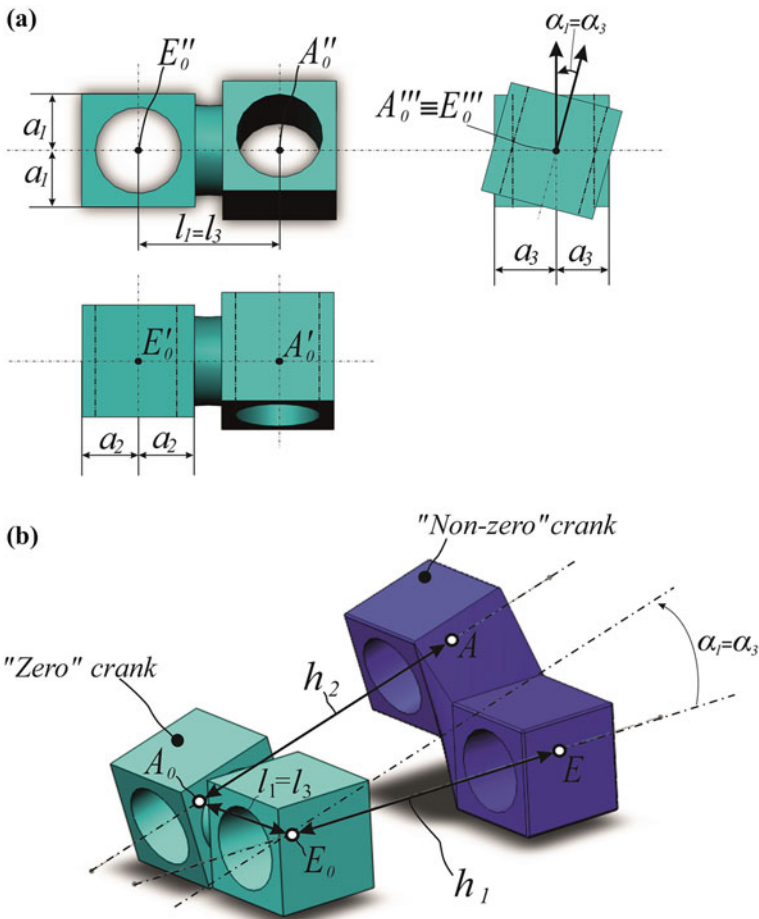
Fig. 3 Link of the Bennett mechanism: **a** the "zero" crank, **b** the "non-zero" link in relationship with the "zero" crank

In these three projections (Fig. 3a), the "zero" crank is illustrated. Figure 3b shows the "non-zero" crank in relation to the "zero" crank in axonometric perspective: heads of hinges of the "non-zero" crank are offset for the distance h_1 and h_2, respectively. Thus, in the resulting "non-zero" crank, the shortest distance between the axes of hinges $l_1 = l_3$ is outside the body.

Examples of the Existing Devices Based on the Bennett Mechanism with "Zero" and "Non-zero" Links

The photo of the current model with "zero" driving and driven cranks is shown (Fig. 4a). The connecting rod and the frame are "non-zero" ($l_2 = l_4, \alpha_2 = \alpha_4 = 90°$).

The photo of the device for washing the equipment on the basis of the Bennett mechanism is represented at Fig. 5a [15, 16]. Driving and driven links are "non-zero"; the connecting rod, used as the container for inertia washing, is "zero". The mechanism frame is the "non-zero" link with the structural parameters of the connecting rod.

Figure 5b is a photo of the existing model [14, 17, 18] of the two-degree-of-freedom disintegrator, developed on the basis of the patent of the RF № 2581487. The drive mechanisms of this parallelogram (upper drive) and the anti-parallelogram (lower drive) of the Bennett linkage.

Here, in connection with the need to provide full-turn rotation of the drives, all links are made "non-zero". Such a design of the Bennett linkage enables providing real full-turn motion without overlaps and jamming [https://www.youtube.com/watch?v=vTu0r9o81KY].
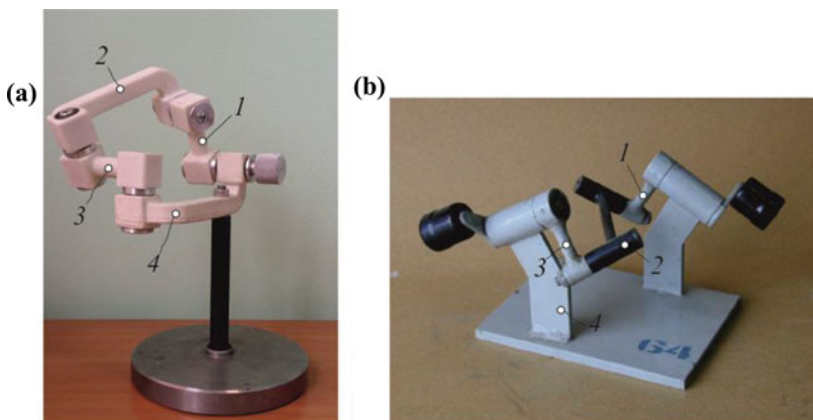
Fig. 4 Photos of the Bennett mechanism model: *1* driving crank; *2* connecting rod; *3* driven crank; *4* frame; **a** mechanism with "non-zero" links, **b** mechanism with "zero" links (A.N. Ermak)
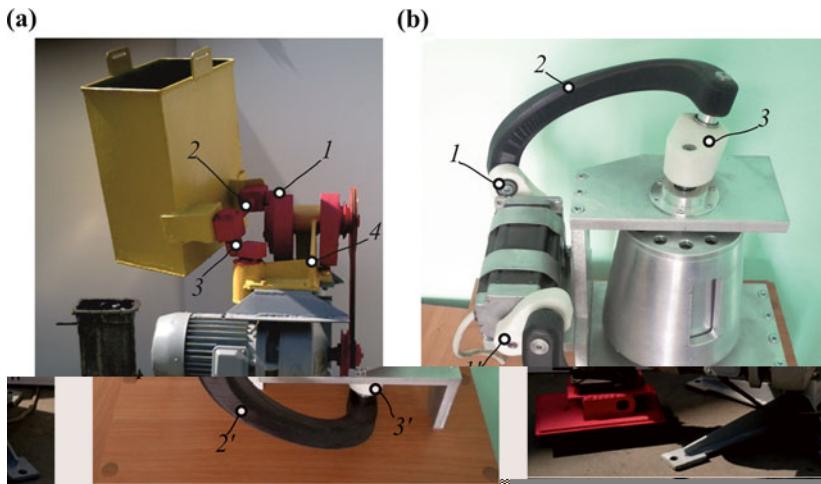
Fig. 5 Devices based on the Bennett linkage, *1* driving crank; *2* connecting rod; *3* driven crank; *4* frame; **a** device for inertial washing of the products, **b** uneven crushing disintegrator

Conclusion

(1) Theoretical conditions of full-turn motion of the Bennett mechanism are the following:

  – opposing links of the Bennett linkage are identical: $l_1 = l_3, l_2 = l_4,$ $\alpha_1 = \alpha_3, \alpha_2 = \alpha_4$;
  – the ends of the shortest distances of neighboring links coincide;
  – the proportion is realized:

$$\frac{l_1}{l_2} = \pm \frac{\sin \alpha_1}{\sin \alpha_2}.$$

(2) The practical condition of the full-turn motion of the Bennett linkage is the fact that at least two links should be "non-zero", for example:

  (a) two cranks (driving and driven) are designed as "non-zero"; the connecting rod and the frame shall be "zero" (Fig. 4a);
  (b) the connecting rod is "zero"; the two cranks and frame are "non-zero" (Fig. 5a);
  (c) all four of the mechanism links (two cranks, connecting rod, and the frame are "non-zero" (Fig. 5b).

References

1. Dvornikov LT (2009) Non-traditional arguments about the existence of Bennett mechanism. In: Theory mechanisms and machines, vol 1(13), pp 5–10 (in Russian)
2. Ioffe ML (2016) On the choice of parameters of the Bennett mechanism and modelling it in MATLAB, news of higher schools. Engineering 2(671):11–19
3. Oliveira AA, Carvalho JCM (2007) Modeling of the Bennett's linkage as leg of a mobile robot. In: 12th IFToMM world congress, 2007, pp 398–402
4. Galiullin RR, Sachenkov OA, Khasanov RF, Andreev PS (2015) Evaluation of external fixation device stiffness for rotary osteotomy. Int J Appl Eng Res 10(24):44855–44860
5. Andreev PS, Konoplev YG, Sachenkov OA, Hasanov RF, Yashina IV (2015) Mathematical modeling of rotary flexion osteotomy. In: Scientific and technical Vestnik of Povolzhye, vol 5, pp 18–21 (in Russian)
6. Perez A, McCarthy JM (2000) Dimensional synthesis of Bennett linkages. In: Proceedings of the ASME. Design engineering technical conferences, 2000, Baltimore, Maryland, USA, paper DETC2000/MECH-14069
7. Evgrafov AN, Petrov GN (2013) Calculation of geometric and kinematic parameters of the spatial linkage with redundant links. In: Problems of mechanical engineering and machine reliability, vol 3, pp 3–8 (in Russian)
8. Liu J, Yu Y, Huang Z, Huang X (2013) General order principle for multi-Bennett linkages. Chin J Mech Eng 26(2):275–281
9. Yarullin MG, Mingazov MR, Galiullin IA (2015) A new classification table for spatial nR linkages. In: TrC-IFToMM symposium on theory of machines and mechanisms, pp 1–7
10. Evgrafov AN, Petrov GN (2016) Drive selection of multidirectional mechanism with excess inputs. Advances in mechanical engineering. Lecture notes in mechanical engineering, pp 31–39
11. Yarullin MG, Mingazov MR, Galiullin IA (2016) Historical review of studies of spatial nR linkages. Int Rev Mech Eng 10(5):348–356
12. Yarullin MG, Mingazov MR (2016) Structural modifications synthesis of Bennett mechanism. Advances in mechanical engineering. Lecture notes in mechanical engineering, pp 9–16
13. Yarullin MG, Mingazov MR (2014) Kinematics of the characteristic points of the working parts of the spatial 4R-mechanism as an activator of mixing processes. In: Vestnik of Izhevsk State Technical University named after M.T. Kalshnikov, vol 3(63). Publishing House of the Izhevsk State Technical University named after M.T. Kalashnikov, Izhevsk, pp 34–38 (in Russian)
14. Yarullin MG (2002) Intensification of cleaning products in immersion washing machines on the basis of spatial mechanisms: abstract of the thesis of Doctor of Technical Sciences: 05.20.03/M.G. Yarullin. - M.: MSAU, 35 p (in Russian)
15. Yarullin MG, Mudrov AG, Mingazov MR, Galiullin IA (2015) The 1DOF and 2DOF spatial mechanisms with revolute pairs: monograph. KNITU—KAI Press, Kazan, 172 p. ISBN 978-5-7579-2091-7
16. Mudrov AG, Yarullin MG (2014) From the Bennett mechanism to the differential gear. Kazan state university press, Kazan, 92 p
17. Yarullin MG, Mingazov MR, Isyanov IR, Khabibullin FF (2016) Disintegrator of non-uniform crushing. Patent 2581487 Russian Federation, IPC V02S 2/10 (in Russian)
18. Yarullin MG, Khabibullin FF, Isyanov IR (2016) Nonlinear crushing dynamics in two-degree of freedom disintegrator based on the Bennett's linkage. In: Vibroengineering procedia, vol 8, pp 477–482. ISSN 2345-0533

Dislocation-Phonon Mechanism and Interpolation Dependence of Fatigue-Damaged Structural Steel

Vladimir A. Zhukov

Abstract Based on the model of phonons superposition, the correlations between the amplitude of the stress, the equivalent plastic deformation, and the number of cycle fatigue damage are developed. This method possesses the ability to evaluate of various technological options.

Keywords Phonons superposition · Fatigue damage · Equivalent cyclic plastic deformation · Dislocation

Introduction

Testing of materials and metal design elements under cyclic stresses requires significant time and financial costs. Usually, we need to weed out the worst of the possible variants of technological processes and engineering designs using a minimum of experimental data and the accepted criteria. In that case, it is necessary to provide sufficient adequacy of the employed interpolation dependences, which is due primarily to the presence of the single mechanism of deformation and destruction for the compared materials.

According to [1, 2], four areas of metal fatigue may be selected in the range from 1 to 10^{10} cycles of changing the stress: quasi-static plastic deformation (I), elastic-plastic deformation (II), micro-plasticity (III), and nano-plasticity (IV). In the transition region from the micro-plasticity (about 5×10^4 cycles of stress change) to elastic-plastic deformation, the generation of submicroscopic damage of steel is associated with the stress concentration in the top of the dislocations group, which are detained by different micro-structural obstacles [3]. It is established that,

V.A. Zhukov (✉)
Peter the Great Saint-Petersburg Polytechnic University, St. Petersburg, Russia
e-mail: v.zhukoff2011@yandex.ru

in the transition area from micro-plasticity (of the order of several million cycles of stress change) to nano-plasticity, fatigue cracks are formed in consequence of interstices coalescence, which disperse initially at random in the volume of the deformed metal.

In the analysis of damage of metals during cyclic deformation, as a rule, the intermittent nature of the dislocations' movement is not taken into account. However, each jump of the dislocation induces fluctuations at the atomic level. Distribution and interaction of these oscillations are regarded as the process of superposition of quasi-particles phonons. Phonons are Bose particles, and, in contrast to electrons and other Fermi particles, there are no restrictions as to the total number of phonons and the number of phonons in the same quantum condition. The local energy of the superposition of phonons can reach the magnitude under which the stability of the crystal is lost [4].

The energy fluctuations of the phonons of the thermal motion may be the cause of the breaks in the atomic lattice; this idea is used in the thermo-fluctuation damage theory of materials [5, 6]. However, the thermo-fluctuation theory does not consider the possibility of the occurrence of phonons in the process of deformation of the material. The idea of ruptured interatomic bonds, due to phonons superposition during plastic deformation metals, is offered in this paper [7]. We assume that the cyclic movement of dislocations reproduces many times the conditions of the formation and superposition of the phonon arising due to a dislocation jump at variable stresses, the amplitude of which is much less than the yield tension of the metal. Using the idea of the possibility of damage to the metals due to the super-position of the phonons, we estimate the value of the cyclical plastic deformation under which the phonons superposition assumes the primary cause underlying the mechanism of fracture.

Theoretical and Experimental Results

The possibility of superposition of phonons depends upon the deformation conditions and the structure of the metal. Due to anharmonizm of state defect-free crystal, the maximum length of the free path of phonons Λ_{anh} depends on the physical properties of the metal and the temperature [8]. For iron at room temperature, Λ_{anh} is equal about $600a$, where a is the average interatomic distance. The crystal lattice defects (dislocations, boundaries of blocks and crystals, pores, etc.) contribute to the scattering of phonons and reduce the length of free length Λ by contrast Λ_{anh}.

The energy emitted by the jump of the dislocation by one interatomic distance b in the direction of the shift is τb^2 into a 1-cm-long linear dislocation, where τ is shear stress. The maximum value of the energy fluctuation, in consequence of the phonon's superposition by the jump of a linear dislocation, is equal, as wells to $\tau b^2 \Lambda$. The energy of vacancy formation is about half of the sublimation energy E_{sbl}. From the equality of the phonons superposition energy and the vacancy formation energy

$\tau b^2 \Lambda = 0.5E_{sbl}$, we estimate the minimum value of shear stress for vacancy formation by the dislocation jump. The minimum value Λ is equal to the distance between the dislocations; the value $\Lambda = \Lambda_{anh} = 600b$ corresponds to a dislocation density of about 10^9 cm^{-2}, which is typical for normalized low-carbon steels. According to the minimum value of shear stress for vacancy formation by the dislocation jump, τ_{vac} equals 25 MPa for the materials under $E_{sbl} \approx 6.8 \times 10^{-19}$ j/atom.

We note that $\tau \Lambda = 0.5E_{sbl}/(b^2 \Lambda)$ is the invariant quantity for any metal. It means that, subject to $\tau > 0.5E_{sbl}/(b^2 \Lambda)$, the spontaneous changes of the metal structure are possible in the direction of Λ decreasing. On the contrary, subject to $\tau < 0.5E_{sbl}/(b^2 \Lambda)$, the value Λ increases. Such processes of self-organization structures are called self-similar. In the first case, the density of structural defects, including dislocations, increases, and there is a cyclic hardening of metal. In the second case, there is a cyclic softening.

Phonons superposition is sufficient for the formation of submicroscopic cracks by a jump of arrested obstacles dislocations. The tension in the top clusters of n dislocations is equal to $n\tau$. The total phonons' energy may achieve values of $n\tau b^2 \Lambda$ under displacement of the general dislocation at the distance b. On the basis of the equality of phonons energy under the jump of only one arrested obstacle dislocation and the energy formation of two free surfaces, we write the condition for the formation of submicroscopic crack in the form $n\tau b^2 \Lambda == 2E_s S$, where E_s is the surface energy of the metal and S—the surface of submicrocrack. Taking values $\Lambda = 600b$, $n = 10$ and $E_s \approx 2$j/m^2 in the case of mild steel, we obtain the value of the surface of a submicrocrack $S \approx 40b^2$ at $\tau = 100$ MPa. Thus, the submicrocrack formation is possible on the condition that the dislocation density of the slip surface is much higher than the dislocation density in the source structure of low-carbon normalized steel. As reported in an article [9], the critical value of the dislocation density at the emergence of submicroscopic fatigue cracks is equal to the order of 10^{10} cm^{-2}. In order of magnitude, the obtained us assessment is consistent with that value.

The increase of the dislocation density is possible if, under the action of stresses, the dislocation overcome the obstacles that impeded their slide (intersections with other dislocations, crystals of hardening phases). For assessing the value of plastic deformation magnitude ε_{pl}, under which there is a single slip of dislocations without departing from their obstacles, we used the simplest model: the distribution of dislocations and their pinning is equable throughout the volume of the material, and the shear stress is the same for all dislocations.

Assume that the increase of shear resistance is provided mainly by the presence of fine particles of secondary phases enjoyed the high shear resistance. In this case, under stresses less than the tension yield, the maximum displacement of the dislocations in the direction of shear stress τ does not exceed $0.5\lambda_p$ (Fig. 1a). Correspondingly, the maximum of shear strain equals $\gamma = \pi b/(8\lambda_p)$. The increase of shear yield by the presence of solid particles equals $\tau_p = Gb/\lambda_p$, where G is the shear modulus. Thus, $\gamma = \pi\tau_p/(8G)$, and $\varepsilon_{pl} = \pi\tau_p/(16G) \approx 0.196\,\tau_p/G$. For structural middle-strength steel ($\tau_p = 250$ MPa), the value of the magnitude of

plastic deformation is estimated $\varepsilon_{pl} = 50 \times 10^{-5}$; for mild steel, it is order $\varepsilon_{pl} = 15 \times 10^{-5}$. According to the above estimates, the local density of dislocations must be an order of magnitude greater for the emergence submicrocrack in mild steel. This is possible due to the passage of dislocations between particles of a strengthening phase and accumulation of dislocations near the obstacles hindering them from slipping.

Assume that shear resistance occurs mainly due to the high density of dislocations distributed uniformly over the volume of the metal. We denote the distance between the points of dislocations intersection per the symbol λ_d (Fig. 1b). Before dislocation release from the pins at the points of intersection, there is the ratio $\tau_R = Gb/R$, where R is the radius of the dislocation curvature. The highest increase of shear yield by the dislocations' density equal $\tau_d \approx 0.5\, Gb/\lambda_d$. The separation of the dislocation will occur at $R = 2\lambda_d$ and $\varepsilon_{pl} \approx 0.043\, \tau_d/G$; for mild steel, the plastic deformation equal $\varepsilon_{pl} \approx 3 \times 10^{-5}$. After the release from the pinning, the dislocation is free to move over a distance λ_d; in this case, the value of plastic deformation is $\varepsilon_{pl} = \tau_d/G$, or about 70×10^{-5} for mild steel.

Note that the cyclic plastic deformation, without the separation of the dislocations from the pinning field, is substantially less than after the separation. Possibly, the presence of a "physical" fatigue limit for carbon structural steels and the multiple increase of cyclic life are caused by this difference.

In the evaluation of the plastic deformation, which corresponds to the formation of "gaps" of atomic bonds with the formation of vacancies and submicrocrack, the structure heterogeneity of the material was not taken into account. However, as shown by the rating values ε_{pl}, there is reason to believe that, in the field of cyclic plastic deformation under the stresses' less technical yield point, the leading mechanism of damage at the atomic level is the superposition of phonons that are aroused by the jump of dislocations.
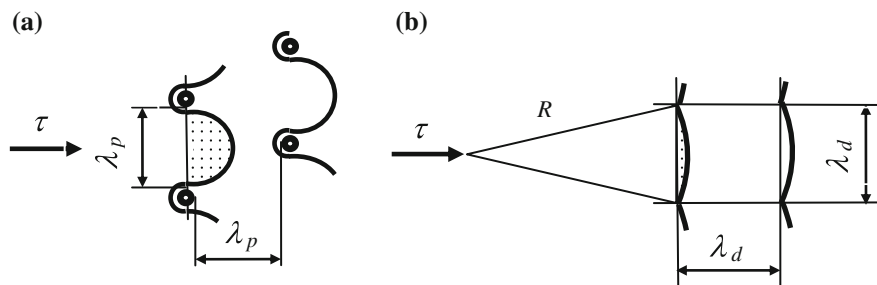
Fig. 1 Scheme of the microplastic deformation structure for the metal: **a** strengthened by means of the fine particles of secondary phases experiencing the high shear resistance; **b** strengthened by means of the high density of dislocations

Assuming that the maximum degree of damage of metals in high-cycle region of fatigue is achieved by summing all of the damage that is generated by each cycle of deformation, we write the ratio as:

$$\sum_N \tau b^2 \Lambda_{anh} \varepsilon_{pl}^p = C, \quad \text{or} \quad \tau \varepsilon_{pl}^p N = C_\tau, \tag{1}$$

where $\sum_N$ means the summation of atomic damages of the definite microscopic volume during N deformation cycles;

$\tau b^2 \Lambda_{anh}$ is the maximum energy of the phonons superposition;
ε_{pl} is the amplitude cyclic plastic deformation;
p and C_τ are constants;
$b^2 \Lambda_{anh}$ is the activation volume according to thermo-fluctuation theory.

It is not possible to experimentally determine the values τ and ε_{pl} individual micro-volumes in each cycle. When changing the parameters of the process damage, the sample or the material of construction must use "averaged" values τ and ε_{pl} in accordance with the engineering approach. As has found at constant stress amplitude after some the number of deformation cycles, the amplitude of plastic deformation remains practically constant or the rate of change plastic deformation is minimal during the greater part of the total number of cycles to complete the fracture of the specimen. According to the Prigogine–Glansdorff theorem [10], that phenomena is evidence of self-organization under these conditions, providing the minimal entropy production inside the object. In our case, it is possible that it corresponds to a minimum speed of damage accumulation in the material.

As the estimated value ε_{pl} (Eq. 1), we accept the average (and conditionally assumed to be permanent during this testing) amplitude of the cyclic plastic deformation, which is equivalent to the variable amplitude of cyclic plastic deformation in relation to the actual damage of the material under the intended stress τ for the same number of cycles. The question of what we constitute as the ultimate degree of damage of metals under varying stresses enjoys paramount importance, as this determines, ultimately, the margin of safety in machines. In some engineering industries (power equipment, equipment of nuclear power plants [11], lifting equipment, and transport), it is considered to be the limiting state in which the length of the emerged defect is 0.5–2.0 mm. On the one hand, such defects can be detected by the equipment control; on the other hand, they do not cause rapid growth of the fatigue crack and, then more, the brittle fracture of middle-strength steel. In determining the number of cycles N corresponding to the limit extent of the damage, we accepted the number of cycles at which the length of the visually observable defect on the surface of the tested specimen (without any special preparation of the surface) was in the range 1.0–2.0 mm.

The value of the equivalent cyclic plastic deformation ε_{pl} was determined in the following procedure.

1. According to the test results of flat specimens under constant amplitude cycle symmetric extension-compression, the parameters of the following dependence were determined:

$$\sigma^m N = C_\sigma, \tag{2}$$

   σ is the stress amplitude; m and C_σ are constant values.

2. According to the test results of flat specimens with a circular hole under constant amplitude cycle symmetric tension-compression, the parameters of the following dependence were determined:

$$\sigma_c^n N = C_c, \tag{3}$$

σ_c is the conditional stress amplitude for the net-section of the specimen with concentrator; *and* n and C_c—constant values.

3. According to Eq. (1), there is correspondence between the intended value τ (or σ under the tension-compression of the flat specimen) and the specific value ε_{pl} for the any value N. To estimate the value ε_{pl}, it was decided that under small deformations the summary elastic-plastic deformation at the base of the concentrator is equal to $\alpha_\sigma \varepsilon_c$ by first approximation, where α_σ is the theoretical stress concentration factor; ε_c is the middle value of the elastic deformation for the net-section of the specimen: and $\varepsilon_c = \sigma_c / E$. The value of elastic deformation at the base of the concentrator was taken to be equal to $\varepsilon = K_\sigma \varepsilon_c$, where K_σ is the effective stress concentration factor, and $K_\sigma = \sigma/\sigma_c = \varepsilon/\varepsilon_c$ for the intended number of cycles N. Consequently, the estimation of the plastic deformation amplitude at the base of the concentrator was calculated by means of $\varepsilon_{pl} \approx (\alpha_\sigma - K_\sigma)\varepsilon_c$.

In the base of the concentrator for flat specimens, the stress state is almost linear. According to Eq. (1) for the specimen without the concentrator, the plastic deformation amplitude was taken to be $\varepsilon_{pl} \approx \varepsilon_{pl.c} \approx (\alpha_\sigma - K_\sigma)\varepsilon_c$ at the same value of the number of cycles N. Table 1 presents the testing results of flat specimens of sheets at the thickness of 12 mm and the width of 50–60 mm without the concentrator or with the hole at diameter of 18 mm from steel Ст.3 and 09Г2Т ($\alpha_\sigma = 2.33$) and the calculated values ε_{pl}.

4. The exponent p is determined by the ratio derived from Eqs. (1) and (2) by replacing in Eq. (1) $\tau = 0.5\sigma$:

$$\varepsilon_{pl}^p / \sigma^{m-1} = C_\Sigma,$$
$$\text{or } \lg \varepsilon_{pl} = (m - 1) \lg \sigma + \lg C_\Sigma. \tag{4}$$

Table 1 The test results and the calculated values ε_{pl}

N, mln.	Steel Ст3, m = 8.30					
	σ, MPa	ε, $\times 10^5$	σ_c, MPa	ε_c $\times 10^5$	K_σ	ε_{pl}, $\times 10^5$
0.1	226.6	113.3	176.6	88.3	1.28	92.4
0.5	185.4	92.7	132.4	66.2	1.40	61.6
1.0	171.7	85.8	117.7	58.8	1.46	51.2
2.0	157.9	79	104	52	1.52	42.2
N, mln.	Сталь 09Г2Т, m = 6.10					
	σ, MPa	ε, $\times 10^5$	σ_c, MPa	ε_c $\times 10^5$	K_σ	ε_{pl}, $\times 10^5$
0.1	270.9	135.4	194.2	97.1	1.40	90.8
0.5	208.1	104	137.3	68.6	1.52	55.8
1.0	185.7	92.8	119.8	59.9	1.55	49.7
2.0	165.8	82.9	104	52	1.60	38.3

The exponent equal $p = 3.37$ for steel Ст.3 and $p = 2.96$ for steel 09Г2Т.

From the equality $\varepsilon_{pl}^p = C_\Sigma \sigma^{m-1}$, it follows that the relations Eqs. (1) and (2) are identical under $\varepsilon_{pl} = C_\Sigma \sigma^r$ and $pr = m - 1$.

For example, the value p for middle-strength steels was estimated by using the results presented in [12]. Specimens at the diameter 4–24 mm were tested by the circular bend with a record of a bending deflection diagram. Qualitatively the bending deflection in the diagram deflection is similar to the width diagram of the hysteresis loop, but this significantly simplifies the fixing of the moment of microcrack occurrence at a length from 20 to 50 µm. As an indirect evaluation of ε_{pl}, we have taken the value of the bending deflection increment Δf from the testing start to the microcrack's detection moment. Figure 2a illustrates the relationships between Δf and the ratio of the testing stress amplitude to the fatigue limit defined on the basis of 5×10^6 cycles; and Fig. 2b presents the dependence between the testing stress amplitude and the number of cycles until the microcrack occurrence moment for specimens with a 8-mm diameter.

The value of the exponent $r = 6.03$ for steel 10X18H10T, $r = 6.45$ for steel 40X (secondary sorbite) and $r = 5.66$ for steel 40X (air-hardening) (Fig. 2a). Accordingly, the value of m is 19.13; 19.47 and 17.45 (Fig. 2b). From the relation $pr = m - 1$, values of p are 3.01, 2.86, and 2.91 that are comparable to the values of p for steels Ст.3 and 09Г2Т obtained by other means and with greater material costs.

In the analysis of fatigue strength of welded joints, it is desirable to separately assess the effect of technology and design. As a rule, the fatigue crack forms near the boundary of HAZ during welding. In addition to the concentrator, there are residual stresses here. Therefore, the experimental value of concentration factor K_σ and the calculated value $\alpha_{\sigma-\exp} \approx K_\sigma + \varepsilon_{PL}/\varepsilon_c$ should depend on the level of the cycle's stresses in the presence of residual stresses.
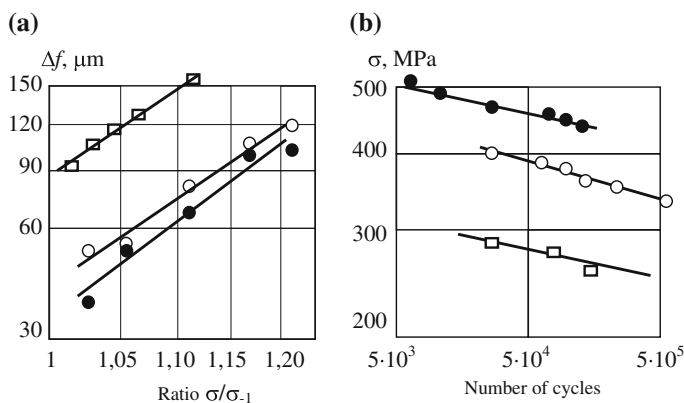
Fig. 2 Dependence of the increment of deflection of the sample *Δf* from σ/σ$_{-1}$ **a** and number of cycles before the moment of detection of microcracks **b**: *square* steel 10X18H10T; *filled circle* steel 40X (secondary sorbite); *circle* steel 40X (air-hardening)

To estimate the conditional values of the stress concentration factors (Table 2), we used the test results obtained by the staff of The Laboratory Lifting-Transport Machinery of the St.-Petersburg Polytechnic University under contracts with industry. As expected, then the more the amplitude stress and, therefore, the more the cyclical plastic deformation of the material in the zone of the weld; therefore; there is less influence of residual stresses on the resistance to fatigue damage and less the estimated value $\alpha_{\sigma-\exp}$ (series I, III, VI). Partial removal of residual stresses and reduction of stress concentration at the back weld lead to less change of the value $\alpha_{\sigma-\exp}$ (series II, IV). With an almost complete removal of residual stresses at the high-temperature tempering, the value $\alpha_{\sigma-\exp}$ of a welded joint does not depend on the amplitude of the cycle stress (series V), and this value can be considered as α_{σ}.

Reducing the cost of testing elements in order to select the most efficient for resistance to fatigue damage is achieved by the fact that we can estimate the values of $\varepsilon_{pl.c}$ at various stresses and use them to influence the studied factors without experimental determination of residual stresses. Considering some uncertainty in the estimated values of equivalent plastic strain at the base of the concentration, this approach can used for comparative evaluation and initial selection of design options and technology.

Table 2 Values $\alpha_{\sigma-\exp}$ for the welded elements of structures

Series, material, specimen	N, 10^{-6}	σ_c, **MPa**	ε_c, 10^5	$\kappa_\sigma == \sigma/\sigma_c$	$\alpha_{\sigma-\exp}$
I. Steel Ст.3 The T-joint without cutting edges for welding, with incomplete penetration of weld root	0.1	117.9	59	1.92	3.49
	0.5	71.6	35.8	2.59	4.31
	1.0	60.8	30.4	2.82	4.50
	2.0	49	24.5	3.22	4.94
II. Steel Ст.3 The T-joint with cutting edges for welding and with back weld	0.1	145.2	72.6	1.56	2.81
	0.5	107.9	54	1.72	2.75
	1.0	94.2	47.1	1.82	2.88
	2.0	84.4	42.2	1.87	2.78
III. Steel 09Г2Т The specimen with two longitudinal reinforcement plates on opposite surfaces	0.1	160	80	1.69	2.82
	0.5	78.5	39.3	2.65	4.07
	1.0	60	30	3.1	4.76
	2.0	45.1	22.5	3.68	5.38
IV. Steel 09Г2Т The specimen with two longitudinal reinforcement plates on opposite surfaces and with machining of the weld	0.1	179.5	89.8	1.51	2.52
	0.5	117.7	58.9	1.77	2.72
	1.0	98.1	49	1.89	2.90
	2.0	82.4	41.2	2.01	2.94
V. Steel 09Г2Т The specimen with two longitudinal reinforcement plates on opposite surfaces and at the high temperature tempering	0.1	176.6	88.3	1.53	2.56
	0.5	127.5	63.8	1.63	2.50
	1.0	112.8	56.4	1.65	2.53
	2.0	98	49	1.66	2.44
VI. Steel 09Г2Т The sample with two transverse reinforcement plates on opposite surfaces with cutting edges for welding	0.1	184.4	92.2	1.47	2.45
	0.5	118.7	59.4	1.75	2.69
	1.0	95.2	47.6	1.95	2.99

Conclusions

1. On the basis of the assumption of the superposition of phonons that occurs during the gliding of the dislocations in the plastic deformation in metals, a generalized dependence between of the number of cycles until damage metals, the stresses and cyclic plastic deformation for the region of limited fatigue endurance under symmetric cycle extension–compression is introduced.
2. The value of the amplitude of the equivalent cyclic plastic deformation that corresponds to the formation of vacancies and submicrocracks by the phonons superposition during the gliding of the dislocations is determined theoretically.
3. The methods of estimation of the equivalent cyclic plastic deformation on basis of the results of comparative tests for the flat specimens without the notch and with the notch are proposed.
4. The possibility of relative evaluation of various structure options on the basis of the proposed approach is evident.

References

1. Sosnovskiy LA, Makhutov NA (1995) About the total fatigue curve. Factory Lab 5:33–34
2. Sosnovskiy LA, Makhutov NA, Troshchenko VT (2010) Evolution of ideas on fatigue of metals by volume loading and friction. In: Zhuravkov MA et al (eds) Proceeding of VI-th international symposium on tribo-fatigue (ISTF 2010), 25 Oct–1 Nov 2010, Minsk (Belarus). BSU, Minsk (1):77–84
3. Feng RC, Rui ZhJ, Zhang PT, Yang ChF, Yi SF (2014) Improved method of evaluating fatigue life TiAl alloys. Probl Strength 2:37–44
4. Reisland G (1975) The physics of phonons (Trans: Zhdanov GS). Mir, Moscow, 365 p
5. Zhurkov SN, Petrov VA (1978) On the physical basis of temperature-time dependence of strength of solids. Report as Academy of Sciences USSR, vol 239(6):1316–1319
6. Petrov VA (1986) Thermal fluctuations as the embryonic cracks generator. Physical concept to strength and plasticity. Leningrad:11–17
7. Zhukov VA (1994) Quantum mechanical approach to the analysis of the phenomena during deformation and fracture of metals. Metals 6:93–97
8. Gurevich VL (1980) Kinetics of phonon systems. Nauka, Moscow, p 400
9. Terent'ev VF (1996) Stages of the process of fatigue fracture of metallic materials. Metals 6:14–20
10. Ebeling V (1979) The formation of structures in irreversible processes: an introduction to the theory of dissipative structures (Trans: Klimontovich YL). Mir, Moscow, 279 p
11. Norms for strength calculation of equipment and pipelines of nuclear power environment (1989). Energy-atomic press, Moscow, 525 p
12. Vinogradova NV (1972) The investigation of the kinetics of fatigue fracture of authorization steels. The dissertation for the PhD Leningrad, LPI by M.I. Kalinin, 201 p

Calculation of Shells of Revolution with Arbitrary Meridian Oscillations

Tatiana V. Zinovieva

Abstract The system of equations and its numerical solution for free and forced oscillations of shells of revolution with an arbitrary meridian is obtained. A variant of the classical theory of shells developed on the basis of Lagrangian mechanics is used. The natural frequencies and amplitudes of oscillations of shells with various meridians are defined by the finite difference method.

Keywords Elastic shells · Linear shell theory · Forced oscillations · Natural frequencies · Finite difference method

Introduction

The calculation of oscillations of thin-walled structures is an actual task of modern engineering; many technological objects undergoing dynamical load are shell-of-revolution shaped, e.g., parts of steam generators or power unit turbines, aircraft fuselages, pipelines, tanks, etc. Of interest here is a determination of the oscillation amplitudes for such shells under the influence of stated forces, as well as finding out their natural frequencies.

As a rule, the full system of equations for shells is obtained from equations contained in third-dimensional theory of elasticity; for that, certain simplifying assumptions are added; it leads to the creation of various shell theories [1–9]. However, the use of the direct approach to shells as deformable surfaces and the use of modern analytical technologies provide the possibility to develop an exact theory.

The given paper is based on a variant of classical theory of shells as surfaces with material normals (particles like needles); it is developed both on the basis of Lagrange mechanics and the virtual work principle [10–13]; the use of this theory in different applications has been described in articles [14–16].

T.V. Zinovieva (✉)
Peter the Great Saint-Petersburg Polytechnic University, St. Petersburg, Russia
e-mail: tatiana.zinovieva@gmail.com

The system of equations and its numerical solution for forced and free oscillations of shells of revolution with an arbitrary meridian is developed. The presented data generalize the results of the study [17], where calculations of the statics for shells of revolution under the influence of axis-symmetrical loads have been described.

Equations of Thin Shell Theory

The shell is considered as a material surface, whose particles have five degrees of freedom: three translations and two rotations. The movement is determined by the vector of small displacements u and the vector of small rotation θ in the tangent plane. For convenience's sake, we introduce here the vector of change of normal toward the shell: $\varphi \equiv \theta \times n = \dot{n}$ (the dot denotes a small increment during the deformation). The expression of the work of external distributed moment is used to introduce the generalized force corresponding to φ: $m \cdot \theta = m^\times \cdot \varphi, m^\times \equiv m \times n$.

The degree of surface deformation can be determined by the tensors

$$\varepsilon = (\nabla u)_\perp^S, \quad \kappa = -(\nabla \varphi)_\perp + b \cdot \nabla u^T, \quad (b \equiv -\nabla n). \tag{1}$$

From this point on $(\ldots)_\perp$ denotes the tensor constituent in the tangent plane; icons $(\ldots)^S, (\ldots)^T$ denote symmetrization and transposition. According to Kirchhoff's kinematic hypothesis, the rotation is connected with the displacement

$$\varphi = -\nabla u \cdot n. \tag{2}$$

The virtual work principle makes it possible to create the whole system of equations, where the characteristics of internal forces inside the shell are introduced as Lagrange multipliers: τ and μ are symmetrical tensors of stresses and moments, Q is a shearing force vector; they all lay in the tangent plane. The variational formulation serves as a basis for derivation of the balance equations for forces and moments:

$$\nabla \cdot (\tau + \mu \cdot b + Qn) + q = 0, \quad (\nabla \cdot \mu)_\perp + Q = m^\times, \tag{3}$$

and boundary conditions on a contour in general form:

$$\left[P^0 - v \cdot (T + Qn) + \partial_l(A \cdot ln) \right] \cdot \delta u - A \cdot vn \cdot \partial_v \delta u = 0, \quad A \equiv M^0 \times n + v \cdot \mu, \tag{4}$$

where q and $m^\times$ are an external distributed force and the moment on the surface, P^0 and M^0 are those on the contour. In total, we have five equilibrium equations in components and four scalar conditions on the shell contour.

The force and the moment are applied (from the side of $\mathbf{v}$) to the section of internal contour with the length of dl and the normal of $\mathbf{v}$

$$dF = \mathbf{v} \cdot (\mathbf{T} + \mathbf{Q}n)dl, \quad dM = \mathbf{v} \cdot (\mathbf{\mu} \times \mathbf{n})dl, \quad (\mathbf{T} \equiv \mathbf{\tau} + \mathbf{\mu} \cdot \mathbf{b}).$$

For the isotropic material, the elasticity ratios are represented as follows:

$$\mathbf{\tau} = C_1 \varepsilon \mathbf{a} + C_2 \mathbf{\varepsilon}, \quad \mathbf{\mu} = D_1 \kappa \mathbf{a} + D_2 \mathbf{\kappa}, \quad \mathbf{a} \equiv \nabla r, \quad \varepsilon \equiv \mathrm{tr}(\mathbf{\varepsilon}), \quad \kappa \equiv \mathrm{tr}(\mathbf{\kappa}),$$
$$C_1 = Ehv/(1 - v^2), \quad C_2 = Eh/(1 + v), \quad D_1 = C_1 h^2/12, \quad D_2 = C_2 h^2/12. \tag{5}$$

Ratios $C_1 - D_2$ are taken as those applied in Kirchhoff plate; E is the elasticity module of the material used for the shell, h is its thickness, v is Poisson ratio. There are no elasticity ratios for shearing force vector $\mathbf{Q}$ in classical theory; instead, we have a relation Eq. (2).

The System of Equations for Shells of Revolution

Let's consider the shell with the surface formed by rotation of the meridian about an axis x [10]. The meridian is set through the dependence of cylindrical coordinates on an arc coordinate $x = x(s), \rho = \rho(s)$, and its placement on the surface is determined by the angle θ (see Fig. 1).

The radius vector of surface points is given by the equality

$$r(\theta, s) = x(s)\mathbf{i} + \rho(s)e_\rho(\theta), \quad e_\rho = \mathbf{j}\cos(\theta) + \mathbf{k}\sin(\theta),$$
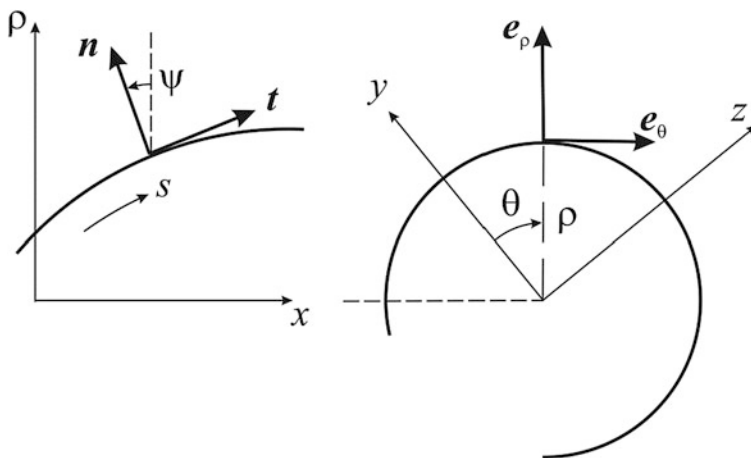

Fig. 1 Revolution surface

where $\boldsymbol{i}$, $\boldsymbol{j}$, $\boldsymbol{k}$ are the axial-oriented unitary vectors of Cartesian system, x, y, z, respectively.

The unitary vector for the line tangent to a parallel is $\boldsymbol{e}_\theta = -\boldsymbol{j}\sin(\theta) + \boldsymbol{k}\cos(\theta) = \boldsymbol{e}'_\rho$. For unit vectors of the line tangent and the normal to the meridian; we have:

$$\boldsymbol{t} = \partial\boldsymbol{r}/\partial s = x'(s)\boldsymbol{i} + \rho'(s)\boldsymbol{e}_\rho(\theta), \quad x' = \cos\psi, \quad \rho' = \sin\psi,$$

$$\partial\boldsymbol{t}/\partial s = \omega\boldsymbol{n}, \quad \omega \equiv \psi'(s), \quad \boldsymbol{n} \equiv -\boldsymbol{i}\sin\psi + \boldsymbol{e}_\rho\cos\psi,$$

here ω is a curvature of the meridian, ρ^{-1} is that for the parallel.

The shell displacement vector has three components: $\boldsymbol{u} = u_\vartheta\boldsymbol{e}_\vartheta + u_t\boldsymbol{t} + u_n\boldsymbol{n}$. Equations (1) and (2) are used to determine the vector for the change of normal and deformation tensors:

$$\varepsilon_\theta = \rho^{-1}\left(\partial_\theta u_\theta + u_\rho\right), u_\rho \equiv u_t\sin\psi + u_n\cos\psi, \varepsilon_t = \partial_s u_t - \omega u_n,$$

$$\varepsilon_{\theta t} = \varepsilon_{t\theta} = \frac{1}{2}\left[\rho^{-1}(\partial_\theta u_t - u_\theta\sin\psi) + \partial_s u_\theta\right],$$

$$\varphi_\theta = \rho^{-1}(u_\theta\cos\psi - \partial_\theta u_n), \varphi_t = -\omega u_t - \partial_s u_n,$$

$$\kappa_\theta = -\rho^{-1}(\partial_\theta\varphi_\theta + \varphi_t\sin\psi) - \rho^{-2}\cos\psi\left(\partial_\theta u_\theta + u_\rho\right),$$

$$\kappa_t = \omega(\partial_s u_t - \omega u_n) - \partial_s\varphi_t, \quad \kappa_{\theta t} = -\rho^{-1}(\partial_\theta\varphi_t - \varphi_\theta\sin\psi + \partial_s u_\theta\cos\psi),$$

$$\kappa_{t\theta} = \omega\rho^{-1}(\partial_\theta u_t - u_\theta\sin\psi) - \partial_s\varphi_\theta. \tag{6}$$

We have these relationships for the forces and moments from Eq. (5):

$$\mu_\theta = (D_1 + D_2)\kappa_\theta + D_1\kappa_t, \mu_t = (D_1 + D_2)\kappa_t + D_1\kappa_\theta,$$

$$\mu_{\theta t} = D_2\kappa_{\theta t}, \mu_{t\theta} = D_2\kappa_{t\theta},$$

$$T_\theta = (C_1 + C_2)\varepsilon_\theta + C_1\varepsilon_t - \rho^{-1}\mu_\theta\cos\psi, T_t = (C_1 + C_2)\varepsilon_t + C_1\varepsilon_\theta + \omega\mu_t,$$

$$T_{\theta t} = C_2\varepsilon_{\theta t} + \omega\mu_{\theta t}, T_{t\theta} = C_2\varepsilon_{\theta t} - \rho^{-1}\mu_{t\theta}\cos\psi. \tag{7}$$

The system in components is enclosed with balance equations (3):

$$\rho^{-1}[\partial_\theta T_\theta + (T_{\theta t} + T_{t\theta})\sin\psi] + \partial_s T_{t\theta} + \rho^{-1}Q_\theta\cos\psi + q_\theta - \beta\ddot{u}_\theta = 0,$$

$$\rho^{-1}[(T_t - T_\theta)\sin\psi + \partial_\theta T_{\theta t}] + \partial_s T_t - \omega Q_t + q_t - \beta\ddot{u}_t = 0,$$

$$-\rho^{-1}T_\theta\cos\psi + \omega T_t + \rho^{-1}(\partial_\theta Q_\theta + Q_t\sin\psi) + \partial_s Q_t + q_n - \beta\ddot{u}_n = 0, \tag{8}$$

$$\rho^{-1}[\partial_\theta\mu_\theta + (\mu_{\theta t} + \mu_{t\theta})\sin\psi] + \partial_s\mu_{t\theta} + Q_\theta = m_\theta^\times,$$

$$\rho^{-1}[(\mu_t - \mu_\theta)\sin\psi + \partial_\theta\mu_{\theta t}] + \partial_s\mu_t + Q_t = m_t^\times.$$

where β is the mass of the shell per unit area.

Four scalar conditions on a shell contour follow from (4). In the case of rigid fixing: $u_\theta = u_t = u_n = 0$, $\gamma_\theta \equiv \partial_s u_n = 0$. On a free contour with the normal of

$\mathbf{v} = \mathbf{t}$, the stretching force $T_t = P_t^0$, bending moment $\mu_t = M_\theta^0$, and two combinations connecting a torque with force components are set up as:

$$F_\theta \equiv T_{t\theta} - \rho^{-1} \cos \psi \mu_{t\theta} = P_\theta^0 + \rho^{-1} \cos \psi M_t^0,$$

$$F_n \equiv Q_t - \rho^{-1} \partial_\theta \mu_{t\theta} = P_n^0 + \rho^{-1} \partial_\theta M_t^0.$$

Forced and Free Oscillations

Equations (6)–(8) can be reduced to a system

$$\partial_s Y(\theta, s, t) = f(Y), \quad Y = (u_\theta, u_t, u_n, \gamma_\theta, F_\theta, T_t, F_n, \mu_t)^{\mathrm{T}} \tag{9}$$

for the column of unknown values set at the shell edges.

Let's consider forced oscillations under the applied periodical load

$$\begin{pmatrix} q_\theta \\ m_\theta^\times \end{pmatrix} = \begin{pmatrix} \bar{q}_\theta(s) \\ \bar{m}_\theta^\times(s) \end{pmatrix} \sin n\theta \sin \Omega t, \quad \begin{pmatrix} q_t \\ q_n \\ m_t^\times \end{pmatrix} = \begin{pmatrix} \bar{q}_t(s) \\ \bar{q}_n(s) \\ \bar{m}_t^\times(s) \end{pmatrix} \cos n\theta \sin \Omega t,$$

where n is an integer and Ω is the loading frequency. We search for the solution for this system equation (9) in analogical form, u_θ, F_θ proportional to $\sin n\theta$ and unknown $u_t, u_n, \gamma_\theta, T_t, F_n, \mu_t$ to $\cos n\theta$.

For amplitudes we'll obtain a system

$$\bar{u}_\theta' = \rho^{-1} \sin \psi \bar{u}_\theta + \frac{C_2}{C_2 + 4D_2 \rho^{-2} \cos^2 \psi} \bar{G},$$

$$\bar{G} \equiv \frac{2}{C_2} \bar{F}_\theta + \rho^{-1} n \bar{u}_t + \frac{4D_2}{C_2} \rho^{-2} \cos \psi \left(-n\omega \bar{u}_t + \rho^{-1} n \sin \psi \bar{u}_n - n \bar{\gamma}_\theta \right),$$

$$\bar{u}_t' = \bar{\varepsilon}_t + \omega \bar{u}_n, \bar{\varepsilon}_t = \frac{1}{C_1 + C_2} (\bar{T}_t - C_1 \bar{\varepsilon}_\theta - \omega \bar{\mu}_t),$$

$$\bar{\varepsilon}_\theta = \rho^{-1} (n\bar{u}_\theta + \sin \psi \bar{u}_t + \cos \psi \bar{u}_n),$$

$$\bar{u}_n' = \bar{\gamma}_\theta, \bar{\gamma}_{\theta'} = -\omega' \bar{u}_t - \omega^2 \bar{u}_n - 2\omega \bar{\varepsilon}_t + \bar{\kappa}_t, \quad \bar{\kappa}_t = \frac{1}{D_1 + D_2} (\bar{\mu}_t - D_1 \bar{\kappa}_\theta),$$

$$\bar{\kappa}_\theta = -\rho^{-1} (n\bar{\varphi}_\theta + \sin \psi \bar{\varphi}_t) - \rho^{-2} \cos \psi (n\bar{u}_\theta + \sin \psi \bar{u}_t + \cos \psi \bar{u}_n),$$

$$\bar{\varphi}_\theta = \rho^{-1} (\cos \psi \bar{u}_\theta + n\bar{u}_n), \quad \bar{\varphi}_t = -\omega \bar{u}_t - \bar{\gamma}_\theta.$$

The remaining four equations follow from balance equations (8):

$$\bar{F}'_\theta = \rho^{-2}\cos\psi[-n\bar{\mu}_\theta + (\bar{\mu}_{\theta t} + \bar{\mu}_{t\theta})\sin\psi] -$$
$$\quad - \rho^{-1}[-n\bar{T}_\theta + (\bar{T}_{\theta t} + \bar{F}_\theta - \omega\bar{\mu}_{t\theta})\sin\psi] - \bar{q}_\theta - \rho^{-1}\cos\psi\bar{m}_\theta^\times - \beta\Omega^2\bar{u}_\theta,$$
$$\bar{T}'_t = \omega(\bar{F}_n + \rho^{-1}n\bar{\mu}_{t\theta}) - \rho^{-1}[(\bar{T}_t - \bar{T}_\theta)\sin\psi + n\bar{T}_{\theta t}] - \bar{q}_t - \beta\Omega^2\bar{u}_t,$$
$$\bar{F}'_n = \rho^{-2}\sin\psi n(\bar{\mu}_{\theta t} + \bar{\mu}_{t\theta}) + \rho^{-1}\cos\psi\bar{T}_\theta - \omega\bar{T}_t - \rho^{-1}\sin\psi\bar{F}_n -$$
$$\quad - \rho^{-2}n^2\bar{\mu}_\theta - \bar{q}_n - \rho^{-1}n\bar{m}_\theta^\times - \beta\Omega^2\bar{u}_n,$$
$$\bar{\mu}'_t = -\rho^{-1}[(\bar{\mu}_t - \bar{\mu}_\theta)\sin\psi + n(\bar{\mu}_{\theta t} + \bar{\mu}_{t\theta})] - \bar{F}_n + \bar{m}_t^\times. \tag{10}$$

Their coefficients are determined in a similar way, with the use of Eqs. (6–7), which are not shown here due to their complexity.

Note that at $n = 0$ from Eq. (10), we'll obtain a system for the amplitudes of axis-symmetrical oscillations, while at $\Omega = 0$ we'll get equations for shell statics.

The ODE system (Eq. 10) is supplemented by four boundary conditions for each edge of the shell, or by eight periodicity conditions for the closed shell. This boundary problem is solved through the method of finite difference on the $s \in [0, L]$ interval. Differential equations are approximated by difference ones with a constant step of $\delta = L/N$; $\bar{u}_\theta \ldots \bar{\mu}_t$ continuous argument s functions are replaced by $(\bar{u}_\theta)_i \ldots (\bar{u}_t)_i$ $(i = 0, \ldots, N)$ grid functions. This numeric scheme enables calculation of approximate function values in nodes. Functions are then restored by interpolation.

During system approximation by Eq. (10), the implicit symmetrical one-step difference scheme is used with second-order accuracy [18]:

$$\bar{Y}'(s) = \bar{f}(\bar{Y}) \Rightarrow \frac{\bar{Y}_{i+1} - \bar{Y}_i}{\delta} = \frac{\bar{f}_i + \bar{f}_{i+1}}{2}, \quad i = 0, \ldots, N, \tag{11}$$

and, for that, one additional node with $i = N + 1$ number is introduced, and the solution is continued from the $[0, L]$ definition range for one more δ interval on the right of the boundary. Therefore, $8N + 16$ values become unknown.

Finite difference equations (11) are the system of $8(N + 1)$ algebraic equations which is supplemented by the difference analogues of eight boundary conditions in nodes numbered $i = 0, N$. In total, we have $8N + 16$ equations for the same number of unknown values, and the problem can be solved through standard algorithms. When it is solved, the values of unknown functions at the additional node are discarded and not used during interpolation. The presented scheme was implemented with the software program Mathematica [19].

In the case of free oscillations of a shell of revolution in Eq. (10) system, all external loads are set as equal to zero ($\boldsymbol{q} = 0$ and $\boldsymbol{m}^\times = 0$), while the frequency Ω is unknown and should be determined. Boundary conditions are homogeneous. Using the finite difference method and the formula (11), we'll come to the homogeneous system of linear algebraic equations for amplitudes:

$$B(\Omega)\Upsilon = 0, \quad \Upsilon = \left(\{\bar{u}_\theta\}_i, \ldots \{\bar{\mu}_t\}_i\right)^{\mathrm{T}}, \quad (i = 0, \ldots, N+1). \tag{12}$$

Since values Ω at which the system (12) has non-trivial solution are natural frequencies of the shell, it'll be possible only upon the condition:

$$\mathrm{Det}\, B(\Omega) = 0. \tag{13}$$

Roots of Eq. (13) can be found, e.g., through secant method [20].

Numerical Results

The presented algorithm can be used for the analysis of the statics and oscillations of shells of revolution with an arbitrary meridian. Such calculations can be illustrated by giving several examples.

Let's consider the problem of static deflection of the shell due to its own weight; the gravity force is directed perpendicular to rotation axis. In this case, the distributed load is $\boldsymbol{q} = -\beta g\boldsymbol{j}$, where g is the acceleration of gravity; we have in components for amplitudes $\bar{q}_\theta = \beta g$, $\bar{q}_t = -\beta g \sin \psi$, $\bar{q}_n = -\beta g \cos \psi$ $(n = 1)$.

For circular cylindrical shell with the radius of R and the length of l, we assume that $\psi \equiv 0$, the meridian is set by equalities: $x(s) = s$, $\rho(s) = R$.

Calculations have been performed for the shell radius of $R = 1$ m, the length of $l = 20$ m, and the thickness of $h = 0.01$ m with both edges rigidly fixed. The shell is made of steel with the elasticity module of $E = 210$ GPa, Poisson ratio of $v = 0.28$, and a volumetric density of 7800 kg/m^3.

Figure 2a shows the displacement of the shell meridian along the y axis. The deformed shell shape is shown in Fig. 2b; when plotting it, all displacements have been scaled.
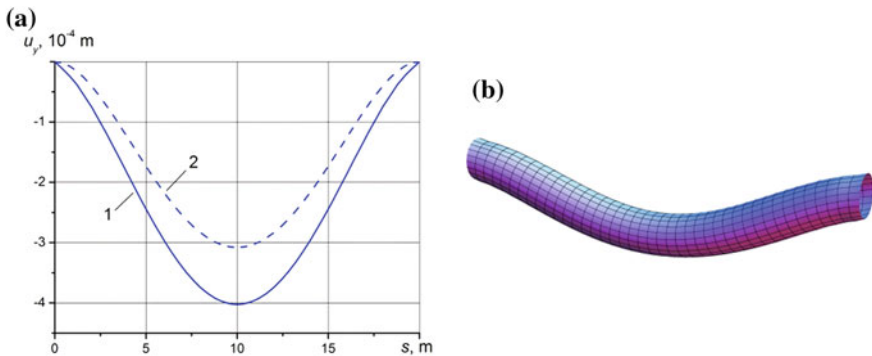
Fig. 2 Displacement under gravity (**a**) *1* cylindrical shell, *2* beam; deformed shape of a cylindrical shell (**b**)

It is easy to calculate the displacement of a thin-wall cylinder under gravity, using beam-based model. The boundary problem

$$u_y^{IV} + \beta_1 g = 0, \quad u_y(0) = u_y(l) = 0, \quad u_y'(0) = u_y'(l) = 0$$

has its solution

$$u_y(s) = -\frac{\beta_1 g}{24EI}\left(s^4 - 2ls^3 + l^2 s^2\right),$$

where β_1 is the mass of the beam per unit length and EI is its bending stiffness. The result is shown at Fig. 2a, and the displacement difference in comparison with that modeled by the shell is 23%. With the increase of relative shell length, this difference is reduced, for instance, it is 7% for $l = 40$ m.

For a cone shell with the length of l, we set the normal inclination $\psi \equiv$ const and the meridian through equalities $x(s) = x_0 + s\cos\psi$, $\rho(s) = y_0 + s\sin\psi$; coordinates x_0, y_0 determine the position of the initial point of the meridian.

To the shell with parameters $\psi = 20°$, $x_0 = 0$ m, $y_0 = 0.1$ m, $l = 1$ m, thickness of $h = 0.01$ m with one edge rigidly fixed, the force of $q_n = 1$ MPa, $q_\theta = 0.01$ MPa was applied; the edge was under the distributed force of $P_t^0 = 2$ MN/m and the bending moment of $M_\theta^0 = 0.1$ MN; the material used is steel with the properties described above. Figure 3 represents the calculated displacements and deformed shape at $n = 3$ and $\Omega = 100$ rad/s; Fig. 4 shows the forces and bending moment at the inside of the shell contour.

For shells with such a complicated form, it is desirable to set the meridian as an array of x and ρ coordinates. Then, having the interpolation function built, one can calculate the arc coordinate for each pair, using the formula:
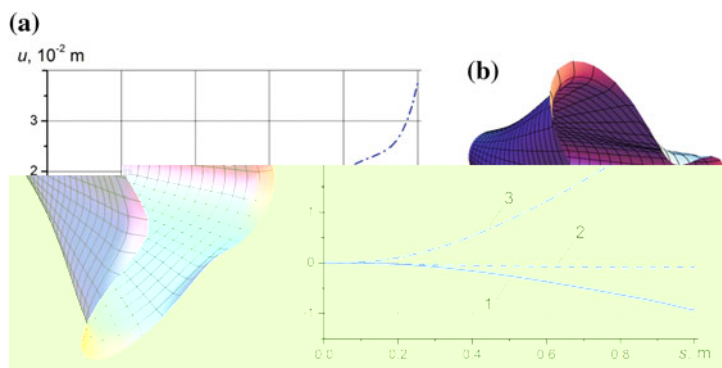
Fig. 3 Cone shape displacements (**a**) *1* circular displacement $\bar{u}_\theta$, *2* axial one $\bar{u}_t$, *3* normal one $\bar{u}_n$; deformed shape of the cone shell (**b**)
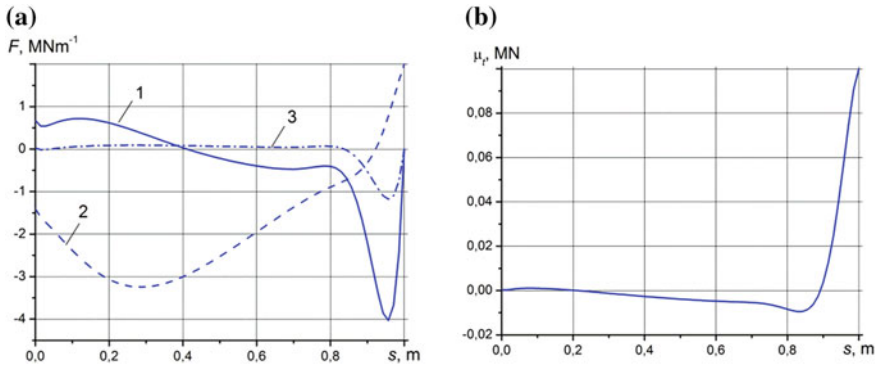
Fig. 4 Forces in cone shell **a** *1* $\bar{F}_\theta$, *2* $\bar{T}_t$, *3* $\bar{F}_n$; bending moment $\bar{\mu}_t$ (**b**)
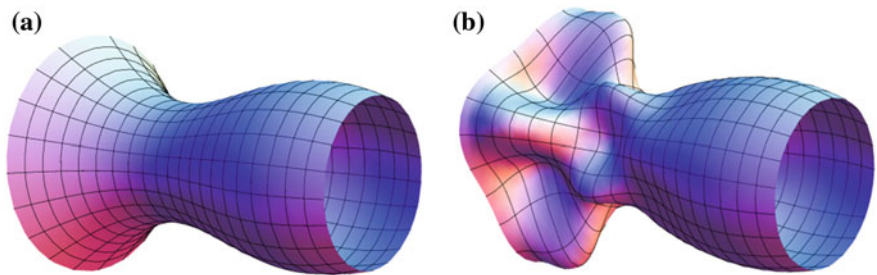

Fig. 5 Wavelike shell before (**a**) and after its deformation (**b**)

$$s(x) = \int\limits_0^x \sqrt{1 + (\rho'_x)^2}\,dx,$$

and then make $x(s)$ and $\rho(s)$ interpolations.

These functions should be smooth, as the remaining coefficients of system Eq. (10) are restored upon them:

$$\cos\psi = x'_s, \quad \sin\psi = \rho'_s, \quad \omega = \rho''_s \left(x'_x\right)^{-1}.$$

An example of such calculations is shown below; Fig. 5a demonstrates wavelike shell before its deformation, while Fig. 5b shows it under an applied distributed axial load of $n = 4$; one shell edge is rigidly fixed; the other is under axial and normal components of the applied force.

In technical applications, corrugated shells are widely used, and this makes it necessary to determine their stressed state under the load applied and their natural frequencies.

The meridian of the corrugated shell is easy to set up as:

$$\rho(x) = R_0 + r \sin \Omega x, \quad \Omega \triangleq 2\pi m/x_L, \tag{11}$$

where R_0 and r are forming radii, m is the number of waves along the length of the shell, and x_L is its length.

Calculations are performed for a steel corrugated shell with the radii of $R_0 = 0.05$ m and $r = 0.01$ m, the length of $x_L = 0.55$ m, the thickness of $h = 0.001$ m and the number of waves $m = 5.5$. The shell edges are rigidly fixed.

Table 1 Natural frequencies

Frequency (Hz)	$n = 0$	$n = 1$	$n = 2$
f_1	2441	938	2567
f_2	2555	2211	2870
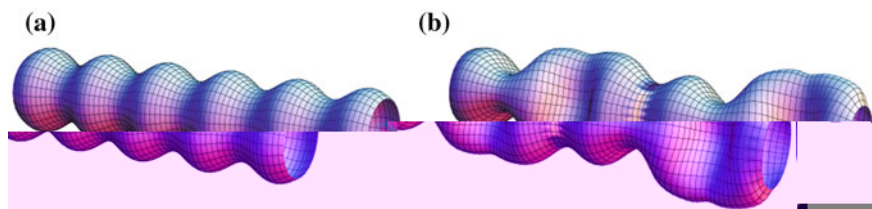
Fig. 6 Corrugated shell before (**a**) and after its deformation (**b**)
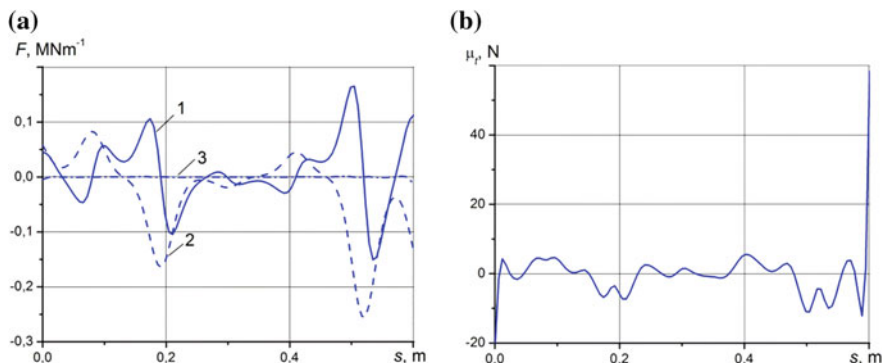
Fig. 7 Forces in corrugated shell **a** *1* $\bar{F}_\theta$, *2* $\bar{T}_t$, *3* $\bar{F}_n$; bending moment $\bar{\mu}_t$ (**b**)

Natural frequencies found for the shell are presented in Table 1. The first two frequencies correspond to beam-like forms ($n = 1$), while the third and fourth ones correspond to axis-symmetrical longitudinal-torsional ones ($n = 0$).

The deformation of this corrugated shell under the normal pressure of $\bar{q}_n(\theta, s) = s^2 \cos 2\theta$ MPa that vary over time with 2800 Hz frequency is considered.

Figures 6 and 7 show the shell shapes before and after deformation and the amplitude of the internal force factors.

Conclusions

The use of a modern variant of classical theory of shells and computer mathematics enable calculating the forced and free oscillations of shells of revolution with the arbitrary meridian. The obtained equations and developed calculation algorithm can be used as a basis for the analysis of shells dynamics with arbitrary loads applied.

References

1. Berdichevsky VL (2009) Variational principles of continuum mechanics. V.2. Applications. Springer, Berlin, p 1014. doi:10.1007/978-3-540-88469-9
2. Birger IA (1992) Rods, plates, shells (Sterzhni, plastinki, obolochki). Nauka, Moscow, p 392 (in Russian)
3. Blaauwendraad J, Hoefakker JH (2014) Structural shell analysis. Springer, The Netherlands, p 300. doi:10.1007/978-94-007-6701-0
4. Chapelle D, Bathe KJ (2011) The finite element analysis of shells—fundamentals, computational fluid and solid mechanics, 2nd edn. Springer, Berlin, p 410. doi:10.1007/978-3-642-16408-8
5. Donnell LG (1982) Beams, plates and shells (Balki, plastiny i obolochki). Nauka, Moscow, p 568 (in Russian)
6. Eremeev VA, Zubov LM (2008) Mechanics of elastic shells (Mekhanika uprugih obolochek). Nauka, Moscow, p 280 (in Russian)
7. Goldenvejzer AL (1976) Theory of elastic thin shells (Teoriya uprugih tonkih obolochek). Nauka, Moscow, p 512 (in Russian)
8. Khanh CL (1999) Vibrations of shells and rods. Springer, Berlin, p 423. doi:10.1007/978-3-642-59911-8
9. Novozhilov VV, Chernykh KF, Mikhajlovskij EM (1991) Linear theory of thin shells (Linejnaya teoriya tonkih obolochek). Politekhnika, Leningrad, p 656 (in Russian)
10. Eliseev VV (2003) Mechanics of elastic bodies (Mekhanika uprugih tel). St. Petersburg State Polytechnic University Publishing House, St Petersburg, p 336 (in Russian)
11. Eliseev VV (2006) To nonlinear theory of elastic shells (K nelineynoy teorii uprugih obolochek) St. Petersburg State Polytechnic University Journal (Nauchno-tekhnicheskie vedomosti SPbGTU). No. 3, pp 35–39 (in Russian)
12. Eliseev VV, Vetyukov YM (2010) Finite deformation of thin shells in the context of analytical mechanics of material surfaces. Acta Mech 209:43–57. doi:10.1007/s00707-009-0154-7

13. Eliseev VV, Vetyukov YM (2014) Theory of shells as a product of analytical technologies in elastic body mechanics. Shell Struct Theor Appl 3:81–85
14. Filippenko GV (2016) The vibrations of reservoirs and cylindrical supports of hydro technical constructions partially submerged into the liquid. In: Evgrafov A (ed) Advances in mechanical engineering, lecture notes in mechanical engineering. Springer International Publishing, Switzerland, pp 115–126
15. Eliseev VV, Vetyukov YM, Zinov'eva TV (2011) Divergence of a helicoidal shell in a pipe with a flowing fluid. J Appl Mech Tech Phys 52:450–458. doi:10.1134/S0021894411030151
16. Yeliseyev VV, Zinovieva TV (2014) Two-dimensional (shell-type) and three-dimensional models for elastic thin-walled cylinder. PNRPU Mech Bull 3:50–70. doi:10.15593/perm.mech/2014.3.04
17. Zinovieva TV (2012) Computational mechanics of elastic shells of revolution in mechanical engineering calculations. In: Modern engineering: science and education. Proceedings of second international scientific and practical conference. State Polytechnic University, St. Petersburg, pp 335–343
18. Bakhvalov NS, Zhidkov NP, Kobelkov GG (2011) Numerical methods (Chislennye metody) Binom. Laboratory of knowledge, Moscow, p 640 (In Russian)
19. Borwein JM, Skerritt MB (2012) An introduction to modern mathematical computing: with Mathematica, vol XVI. Springer, p 224
20. Chapra SC, Canale RP (2014) Numerical methods for engineers. McGraw-Hill Education, New York, p 992

Wheelsets and Railways. Determining Contact-Points Coordinates

Kirill V. Eliseev

Abstract Systems that contain instrumented wheelsets and algorithms for strain-measurement evaluations are used to obtain contact between wheels and railway parameters while the car is moving. So a method for the evaluation of contact point coordinates was developed. Some results of it's application are presented here.

Introduction

Wheelset is an important part of car suspension system: it determines the movement along the railway and transfer of loads between the car and railway.

An experimental evaluation of contact-point coordinates, together with contact forces, enables analysis of the quality of equipment and the condition of the railway. Results can be used for the development of new equipment.

Variants of Relative Positions of Wheels and Rails for Nominal Dimensions

The parameters of wheel–rail contact depend on the nominal dimensions of the wheels used and the rail profiles, see Figs. 1 and 2.

According to GOST 10791-2011 [1], see Fig. 1, the roll surface corresponds to the rail head profile. Starting from the flange, the roll surface is conical, with an

K.V. Eliseev (✉)
Peter the Great Saint-Petersburg Polytechnic University, Saint Petersburg, Russia
e-mail: kir.eliseev@gmail.com
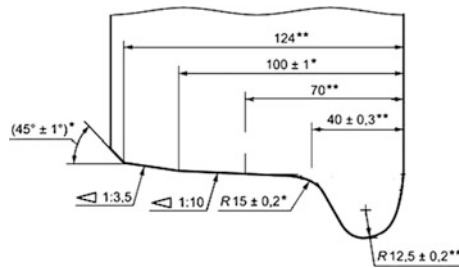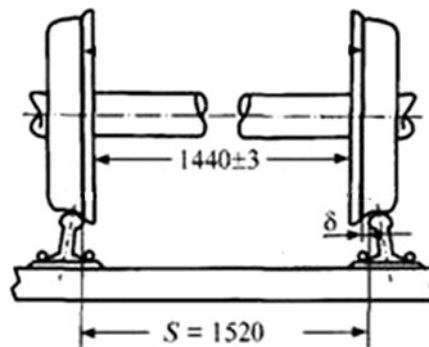
Fig. 1 Roll surface GOST 10791-2011

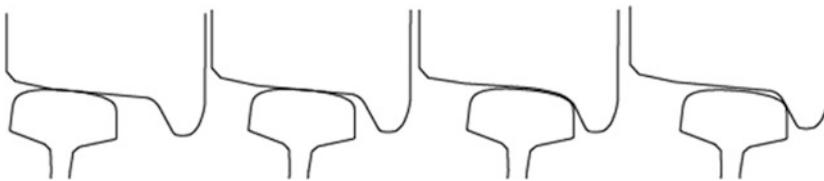**Fig. 2** Wheelset dimensions and railway width

Fig. 3 Relative positions of wheel and rail variants

inclination of 1:20 that corresponds to the rail canting. The conical surface retains a middle wheelset position relative to the railway axis, preventing deviations when moving along straight railway.

If one wheel with a smaller diameter rotates, while the other of the same pair with a larger diameter rotates, the former will move ahead, and a twisting movement will occur. If one wheel contact point lies on circle with smaller diameter while other of the same pair on circle with larger diameter, the former will move ahead, and twisting movement will occur. When the wheelset is not in the middle position relative to rails, it tends to take it again.

During movement, the wheels and the railway can achieve different relative positions, see Fig. 3.

Single area and double area contact can occur. By area, we mean the relatively small simply connected zone where contact interaction exists.

There exists a considerable number of studies devoted to the investigation of the geometric contact, i.e., section curves without deformations of corresponding parts [2, 3].

## General Information About the System of Measurement

The measurement system consists of a wheelset with installed strains gauges, a radio telemetering complex with a limited number of measuring channels (64), a calibration stand [4], an algorithm of contact forces and coordinates evaluation [5–7]. Contact forces and coordinates are determined based on the measured strains.

The following results are for a fixed, not rotating, wheelset. Cubic spline interpolation of strains is used in case of rotating wheelset, but procedure is not considered here.

Model of Wheel Set on Rails

A wheelset numerical model with wheel–rail interaction must be created to develop an evaluation algorithm. A finite-element model was created in Ansys [8] that includes wheelset and rail fragments, Fig. 4.

Forces F_{x1}, F_{z1} and torque M_{x1} are acting between a car and a bearing near wheel 1, and similar forces at the wheel 2 bearing. Column of loads $F = [F_1, \ldots, F_m]^T$ with six components can be introduced. Movements along the railway are disabled at the bearings.
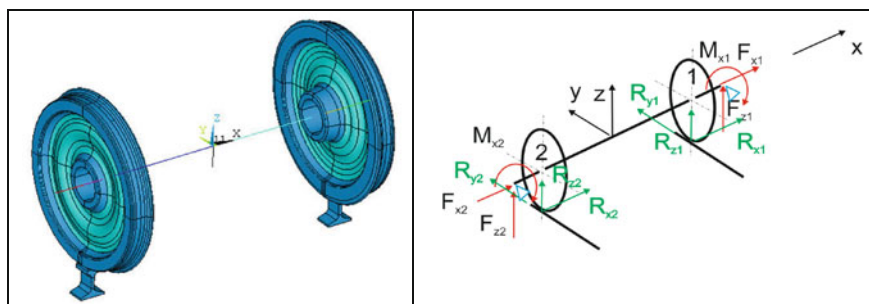
Fig. 4 Wheelset model, loads, and scheme of boundary conditions

Contact interaction between wheels and rails with friction leads to reaction forces R_{x1}, R_{y1}, R_{z1} at the wheel 1 and R_{x2}, R_{y2}, R_{z2}, at the wheel 2 that form column $R = \begin{bmatrix} R_1, \ldots, R_p \end{bmatrix}^T$ with six components.

Column $\varepsilon = [\varepsilon_1, \ldots, \varepsilon_n]^T$ with $n = 64$ consists of strains that can be obtained during analysis post-processing. These results correspond to measured strains. Gauges positions were developed in [5].

The procedure for the reconstruction of forces is as follows. At first, base loading with base vertical forces F_0 at the bearings is performed for a predefined relative configuration of wheels and rails. The results of this analysis are base strains ε_0 and reaction forces R_0 columns.

Then, one performs a series of numerical experiments when one of the force components is changed by small increments ΔF_i. Considering that the relationship between strain and the force increments is linear, we can write the relationship as:

$$\Delta\varepsilon = A\Delta F \tag{1}$$

Here, the number of equations (64) is higher than the number of applied forces (6), and the system of equations usually does not have an exact solution. So "pseudo solution" ΔF is used to minimize the Euclid norm of error $\|A\Delta F - \Delta\varepsilon\|$ [9].

The second system of linear equations connects small increments of reaction forces and applied forces:

$$\Delta R = B\Delta F \tag{2}$$

Reaction forces $\tilde{R}$ during the experiment can be evaluated based on measured strains $\tilde{\varepsilon}$ by:

$$\tilde{R} = R_0 + \Delta R = R_0 + B \left(A^T A \right)^{-1} A^T (\tilde{\varepsilon} - \varepsilon_0). \tag{3}$$

Numerical experiments prove the accuracy of this procedure. For predefined configurations, forces were determined with low errors.

We assume a linear relationship between forces and strains. A numerical experiment with increasing vertical forces was conducted, and strains and reaction forces changed nonlinearly.

At first sight, the analysis appears to be nonlinear due to the contact interaction. One can recall the most well-known contact problem, i.e., Hertz contact between two bodies analysis [10]. The relationship between bodies approach h and contact force F is $F \sim h^{3/2}$. But one can also recall that the analysis can contain both linear and nonlinear relationships between various parameters simultaneously. Here we are interested in the relationship between contact forces and the strains far from contact area, and this relationship must be linear for elastic material.

Analysis of the results has shown that, while the force is increasing, the contact area moves, see Figs. 5 and 6. It is happening due to contact changes, as the wheels and rails bend.

The stated algorithm has shown its efficiency in general, but with some limitations:

- it is difficult to take contact coordinates into account;
- results depend on model configuration, friction, and railway parameters;
- the solution is not unique due to friction.

Fig. 5 Contact point coordinate versus press force
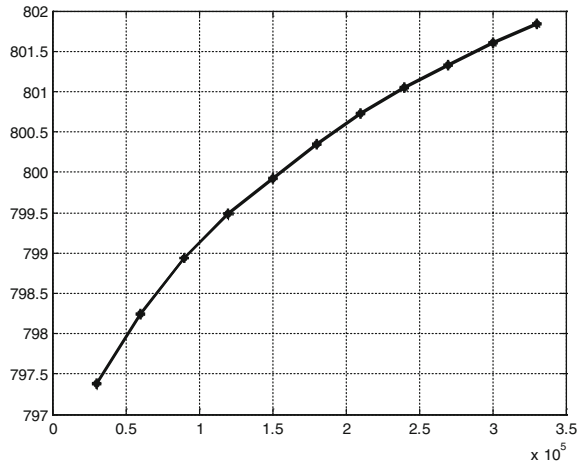
Fig. 6 Contact nodal force distribution for increasing press force
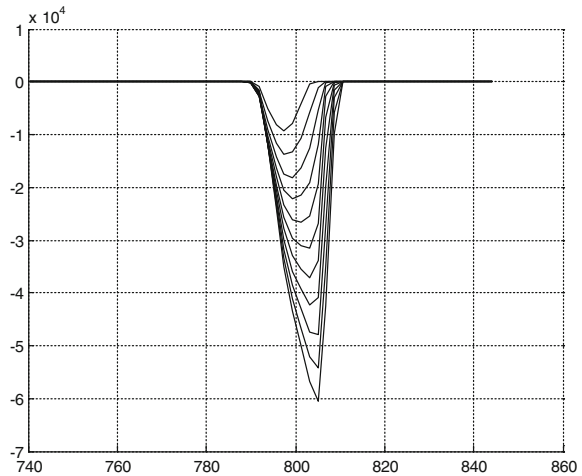
Model with Concentrated Loads

The second model of a wheelset was developed to introduce a modified algorithm. We assume that the contact area is relatively small. For every contact area, three forces that act at one point, instead of normal contact and tangential pressures, are introduced.

The following boundary conditions at the bearings are used, see Fig. 7:

- springs in direction along the rail and for rotation about the vertical axis at bearings; stiffness corresponds to the intermediate plate between bogie and wheelset
- zero displacements $u_{xi} = 0$, $u_{zi} = 0$ and rotations $\theta_{xi} = 0$.

Here we can apply different concentrated forces acting between the rails and wheels, and we do not have to work with forces and torques between the wheelset and bogie.

A number of experiments were conducted where one force component or contact point coordinate was changed. We can obtain a system of linear algebraic equations that connect strains and forces $\varepsilon = AR$.

Here, R is an extended column of vectors that consists of contact forces components and contact points coordinates x_i, $R = \left[R_{x1}, R_{y1}, R_{z1}, R_{x2}, R_{y2}, R_{z2}, x_1, x_2 \right]^T$. Similar to the first model, we have to use pseudo solution to restore forces by measured strains

$$R = C\varepsilon, \quad \text{where } C = \left(A^T A \right)^{-1} A^T. \tag{4}$$

Both matrices consist of two independent parts that connect forces and strains for one wheel, so no cross terms exist. Thus any wheel can be analyzed independently. The influence of the contact-point coordinate on measured strains and matrices A and C coefficients was analyzed. Forces were kept constant. It appeared that strains were changing almost linearly, with small deviations from linear dependency when the contact point was close to the flange.

Analysis of matrix A for one wheel showed that there are two groups of columns in the matrix. The elements of columns 1–3 (corresponding to forces) change almost linearly, while the change in the elements of column 1 are very small. Elements of
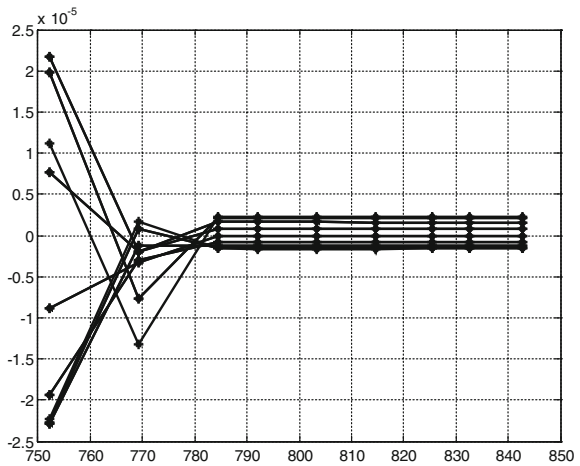
Fig. 7 Wheelset model, no contact with rails
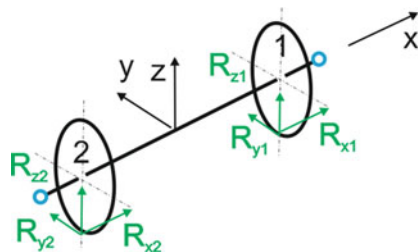
Fig. 8 Matrix A elements versus contact point coordinate. Column 1
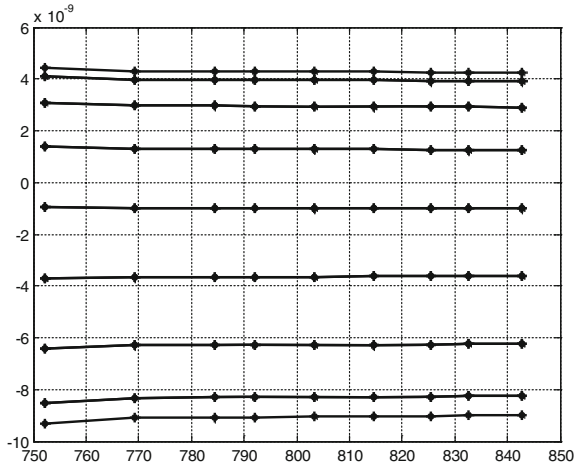
Fig. 9 Matrix A elements versus contact point coordinate. Column 4

column 4 (corresponding to contact coordinate) are changing considerably in a nonlinear manner when the contact is close to the flange, see Figs. 8 and 9.
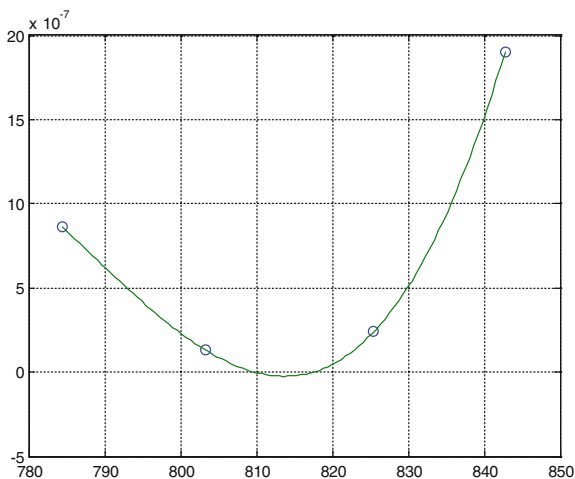
Algorithm of Contact Forces and Coordinates Determining

The algorithm of contact forces and coordinates determining is as follows.

We have a set of matrices C that were evaluated for various base variants of contact positions (up to 14 variants were used). Matrices from numerical experiments with the finite element model or measured by means of calibration stand [4] can be used. A set of 32 measured strains on one wheel at selected positions is available.

Table 1 Results of forces and coordinates restoration

Contact point variant		Exact values	Result using residual	1	6	12	17
Base contact coordinates (mm)	x1			842.8	825.5	803.2	784.4
	x2			−842.8	−825.5	−803.2	−784.4
Contact forces 1.0e+005 (N)	Rx1	0.0000	0.0000	−0.0005	0.0000	0.0000	0.0001
	Ry1	0.0000	0.0000	0.0000	0.0000	0.0000	0.0000
	Rz1	1.4500	1.4499	1.4538	1.4505	1.4501	1.4494
	Rx2	0.0000	0.0000	0.0004	0.0000	0.0000	0.0001
	Ry2	0.0000	0.0000	0.0000	0.0000	0.0000	0.0000
	Rz2	1.3500	1.3499	1.3533	1.3505	1.3501	1.3494
Evaluated contact coordinates (mm)	Wh1	814.5	814.6	812.3	813.7	815.4	816.8
	Wh2	−814.5	−814.5	−814.3	−814.5	−814.5	−814.5
$\|A_kR_k - \varepsilon\|$				1.6e−08	1.9e−06	2.4e−07	1.3e−07	8.6e−07

Fig. 10 Typical interpolation spline for residual $\|A_{1k}R_{1k} - \varepsilon_1\|$

In the first modification of the algorithm, contact forces and position are restored for all variants of C matrices, and the obtained contact coordinates are analyzed. We choose variants with coordinates that is close to the variant's base value.

Table 1 presents example of such a procedure. Forces are applied at points with coordinates ±814.5 mm. The evaluated contact coordinates for base points 6 and 12 are close to the base contact point coordinates and close to applied. Generally speaking, the results here for base points 1 and 12 are also close to applied.

In the second modification of the algorithm, only forces using reduced matrices C are evaluated. For all base variants, a norm of deviation $\|A_kR_k - \varepsilon\|$ is evaluated for every wheel, and the interpolating cubic spline [7] is analyzed, see Fig. 10.

The position of points with minimum residual values is an estimation of the contact-point coordinate. Then we can make interpolation splines [11] for all C matrix coefficients and obtain this matrix for the contact-point coordinate. After all, this new matrix is used to determine contact forces. Results of this procedure are presented in Table 1, in column 4 for the previous example.

Method Verification. Case of Single-Area Contact

The algorithms were checked by means of a series of numerical experiments. The first model of the wheelset on rails was used. One of the rails is moved along the X-axis to get different contact-point positions. The model contact point is determined using the condition for torque relative to that point: $M_y = 0$.

For relatively small rail movements, the contact remains a single-area contact. Both algorithm variants generate close results, with small errors of the contact coordinate, being less than 2 mm.

Method Verification. Case of Double-Area Contact

When one of the rails is moved 10 mm away from the railway center, the corresponding contact interaction is a double-area contact. The typical nodal force distribution is presented in Fig. 11. In this example, there are two contact areas with contact points of 754 mm (on flange) and 785 mm. The second method modification gives good agreement for the total contact forces and a value of 782 mm for the contact position.

Analysis of tests results has shown that, in the case of double area contact, the algorithm generates equivalent parameters of some single-area contact, i.e., good agreement for total values of contact forces and coordinates of an equivalent contact point.

Let's look at a beam model analogy. The plane-beam configuration with two beams corresponds to the wheel section near the connection between the disk and rim, see Fig. 12.

Contact forces are acting at contact positions 1 and 2. Longitudinal strains are measured in the inclined beam cross section, and they depend on the stretching force and bending torque in the cross section.

To replace contact points 1 and 2 by one equivalent point (*), force and torque in the cross section must retain their values. Also, the arbitrariness of the measuring section produces the following formulae for the coordinates of equivalent point bases on coordinates of real points 1 and 2 and applied forces:

Fig. 11 Contact nodal force
distribution. Here side forces
are positive, and vertical
forces are negative
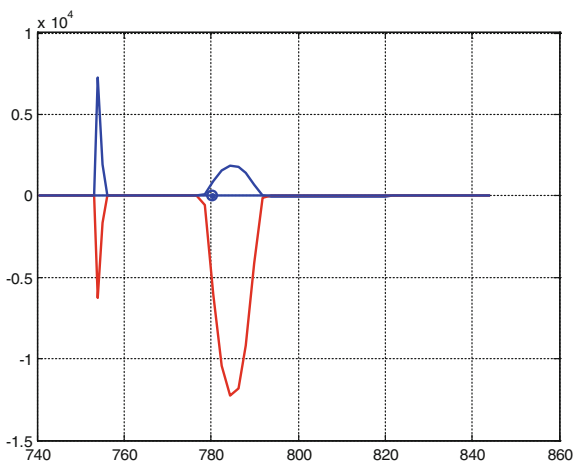
Fig. 12 Beam analogy for
double- and single-area
contact
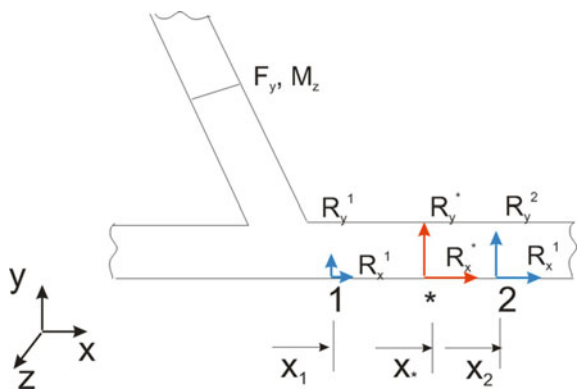
$$x^* = \frac{R_y^1 x_1 + R_y^2 x_2}{R_y^1 + R_y^2} \tag{5}$$

The above formulae for previous example gives value for equivalent contact point
coordinate 782.7 mm, compare with value 782 mm obtained in the numerical procedure.

Conclusion

The algorithm of the estimation of contact points between wheel and rail coordi-
nates is presented. Numerical tests have shown that, in the case of single-area
contact, the error is less than 2 mm. In the case of double-area contact, the results
are coordinates of equivalent contact points for single-area contact.

References

1. GOST 10791-2011 Solid-rolled wheels. Technical conditions. Moscow, Standartinform (Rus)
2. Shevtsov I (2008) Wheel/rail interface optimization. Delft University of Technology, The Netherlands
3. Wickens A (2003) Fundamentals of rail vehicle dynamics. Guidance and stability. Swets & Zeitlinger Publishers
4. Eliseev K, Migrov A, Orlova A (2012) Design of test-rig for the calibration of instrumented wheelsets. Transport Problems 2012, Silesian University of Technology Faculty of Transport, pp 474–479 (Rus)
5. Eliseev K, Ispolov I, Orlova A (2013) Contact forces between wheelset and rails determining. St. Petersburg State Polytechnical Univ J 4–1(183):262–270 (Rus)
6. Eliseev K (2014) Modern methods of contact forces between wheelset and rails determining. Advances in mechanical engineering selected contributions from the conference "modern engineering: science and education", Saint Petersburg, Russia, June 2014
7. Ronasi H, Nielsen J (2013) Inverse identification of wheel–rail contact forces based on observation of wheel disc strains: an evaluation of three numerical algorithms. Veh Syst Dyn Int J Veh Mech Mobility 51(1):74–90
8. ANSYS (2014) Release 15 user guide
9. Albert A (1972) Regression and Moor-Penrose pseudoinverse, vol 94. Academic Press
10. Landau L, Lifshits E (1987) Theoretical physics. Theory of elasticity. Moscow, Science (Rus)
11. Zavialov J, Kvasov B, Miroshnichenko V (1980) Spline functions methods. Moscow, Science (Rus)

Author Index